Crystallographic Lattice Boltzmann Method

A Thesis
Submitted for the Degree of
Doctor of Philosophy

by

N L D B Manjusha Namburi

Engineering Mechanics Unit
Jawaharlal Nehru Centre for Advanced Scientific Research
(A Deemed University)
Bangalore – 560 064

JULY 2018

Dedicated to my parents and husband

DECLARATION

I hereby declare that the matter embodied in the thesis entitled "**Crystallographic Lattice Boltzmann Method**" is the result of investigations carried out by me at the Engineering Mechanics Unit, Jawaharlal Nehru Centre for Advanced Scientific Research, Bangalore, India under the supervision of **Prof. Santosh Ansumali** and that it has not been submitted elsewhere for the award of any degree or diploma.

In keeping with the general practice in reporting scientific observations, due acknowledgment has been made whenever the work described is based on the findings of other investigators.

N L D B Manjusha Namburi

CERTIFICATE

I hereby certify that the matter embodied in this thesis entitled "**Crystallographic Lattice Boltzmann Method**" has been carried out by **Ms. N L D B Manjusha Namburi** at the Engineering Mechanics Unit, Jawaharlal Nehru Centre for Advanced Scientific Research, Bangalore, India under my supervision and that it has not been submitted elsewhere for the award of any degree or diploma.

Prof. Santosh Ansumali
(Research Supervisor)

Acknowledgements

I would like to express my sincere gratitude to Prof. Santosh Ansumali for his constant support and encouragement during the course of my Ph. D. It was a pleasure to learn the intricacies of kinetic theory and lattice Boltzmann method from him.

I have learned a lot from the courses taught by Prof. Rama Govindarajan, Prof. Ganesh Subramanian and Prof. Subir K Das.

I would like to thank the thesis reviewer for the insightful question related to Bandwidth limited solutions of PDEs.

I would like to thank Siddharth and Chakri for helping me on various computational issues from time to time. I would like to thank Ponnu who helped me on various theoretical aspects of fluid dynamics. I enjoyed discussions on various topics with my other lab-mates: Shiwani, Reddy, Praveen, Mahan,Atif, Samarth, Shourya, Nishanth. I would like to thank all EMU friends for the enjoyable time. Special thanks to my friends Loukya, Prasoona who made my life enjoyable in JNC.

I thank our administrative officer, A. Jayachandra, Dr. Princy, library, complab, hostel and other admin staff for their cooperation.

I am indebted to my husband who extended his support through my highs and lows and in finishing the Ph. D. Finally, I wish to thank my parents, brother and in-laws for their unconditional support and encouragement.

Abstract

In the last two decades, Lattice Boltzmann Method (LBM) has emerged as an efficient alternative for hydrodynamic simulations. In LBM, a fictitious lattice with suitable isotropy in the velocity space is considered to recover Navier-Stokes hydrodynamics in macroscopic limit. The same lattice is mapped onto a Cartesian grid for spatial discretization of the kinetic equation. In this thesis, we present an inverted argument of the LBM, by making spatial discretization as the central theme. We argue that the optimal spatial discretization for LBM is a Body Centered Cubic (BCC) arrangement of grid points. This thesis shows that this inversion of the argument of LBM and making of spatial discretization the central point indeed provides lot more freedom and accuracy in the velocity space discretization. We illustrate an order-of-magnitude gain in efficiency for LBM and thus a significant progress towards the feasibility of DNS for realistic flows. This thesis systematically investigates requirements for higher order Lattice Boltzmann Models and shows that it is possible to construct models for compressible flows as well as the description of finite temperature variations on a BCC lattice. For compressible flows, a hybrid methodology to compute discrete equilibrium in an efficient fashion is proposed.

List of Figures

List of Tables

Contents

Chapter 1
Introduction

Fluid dynamics simulations are an integral part of science and engineering applications. Fluid flows occurring in nature exhibit a plethora of characteristics and their behavior can usually be gauged using non-dimensional parameters. For example, the marked qualitative difference between the cardiovascular flows and flow induced from a swimming blue whale can be explained using the stark difference between their respective Reynold's number [1] (10^{-3} as compared to 10^8). Such non-dimensional parameters provide only a rough idea of the behavior of the fluid flow, and one must resort to solving the Navier-Stokes equation, the governing equations of fluid flow, to gain a deeper understanding of the flow field. However, the complexity associated with these highly non-linear partial differential equations (PDE) makes them difficult to solve analytically and hence computational methods must be employed.

In practice, applications of Computational Fluid Dynamics (CFD) to the physics of complex flows often requires highly accurate and adaptive methods for complex geometries. However, the size of the grid required to resolve all length-scales to perform "Direct Numerical Simulations" (DNS) of turbulent flow is often too high for practical applications (Pope, 2000). Here we remind that for DNS of homogeneous turbulence, the most accepted methodology is Pseudo-Spectral (PS) method, which has spectral accuracy unmatched by alternative methods. However, it has relatively poor parallel scaling and is limited mainly to periodic domains and to a few other simple geometries such as channel flow (Hussaini & Zang, 1987). Thus, one looks for alternate methods for DNS of turbulent flows. With existing approaches, it is widely accepted that DNS of separated turbulent flows will be feasible only after a decade (Larsson & Wang, 2014; Slotnick *et al.*, 2014; Thantanapally *et al.*, 2013*a*). Indeed, recent studies have advocated the use of a hybrid approach where both Large Eddy Simulation (LES) and Reynolds Averaged Navier-Stokes (RANS) are used in appropriate parts of the domain (Larsson & Wang, 2014; Slotnick *et al.*, 2014). Thus an algorithmic improvement which can make DNS feasible and realistic for hydrodynamic simulation is critically required.

In recent years, structured grid methods have gained attention due to their simplicity and ease of parallelization. The expectation is that a simple but highly parallelizable algorithm will be able to efficiently utilize modern super-computing clusters, which are often quite heterogeneous. Furthermore, these class of methods also tend to be more efficient in terms of memory bandwidth utilization, an important bottleneck in high performance computing (Shet *et al.*, 2013). Thus, in the last two decades, many algorithms such as Lattice Boltzmann Method (LBM) were developed for accelerating hydrodynamic simulations. LBM, with its simplified kinetic picture on a lattice, is highly parallelizable and scalable. It has emerged as an alternative numerical method for applications ranging from fluid turbulence to polymer dynamics, density functional theory, soft matter, etc (Thantanapally *et al.*, 2013*a*; Chen *et al.*, 2003; Singh *et al.*, 2013*b*; Thampi *et al.*, 2013; Mendoza *et al.*, 2010*b*; Benzi *et al.*, 2013; Chen *et al.*, 2004; Ansumali *et al.*, 2007*b*; Chen *et al.*, 1992; Qian *et al.*, 1992; Lallemand & Luo, 2000; Chen & Doolen, 1998*a*; Aidun & Clausen, 2010*b*; Benzi *et al.*, 1992; Higuera *et al.*, 1989; Succi, 2001*a*).

The LBM is a kinetic level description with its roots in the Boltzmann equation. The continuous Boltzmann equation describes the evolution of the distribution function $f(\mathbf{x}, \mathbf{v}, t)$ which represents the probability of finding a particle at $(\mathbf{x}, \mathbf{x} + d\mathbf{x})$ with a velocity between

[1] The ratio of inertial force to the viscous force.

$(\mathbf{v}, \mathbf{v} + d\mathbf{v})$ in phase space as (Cercignani, 1975):

$$\frac{\partial f}{\partial t} + \frac{\partial}{\partial x_\alpha}\left(c_\alpha f\right) + g_\alpha \frac{\partial f}{\partial c_\alpha} = \mathcal{J}\left(f, f\right). \tag{1.1}$$

The macroscopic quantities such as the mass, momentum, energy etc emerge as appropriate moments of the distribution function in velocity space as follows:

$$\rho = \int_{-\infty}^{\infty} f \, d\mathbf{c}, \qquad j_\alpha = \int_{-\infty}^{\infty} f c_\alpha \, d\mathbf{c}, \qquad E = \int_{-\infty}^{\infty} f c_\alpha^2 \, d\mathbf{c}. \tag{1.2}$$

However, the continuous Boltzmann equation is too complex to solve. Hence, one looks for alternate numerical tools which capture the dynamics and are computationally attractive. It has been found that restricting the velocity space to a fictitious lattice that can be mapped onto a Cartesian grid for spatial discretization simplifies the equation and a solution is readily obtained. The choice of the lattice dictates the accuracy and ease of parallelization and is the subject of this thesis.

In LBM model, the velocities of the particles in D dimensions, are restricted to a discrete velocity set $\mathcal{C} = \{c_1, c_2, \cdots, c_{N_d}\}$ with N_d being the number of velocities in the set. For every element $\mathbf{c}_i \in \mathcal{C}$, one defines a set of discrete populations f_i. The set $\mathcal{C}$ is chosen to satisfy an appropriate set of symmetries needed to recover hydrodynamics in long time limit from the evolution equation of discrete populations f_i (Yudistiawan *et al.*, 2010). The hydrodynamic quantities such as mass density ρ, the momentum density $j_\alpha = \rho u_\alpha$ with u_α as fluid velocity and energy E are defined as the moments of the distribution function as:

$$\sum_{i=1}^{N_d} f_i = \rho, \qquad \sum_{i=1}^{N_d} f_i c_{i\alpha} = j_\alpha = \rho u_\alpha, \qquad \sum_{i=1}^{N_d} f_i c_\alpha^2 = E = \rho u^2 + 3\rho\theta, \tag{1.3}$$

where θ is temperature measured in units of k_B/m with k_B as the Boltzmann constant and m being the mass of the molecule. Typically, the discrete version of the evolution equation for f_i is written as:

$$f_i(\mathbf{r} + \mathbf{c}_i \Delta t, t + \Delta t) = f_i(\mathbf{r}, t) + 2\beta[f_i^{\mathrm{eq}}(\mathbf{r}, t) - f_i(\mathbf{r}, t)], \tag{1.4}$$

where Δt is the chosen time step and $\beta = \Delta t/(2\tau + \Delta t)$ denotes the discrete dimensionless relaxation parameter. Here, the choice of the discrete version of Maxwell Boltzmann distribution f^{MB}, here onwards termed as discrete equilibrium $f_i^{\mathrm{eq}}(\rho(\mathbf{r}, t), u_\alpha(\mathbf{r}, t))$, is crucial for recovering the correct hydrodynamic limit and different formulations of lattice Boltzmann differ from each other mainly in choice of this discrete equilibrium. A common choice is to project the Maxwell-Boltzmann on the Hermite basis to get a computationally attractive polynomial expression of the equilibrium as (Chen *et al.*, 1992; Qian *et al.*, 2007; Benzi *et al.*, 1992; Shan & He, 1998):

$$f_i^{\mathrm{eq}} = w_i \rho \left[1 + \frac{u_\alpha c_{i\alpha}}{\theta_0} + \frac{u_\alpha u_\beta}{2\,\theta_0^2}\left(c_{i\alpha} c_{i\beta} - \theta_0 \delta_{\alpha\beta}\right)\right], \tag{1.5}$$

where w_i is the weight chosen in such a way that the following constraints are ensured

$$\sum_{i}^{N_d} f_i^{\mathrm{eq}} = \rho, \qquad \sum_{i}^{N_d} f_i^{\mathrm{eq}} c_{i\alpha} = \rho u_\alpha, \qquad \sum_{i}^{N_d} f_i^{\mathrm{eq}} c_{i\alpha} c_{i\beta} = \rho u_\alpha u_\beta + \rho\theta_0 \delta_{\alpha\beta}, \tag{1.6}$$

and θ_0 is some reference temperature associated with the chosen lattice.

1.1 Motivation

To achieve spectral accuracy that PS method can achieve, LBM requires an order-of-magnitude (2 to 2.5 times in each direction) larger grid points in 3D as compared to PS method. Nevertheless, in practice, LBM is competitive with respect to PS due to very high parallel efficiency and flexibility in handling complex geometries. Indeed, in a heterogeneous computing environment, LBM and PS can perform DNS at comparable Reynolds Numbers for simple flows (Thantanapally *et al.*, 2013*a*; Chikatamarla *et al.*, 2010).

Historically, the lattice chosen for LBM has been the Simple Cubic (SC) cell which demands that the grid be refined near the solid body or in zones of extreme flow variations (Filippova & Hänel, 1998; Succi *et al.*, 2002*a*). A fundamental problem with such refinements is that the local accuracy of the method remains unchanged and optimization is done only with respect to the global distribution of grid points. For example, for decaying turbulence in a periodic geometry, local grid refinements cannot improve the accuracy of LBM. Thus improving the accuracy and ability to capture local curvatures, while keeping its parallel efficiency intact is an important challenge in LBM. This can be achieved by the principles of crystallography in defining the base lattice which has superior packing efficiency.

A better choice for spatial grid distribution is a Body-Centered Cubic (BCC) with highest packing efficiency in the 3-dimensional arrangement of grid points for which the Wigner-Seitz cell is a truncated octahedron (Conway & Sloane, 2013). With this lattice, we achieve better space coverage and also a unification of the discretization of space and velocities. This can be seen in Fig.1.1 by the representation of a circle and sphere on the SC and BCC lattice.

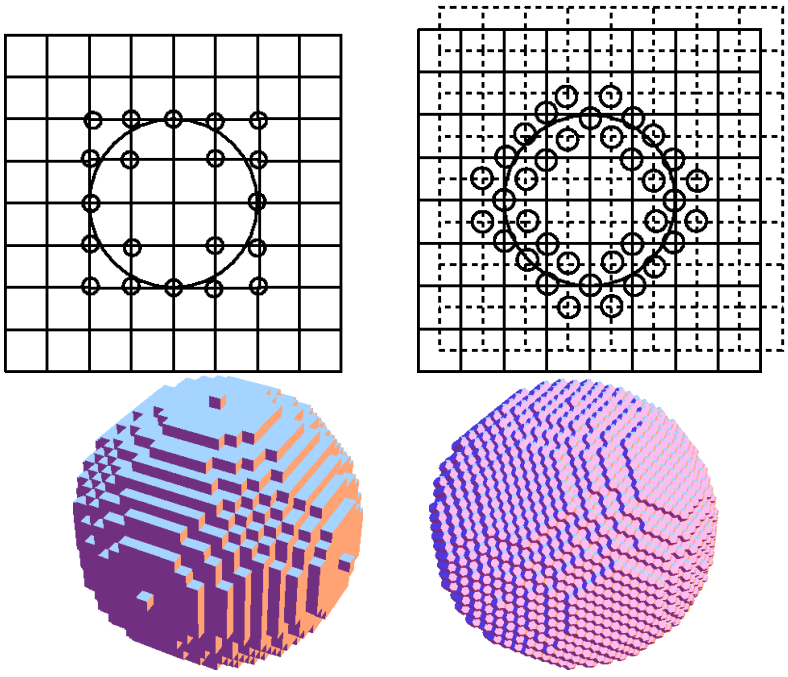

Figure 1.1: Representation of the shapes on SC (left) and BCC (right)

In this thesis, we present a model developed based on modifing the base grid of the LBM from SC to BCC which will bridge the gap between spectral accuracy and the optimization in grid requirement for the problems involving high flow variations and solid-fluid boundaries. Finally, we illustrate an order-of-magnitude gain in efficiency for LBM and thus a significant progress towards the feasibility of DNS for realistic flows.

1.2 Outline of the thesis

Motivated by the need for a better accuracy and efficiency of the Lattice Boltzmann Method, the present thesis work addresses following main technical issues:

- **LBM formulation on Body-Centered Cubic Lattice:** In LBM, a fictitious lattice with suitable isotropy in the velocity space is considered to recover Navier-Stokes hydrodynamics in macroscopic limit. The same lattice is mapped onto a Cartesian grid for spatial discretization of the kinetic equation. In this thesis, we present an inverted argument of the LBM, by making spatial discretization as the central theme. We argue that the optimal spatial discretization for LBM is a Body Centered Cubic (BCC) arrangement of grid points. We illustrate an order-of-magnitude gain in efficiency for LBM and thus a significant progress towards the feasibility of DNS for realistic flows.

- **Higher order Lattice Boltzmann:** The application of LBM to incompressible flows and the problems involving low Mach number(Ma) flows is well known. However, applying LBM for compressible thermal flows and high Ma flows is a challenging problem due to higher order isotropy condition on discrete velocities sampled from link of the underlying lattice. This thesis systematically investigates requirements on higher order lattice Boltzmann models and show that it is possible to construct models for compressible flows as well as the description of finite temperature variations. Finally, a three-dimensional model which can operate in transonic regime is constructed.

- **Efficient evaluation of exact equilibrium distribution:** In addition to the choice of the lattice with appropriate isotropy, the choice of discrete equilibrium distribution function is crucial for recovering the correct hydrodynamics. A common choice of calculating the discrete equilibrium distribution is to project the Maxwell-Boltzmann distribution on the Hermite basis to get a computationally attractive polynomial expression (Chen *et al.*, 1992; Qian *et al.*, 2007; Benzi *et al.*, 1992; Shan & He, 1998). This procedure allows writing the equilibrium distribution as a power series in terms of the Mach number with expansion point being no flow case of zero Mach number. It is also important to ensure the positivity of the equilibrium distribution and restoration of the H-theorem for discrete space-time evolution (Karlin *et al.*, 1999; Boghosian *et al.*, 2001; Ansumali *et al.*, 2003; Karlin *et al.*, 1998; Boghosian *et al.*, 2003; Wagner, 1998; Chen & Teixeira, 2000; Succi *et al.*, 2002*b*). However, the computational simplifications for the equilibrium evaluation can lead to loss of positivity of the equilibrium and thus H-theorem. Thus, the existing methodology of finding perturbative equilibrium is not expected to work for the case of strong flow characterized by either finite Mach number (Ma) or finite temperature variations (while using energy conserving equilibrium). Thus, for higher order LBM, where these issues are more important, one often employs iterative algorithms to find equilibrium. In this thesis, we provide a hybrid methodology to compute discrete equilibrium efficiently. The basic idea is to derive the Lagrange multipliers for discrete equilibrium at high precision for a general discrete velocity model and then use this expression in a Newton-like iterative scheme. We provide examples to illustrate that such a method converges in very few iterations. As the number of iterations required is very few, the use of "if" condition branching such as to check convergence can be eliminated entirely in numerical implementations.

- **Exact solutions of kinetic equation for canonical flows:** It is well understood that discrete velocity model simulated by the standard lattice Boltzmann form a hierarchy of approximations to the Boltzmann BGK equation. Indeed as the number of discrete velocities increases, one finds that the method can provide a quantitative prediction, especially in the transition regime. However, the same can not be said about the most widely used three dimensional model with 27 velocities (typically termed as D3Q27 model). Though, this

model predicts the velocity slip correctly, it fails to reproduce Kinetic boundary layer (an essential feature of Boltzmann BGK equation). This thesis investigates the improvement in the velocity space accuracy of the lattice Boltzmann formulated on the BCC grid. The canonical flow setups for which exact solutions are known for the standard D3Q27 model provide a convenient test for such investigations. It is shown that even a 27 velocity model, when formulated on the BCC grid reproduces Kinetic boundary layer. Thus, for gaseous microflow, the current approach provides a distinct advantage over the conventional LBM.

In subsequent chapters, these progress in Lattice Boltzmann method will be reported. The thesis is organized as follows:

- In chapter 2 we review the basic definitions of Crystallography such as point lattices, and packing of hypersphere problem. We also described the efficient sampling lattice and the Nyquist theorem of sampling lattices, finally the isotropy conditions on the moments. Using the sampling theory and the Crystallographic viewpoint, we conclude that BCC is the most efficient lattice for sampling a bandwidth limited function.

- In chapter 3, we will briefly review the principles of the kinetic theory and the Boltzmann equation for dilute gases along with the properties of the Maxwell-Boltzmann distribution function for the continuous kinetic theory. From Boltzmann equation, construction of the continuous grad moment system and the moment chain representation will be discussed. Finally, evolution equations for the moments along with different methods to obtain closure relation has been presented in this chapter.

- In chapter 4, we will examine the minimum requirement for any moment based method to capture the Knudsen boundary layer in continuous Kinetic theory. The solution to the unidirectional flows using the continuous grad method, and predicting the Kinetic boundary layer are discussed. The minimum condition on the fourth order moment for predicting the Knudsen boundary layer is obtained by analyzing the closure relations of continuous Grad 13, 26 moment systems Finally, it has been shown that Grad's 26-moment method can indeed capture the Knudsen boundary layer.

- In the chapter 5, the detailed description of constructing Lattice Boltzmann Method from the continuous Boltzmann equation has been presented.

- In chapter 6, LB method developed on the principles of Crystallography will be presented. This model will be validated for the flow with the Kida-Peltz vortex initial conditions and applied to the classical case of flow past sphere problem to determine the accuracy of the model at high Re flow which involves the solid-fluid boundaries. Indeed it will be shown that the model is capable of capturing the drag crisis. To verify the validity of the model for high Knudsen number (Kn) flows, the canonical problem of Couette and Poiseuille flows will be solved and in fact, the model can trace the Knudsen boundary layer.

- In chapter 8, The importance of finding the equilibrium distribution and calculating it via perturbative series expansion is described. We also provided a hybrid methodology to compute discrete equilibrium in an efficient fashion by solving the Lagrange multipliers for discrete equilibrium at high precision for a general discrete velocity model and then use these expressions in a Newton-like iterative scheme. The numerical method to find the discrete equilibrium is discussed, which ensures the positivity of discrete populations. The error in important moments calculated using the numerical method for different models are shown in this chapter.

- The chapter 9 describes the higher order LB method on BCC grid. To extend our method to higher Ma flow simulations and the flows with thermal gradients, we have used the

higher order LB methods. These models are tested for the Rayleigh-Benard simulations where thermal gradients are involved and Shockwave simulations at high Ma.

Chapter 2
Lattices and sampling efficiency

2.1 Introduction

An important reason for computational efficiency of LBM is that the lattice used in the velocity space discretization is mapped onto a Cartesian grid for spatial discretization of the kinetic equation. This has an extra advantage that the characteristic discretization always leads to a move from one site to another on a lattice. Thus, there is no explicit need for any spatial discretization. This search of discrete velocity set in LBM was merely restricted to a search of appropriate connectivity vectors on Simple Cubic (SC) lattice (also hexagonal lattice in 2-D) itself. In this thesis, we present an inverted argument of the LBM, wherein spatial domain sampling efficiency of the lattice is made a central theme. Before doing so, in this chapter, we review lattices and their sampling efficiency along with the isotropy of the link vectors.

The problem of discretizing the continuous signal into discrete space and capturing the most information can be related to the optimal sampling theory. A lattice is the periodic arrangement of the samples, and by using this sampling theory, one can find out the most efficient sampling lattice which in turn can be related to the efficient discretization of the continuous sampling. For a fully resolved three-dimensional simulation in periodic geometry, a reasonable approximation is to assume that the functions to be modeled are isotropic and are bandwidth limited (Fourier coefficients are zero above a cut-off wavenumber). The best approximation for any band-limited function can be obtained by maximizing the packing efficiency in Fourier space domain without any overlap of the samples. This problem can be viewed as the close packing of spheres (Entezari *et al.*, 2009). It can be concluded that an optimal sampling of a band-limited function is equivalent of the lattice with close packing of spheres in Fourier domain.

In order to ensure that the lattice Boltzmann models have appropriate hydrodynamic limits, one needs to ensure that the underlying lattice in the velocity space is isotropic. Thus, in this chapter, we also analyze a procedure to evaluate and systematically construct the isotropic moment on a lattice with a given set of discrete velocities. These conditions can be used to construct a lattice model with n^{th} order isotropy of moments to capture the deeper physics of a problem.

The chapter is organized as follows: In section 2.2, the Nyquist theorem of sampling lattices will be reviewed. In section 2.3, basic definitions of point lattice, fundamental Parallelepiped and reciprocal lattice will be presented. Section 2.4 will describe the closest packing of hyperspheres problem in detail, and in section 2.5, the efficient sampling lattice will be discussed. Finally, the section 2.6 will deal with the isotropy on the lattices and gives the detail information for Simple Cubic, Face Centered Cubic and Body-Centered Cubic lattice structures.

2.2 Nyquist-Shannon sampling theorem

When a continuous signal is periodically measured in some discrete interval, it is termed as sampling the signal. The discrete signal is a faithful representation of the original signal and it depends on the sampling frequency (Shannon, 1949). The theory of sampling asks the question that at what rate discrete signals should be sampled to reconstruct a given continuous signal faithfully. For example, if we are sampling a sinusoidal wave and if the sampling frequency is one per cycle, the sample wave can be interpreted as a constant function. On the other hand, if we sample two times per cycle, then the signal is close to the actual sinusoidal waveform. This

is shown in the Fig. 2.1. Nyquist-Shannon sampling theorem answered this question for generic band-limited functions. A waveform is said to be bandwidth limited if its Fourier transform vanishes outside a finite subspace. Let $g(t)$ is a function, whose Fourier transform is $G(f)$ then the function is bandwidth limited to the frequency ω if,

$$G(f) = 0 \text{ for } |f| < \omega. \tag{2.1}$$

Nyquist-Shannon sampling theorem states that a band-limited function g(t) with the maximum bandwidth ω can be reconstructed perfectly from its samples if the sampling frequency is at least 2ω (i.e., the samples are spaced with $1/2\omega$ apart).

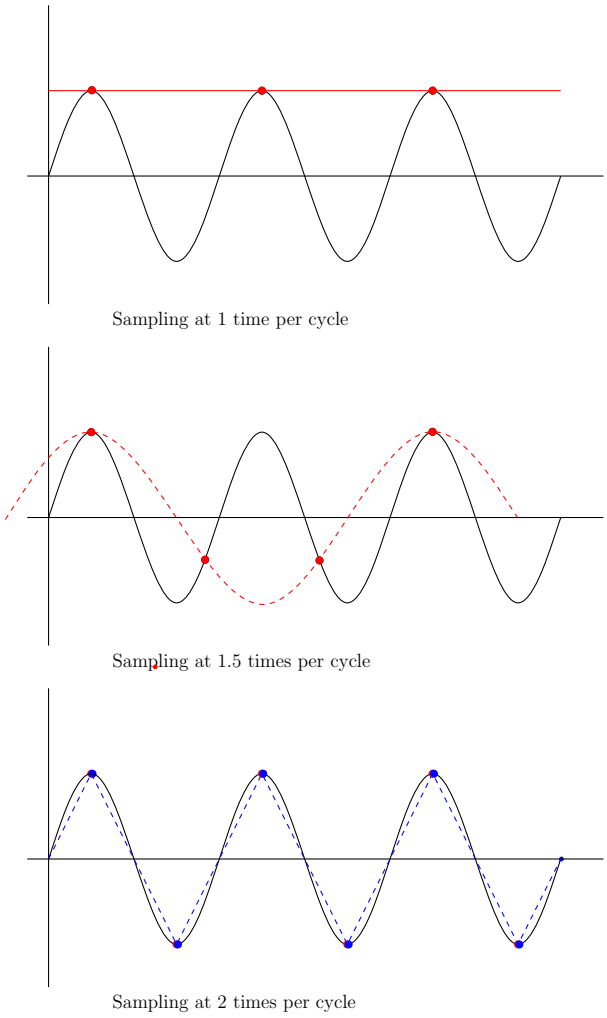

Figure 2.1: Sampling of sinusoidal wave at different rates.

The generation of regular sampling points in any dimensions can be generalized as a point lattice. The next section reviews the point lattices and its properties.

2.3 Point lattices

A point lattice is an infinite arrangement of points in space which looks the same when viewed from any lattice point. The point lattice has the properties that the set contains the origin and is closed under addition and negation. In other words, the set contains $\mathbf{0} = \{0, 0, \cdots, 0\}$ and if there are position vectors for two points as a and b then there exist points with position vectors $a + b$ and $a - b$ also. A point lattice L in N-dimensional real space $\mathcal{R}^N$ is a discrete subgroup

of $\mathcal{R}^N$. The point lattice L can be defined mathematically as the integer linear combination of the set of N linearly independent vectors $v_1, v_2, \cdots v_N$, termed as the basis vectors,

$$L = \{\mathbf{Mj} : j \in \mathcal{Z}^N\}, \tag{2.2}$$

where $\mathbf{M}$ is a matrix constructed with the basis vectors as the columns and is termed as a generator matrix for the lattice. The generator matrix $\mathbf{M}$ can be represented as:

$$\mathbf{M} = \{\mathbf{v_1}\ \mathbf{v_2}\ \cdots \mathbf{v_N}\}. \tag{2.3}$$

The elements in L are called lattice points or lattice vectors.

For any lattice in Cartesian space, the generator matrix is non-unique. If $\mathbf{M}$ is a generator matrix there exist another generator matrix $\mathbf{M'}$ defined as:

$$\mathbf{M'} = U\mathbf{M}, \tag{2.4}$$

such that U is a matrix of integers and det(U)= ± 1.

As an example, for a lattice in Cartesian space as shown in the fig 2.2(a) the generator matrix is

$$\mathbf{M}_a = \begin{pmatrix} 1 & 0 \\ 0 & 1 \end{pmatrix}, \tag{2.5}$$

an alternate basis is shown in fig 2.2(b), for which the generator matrix is

$$\mathbf{M}_b = \begin{pmatrix} 2 & 1 \\ 1 & 1 \end{pmatrix}. \tag{2.6}$$

$\mathbf{M}_a$ and $\mathbf{M}_b$ are related by Eq. (2.4). In other words, the basis will define the lattice uniquely, but the basis associated with the lattice is not unique.

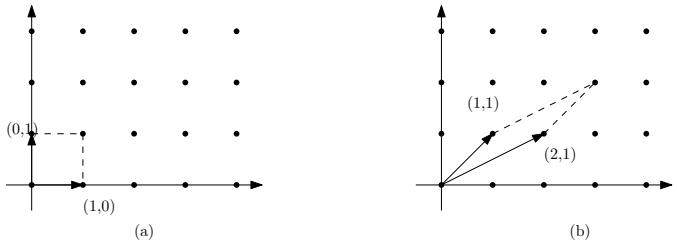

Figure 2.2: Different possible basis for the Cartesian lattice.

A three-dimensional space lattice can be adequately defined using just three (non-coplanar) basis vectors. The lattice is constructed by placing a point at every possible combination of the three vectors and any integer multiples of them (positive or negative). The vectors used for this operation are known as the primitive vectors for the lattice. A given lattice can be constructed from different sets of primitive vectors, so there is no uniquely prescribed set of primitive vectors associated with a lattice. However, a given set of primitive vectors does uniquely define a lattice. For SC lattice, the primitive vectors are

$$a_1 = a\hat{i}, \quad a_2 = a\hat{j}, \quad a_3 = a\hat{k}. \tag{2.7}$$

The generator matrix for SC lattice is

$$\mathbf{M}_{SC} = \begin{bmatrix} 1 & 0 & 0 \\ 0 & 1 & 0 \\ 0 & 0 & 1 \end{bmatrix}. \tag{2.8}$$

Similarly, for Face Centered Cubic (FCC) lattice, the primitive vectors are

$$a_1 = \frac{a}{2}\left(\hat{j} + \hat{k}\right), \quad a_2 = \frac{a}{2}\left(\hat{i} + \hat{k}\right), \quad a_3 = \frac{a}{2}\left(\hat{i} + \hat{j}\right), \tag{2.9}$$

and the generator matrix for the FCC lattice is

$$\mathbf{M}_{FCC} = \begin{bmatrix} 0 & 1 & 1 \\ 1 & 0 & 1 \\ 1 & 1 & 0 \end{bmatrix}.$$

Finally, for the Body-Centered Cubic (BCC) lattice, the primitive vectors are

$$a_1 = \frac{a}{2}\left(-\hat{i} + \hat{j} + \hat{k}\right), \quad a_2 = \frac{a}{2}\left(\hat{i} - \hat{j} + \hat{k}\right), \quad a_3 = \frac{a}{2}\left(\hat{i} + \hat{j} - \hat{k}\right), \tag{2.10}$$

and the generator matrix for BCC lattice is

$$\mathbf{M}_{BCC} = \begin{bmatrix} -1 & 1 & 1 \\ 1 & -1 & 1 \\ 1 & 1 & -1 \end{bmatrix}.$$

The corresponding figures for SC, FCC and BCC are shown in Fig. 2.3.

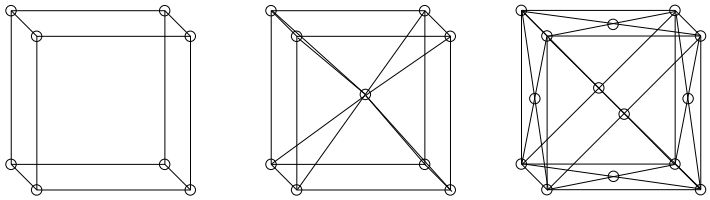

Figure 2.3: Cubic Bravais lattices in 3-dimensions (left to right: SC, BCC and FCC).

2.3.1 Fundamental Parallelepiped

Another important feature of the lattice is its fundamental parallelepiped or unit cell. It is defined as the smallest unit of volume that permits identical cells to be stacked together to fill the space without overlaps and gaps. By repeating the pattern of the unit cell over and over in all directions, the entire crystal lattice can be constructed. Different unit cells for the same lattice are shown in the Fig. 2.4. For any lattice L, the fundamental parallelepiped $\mathcal{P}(L)$ can be defined as,

$$\mathcal{P}(L) = \left\{ Lx = \sum_{i}^{N} x_i v_i | x \in \mathcal{R}^N, \forall i : 0 \leq x_i \leq 1 \right\}. \tag{2.11}$$

The parallelepiped itself may not be unique, but its volume is (Conway & Sloane, 2013). For convenience, one defines a matrix $\mathbf{A}$, which is $\mathbf{M}\,\mathbf{M}^{\mathrm{T}}$. This matrix $\mathbf{A}$ is called the Gram matrix. This volume (Λ) defined as

$$\Lambda = \det\left(\mathbf{M}\,\mathbf{M}^{\mathrm{T}}\right) = \det\left(\mathbf{A}\right), \tag{2.12}$$

is called the determinant of the lattice. Since $\det\left(UU^{\mathrm{T}}\right) = 1$, we have

$$\Lambda = \det\left(\mathbf{M}\,\mathbf{M}^{\mathrm{T}}\right) = \det\left(\mathbf{M}\,UU^{\mathrm{T}}\mathbf{M}^{\mathrm{T}}\right) = \det\left(\mathbf{M}'\,\mathbf{M}'^{\mathrm{T}}\right), \tag{2.13}$$

where $\mathbf{M}'$ is another choice of generator matrix of the lattice L, this implies that the determinant of L is unique.

As an example, let us consider SC lattice in 2-dimensions, for which a particular choice for generator matrix $\mathbf{M}_{\mathrm{SC1}}$ as:

$$\mathbf{M}_{\mathrm{SC1}} = \begin{pmatrix} 1 & 0 \\ 0 & 1 \end{pmatrix}, \tag{2.14}$$

which gives $\Lambda = 1$. Yet another choice of generator matrix for the SC lattice $\mathbf{M}_{\mathrm{SC2}}$ is,

$$\mathbf{M}_{\mathrm{SC2}} = \begin{pmatrix} 0 & 1 \\ -1 & 0 \end{pmatrix}, \tag{2.15}$$

and it is easy to check that the determinant $\Lambda = 1$ for both $\mathbf{M}_{\mathrm{SC1}}$ and $\mathbf{M}_{\mathrm{SC2}}$.

In 3-D, it is instructive to compute the value of Λ for three representative lattices of SC, FCC and BCC. For SC lattice using Eq.(2.8), we have

$$\mathbf{A} = \begin{bmatrix} 1 & 0 & 0 \\ 0 & 1 & 0 \\ 0 & 0 & 1 \end{bmatrix} \cdot \begin{bmatrix} 1 & 0 & 0 \\ 0 & 1 & 0 \\ 0 & 0 & 1 \end{bmatrix} = \begin{bmatrix} 1 & 0 & 0 \\ 0 & 1 & 0 \\ 0 & 0 & 1 \end{bmatrix} \tag{2.16}$$

Thus, we have $\Lambda^{\mathrm{SC}} = 1$. Similarly, for FCC we have

$$\mathbf{A} = \begin{bmatrix} 0 & 1 & 1 \\ 1 & 0 & 1 \\ 1 & 1 & 0 \end{bmatrix} \cdot \begin{bmatrix} 0 & 1 & 1 \\ 1 & 0 & 1 \\ 1 & 1 & 0 \end{bmatrix} = \begin{bmatrix} 2 & 1 & 1 \\ 1 & 2 & 1 \\ 1 & 1 & 2 \end{bmatrix} \tag{2.17}$$

Thus, we have $\Lambda^{\mathrm{FCC}} = 4$. Similarly, for BCC we have

$$\mathbf{A} = \begin{bmatrix} -1 & 1 & 1 \\ 1 & -1 & 1 \\ 1 & 1 & -1 \end{bmatrix} \cdot \begin{bmatrix} -1 & 1 & 1 \\ 1 & -1 & 1 \\ 1 & 1 & -1 \end{bmatrix} = \begin{bmatrix} 3 & -1 & -1 \\ -1 & 3 & -1 \\ -1 & -1 & 3 \end{bmatrix} \tag{2.18}$$

Thus, we have $\Lambda^{\mathrm{BCC}} = 16$.

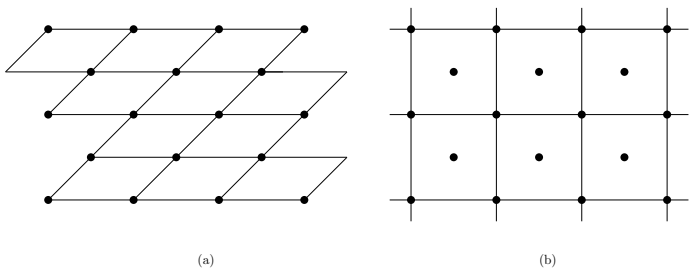

Figure 2.4: Different types of unit cells.

There are various ways to define unit cells, and a few important ones are as follows:

- **Primitive cell**: A primitive cell is a unit cell (minimum volume cell) that contains only one lattice point. It should be noted that all primitive cells are unit cells but not all unit cells are primitive cells.
- **Voronoi Cell**: The Voronoi cell or Wigner-Seitz cell around a lattice point l_i is defined as the locus of points in space that are closer to that lattice point than to any of the other lattice points.

  $$\mathcal{V}(l_i) = \left\{ x \in \mathcal{R}^N | d(x, l_i) \leq d(x, l_j) \forall j \right\} \tag{2.19}$$

  where $d(x, l_i)$ is the distance between the points x and l_i.

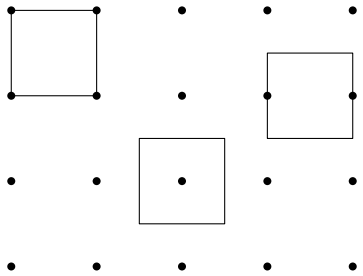

Figure 2.5: The possible choices of primitive cells for a set of points.

The Wigner-Seitz cell is constructed by taking the perpendicular bisectors of all the nearby points around a lattice point as shown in Fig. 2.6. The Wigner-Seitz cell for FCC in 3D is a rhombic dodecahedron, and for BCC, it is truncated octahedron. These are shown in the Fig. 2.7.

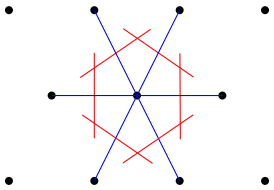

Figure 2.6: Construction of Wigner-Seitz cell around a lattice point.

2.3.2 Reciprocal Lattice

If L is an n-dimensional lattice with the basis $\{v_i\}$, the reciprocal lattice L^* with the basis $\{u_j\}$ is defined as:

$$L^* = \{\mathbf{M}^*\mathbf{j} : j \in \mathcal{Z}^N\} \text{where } \mathbf{M}^* = \left(\mathbf{M}^{-1}\right)^{\mathrm{T}}, \tag{2.20}$$

such that,

$$u_i.v_j = 2\pi\delta_{ij}. \tag{2.21}$$

As for an example, the primitive vectors for reciprocal lattice of SC lattice are (Kittel, 2005)

$$b_1 = \frac{2\pi}{a}\hat{i}, \quad b_2 = \frac{2\pi}{a}\hat{j}, \quad b_3 = \frac{2\pi}{a}\hat{k}, \tag{2.22}$$

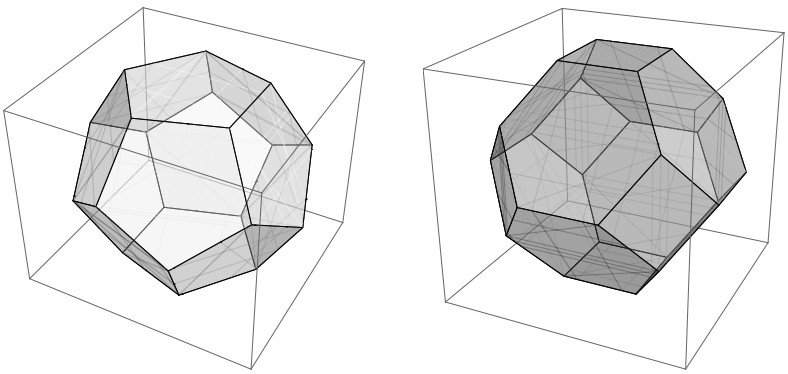

Figure 2.7: WignerSeitz cell for BCC (left) and FCC (right) grids.

which is again a SC lattice itself with a lattice constant $2\pi/a$. The primitive vectors for reciprocal lattice of FCC lattice are

$$b_1 = \frac{2\pi}{a}\left(-\hat{i}+\hat{j}+\hat{k}\right), \quad b_2 = \frac{2\pi}{a}\left(\hat{i}-\hat{j}+\hat{k}\right), \quad b_3 = \frac{2\pi}{a}\left(\hat{i}+\hat{j}-\hat{k}\right), \tag{2.23}$$

which is the basis for BCC lattice i.e., reciprocal lattice for FCC lattice is BCC. Similarly, the primitive vectors for reciprocal lattice of the BCC lattice are

$$b_1 = \frac{2\pi}{a}\left(\hat{j}+\hat{k}\right), \quad b_2 = \frac{2\pi}{a}\left(\hat{i}+\hat{k}\right), \quad b_3 = \frac{2\pi}{a}\left(\hat{i}+\hat{j}\right), \tag{2.24}$$

which is the basis for FCC lattice i.e., reciprocal lattice for BCC lattice is FCC. Indeed it is easy to see that in general, the reciprocal lattice of a reciprocal lattice is the original lattice.

2.4 Closest packing problem

The classical sphere packing problem is to solve how densely the identical spheres can be packed together (Conway & Sloane, 2013). The packing density Δ of a lattice is the ratio of the volume filled by the spheres within a unit cell to the volume of the unit cell, i.e.,

$$\Delta = \frac{\text{volume of one sphere}}{\text{volume of fundamental region}} = \frac{\text{volume of one sphere}}{\Lambda^{\frac{1}{2}}}, \tag{2.25}$$

where Λ is the determinant of the lattice.

The packing density for 3-dimensional lattices using the generator matrix can be understood by considering the examples of SC, FCC and BCC lattices. The determinant of generator matrix for SC lattice is $\Lambda_{SC} = 1$. The packing radius is taken as half of the shortest non-zero vector length (Bowick *et al.*, 2017) and thus in case of SC lattice, it is 1/2. This is also apparent from Fig 2.8, from where it is evident that $2r = a$, where r is the radius of the sphere and a is the side of the unit cell.

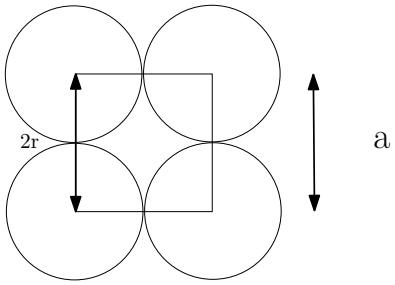

Figure 2.8: One face of a SC arrangement of spheres.

Thus the volume of the sphere is

$$V = \frac{4}{3}\pi\left(\frac{1}{2}\right)^3 = \frac{\pi}{6}. \tag{2.26}$$

Thus, on SC lattice where $\Lambda_{SC} = 1$, the packing density is

$$\Delta_{SC} = \frac{V}{\Lambda_{SC}} = 0.5236. \tag{2.27}$$

In other words, the percentage of packing density is 52.36%.

Similarly, determinant of generator matrix for FCC lattice is $\Lambda_{FCC} = 4$. The packing radius is taken as the half shortest non-zero vector length and thus in case of FCC lattice it is $1/\sqrt{2}$.

Thus the volume of a single sphere is

$$V = \frac{4}{3}\pi\left(\frac{1}{\sqrt{2}}\right)^3 = \frac{2\pi}{3\sqrt{2}}. \tag{2.28}$$

Thus, the packing density calculated is

$$\Delta_{FCC} = \frac{1}{\sqrt{4}}\frac{2\pi}{3\sqrt{2}} = 0.7405. \tag{2.29}$$

Finally, for BCC lattice the determinant is $\Lambda_{BCC} = 16$. The packing radius is taken as the half shortest non-zero vector length and thus in case of BCC lattice it is $\sqrt{3}/2$. Thus the volume of a single sphere is

$$V = \frac{4}{3}\pi\left(\sqrt{\frac{3}{4}}\right)^3 = \pi\sqrt{\frac{3}{4}}. \tag{2.30}$$

Thus, the packing density calculated is

$$\Delta_{BCC} = \frac{1}{\sqrt{16}}\pi\sqrt{\frac{3}{4}} = 0.6802. \tag{2.31}$$

Thus, in 3-dimensions FCC has the highest packing density.

2.5 Efficient sampling lattice

A regular sampling of a function is similar to a point lattice. For sampling a function f on a lattice L, the function has to be bandwidth limited. An efficient sampling lattice is the one which uses a minimum number of sampling points to achieve exact reproduction of a bandwidth-limited function (Petersen & Middleton, 1962). To distribute the samples in the spatial domain in the most economical (sparse) fashion, the reciprocal lattice $\tilde{L}$ needs to be as densely packed as possible. The dense packing of the spectra in the Fourier domain can be addressed by the sphere packing problem. In 3-dimensions, the packing fraction for FCC lattice in Fourier space is the least (i.e., the packing density is highest) of all the lattices i.e., BCC lattice in real space is the most efficient lattice.

The problem of finding most efficient sampling lattice in N- Dimensions is equivalent to the closest sphere packing problem in Fourier space and vice versa (Entezari *et al.*, 2009). In 3-Dimensions, the packing fraction for FCC lattice in Fourier space is the least (i.e., the packing density is highest) of all the lattices i.e., BCC lattice in real space is the most efficient lattice. The packing density values of different lattices in 3-dimensions that are calculated in Section 2.3 are tabulated in Table 2.1. It is well known that volume representation (or rendering) will be better on BCC lattice. Indeed this fact is well known in computer graphics literature. To illustrate the difference between SC and BCC lattices, Fig 2.9 shows the rendered image of a sphere on SC and BCC lattice. The advantages of using BCC lattice is evident in this figure.

Lattice	Dual	Packing density
Simple Cubic	Simple Cubic	$\frac{\pi}{6} = 0.5235$
Body Centered Cubic	Face Centered Cubic	$\frac{\pi\sqrt{3}}{8} = 0.68017$
Face Centered Cubic	Body Centered Cubic	$\frac{\pi}{\sqrt{18}} = 0.74048$

Table 2.1: The packing densities of different lattices in 3-Dimensions.

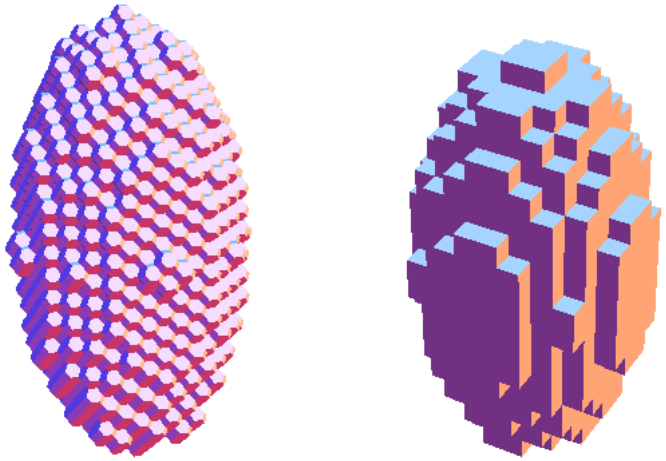

(a) BCC (b) SC

Figure 2.9: Representation of an ellipsoid on BCC (left) and SC (right) grids.

2.6 Isotropy on lattice

A typical fluid system does not show preference towards any particular coordinate orientation. In the context of Boltzmann dynamics, since molecular velocity can take any value and there is no intrinsic preference for a particular direction, the equilibrium distribution is invariant under arbitrary rotations of the axis rather than just a few particular discrete rotations. However, any discrete representation by definition can preserve invariance with respect to few discrete rotations only. Thus, any discrete representation of the fluid system will preserve isotropy in an approximate sense only. A systematic way to analyze the behavior of the discrete velocity models is to notice that the discrete velocity set forms a D-dimensional crystallographic structure. The symmetries of such a crystallographic structure and possibility of describing fluid like isotropic structure is best analyzed in terms of n^{th} order moment tensor M defined in terms of the link vector $c_{a,i}$ as

$$M^{(n)}_{i_1 i_2 \cdots i_n} = \sum_{a=1}^{N} w_j \, c_{a,i_1} \, c_{a,i_2} \cdots c_{a,i_n} \tag{2.32}$$

where w_i are certain weights associated with individual vectors and $c_{a,i_1}, c_{a,i_2} \cdots$ are the cartesian components of the vector and N denotes the number of such vectors. For simplicity we will restrict our attention to the case where weights w_i are function of magnitude of link vector only, i.e., $w_i \equiv w_i(c_{ai}^2)$. In this section, we largely follow (Chen *et al.*, 2008) in analyzing the isotropy of such a tensor. As we are working with Bravais lattices, we can utilize certain group related properties of these lattices. In particular, if c_i are the lattice vectors corresponding to a lattice, then they have to satisfy following conditions:

- **Closure under inversion**: The discrete vector set should be closed under inversion i.e if $c_i \in C$ then the inverse of it should also belong to the same set ($-c_i \in C$). Two examples of such link vectors on 2-dimensional simple cubic lattice is shown in Fig.2.10.

  This condition implies that all odd ordered moments constructed with the vector set C are zero, i.e.,

$$\sum_i w_i c_{i\alpha} = 0, \quad \sum_i w_i c_{i\alpha} c_{i\beta} c_{i\gamma} = 0. \tag{2.33}$$

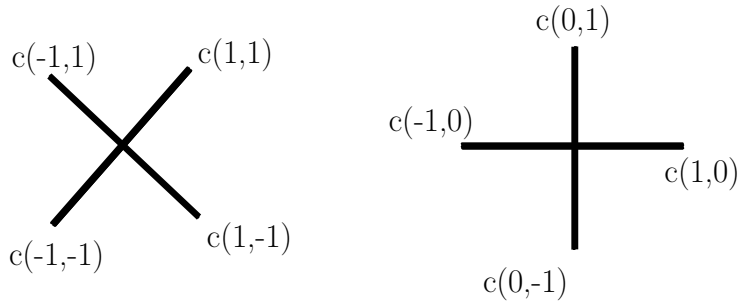

Figure 2.10: Two examples of such link vectors on 2-dimensional simple cubic lattice

- **Closure under reflection**: The discrete vector set should be closed under reflection. In other words, if $c_i = (a_1, a_2, a_3) \in C$ all possible reflections of $c_i = (a_2, a_1, a_3), (a_3, a_2, a_1), \cdots$ should also be in C. It is evident that both examples shown in Fig.2.10 also satisfy this condition. This condition implies that the even order moments do not show preference towards any particular cartesian components. In particular:

$$\begin{aligned} \sum_i w_i c_{ix}^{2n} = \sum_i w_i c_{iy}^{2n} = \sum_i w_i c_{iz}^{2n}, \\ \sum_i w_i c_{ix}^{2m} c_{iy}^{2n} = \sum_i w_i c_{iy}^{2m} c_{iz}^{2n} = \sum_i w_i c_{ix}^{2m} c_{iz}^{2n}. \end{aligned} \tag{2.34}$$

On these lattices, we can analyze the behavior of nth order moment tensor by recognizing that any n^{th} order tensor can be written as the combination of isotropic delta function $\Delta^{(n)}_{i_1,i_2,\cdots i_n}$ and appropriate anisotropic tensor of that order. Thus, the generic form of few lower order moment tensors are

$$\begin{aligned} M^{(2)}_{i_1 i_2} &= C^{(2)}_1 \delta_{i_1 i_2}, \\ M^{(4)}_{i_1 i_2 i_3 i_4} &= C^{(4)}_1 \Delta^{(4)}_{i_1 i_2 i_3 i_4} + C^{(4)}_2 \delta_{i_1 i_2 i_3 i_4}, \\ M^{(6)}_{i_1 i_2 i_3 i_4 i_5 i_6} &= C^{(6)}_1 \Delta^{(6)}_{i_1 i_2 i_3 i_4 i_5 i_6} + C^{(6)}_2 \delta^{(6)}_{i_1 i_2 i_3 i_4 i_5 i_6} + C^{(6)}_3 \delta^{(4,2)}_{i_1 i_2 i_3 i_4 i_5 i_6}, \\ M^{(8)}_{i_1 i_2 i_3 i_4 i_5 i_6 i_7 i_8} &= C^{(8)}_1 \Delta^{(8)}_{i_1 i_2 i_3 i_4 i_5 i_6 i_7 i_8} + C^{(8)}_2 \delta^{(8)}_{i_1 i_2 i_3 i_4 i_5 i_6 i_7 i_8} + C^{(8)}_3 \delta^{(4,4)}_{i_1 i_2 i_3 i_4 i_5 i_6 i_7 i_8} \\ &\quad + C^{(8)}_4 \delta^{(6,2)}_{i_1 i_2 i_3 i_4 i_5 i_6 i_7 i_8} + C^{(8)}_5 \delta^{(2,2,4)}_{i_1 i_2 i_3 i_4 i_5 i_6 i_7 i_8}. \end{aligned} \tag{2.35}$$

where c is the lattice speed and the coefficients $C^{(n)}_m$ are specific to the type of lattice we consider and Kronecker delta function of order n is

$$\delta_{i_1 i_2 \cdots i_n} = \begin{cases} 1, & \text{if } i_1 = i_2 \cdots = i_n \\ 0, & \text{otherwise} \end{cases} \tag{2.36}$$

Further, the isotropic delta function $\Delta^{(n)}_{i_1,i_2,\cdots i_n}$ can be written in terms of second order isotropic delta function called Kronecker delta function ($\delta_{i_1 i_2}$) and lower order isotropic delta function ($\Delta^{(m)}_{i_1 i_2 \cdots i_m}$ where $m < n$). As for an example

$$\begin{aligned} \Delta^{(4)}_{ijkl} &= \delta_{ij}\delta_{kl} + \delta_{ik}\delta_{jl} + \delta_{il}\delta_{jk}, \\ \Delta^{(6)}_{ijklmn} &= \delta_{ij}\Delta^{(4)}_{klmn} + \delta_{ik}\Delta^{(4)}_{jlmn} + \delta_{il}\Delta^{(4)}_{kjmn} + \delta_{im}\Delta^{(4)}_{kljn} + \delta_{in}\Delta^{(4)}_{jklm}. \end{aligned} \tag{2.37}$$

The delta function of the form $\delta^{(m,n-m)}_{i_1 i_2 \cdots i_n}$ is product of two Kronecker deltas of order m and n-m

i.e., $\delta^{(m,n-m)}_{i_1 i_2 \cdots i_n} = \delta_{i_1 i_2 \cdots i_{(n-m)}} \delta_{i_1 i_2 \cdots i_m}$ and all the possible permutations of indices.

For the lattice A shown in Fig. 2.10, the 4th order isotropic condition implies, $\sum_i c_{i\alpha} c_{i\beta} c_{i\gamma} c_{i\kappa} = 2c^4 \delta_{\alpha\beta\gamma\kappa}$ and for lattice B, it is $\sum_i c_{i\alpha} c_{i\beta} c_{i\gamma} c_{i\kappa} = 4c^4 \left[\Delta_{\alpha\beta\gamma\kappa} - 2\delta_{\alpha\beta\gamma\kappa}\right]$. Similarly, the coefficients for SC,FCC and BCC shells can be calculated. The coefficients of second and fourth order tensors for different lattices are listed in Table 2.2. where as, c_{sc}, c_f, c_b are the lattice velocities for

	$C_1^{(2)}$	$C_1^{(4)}$	$C_2^{(4)}$
SC	2 c_{sc}^2	0	$2c_{sc}^4$
FCC	8 c_f^2	4 c_f^4	-4 c_f^4
BCC	8 c_b^2	$8c_b^4$	-16 c_b^4

Table 2.2: Second and Fourth order tensor coefficients

SC, FCC and BCC.

For sixth order tensor, the coefficients for different lattices are tabulated in Table 2.3.

	$C_1^{(6)}$	$C_2^{(6)}$	$C_3^{(6)}$
SC	0	$2c_{sc}^6$	0
FCC	0	- 52 c_{sc}^4	$4c_{sc}^4$
BCC	8 c_b^6	128 c_b^6	- 16 c_b^6

Table 2.3: Sixth order tensor coefficients

For eighth order tensor the coefficients for different lattices are tabulated in Table 2.4. We

	$C_1^{(8)}$	$C_2^{(8)}$	$C_3^{(8)}$	$C_4^{(8)}$	$C_5^{(8)}$
SC	0	$2c_{sc}^6$	0	0	0
FCC	0	$-384c_f^8$	$4c_f^8$	$4c_f^8$	0
BCC	8/3 c_b^8	1744 c_b^8	-32 c_b^8	- 16 c_b^8	0

Table 2.4: Eighth order tensor

will construct a discrete velocity set for LBM using these conditions of isotropy in subsequent chapters.

Chapter 3
Boltzmann equation

3.1 Introduction

In hydrodynamic theories, fluid is treated as a continuum and its motion is described in terms of the macroscopic quantities such as the mass density, velocity, and temperature at a point. The underlying assumption behind this continuum hypothesis is that we can associate macroscopic quantities with any volume of fluid, no matter how small it is (Batchelor, 2000; Landau & Lifshitz, 1959). Physically, this approximation is valid provided the volume element considered is much larger than the mean free path. The evolution equations for the macroscopic quantities are obtained in terms of conservation laws for mass, momentum, and energy. These conservation laws need to be supplemented with the constitutive relations for stress tensor and heat flux tensor. For instance, in case of "Newtonian fluid", one assumes that the stress varies linearly with the velocity gradient tensor (Batchelor, 2000). The basic equation of motion for the Newtonian fluid is Navier-Stokes-Fourier equations, along with the linear relationship between stress tensor and velocity gradient tensor, Fourier law of heat conduction is also assumed. The central theme of the computational fluid dynamics is to obtain efficient schemes to solve the non-linear Navier-Stokes-Fourier equation in the incompressible limit for which the equation is highly non-local because of the pressure term (Ansumali *et al.*, 2005; Holmes *et al.*, 1998; Chorin *et al.*, 1990).

The other end of fluid modeling is a fully microscopic approach where the fluid is modeled as a many-body system of microscopic particles. The motion of this microscopic system is governed by the coupled Newton equations, within the framework of classical mechanics. In this approach, the uncertainty over initial position and velocities of N-particle system is handled by averaging over all possible initial conditions. All macroscopic quantities are computed as appropriate averages of microscopic system (Liboff, 2003). For understanding long-time dynamics, such a procedure is very inefficient and often provides detailed information which is far beneath the usual realm of interest for continuum fluid mechanics (Koplik & Banavar, 1995).

For dilute gases, kinetic theory of gases provides an intermediate description in terms of the single particle distribution function (Cercignani, 1975). In this description, single particle distribution function $f(\mathbf{x}, \mathbf{c}, t)$, describes the state of the gas at any location $\mathbf{x}$ with velocity $\mathbf{c}$ at time $t \geq 0$. Physically, $f(\mathbf{x}, \mathbf{c}, t)\, d\mathbf{x}\, d\mathbf{c}$ is the probability of finding a particle centered at the point $(\mathbf{x}, \mathbf{c})$ in infinitesimal volume $d\mathbf{x}\, d\mathbf{c}$ in *phase space*(Cercignani, 1975; Struchtrup, 2005). The evolution equation of the distribution function, first derived by Boltzmann, provides a quantitatively correct dynamics of the dilute gas in the hydrodynamic regime as well as molecular regimes even when the gas is far from equilibrium (Cercignani, 1975). Thus, Boltzmann equation occupies the central position in non-equilibrium statistical mechanics and is key to our understanding of how the averaged macroscopic behavior emerges from microscopic motion.

In this chapter, a brief review of the kinetic theory of gases will be presented. The chapter is organized as follows. A brief introduction to distribution function approach is discussed in Sec.3.2. The Boltzmann equation for dilute gases is introduced in Sec.3.3 which is followed by a brief discussion on Maxwell-Boltzmann distribution function in Sec.3.4. The approximation for Boltzmann collision operator, known as kinetic models are introduced in Sec.3.5. Finally, evolution equations for the moments along with different methods to obtain closure relation has been presented in Sec.3.6.

3.2 Distribution function and moments

The macroscopic quantities such as mass density (ρ), momentum density (j_α, the mean velocity of the fluid) and energy density (E) are defined as lower order moments of the probability distribution function. The explicit expressions are

$$\rho = \langle 1, f \rangle, \qquad j_\alpha = \langle c_\alpha, f \rangle, \qquad E = \left\langle \frac{c_\alpha^2}{2}, f \right\rangle, \tag{3.1}$$

where angular bracket denotes the inner product defined as:

$$\langle \phi_1, \phi_2 \rangle = \int_{-\infty}^{\infty} \int_{-\infty}^{\infty} \int_{-\infty}^{\infty} d\mathbf{c} \phi_1 \, \phi_2. \tag{3.2}$$

It is often convenient to define the moments in the co-moving reference frame in terms of mean velocity of the fluid u_α ($\equiv j_\alpha/\rho$). For example, the internal energy (e) of the fluid in the co-moving reference frame is

$$\rho e = \left\langle \frac{\xi^2}{2}, f \right\rangle = \left\langle \frac{(\mathbf{c} - \mathbf{u})^2}{2}, f \right\rangle, \tag{3.3}$$

which is related to total energy (E) in absolute frame as:

$$E = \frac{1}{2}\rho u^2 + \rho e, \tag{3.4}$$

where $\boldsymbol{\xi} = \mathbf{c} - \mathbf{u}$ is the peculiar velocity. As we are dealing with dilute gases, the equation of state is that of an ideal gas and the temperature T is defined by the relation $e = 3k_\mathrm{B}T/(2m)$, where k_B is the Boltzmann constant and m is the mass of a molecule. Here onwards, a scaled temperature defined as $\theta = k_\mathrm{B}T/m$ will be used for convenience.

The traceless part of momentum flux in co-moving reference frame is stress tensor ($\sigma_{\alpha\beta}$) and energy flux in this reference frame is heat flux (q_α). These quantities defined in terms of the distribution function are

$$\sigma_{\alpha\beta} = \langle \overline{\xi_\alpha \xi_\beta}, f \rangle, \quad q_\alpha = \left\langle \frac{\xi_\alpha \xi^2}{2}, f \right\rangle, \tag{3.5}$$

where for any second order tensor $A_{\alpha\beta}$ in D dimension, the traceless part $\overline{A}_{\alpha\beta}$ is defined as:

$$\overline{A}_{\alpha\beta} = \frac{1}{2}(A_{\alpha\beta} + A_{\beta\alpha}) - \frac{1}{D} A_{\gamma\gamma}\delta_{\alpha\beta}. \tag{3.6}$$

Similarly, for third order symmetric tensor $B_{\alpha\beta\gamma}$ traceless part $\overline{B}_{\alpha\beta\gamma}$ is defined as:

$$\overline{B}_{\alpha\beta\gamma} = B_{\alpha\beta\gamma} - \frac{1}{D+2} \left(B_{\alpha\kappa\kappa}\delta_{\gamma\beta} + B_{\beta\kappa\kappa}\delta_{\alpha\gamma} + B_{\kappa\kappa\gamma}\delta_{\alpha\beta} \right). \tag{3.7}$$

The next important higher order moments that we use in kinetic theory are, traceless part of flux of momentum flux $\overline{Q}_{\alpha\beta\gamma}$, traceless part of fourth order moment ($\overline{R}_{\alpha\beta\gamma\kappa}$), the traceless and trace part of the contracted fourth order moment $\overline{R}_{\alpha\beta}$ (flux of heat flux) and R which can be defined as:

$$\overline{Q}_{\alpha\beta\gamma} = \left\langle \overline{\xi_\alpha \xi_\beta \xi_\gamma}, f \right\rangle, \quad \overline{R}_{\alpha\beta\gamma\kappa} = \left\langle \overline{\xi_\alpha \xi_\beta \xi_\gamma \xi_\kappa}, f \right\rangle, \quad \overline{R}_{\alpha\beta} = \left\langle \frac{1}{2}\xi^2 \overline{\xi_\alpha \xi_\beta}, f \right\rangle, \quad R = \left\langle \xi^4, f \right\rangle. \tag{3.8}$$

We also define the contracted fifth order and double contracted fifth order moments as:

$$N_{\alpha\beta\gamma} = \left\langle \xi^2 \xi_\alpha \xi_\beta \xi_\gamma, f \right\rangle, \quad n_\alpha = \left\langle \xi^2 \xi^2 \xi_\alpha, f \right\rangle. \tag{3.9}$$

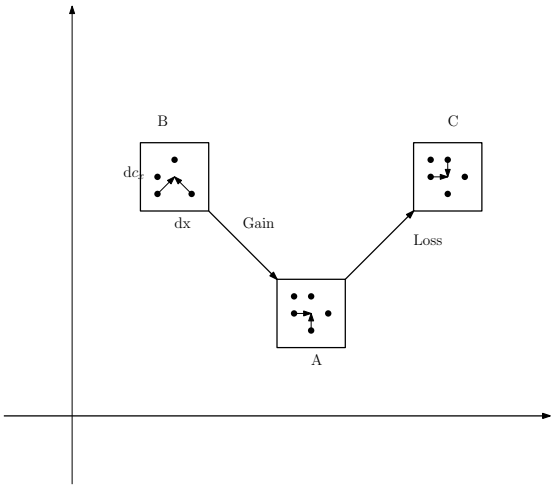

Figure 3.1: Evolution of distribution function in phase space.

In the later part of this chapter these moments will be used for extended hydrodynamic description.

3.3 Boltzmann equation for dilute gases

The Boltzmann equation describes the time evolution of the distribution function under the action of external forces and internal collisions. This equation states that the time rate of change of the distribution function in an elemental volume is due to the flux of particles across the bounding surfaces and non-locally through collisions among particle which leads to particles jumping from one elemental volume to other in the velocity space (See Fig 3.1). In explicit form, the Boltzmann equation is (Cercignani, 1975)

$$\frac{\partial f}{\partial t} + \frac{\partial}{\partial x_\alpha}\left(c_\alpha f\right) + g_\alpha \frac{\partial f}{\partial c_\alpha} = \mathcal{J}\left(f, f\right), \tag{3.10}$$

where g_α is the acceleration due to external force and $\mathcal{J}$ is the collision term which denotes the effect of binary collisions between the particles. The Boltzmann equation relies on the famous molecular chaos (*Stosszahlansatz*) assumption that the velocities of the colliding particles before collision are uncorrelated, i.e.,

$$f_{12}\left(\mathbf{x_1}, \mathbf{c_1}, \mathbf{x_2}, \mathbf{c_2}, t\right) = f\left(\mathbf{x_1}, \mathbf{c_1}, t\right) f\left(\mathbf{x_2}, \mathbf{c_2}, t\right). \tag{3.11}$$

The collision operator with molecular chaos approximation is

$$\mathcal{J} = \int d\mathbf{c}' \int d\mathbf{c} \int d\mathbf{c_1} \int d\mathbf{c_2} \left[w\left(\mathbf{c}, \mathbf{c}'|\mathbf{c_1}, \mathbf{c_2}\right) f(\mathbf{c_1}) f(\mathbf{c_2}) - w\left(\mathbf{c_1}, \mathbf{c_2}|\mathbf{c}, \mathbf{c}'\right) f(\mathbf{c}) f(\mathbf{c}')\right], \tag{3.12}$$

where c_1 and c_2 are pre-collisional velocities and c' and c are post-collisional velocities. Also, $w\left(\mathbf{c}, \mathbf{c}'|\mathbf{c_1}, \mathbf{c_2}\right)$ is the transition probability that as a result of collision between molecules with velocities c_1 and c_2 acquires velocities c' and c according to the laws of elastic collisions, i.e.,

$$\begin{aligned} \mathbf{c} + \mathbf{c'} &= \mathbf{c_1} + \mathbf{c_2}, \\ \mathbf{c^2} + \mathbf{c'^2} &= \mathbf{c_1}^2 + \mathbf{c_2}^2. \end{aligned} \tag{3.13}$$

The transition probability follows the symmetry relation (Landau *et al.*, 1981)

$$w(\mathbf{c}, \mathbf{c}'|\mathbf{c}_1, \mathbf{c}_2) = w(\mathbf{c}_1, \mathbf{c}_2|\mathbf{c}, \mathbf{c}'). \tag{3.14}$$

This implies that in statistical equilibrium the number of collisions in which the collisional velocities changes from c_1, $c_2 \to c$, c' is equal to number of collisions with the collisional velocities to be changing from c, $c' \to c_1$, c_2. This is the principle of detailed balance.

Using the above symmetry of the transition probability, one can show that for an arbitrary function $\phi(\mathbf{c})$ of the molecular velocity, following relation holds

$$\left\langle \phi(\mathbf{c}), \Omega^{\mathrm{B}} \right\rangle = \int d\mathbf{c}' d\mathbf{c}_1 d\mathbf{c}_2 d\mathbf{c}\, w \left\{ f(\mathbf{c}_1) f(\mathbf{c}_2) - f(\mathbf{c}) f(\mathbf{c}') \right\} \frac{\phi(\mathbf{c}) + \phi(\mathbf{c}') - \phi(\mathbf{c}_1) - \phi(\mathbf{c}_2)}{4}. \tag{3.15}$$

A few important properties of the Boltzmann equation are:

1. **Collisional invariants:** Due to the elastic collisions Eq.(3.13) and Eq.(3.15), for any ϕ of the form,

$$\phi_0(c) = a_1 + a_2\mathbf{c} + a_3\mathbf{c}^2 \tag{3.16}$$

it is evident that $\left\langle \phi_0(\mathbf{c}), \Omega^{\mathrm{B}} \right\rangle = 0$. In other words

$$\langle \mathcal{J}, \{1, c_\alpha, \mathbf{c}^2\} \rangle = 0. \tag{3.17}$$

This also implies that collision term is satisfying the conservation of mass, momentum and energy.

2. **Conservation laws:** By taking the moments of the Boltzmann equation (3.10) and using Eq.(1) it is evident that the macroscopic conservation laws have the following form

$$\begin{aligned} \frac{\partial \rho}{\partial t} + \frac{\partial j_\alpha}{\partial x_\alpha} &= 0, \\ \frac{\partial j_\alpha}{\partial t} + \frac{\partial}{\partial x_\beta}\left(\rho u_\alpha u_\beta + p\delta_{\alpha\beta}\right) + \frac{\partial \sigma_{\alpha\beta}}{\partial x_\beta} &= \rho g_\alpha, \\ \frac{\partial E}{\partial t} + \frac{\partial}{\partial x_\alpha}\left((E+p)u_\alpha + \sigma_{\alpha\gamma}u_\gamma\right) + \frac{\partial q_\alpha}{\partial x_\alpha} &= \rho u_\alpha g_\alpha, \end{aligned} \tag{3.18}$$

where $p = \rho\theta$. It should be noted here that the conservation laws emerges from set of collisional invariants only and should hold irrespective of form of the collision term.

3. **Zero of collision:** At equilibrium the collision term in the Boltzmann equation reduces to

$$\mathcal{J}(f, f) = 0. \tag{3.19}$$

The collision integral vanishes if,

$$f(\mathbf{c}) f(\mathbf{c}') = f(\mathbf{c_1}) f(\mathbf{c_2}), \tag{3.20}$$

or

$$\ln f(\mathbf{c}) + \ln f(\mathbf{c}') = \ln f(\mathbf{c_1}) + \ln f(\mathbf{c_2}), \tag{3.21}$$

which implies that $\ln f$ is a collisional invariant. As mentioned earlier, mass, momentum and energy are only collisional invariants for binary collisions which implies $\ln f$ should be a linear combination of these invariants. This also yields that the equilibrium distribution function f^{MB} has form:

$$f^{\mathrm{MB}} = \frac{\rho}{(2\pi\theta)^{\frac{3}{2}}} \exp\left(-\frac{\xi^2}{2\theta}\right). \tag{3.22}$$

This distribution function is known as Maxwell-Boltzmann distribution function.

4. ***H*-theorem:** Boltzmann generalized the concept of entropy to a non-equilibrium situations by defining H-function in terms of the distribution function as (Cercignani, 1975):

$$H = \int d\mathbf{c}\,(f \ln f - f)\,. \tag{3.23}$$

The evolution equation for the H-function can be written as:

$$\frac{\partial H}{\partial t} + \frac{\partial J_\alpha^H}{\partial x_\alpha} = -\sigma^{(B)}, \tag{3.24}$$

where the entropy flux J_α^H and the production term $\sigma^{(B)}$ are

$$J_\alpha^H = \int c_\alpha\,(f \ln f - f)\,, \qquad \sigma^{(B)} d\mathbf{c} = -\langle \Omega^{(B)}, \ln f \rangle. \tag{3.25}$$

The H-theorem states that for any solution of the Boltzmann equation, H-function is a non-increasing function of time, i.e., $\Omega^{(B)} \geq 0$. The rate of variation of entropy is

$$\Omega^{(B)} = -\int d\mathbf{c}' \int d\mathbf{c} \int d\mathbf{c_1} \int d\mathbf{c_2}\left[f(\mathbf{c_1})f(\mathbf{c_2}) - f(\mathbf{c})f(\mathbf{c}')\right] \log \frac{f(\mathbf{c})f(\mathbf{c}')}{f(\mathbf{c_1})f(\mathbf{c_2})} \geq 0. \tag{3.26}$$

It can be seen that the rate of variation of entropy is always negative and the entropy is non-decreasing quantity in time. This relation shows that H-theorem is a generalized version of the second law of thermodynamics (or law of entropy). It should also be noted that, entropy production is zero when $f(\mathbf{c})f(\mathbf{c}') = f(\mathbf{c_1})f(\mathbf{c_2})$ and as shown earlier this corresponds to Maxwell-Boltzmann state.

This description of dilute gases in terms of the single particle distribution function is valid only in the Boltzmann-Grad limit (Grad, 1958; Liboff, 2003). This is a limiting process where the number of particles (n) is allowed to approach infinity ($n \to \infty$) and the mass of each particle (m) is allowed to go to zero in such a way that the total mass is constant ($mn = \text{const}$). The size of the molecules tends to zero ($d_m \to 0$) keeping the surface area constant ($nd_m^2 = \text{const}$) which also means that the mean free path (the average distance traveled by the particle between two successive collisions) is held constant ($1/nd_m^2 = \text{const}$). Finally, we observe that the volume occupied by the molecule is tending to zero ($nd_m^3 \to 0$) in this limit while surface area is kept constant. This limit is the Boltzmann-Grad limit, and it provides the measure for rarefaction.

3.4 Maxwell distribution function

Maxwell distribution is the zero of the collision term and the entropy production is zero in this state hence it can be interpreted as the minimization of H-function under the constraints of mass, momentum and energy conservation. This constrained minimization can be done as minimization of a potential of the form (Ansumali & Karlin, 2005)

$$\Xi = \int d\mathbf{c} f\ (\ln f - 1) + f\ \left(\alpha + \beta_\kappa c_\kappa + \gamma c^2\right), \tag{3.27}$$

where α, β_κ and γ are the Lagrange multipliers corresponding to the mass, momentum and energy conservation respectively. The minimization of the potential Ξ is

$$\frac{d\Xi}{df} = 0 \Rightarrow f^{\text{eq}} = exp\left[-\left(\alpha + \beta_\kappa c_\kappa + \gamma c^2\right)\right], \tag{3.28}$$

where the explicit form of the Lagrange multipliers are

$$\alpha = -\ln\rho + \frac{3}{2}\log(2\pi\theta) + u^2, \qquad \beta_\kappa = -\frac{u_\kappa}{\theta}, \qquad \gamma = \frac{1}{2\theta}. \tag{3.29}$$

Using these expressions the equilibrium distribution f^{MB} is found as:

$$f^{\mathrm{MB}} = \frac{\rho}{(2\pi\theta)^{\frac{3}{2}}}\exp\left(\frac{-\xi^2}{2\theta}\right). \tag{3.30}$$

The moments of the Maxwell distribution are

$$\rho = \langle 1, f^{\mathrm{MB}}\rangle, \qquad j_\alpha = \langle c_\alpha, f^{\mathrm{MB}}\rangle, \qquad E \equiv \frac{\rho u^2}{2} + e = \left\langle \frac{c^2}{2}, f^{\mathrm{MB}}\right\rangle. \tag{3.31}$$

The equilibrium values of the higher order moments using Maxwell-Boltzmann distribution are

$$\sigma^{\mathrm{eq}}_{\alpha\beta} = \rho u_\alpha u_\beta \delta_{\alpha\beta}, \qquad Q^{\mathrm{eq}}_{\alpha\beta\gamma} = 0. \tag{3.32}$$

The zeroth moment of distribution f^{MB} is the particle number density and the odd moments vanish. The second velocity moment is related to the temperature.

3.5 Kinetic models

The Boltzmann equation is difficult to solve because of the complexity of collision term. Several approaches have been developed to simplify the Boltzmann equation and preserve the collisional properties. Such models are termed as kinetic models (Bhatnagar *et al.*, 1954; Lebowitz *et al.*, 1960; Cercignani, 1975). In this section, we list a few models of the collision term.

3.5.1 Bhatnagar-Gross-Krook model

One of the most widely used models for Boltzmann equation is due to Bhatnagar-Gross-Krook (Bhatnagar *et al.*, 1954). This model assumes that the role of collisions is to relax the distribution function to its equilibrium f^{MB}. Collision term for this model reads

$$\mathcal{J}_{\mathrm{BGK}} = \frac{1}{\tau}\left(f^{\mathrm{MB}}(\rho, \mathbf{u}, \theta) - f\right), \tag{3.33}$$

where the time parameter τ is the relaxation time. This model provides a qualitatively correct dynamics of Boltzmann equation. This can be seen from following properties of the BGK model:

- **Collision invariant:** From the definition (3.1) it is obvious that

$$\langle \mathcal{J}_{\mathrm{BGK}}, \left\{1, \mathbf{c}, c^2\right\}\rangle = 0, \tag{3.34}$$

  i.e., mass, momentum and energy are collisional invariants. Thus, the collisional invariants of BGK model are same as the Boltzmann equation.

- **Conservation laws:** Since the collisional invariants for BGK model are same as the Boltzmann equation, the conservation laws remain the same.

- **Zero of Collision:** At the equilibrium state, where the collision term is zero, the BGK collision term implies that, $f = f^{\mathrm{MB}}(\rho, \mathbf{u}, \theta)$. The zero of collision for BGK model, like the Boltzmann equation, is Maxwellian.

- ***H*-theorem:** The evolution for the H-function for BGK model is

$$\frac{\partial H}{\partial t} + \frac{\partial J_\alpha^H}{\partial x_\alpha} = -\sigma^{\mathrm{BGK}}, \tag{3.35}$$

where the production term σ^{BGK} is

$$\sigma^{\mathrm{BGK}} = \langle \sigma^{\mathrm{BGK}}, \ln f \rangle = \frac{1}{\tau}\left[-\int dc \left(f^{\mathrm{MB}} - f\right) \log\left(\frac{f}{f^{\mathrm{MB}}}\right) - \int dc \left(f^{\mathrm{MB}} - f\right) \log f^{\mathrm{MB}} \right]. \tag{3.36}$$

Since the mass, momentum and energy are conserved, the second term in the above equation is zero. Now the entropy production is

$$\sigma^{\mathrm{BGK}} = \frac{1}{\tau}\left[-\int dc \left(f^{\mathrm{MB}} - f\right) \log\left(\frac{f}{f^{\mathrm{MB}}}\right) \right] \geq 0. \tag{3.37}$$

Furthermore, $\Omega^{(\mathrm{BGK})} = 0$ only if $f = f^{\mathrm{MB}}(\rho, \mathbf{u}, \theta)$. Thus, the model has correct H-theorem too.

However, an important defect of the model is the constraint on Prandtl number. This aspect will be analyzed in the later part of this chapter. Many modifications of BGK model are available in the literature. The aim is often to correct the Prandtl number. Ellipsoidal BGK and Shakov models are two good examples of such models.

3.5.2 Fokker-Planck model

A different nonlinear model, proposed by Lebowitz et al, (Lebowitz *et al.*, 1960) which introduces the diffusion term to the Boltzmann collision model is

$$\mathcal{J}_{\mathrm{FP}} = \frac{1}{\tau_{\mathrm{FP}}} \partial_{c_\alpha} \left(\xi_\alpha f + \frac{k_{\mathrm{B}} T}{m} \partial_{c_\alpha} f \right). \tag{3.38}$$

The Fokker-Planck model also has the same collisional invariants, conservation laws and zero of the collision. This model also satisfies the H-theorem.

3.6 Moment chain of Boltzmann-BGK model

The moment equations can be obtained by multiplying the Boltzmann equation (3.10) with the velocities $\xi_{i1}\xi_{i2}\cdots\xi_{in}$ and subsequent integration over the velocity space. We have derived conservation laws in Sec. 3.3.

The evolution equation for the stress tensor (traceless second order moment) is

$$\frac{\partial \sigma_{\alpha\beta}}{\partial t} + u_\gamma \frac{\partial \sigma_{\alpha\beta}}{\partial x_\gamma} + \frac{\partial \overline{Q}_{\alpha\beta\gamma}}{\partial x_\gamma} + \sigma_{\alpha\beta}\frac{\partial u_\gamma}{\partial x_\gamma} + 2\,\overline{\sigma_{\gamma\beta}\frac{\partial u_\alpha}{\partial x_\gamma}} + 2\,p\,\overline{\frac{\partial u_\alpha}{\partial x_\beta}} + \frac{4}{5}\overline{\frac{\partial q_\alpha}{\partial x_\beta}} = -\frac{1}{\tau}\sigma_{\alpha\beta}^{\mathrm{neq}}, \tag{3.39}$$

where symmetrized traceless part of the velocity gradient tensor is

$$\overline{\frac{\partial u_\alpha}{\partial x_\beta}} = \frac{1}{2}\left(\frac{\partial u_\beta}{\partial x_\alpha} + \frac{\partial u_\alpha}{\partial x_\beta} - \frac{2}{3}\frac{\partial u_\gamma}{\partial x_\gamma}\delta_{\alpha\beta} \right). \tag{3.40}$$

Thus, the evolution of stress $\sigma_{\alpha\beta}$ requires knowledge of its flux $Q_{\alpha\beta\gamma}$. Similarly, the evolution

equations for traceless energy tensor and the heat flux are

$$\frac{\partial \overline{Q}_{\alpha\beta\gamma}}{\partial t} + \frac{\partial}{\partial x_\kappa}\left(u_\kappa \overline{Q}_{\alpha\beta\gamma}\right) + \frac{\partial \overline{R}_{\alpha\beta\gamma\kappa}}{\partial x_\kappa} + \frac{3}{7}\overline{\frac{\partial R_{\alpha\beta}}{\partial x_\gamma}} - \frac{3}{\rho}\overline{\sigma_{\alpha\beta}\frac{\partial p}{\partial x_\gamma}} - \frac{3}{\rho}\overline{\sigma_{\alpha\beta}\frac{\sigma_{\gamma\kappa}}{\partial x_\kappa}} + 3\rho\overline{Q}_{\alpha\beta\kappa}\overline{\frac{\partial u_\gamma}{\partial x_\kappa}} + \frac{12}{5}\overline{q_\alpha \frac{\partial u_\beta}{\partial x_\gamma}} = -\frac{1}{\tau}\overline{Q}^{\mathrm{neq}}_{\alpha\beta\gamma}, \tag{3.41}$$

$$\frac{\partial q_\alpha}{\partial t} + \frac{1}{2}\frac{\partial \overline{R}_{\alpha\beta}}{\partial x_\beta} + \frac{1}{6}\frac{\partial R}{\partial x_\alpha} + \overline{Q}_{\alpha\beta\gamma}\frac{\partial u_\beta}{\partial x_\gamma} + \frac{\partial\left(q_\alpha u_\beta\right)}{\partial x_\beta} + \frac{7}{5}q_\beta\frac{\partial u_\alpha}{\partial x_\beta} + \frac{2}{5}q_\alpha\frac{\partial u_\beta}{\partial x_\beta} + \frac{2}{5}q_\beta\frac{\partial u_\beta}{\partial x_\alpha} - \frac{5}{2}\frac{p}{\rho}\frac{\partial p}{\partial x_\alpha} - \frac{\sigma_{\alpha\beta}}{\rho}\frac{\partial p}{\partial x_\beta} - \frac{5}{2}\frac{p}{\rho}\frac{\partial \sigma_{\alpha\beta}}{\partial x_\beta} - \frac{\sigma_{\alpha\beta}}{\rho}\frac{\partial \sigma_{\beta\gamma}}{\partial x_\gamma} = -\frac{1}{\tau}\,q^{\mathrm{neq}}_\alpha. \tag{3.42}$$

The evolution equation for the contracted fourth order traceless tensor $\overline{R}_{\alpha\beta}$ and double contracted fourth order moment R are,

$$\frac{\partial \overline{R}_{\alpha\beta}}{\partial t} + \frac{\partial u_\kappa \overline{R}_{\alpha\beta}}{\partial x_\kappa} + \frac{\partial \overline{N}_{\alpha\beta\kappa}}{\partial x_\kappa} + \frac{2}{5}\overline{\frac{\partial n_\alpha}{\partial x_\beta}} - \frac{2}{\rho}\overline{Q}_{\alpha\beta\kappa}\frac{\partial P_{\kappa\eta}}{\partial x_\eta} - \frac{28}{5}\overline{q_\alpha\frac{\partial P_{\beta\kappa}}{\partial x_\kappa}} + 2\overline{R}_{\alpha\beta\kappa\eta}\frac{\partial u_\kappa}{\partial x_\eta} + 2\overline{R_{\alpha\kappa}\frac{\partial u_\beta}{\partial x_\kappa}} = -\frac{1}{\tau}\overline{R}^{\mathrm{neq}}_{\alpha\beta}, \tag{3.43}$$

$$\frac{\partial R}{\partial t} + \frac{\partial\left(u_\kappa R\right)}{\partial x_\kappa} + \frac{\partial n_\kappa}{\partial x_\kappa} + 4R_{\eta\kappa}\frac{\partial u_\kappa}{\partial x_\eta} - \frac{8}{\rho}q_\kappa\frac{\partial P_{\kappa\eta}}{\partial x_\eta} = -\frac{1}{\tau}R^{\mathrm{neq}}, \tag{3.44}$$

where $P_{\alpha\beta} = p\delta_{\alpha\beta} + \sigma_{\alpha\beta}$. It can be seen from this hierarchy of evolution equations that the equation for N^{th} order moment contain a higher order $(\mathrm{N}+1)^{\mathrm{th}}$ moment as a flux term. This system forms a chain which is not closed at any order; thus one requires closure approximations (Liboff, 2003). In order to give a reduced description of the system in terms of the finite set of moments several methods have been developed. Two important methods used for finding closure approximation are Grad moment method (Grad, 1949) and Chapman-Enskog approximation (Chapman & Cowling, 1970; Liboff, 2003).

3.6.1 Chapman-Enskog method

Chapman-Enskog method allows us to compute transport coefficients of macroscopic laws from the microscopic details of the gas (Chapman & Cowling, 1970). This method yields the explicit expressions for viscosity and heat conductivity. This method is based on perturbative expansion in space-time variables. In this method, the equation of motion itself is expanded into fast and slow components. Here, the fast time scale is the collisional time scale and the macroscopic time scale is the slow time scale. The iterative procedure is built as follows:

- The distribution function is expanded in series of τ

$$f_{\mathrm{CE}} = \sum_{k=0}^{\infty} \tau^k\, f^{(k)}_{\mathrm{CE}}. \tag{3.45}$$

The physical rationale of this expansion is smallness of Knudsen number which is a non-dimensional number defined as the ratio of the mean free path to the macroscopic length scale (L)

$$\mathrm{Kn} = \frac{l_{\mathrm{mfp}}}{L} = \frac{\tau c_s}{L}, \qquad c_s = \sqrt{\frac{\gamma k_{\mathrm{B}} T}{m}}. \tag{3.46}$$

Since $Kn \approx \tau$, essentially this is an expansion in Kn.

- In this expansion, conserved moments are left unexpanded in order to keep the consistency with the conservation laws, i.e.,

$$\begin{aligned} \int dc\{1, c, c^2\} f_{\mathrm{CE}}^{(0)} &= \{\rho, \rho\mathbf{u}, E\}, \\ \int dc\{1, c, c^2\} f_{\mathrm{CE}}^{(k)} &= \{0, 0, 0\}, \quad k \geq 0. \end{aligned} \tag{3.47}$$

- This implies that, all higher order moments can be expanded as:

$$\begin{aligned} \sigma_{\alpha\beta} &= \sigma_{\alpha\beta}^{(0)} + \tau\sigma_{\alpha\beta}^{(1)} + \tau^2\sigma_{\alpha\beta}^{(2)} + \cdots, \\ q_\alpha &= q_\alpha^{(0)} + \tau q_\alpha^{(1)} + \tau^2 q_\alpha^{(2)} + \cdots, \\ Q_{\alpha\beta\gamma} &= Q_{\alpha\beta\gamma}^{(0)} + \tau Q_{\alpha\beta\gamma}^{(1)} + \tau^2 Q_{\alpha\beta\gamma}^{(2)} + \cdots, \\ R_{\alpha\beta} &= R_{\alpha\beta}^{(0)} + \tau R_{\alpha\beta}^{(1)} + \tau^2 R_{\alpha\beta}^{(2)} + \cdots. \end{aligned} \tag{3.48}$$

- The time derivative is expanded as:

$$\partial_t\phi = \partial_t^{(0)}\phi + \tau\partial_t^{(1)}\phi + \cdots, \tag{3.49}$$

where the time derivatives are defined using conservation laws Eq. (3.18). For example, at O(1) we have

$$\begin{aligned} \partial_t^{(0)}\rho + \partial_\alpha j_\alpha &= 0, \\ \partial_t^{(0)} j_\alpha + \partial_\beta\left(\rho\theta\delta_{\alpha\beta} + \rho u_\alpha u_\beta\right) &= \rho g_\alpha, \\ \partial_t^{(0)}\left(\rho u^2 + 3\rho\theta\right) + \partial_\beta\left(\rho u^2 u_\alpha + 3\rho\theta u_\alpha\right) &= 2\rho u_\alpha g_\alpha, \end{aligned} \tag{3.50}$$

which are Euler equations of hydrodynamics.

At $\mathrm{O}(\tau^1)$ we have,

$$\begin{aligned} \partial_t^{(1)}\rho &= 0, \\ \partial_t^{(1)} j_\alpha + \partial_\beta\sigma_{\alpha\beta}^{(1)} &= 0, \\ \partial_t^{(1)}\left(\rho u^2 + 3\rho\theta\right) + \partial_\beta\left(2q_\alpha^{(1)} + 2u_\beta\sigma_{\alpha\beta}^{(1)}\right) &= 0. \end{aligned} \tag{3.51}$$

By considering the $\mathrm{O}(\tau^0)$ terms from the stress tensor equation (3.39)

$$2p\overline{\partial_\alpha u_\beta} = \sigma_{\alpha\beta}^{(1)}, \tag{3.52}$$

and from the heat flux dynamics (3.42) we get

$$\frac{5}{2}\frac{p}{\rho}\partial_\alpha p = q_\alpha^{(1)}. \tag{3.53}$$

The above relations implies that the stress tensor and heat flux have the form

$$\sigma_{\alpha\beta} = 2\mu\overline{\partial_\alpha u_\beta}, \tag{3.54}$$

$$q_\alpha = \kappa\partial_\alpha\theta, \tag{3.55}$$

with $\mu = p\tau$ as the dynamic viscosity and $\kappa = (5/2)\, p\tau$ as the heat conductivity. This implies a Prandtl number of 1, while Prandtl number obtained from the Boltzmann equation is 2/3.

3.6.2 Grad's moment method

The essence of the Grad method is to introduce an approximation to the one-particle distribution function f, which would depend only on a finite number N of moments. We take the moments of the Boltzmann equation and the number of moments depends on the problem we are interested in. Subsequently, the approximation is used to close the system of N moment equations from the kinetic equation.

Grad considered the separation of time scales associated with the evolution of the finite set of moments M' (which include hydrodynamic moments and certain higher order moments) and the rest of the higher order moments (M''). The assumption is that the moments (M') evolve significantly slower than the higher order moments (M''). Then for the time scales larger than the characteristic time scale t$'$, the dynamics of the distribution function is governed by the evolution of slower moments (M'). Thus, the key idea in this method was to introduce the hierarchy of time scale and assume that quasi-slow variables such as stress tensor and heat flux have their independent dynamics. The closure is provided only for fast variables, and conservation laws are appended with the evolution of quasi-slow variables. This separation of time scales is formally introduced by projecting the distribution function in the finite sub-space created by Hermite polynomials $\mathcal{H}^i$, which are the appropriate orthogonal polynomials with Maxwell-Boltzmann distribution as weight for the inner product (Grad, 1949). The distribution function with this approximation is

$$f^{\mathrm{Grad}}(M', c) = f^{\mathrm{MB}}(\rho, u, \theta) \left[\sum_{i=0}^{N} \mathcal{A}^{(i)} \mathcal{H}^{(i)}(\xi) \right], \tag{3.56}$$

where N is the highest order of Hermite polynomial and coefficients $A^{(i)}$ are i^{th} order tensor created from moments of the distribution function. A few lower order Hermite polynomials are

$$\begin{aligned}
\mathcal{H}^{(0)} &= 1, \\
\mathcal{H}_i^{(1)} &= \xi_i, \\
\mathcal{H}_{ij}^{(2)} &= \xi_i \xi_j - \theta \delta_{ij}, \\
\mathcal{H}_{ijk}^{(3)} &= \xi_i \xi_j \xi_k - \theta \left(\xi_i \delta_{jk} + \xi_j \delta_{ik} + \xi_k \delta_{ij} \right), \\
\mathcal{H}_{ijkl}^{(4)} &= \xi_i \xi_j \xi_k \xi_l - \theta \left(\xi_i \xi_j \delta_{kl} + \xi_i \xi_k \delta_{jl} + \xi_i \xi_l \delta_{jk} + \xi_k \xi_j \delta_{il} + \xi_l \xi_j \delta_{ik} + \xi_k \xi_l \delta_{ij} \right) + \theta^2 \Delta_{ijkl},
\end{aligned} \tag{3.57}$$

where Δ_{ijkl} is fourth order isotropic tensor defined as $\Delta_{ijkl} = (\delta_{ij}\delta_{kl} + \delta_{ik}\delta_{jl} + \delta_{il}\delta_{jk})$. One often works with the contracted third and fourth order polynomials and the corresponding polynomials with trace and traceless forms

$$\begin{aligned}
\mathcal{H}_i^{(3)} &= \xi^2 \xi_i - (D+2)\theta \xi_i, \\
\overline{\mathcal{H}}_{ijk}^{(3)} &= \xi_i \xi_j \xi_k - \frac{1}{5} \xi^2 \left(\xi_i \delta_{jk} + \xi_j \delta_{ik} + \xi_k \delta_{ij} \right), \\
\mathcal{H}_{ij}^{(4)} &= \xi^2 \xi_i \xi_j - 7\theta \xi_i \xi_j - \theta \xi^2 \delta_{ij} + 5\theta^2 \delta_{ij}, \\
\mathcal{H}^{(4)} &= \xi^4 - (2D+4)\theta \xi^2 + D(D+2)\theta^2, \\
\bar{\mathcal{H}}_{ij}^{(4)} &= \left(\xi^2 - 7\theta \right) \overline{\xi_i \xi_j}.
\end{aligned} \tag{3.58}$$

In the subsequent sections we will consider the cases of 13 and 26 moments.

3.6.3 Grad-13 moment method

The most commonly used method is Grad-13 moment (the slow moments are the five hydrodynamic moments, five moments from the traceless stress tensor (σ_{ij}) and three components of heat flux vector) and the constructed distribution function in terms of peculiar velocity is then given by

$$f_{13}^{\mathrm{Grad}} = f^{\mathrm{MB}}\left[1 + \frac{\sigma_{ij}}{2\rho\theta^2}\left(\xi_i\xi_j - \delta_{ij}\theta\right) + \frac{q_i}{5\rho\theta^3}\xi_i\left(\xi^2 - 5\theta\right)\right]. \tag{3.59}$$

The evolution equation for moments can then be obtained by taking appropriate moments of Boltzmann equation (3.10) and using the Grad distribution function (3.56). The closure for the higher order moments computed from the distribution function (3.59) are

$$\overline{Q}_{\alpha\beta\gamma} = 0, \qquad \overline{R}_{\alpha\beta} = 7\theta\sigma_{\alpha\beta}, \qquad R = 15\rho\theta^2. \tag{3.60}$$

Here $R = \langle\xi^4, f\rangle$ is the double contracted fourth order tensor and $\overline{R}_{\alpha\beta} = \langle\overline{\xi^2\xi_\alpha\xi_\beta}, f\rangle$ is traceless part of the contracted fourth order tensor. Using these closure relations, the evolution equations (3.18 and 3.39 -3.42) reduce to

$$\begin{aligned}
\frac{\partial\rho}{\partial t} + \frac{\partial j_\alpha}{\partial x_\alpha} &= 0,\\
\frac{\partial j_\alpha}{\partial t} + \frac{\partial}{\partial x_\beta}\left(\rho\theta\delta_{\alpha\beta} + \rho u_\alpha u_\beta + \sigma_{\alpha\beta}\right) &= 0,\\
\frac{\partial}{\partial t}\left(\rho u^2 + 3\rho\theta\right) + \frac{\partial}{\partial x_\alpha}\left(\rho u^2 u_\alpha + 3\rho\theta u_\alpha + 2q_\alpha + 2u_\beta\sigma_{\alpha\beta}\right) &= 0,\\
\frac{\partial\sigma_{\alpha\beta}}{\partial t} + u_\gamma\frac{\partial\sigma_{\alpha\beta}}{\partial x_\gamma} + \sigma_{\alpha\beta}\frac{\partial u_\gamma}{\partial x_\gamma} + 2\,\overline{\sigma_{\gamma\beta}\frac{\partial u_\alpha}{\partial x_\gamma}} + 2\,p\,\overline{\frac{\partial u_\alpha}{\partial x_\beta}} + \frac{4}{5}\overline{\frac{\partial q_\alpha}{\partial x_\beta}} &= -\frac{1}{\tau}\sigma_{\alpha\beta},\\
\frac{\partial q_\alpha}{\partial t} + \frac{7\sigma_{\alpha\beta}}{2}\frac{\partial\theta}{\partial x_\beta} + \theta\frac{\partial\sigma_{\alpha\beta}}{\partial x_\beta} + \frac{5}{2}\frac{\partial\rho\theta^2}{\partial x_\alpha} + \frac{\partial\left(q_\alpha u_\beta\right)}{\partial x_\beta} + \frac{7}{5}q_\beta\frac{\partial u_\alpha}{\partial x_\beta} +&\\
\frac{2}{5}q_\alpha\frac{\partial u_\beta}{\partial x_\beta} + \frac{2}{5}q_\beta\frac{\partial u_\beta}{\partial x_\alpha} - \frac{5}{2}\frac{p}{\rho}\frac{\partial p}{\partial x_\alpha} - \frac{\sigma_{\alpha\beta}}{\rho}\frac{\partial p}{\partial x_\beta} - \frac{\sigma_{\alpha\beta}}{\rho}\frac{\partial\sigma_{\beta\gamma}}{\partial x_\gamma} &= -\frac{1}{\tau}q_\alpha^{\mathrm{neq}}.
\end{aligned} \tag{3.61}$$

The above set of symmetric hyperbolic equations are closed and can be solved for a particular configuration.

3.6.4 Grad-26 moment method

An important extension of Grad-13 moment equation is G26, i.e., 26 moments are used to construct the distribution function f. The distribution function can be written as:

$$f_{26}^{\mathrm{Grad}} = f^{\mathrm{MB}}\left[1 + \frac{\sigma_{ij}}{2\rho\theta^2}\mathcal{H}_{ij}^{(2)} + \frac{\overline{Q}_{ijk}}{6\rho\theta^3}\overline{\mathcal{H}}_{ijk}^{(3)} + \frac{q_i}{5\rho\theta^3}\mathcal{H}_i^{(3)} + \frac{\left(\overline{R}_{ij} - 7\theta\sigma_{ij}\right)}{28\rho\theta^4}\overline{\mathcal{H}}_{ij}^{(4)} + \frac{R}{120\rho\theta^4}\mathcal{H}^{(4)}\right]. \tag{3.62}$$

With the above distribution function, we can compute the closure for the fourth order, contracted fifth order ($\overline{N}_{\alpha\beta\gamma}$) and double contracted fifth order (n_α) moments as:

$$\begin{aligned}
\overline{R}_{\alpha\beta\gamma\kappa} =& \frac{1}{7}\left(C_{\alpha\beta}\delta_{\gamma\kappa} + C_{\alpha\gamma}\delta_{\beta\kappa} + C_{\alpha\kappa}\delta_{\beta\gamma} + C_{\beta\gamma}\delta_{\alpha\kappa} + C_{\beta\kappa}\delta_{\alpha\gamma} + C_{\gamma\kappa}\delta_{\alpha\beta}\right) + \left(R + 12\theta P\right)\frac{2}{21}\Delta_{\alpha\beta\gamma\kappa},\\
\overline{N}_{\alpha\beta\gamma} =& 9\theta\overline{Q}_{\alpha\beta\gamma}, \qquad n_\alpha = 28\theta q_\alpha.
\end{aligned} \tag{3.63}$$

where $C_{\alpha\beta} = \left(\overline{R}_{\alpha\beta} - \theta\sigma_{\alpha\beta}\right)$. Then the corresponding evolution equations with the above closure can be written as:

$$
\begin{aligned}
\frac{\partial \rho}{\partial t} + \frac{\partial j_\alpha}{\partial x_\alpha} &= 0, \\
\frac{\partial j_\alpha}{\partial t} + \frac{\partial}{\partial x_\beta}\left(\rho\theta\delta_{\alpha\beta} + \rho u_\alpha u_\beta + \sigma_{\alpha\beta}\right) &= \rho g_\alpha, \\
\frac{\partial}{\partial t}\left(\rho u^2 + 3\rho\theta\right) + \frac{\partial}{\partial x_\alpha}\left(\rho u^2 u_\alpha + 3\rho\theta u_\alpha + 2q_\alpha + 2u_\beta\sigma_{\alpha\beta}\right) &= 2\rho u_\alpha g_\alpha, \\
\frac{\partial \sigma_{\alpha\beta}}{\partial t} + u_\gamma\frac{\partial \sigma_{\alpha\beta}}{\partial x_\gamma} + \frac{\partial \overline{Q}_{\alpha\beta\gamma}}{\partial x_\gamma} + \sigma_{\alpha\beta}\frac{\partial u_\gamma}{\partial x_\gamma} + 2\,\overline{\sigma_{\gamma\beta}\frac{\partial u_\alpha}{\partial x_\gamma}} + 2\,p\,\overline{\frac{\partial u_\alpha}{\partial x_\beta}} + \frac{4}{5}\overline{\frac{\partial q_\alpha}{\partial x_\beta}} &= -\frac{1}{\tau}\,\sigma_{\alpha\beta}, \\
\frac{\partial q_\alpha}{\partial t} + \frac{1}{2}\frac{\partial \overline{R}_{\alpha\beta}}{\partial x_\beta} + \frac{1}{6}\frac{\partial R}{\partial x_\alpha} + \overline{Q}_{\alpha\beta\gamma}\frac{\partial u_\beta}{\partial x_\gamma} + \frac{\partial\left(q_\alpha u_\beta\right)}{\partial x_\beta} + \frac{7}{5}q_\beta\frac{\partial u_\alpha}{\partial x_\beta} + \frac{2}{5}q_\alpha\frac{\partial u_\beta}{\partial x_\beta} + \frac{2}{5}q_\beta\frac{\partial u_\beta}{\partial x_\alpha} & \\
-\frac{5}{2}\frac{p}{\rho}\frac{\partial p}{\partial x_\alpha} - \frac{\sigma_{\alpha\beta}}{\rho}\frac{\partial p}{\partial x_\beta} - \frac{5}{2}\frac{p}{\rho}\frac{\partial \sigma_{\alpha\beta}}{\partial x_\beta} - \frac{\sigma_{\alpha\beta}}{\rho}\frac{\partial \sigma_{\beta\gamma}}{\partial x_\gamma} &= -\frac{1}{\tau}\,q_\alpha^{\mathrm{neq}}, \\
\frac{\partial \overline{Q}_{\alpha\beta\gamma}}{\partial t} + \frac{\partial\left(u_\kappa\overline{Q}_{\alpha\beta\gamma}\right)}{\partial x_\kappa} + \frac{\partial \overline{R}_{\alpha\beta\gamma\kappa}}{\partial x_\kappa} + \frac{3}{7}\overline{\frac{\partial R_{\alpha\beta}}{\partial x_\gamma}} - \frac{3}{\rho}\overline{\sigma_{\alpha\beta}\frac{\partial p}{\partial x_\gamma}} - \frac{3}{\rho}\overline{\sigma_{\alpha\beta}\frac{\partial \sigma_{\gamma\kappa}}{\partial x_\kappa}} & \\
+3\rho\overline{Q}_{\alpha\beta\kappa}\frac{\partial u_\gamma}{\partial x_\kappa} + \frac{12}{5}\overline{q_\alpha\frac{\partial u_\beta}{\partial x_\gamma}} &= -\frac{1}{\tau}\overline{Q}_{\alpha\beta\gamma}^{\mathrm{neq}}, \\
\frac{\partial \overline{R}_{\alpha\beta}}{\partial t} + \frac{\partial\left(u_\kappa\overline{R}_{\alpha\beta}\right)}{\partial x_\kappa} + 9\frac{\partial\left(\theta\overline{Q}_{\alpha\beta\kappa}\right)}{\partial x_\kappa} + \frac{56}{5}\overline{\frac{\partial\left(\theta q_\alpha\right)}{\partial x_\beta}} - \frac{2}{\rho}\overline{Q}_{\alpha\beta\kappa}\frac{\partial P_{\kappa\eta}}{\partial x_\eta} - \frac{28}{5}\overline{q_\alpha\frac{\partial P_{\beta\kappa}}{\partial x_\kappa}} & \\
+2\overline{R}_{\alpha\beta\kappa\eta}\frac{\partial u_\kappa}{\partial x_\eta} + 2\overline{R_{\alpha\kappa}\frac{\partial u_\beta}{\partial x_\kappa}} &= -\frac{1}{\tau}\overline{R}_{\alpha\beta}^{\mathrm{neq}}, \\
\frac{\partial R}{\partial t} + \frac{\partial\left(u_\kappa R\right)}{\partial x_\kappa} + 28\frac{\partial\left(\theta q_\kappa\right)}{\partial x_\kappa} + 4R_{\eta\kappa}\frac{\partial u_\kappa}{\partial x_\eta} - \frac{8}{\rho}q_\kappa\frac{\partial P_{\kappa\eta}}{\partial x_\eta} &= -\frac{1}{\tau}R^{\mathrm{neq}}.
\end{aligned}
\tag{3.64}
$$

These transport equations along with their closure relations form a closed set and can be solved in principle. This will be shown in the next chapter for a simplified case of unidirectional flow, wherein the simplification of linearization make the equations to be solved analytically. Further, the necessary conditions for a method to capture Knudsen boundary layer and other rarefaction effects will be discussed in the next chapter. This is achieved by analyzing the closure relations for the higher order asymmetric moments.

Chapter 4
Unidirectional flows

4.1 Introduction

Transport phenomena of the gases at micrometer scale have seen renewed interest in recent years due to possible applications in areas of micro-mechanical devices, semiconductor manufacturing, etc. For these applications, standard tools *used to predict the quantities of interest* are Direct simulation Monte Carlo (Alexander & Garcia, 1997), the Moment method based extension of Navier-Stokes-Fourier equation and the mesoscale tool such as lattice Boltzmann method (Succi, 2001*a*). The numerical tool to be used is selected based on the operating condition such as Knudsen number and Mach number. For instance, the particle-based method DSMC is preferable for high Mach number and high Knudsen number. For the low Mach number flows in the transition regime, this is computationally expensive. Hence considerable attention is focused on computationally less expensive methods based on Chapman-Enskog and moment-based methods (Struchtrup & Torrilhon, 2003). Ansumali et al. (Ansumali *et al.*, 2007*b*) first showed that many canonical problems could be solved analytically for different Knudsen numbers beyond the continuum limit using the moment chain of lattice Boltzmann models constructed based on Gauss-Hermite quadrature. It was shown that with the application of diffusive boundary condition at the wall, these models reproduced many characteristics of rarefied gas flow in a micro-channel. In particular, it was found that while the lower order LB models were able to reproduce slip flow effect correctly, only higher order models could predict the Knudsen boundary layer accurately. Kim and sader et al. (Kim *et al.*, 2008*a*) found that this approach of Gauss-Hermite quadrature does not lead to uniform convergence and models with the even number of discrete velocities behave quite differently from models with an odd number of discrete velocities. Wahyu et al., 2010 (Yudistiawan *et al.*, 2010) argued that this oscillatory convergence is related to the fact that Gauss-Hermite quadrature is not optimal in 3-D, and they showed that the primary effect of Knudsen boundary layer could be reproduced with just 27 discrete velocity set provided one work with off-lattice models. It was shown later that the same Knudsen boundary layer is also observed with the R13 model, which is an extension of Grad-13 model (Struchtrup & Torrilhon, 2003). The R13 model can also be understood as slow dynamics of Grad-26 moment equation.

In this chapter, we attempt to provide the minimum requirement for any moment based method to capture the boundary layer and show that the Grad's 26 moment method can indeed capture the Knudsen boundary layer. We conjecture that highly anisotropic moments such as Q_{xxx}, Q_{xyy} and R_{xyyy} play an important role in describing the boundary layer. Towards this, we work with the continuous Boltzmann equation where the collision is modeled using BGK model and consider canonical unidirectional flow at steady state. We then analyze the effect of various closure models for anisotropic quantities such as Q_{xxx}, Q_{xyy} and R_{xyyy}. We show that most widely used model such as Grad-13 (hereafter referred as G13) cannot reproduce boundary layer. The minimal model which can have this effect is the Grad-26 model (hereafter G26).

The chapter is organized as follows: In section 4.2, the general transport equations for the general unidirectional flow are described, in section 4.3, the transport equations for the Grad-13 moment method is explained along with the solution for the form of the velocity profile, in section 4.4, the transport equations for the Grad-26 moment method is explained along with the solution for the form of the velocity profile.

4.2 Unidirectional flow

We consider the case of uni-directional steady flow along x-direction and with infinitely long walls at $y = \pm L/2$ which are maintained at a constant temperature θ_0. As seen from the schematic of the flow set-up in figure 4.1, the flow occurs due to the motion of walls and/or an external force g_α (or pressure gradient). For this setup, it is reasonable to neglect the variation of all the flow quantities such as velocity and all the higher order moments along the flow direction and assume they vary only in the normal direction i.e., $M(\mathbf{x}, t) \equiv M(y)$. For this set-up, important simplifications in the equations of motion arise, and often one can find closed-form analytical solutions even for flow far away from hydrodynamics (Ansumali *et al.*, 2007*b*). In this case it is reasonable to expect $\rho = \rho_0$, and $\theta = \theta_0$.

Due to unidirectionality of the set-up, the continuity equation Eq.(3.18) reduces to the condition $\partial_y j_y = 0$ which implies $j_y = 0$ due to the no penetration condition at the walls. Similarly, the momentum conservation equations reduces to

$$\frac{\partial \sigma_{xy}}{\partial y} = \rho g_x, \qquad \frac{\partial \left(\rho\theta + \sigma_{yy}\right)}{\partial y} = 0, \qquad \frac{\partial \sigma_{yz}}{\partial y} = 0 \tag{4.1}$$

which implies that, for any general unidirectional flow set up, the components of the stress tensor has the form

$$\sigma_{xy} = \rho g_x y + \text{constant}, \qquad \sigma_{yy} = \text{constant}, \qquad \sigma_{yz} = \text{constant}. \tag{4.2}$$

In the energy conservation equation, $\sigma_{yy}\left(\partial u_x/\partial y\right)$ term is neglected for the linear case, since it is of $O(U^3)$. Hence, the governing equations for the energy conservation reduces to

$$\frac{\partial q_y}{\partial y} = 0. \tag{4.3}$$

The simplified evolution equation for the stress tensor are

$$\begin{aligned}
\frac{\partial \overline{Q}_{xyy}}{\partial y} + \underline{(p + \sigma_{yy})\frac{\partial u_x}{\partial y}} + \frac{2}{5}\frac{\partial q_x}{\partial y} &= -\frac{1}{\tau}\sigma_{xy} \\
\frac{\partial \overline{Q}_{xxy}}{\partial y} + \frac{4}{3}\sigma_{xy}\frac{\partial u_x}{\partial y} &= -\frac{1}{\tau}\sigma_{xx} \\
\frac{\partial \overline{Q}_{yyy}}{\partial y} &= -\frac{1}{\tau}\sigma_{yy}, \\
\frac{\partial \overline{Q}_{yyz}}{\partial y} + \frac{2}{5}\frac{\partial q_z}{\partial y} &= -\frac{1}{\tau}\sigma_{yz}, \\
\frac{\partial \overline{Q}_{xyz}}{\partial y} &= -\frac{1}{\tau}\sigma_{xz}.
\end{aligned} \tag{4.4}$$

Similarly, the evolution for the heat flux along the streamwise and normal direction can be written as:

$$\begin{aligned}
\frac{\partial \overline{R}_{xy}}{\partial y} + \underline{(\overline{Q}_{xxy} + \frac{7}{5}q_y)\frac{\partial u_x}{\partial y}} - \underline{(\frac{5p}{2\rho} + \frac{\sigma_{xx}}{\rho})\rho g_x} &= -\frac{1}{\tau}q_x \\
\frac{\partial \overline{R}_{yy}}{\partial y} + \left(\overline{Q}_{xyy} + \frac{2}{5}q_x\right)\frac{\partial u_x}{\partial y} - \sigma_{xy}g_x &= -\frac{1}{\tau}q_y
\end{aligned} \tag{4.5}$$

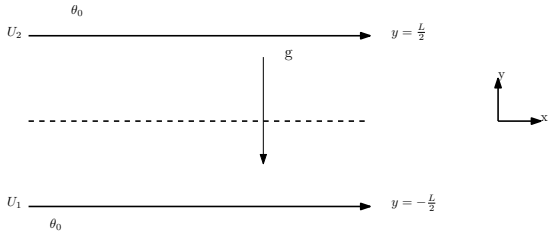

Figure 4.1: The figure shows the schematic of the unidirectional flow set-up where the flow is due to the movement of boundaries at different velocities U_1 and U_2

Similarly, the evolution of the heat flux along z-direction can be written as:

$$\frac{\partial \overline{R}_{yz}}{\partial y} - \frac{\sigma_{yz}}{\rho}\frac{\partial \sigma_{xz}}{\partial y} = -\frac{1}{\tau}q_z \tag{4.6}$$

The above set of equations (4.4)-(4.6), govern the behavior of lower order moments for unidirectional flow. These equations need to be supplemented with the evolution equations for the higher order moments in case of Boltzmann or Boltzmann-BGK equation. We will analyze the effect of higher order moments by examining these equations along with various closure for higher order moments. The closure relations for these model will reveal that the anisotropic moments such as Q_{xxx} and R_{xyyy} contribute to the accurate prediction of Knudsen boundary layer.

4.3 Grad-13 moment closure

We have written down the necessary evolution equations and the moment chain for G13 and G26 in section 4.2. The closure for the higher order moments computed using Grad-13 moment approximation for the distribution function (Eq. (3.59)) are:

$$\overline{Q}_{\alpha\beta\gamma} = 0 \qquad \overline{R}_{\alpha\beta} = 7\theta\sigma_{\alpha\beta} \qquad R = 15\rho\theta^2. \tag{4.7}$$

This allow us to conclude using stress equation (4.4) that,

$$\begin{aligned} p\frac{\partial u_x}{\partial y} + \frac{2}{5}\frac{\partial q_x}{\partial y} &= -\frac{1}{\tau}\sigma_{xy} \\ \frac{4}{3}\sigma_{xy}\frac{\partial u_x}{\partial y} &= -\frac{1}{\tau}\sigma_{xx} \\ \sigma_{yy} &= 0, \\ \frac{\partial q_z}{\partial y} &= -\frac{5}{2\,\tau}\sigma_{yz}, \\ \sigma_{xz} &= 0. \end{aligned} \tag{4.8}$$

Similarly, the heat flux equations (4.5) and (4.6) simplifies as $q_z = 0$ and,

$$\frac{9}{2}\rho\theta g_x + \frac{7}{5}q_y\frac{\partial u_x}{\partial y} = -\frac{1}{\tau}q_x, \tag{4.9}$$

$$\left(\frac{2}{5}q_x\right)\frac{\partial u_x}{\partial y} - \sigma_{xy}g_x = -\frac{1}{\tau}q_y. \tag{4.10}$$

To solve the system of equations we work with semi-linearized equations. In this, we retain terms up to quadratic in shear stress (σ_{xy}) and velocity and neglect the higher order terms

(Struchtrup & Torrilhon, 2003). The above system of equations with this approximation reduce to:

$$\begin{aligned} \sigma_{xx} = \sigma_{yy} = \sigma_{xz} = \sigma_{yz} = 0, \\ q_x = -\frac{9\tau}{2}\rho\theta g_x, \\ q_y = q_z = 0. \end{aligned} \tag{4.11}$$

From the evolution of heat flux along the flow direction (q_x) it can be seen that the variation of q_x in the normal y direction is zero for constant driving force ($\partial q_x/\partial y = 0$).

$$\frac{\partial u_x}{\partial y} = -\frac{\sigma_{xy}}{\tau\, p} \tag{4.12}$$

Using this in the evolution of shear stress (σ_{xy}), the velocity profile can be obtained as:

$$u_x = -\frac{1}{2\,\tau\rho\theta}\left(\rho g_x y^2 + k_1 y + k_2\right), \tag{4.13}$$

where k_1 and k_2 are constants obtained from the boundary condition.

The profile doesn't predict any Knudsen boundary layer, and the profile is precisely of the form predicted by macroscopic Navier-Stokes equation with the prefactor being the inverse of dynamic viscosity ($\mu \approx \tau\rho\theta$). This was first pointed out by Grad (Grad, 1949).

4.4 Grad-26 moment closure

Now, we consider the next widely used Grad-26 model for the moment construction. In Grad's 26 moment representation, $\overline{Q}_{\alpha\beta\gamma}$ and contracted fourth moments $\overline{R}_{\alpha\beta}$ are included in the list of relevant moments. Unlike, the previous method, these moments are considered as the unknown moment and has to be solved explicitly. The closure for the higher order moments computed using Grad-26 moment approximation for the distribution function (Eq. (3.62)) can be computed and are:

$$\overline{R}_{\alpha\beta\gamma\kappa} = \frac{1}{7}\left(C_{\alpha\beta}\delta_{\gamma\kappa} + C_{\alpha\gamma}\delta_{\beta\kappa} + C_{\alpha\kappa}\delta_{\beta\gamma} + C_{\beta\gamma}\delta_{\alpha\kappa} + C_{\beta\kappa}\delta_{\alpha\gamma} + C_{\gamma\kappa}\delta_{\alpha\beta}\right) + \left(R + 12\theta P\right)\frac{2}{21}\Delta_{\alpha\beta\gamma\kappa}, \tag{4.14}$$

with $C_{\alpha\beta} = \left(\overline{R}_{\alpha\beta} - \theta\sigma_{\alpha\beta}\right)$ and the fifth order moment closure reads as:

$$\overline{N}_{\alpha\beta\gamma} = 9\theta\overline{Q}_{\alpha\beta\gamma}, \qquad n_\alpha = 28\theta q_\alpha. \tag{4.15}$$

The solution for the set of G26 equations for unidirectional flow can be obtained by linearizing the equations as done in the previous section. However, the difference being, we consider, the contracted fourth order moment as an independent variable rather than being calculated from the closure relations as done by (Struchtrup & Torrilhon, 2003)). This simplification makes the solution to the set of equations to be tractable.

With this approximation and closure relations Eq. (4.15) the third order moment equations

reduce to:

$$\frac{\partial \overline{R}_{xyyy}}{\partial y} + \frac{8}{35}\frac{\partial \overline{R}_{xy}}{\partial y} - \underbrace{g_x\left(\sigma_{yy} - \frac{2}{5}\sigma_{xx}\right) + \left(\overline{Q}_{yyy} + \frac{16}{25}q_y - \frac{2}{5}\overline{Q}_{xxy}\right)\frac{\partial u_x}{\partial y}} = -\frac{1}{\tau}\overline{Q}_{xyy} \quad (4.16)$$

$$\frac{\partial \overline{R}_{xxyy}}{\partial y} + \underbrace{\frac{1}{7}\frac{\partial R_{xx}}{\partial y} - \frac{2}{35}\frac{\partial R_{yy}}{\partial y} - \frac{1}{35}\frac{\partial R}{\partial y} - \frac{8}{5}\sigma_{xy}g_x + \left(\frac{8}{5}\overline{Q}_{xyy} + \frac{12}{5}q_x\right)\frac{\partial u_x}{\partial y}} = -\frac{1}{\tau}\overline{Q}_{xxy} \quad (4.17)$$

$$\frac{\partial \overline{R}_{xxyz}}{\partial y} - \frac{2}{35}\frac{\partial \overline{R}_{yz}}{\partial y} + \underbrace{\frac{8}{5}\sigma_{xz}g_x + \frac{8}{5}\overline{Q}_{xyz}\frac{\partial u_x}{\partial y}} = -\frac{1}{\tau}\overline{Q}_{xxz}, \quad (4.18)$$

$$\frac{\partial \overline{R}_{yyyz}}{\partial y} + \frac{8}{35}\frac{\partial \overline{R}_{yz}}{\partial y} - \underbrace{\frac{2}{5}\sigma_{xz}g_x - \frac{2}{5}\overline{Q}_{xyz}\frac{\partial u_x}{\partial y}} = -\frac{1}{\tau}\overline{Q}_{yyz}, \quad (4.19)$$

$$\frac{\partial \overline{R}_{xyzz}}{\partial y} - \frac{2}{35}\frac{\partial \overline{R}_{xy}}{\partial y} + \underbrace{\frac{2}{5}\sigma_{xx}g_x + \left(\overline{Q}_{yzz} - \frac{4}{25}q_y - \frac{2}{5}\overline{Q}_{xxy}\right)\frac{\partial u_x}{\partial y}} = -\frac{1}{\tau}\overline{Q}_{xzz}, \quad (4.20)$$

$$\frac{\partial \overline{R}_{yyzz}}{\partial y} + \underbrace{\frac{1}{7}\frac{\partial R_{zz}}{\partial y} - \frac{2}{35}\frac{\partial R_{yy}}{\partial y} - \frac{1}{35}\frac{\partial R}{\partial y} + \frac{2}{5}\sigma_{xy}g_x - \left(\frac{2}{5}\overline{Q}_{xyy} + \frac{4}{25}q_x\right)\frac{\partial u_x}{\partial y}} = -\frac{1}{\tau}\overline{Q}_{zzy}, \quad (4.21)$$

$$\frac{\partial \overline{R}_{xyyz}}{\partial y} + \frac{1}{7}\frac{\partial \overline{R}_{xz}}{\partial y} - \underbrace{\sigma_{yz}g_x + \left(\overline{Q}_{yyz} + \frac{2}{5}q_z\right)\frac{\partial u_x}{\partial y}} = -\frac{1}{\tau}\overline{Q}_{xyz}, \quad (4.22)$$

$$\frac{\partial \overline{R}_{xxxy}}{\partial y} - \frac{6}{35}\frac{\partial \overline{R}_{xy}}{\partial y} - \underbrace{\frac{9}{5}\sigma_{xx}g_x + \left(\frac{9}{5}\overline{Q}_{xxy} - \frac{12}{25}q_y\right)\frac{\partial u_x}{\partial y}} = \frac{1}{\tau}\overline{Q}_{xxx} \quad (4.23)$$

$$\frac{\partial \overline{R}_{yyyy}}{\partial y} + \underbrace{\frac{9}{35}\frac{\partial R_{yy}}{\partial y} - \frac{3}{35}\frac{\partial R}{\partial y} - \frac{6}{5}\sigma_{xy}g_x - \left(\frac{6}{5}\overline{Q}_{xyy} + \frac{12}{25}q_x\right)\frac{\partial u_x}{\partial y}} = \frac{1}{\tau}\overline{Q}_{yyy}, \quad (4.24)$$

$$\frac{\partial \overline{R}_{yzzz}}{\partial y} - \frac{6}{35}\frac{\partial \overline{R}_{yz}}{\partial y} - \underbrace{\frac{6}{5}\sigma_{xz}g_x - \frac{6}{5}\overline{Q}_{xyz}\frac{\partial u_x}{\partial y}} = \frac{1}{\tau}\overline{Q}_{zzz}, \quad (4.25)$$

and the evolution of the contracted fourth order tensor are:

$$9\theta\frac{\partial \overline{Q}_{xyy}}{\partial y} - 2g_x\left(\overline{Q}_{xxy} + \frac{14}{5}q_y\right) + \frac{28\theta}{5}\frac{\partial q_x}{\partial y} + \underbrace{(2\overline{R}_{xxyy} + R_{yy})\frac{\partial u_x}{\partial y}} = -\frac{1}{\tau}\overline{R}_{xy}, \quad (4.26)$$

$$9\theta\frac{\partial \overline{Q}_{xxy}}{\partial y} - \underbrace{\frac{56}{15}\frac{\partial q_y}{\partial y} - \left(2\overline{Q}_{xxx} + \frac{56}{15}q_x\right)g_x + \left(2\overline{R}_{xxxy} + \frac{4}{3}R_{xy}\right)\frac{\partial u_x}{\partial y}} = -\frac{1}{\tau}\overline{R}_{xx}, \quad (4.27)$$

$$9\theta\frac{\partial \overline{Q}_{yyy}}{\partial y} + (\frac{4}{21}R_{xy} - \underbrace{\frac{6}{7}\sigma_{yy})\frac{\partial u_x}{\partial y}} = -\frac{1}{\tau}\overline{R}_{yy}, \quad (4.28)$$

$$9\theta\frac{\partial \overline{Q}_{xyz}}{\partial y} - \frac{2}{\rho}\overline{Q}_{xxz}\frac{\partial \sigma_{xy}}{\partial y} + \underbrace{(2\overline{R}_{xxyz})\frac{\partial u_x}{\partial y}} = -\frac{1}{\tau}\overline{R}_{xz}, \quad (4.29)$$

$$9\theta\frac{\partial \overline{Q}_{yyz}}{\partial y} - \frac{2}{\rho}\overline{Q}_{xyz}\frac{\partial \sigma_{xy}}{\partial y} + \underbrace{(2\overline{R}_{xyyz})\frac{\partial u_x}{\partial y}} = -\frac{1}{\tau}\overline{R}_{yz}, \quad (4.30)$$

$$9\theta\frac{\partial \overline{Q}_{yzz}}{\partial y} - \underbrace{\frac{56\theta}{15}\frac{\partial q_y}{\partial y} - \left(2\overline{Q}_{xzz} + \frac{56}{12}q_x\right)g_x + \left(2\overline{R}_{xyzz} + \frac{4}{3}R_{xy}\right)\frac{\partial u_x}{\partial y}} = -\frac{1}{\tau}\overline{R}_{zz}, \quad (4.31)$$

$$\underbrace{4R_{xy}\frac{\partial u_x}{\partial y}} = -\frac{1}{\tau}R. \quad (4.32)$$

The equations are linearized as done in the previous section, to make the system of equations to be solved analytically. In this limit, the terms which are underlined are higher than O(u) and hence can be neglected. With this assumption, the above set of equations can be solved to obtain the velocity profile.

Here, it should be noted that, $\overline{Q}^{\rm eq}_{\alpha\beta\gamma} = 0$ and $\overline{R}^{\rm eq}_{\alpha\beta} = 0$. To obtain the velocity profile, we consider the evolution equation for $\overline{R}_{xy}$ and σ_{xy}. This equation involves finding of $\overline{Q}_{xyy}$, $\overline{Q}_{xxy}$, $\overline{R}_{xyyy}$. This can be obtained from the corresponding evolution equations. All these quantities are in terms of $\overline{R}_{xy}$, σ_{xy} and u_x. Hence from the evolution equation of σ_{xy} and using the other higher order moment transport equations,

$$\frac{\sigma_{xy}}{\tau^2} = \frac{37}{35}\frac{\partial^2 \overline{R}_{xy}}{\partial y^2} + \rho\theta\frac{\partial u_x}{\partial y}. \tag{4.33}$$

Now, substituting in the evolution equation of $\overline{R}_{xy}$, one can obtain a second order differential equation for $\overline{R}_{xy}$ as:

$$\frac{\partial^2 \overline{R}_{xy}}{\partial y^2} - \frac{5}{27\theta\tau^2}\overline{R}_{xy} - \frac{80\theta}{189\tau^2}\sigma_{xy} = 0. \tag{4.34}$$

The resultant equation can be solved for $\overline{R}_{xy}$ which can be written as:

$$\overline{R}_{xy} = A_1\cosh(\lambda y) + A_2\sinh(\lambda y) - \frac{\theta_0}{\tau}\frac{560}{3729}\sigma_{xy}, \tag{4.35}$$

where A_1 and A_2 are the integration constants obtained from the boundary conditions, and $\lambda = \tau^{-1}\sqrt{5/27}$. From the equations Eq. (4.33) and (4.34) and the solution for $\overline{R}_{xy}$ from (4.35), one can obtain the solution for velocity profile as:

$$u_x = \frac{1}{\rho\theta^2}\left[A_1\sinh(\lambda y) + A_2\cosh(\lambda y)\right] - \frac{1}{\rho\theta\tau}\left(\rho g_x y^2 + K_1 y + K_2\right). \tag{4.36}$$

The above profile indeed predicts a Knudsen boundary layer. It is also worth noting that the heat flux along the streamwise direction is driven by the gradient of this contracted moment $(\overline{R}_{xy})$.

The above conclusion is not altered even if we include one more moment. This is important when we discuss Lattice Boltzmann equation in the chapter 5. To see this, we include another fourth order moment $\overline{R}_{xxxx}+\overline{R}_{yyyy}+\overline{R}_{zzzz}$ as an independent moment. The modified distribution function is

$$f^{\rm grad}_{27} = f^{\rm grad}_{26} + \psi\left(\xi_x^4 + \xi_y^4 + \xi_z^4 + \frac{9}{35}\xi^4 - \frac{6}{7}\theta\xi^2\right), \tag{4.37}$$

where $\psi = R_{xxxx} + \overline{R}_{yyyy} + \overline{R}_{zzzz} + \frac{9}{35}R - \frac{6}{7}\theta(\sigma_{xx}+\sigma_{yy}+\sigma_{zz})$. The transport equation however, doesn't change the form of the equation written in the section 4.2 but the closure relation has to be modified. The additional transport equation for the new moment ψ is:

$$\frac{\partial}{\partial y}\left[\frac{156}{7\rho\theta^3}q_y - \frac{8}{5\rho\theta^3}\overline{Q}_{yyy}\right] - \left[4R_{xxxy} + \frac{36}{35}\overline{R}_{xy} - \frac{12}{7}\sigma_{xy}\right]\frac{\partial u_x}{\partial y} = -\frac{1}{\tau}\psi. \tag{4.38}$$

$$\overline{R}_{\alpha\beta\gamma\kappa} = \frac{1}{7}\left(C_{\alpha\beta}\delta_{\gamma\kappa} + C_{\alpha\gamma}\delta_{\beta\kappa} + C_{\alpha\kappa}\delta_{\beta\gamma} + C_{\beta\gamma}\delta_{\alpha\kappa} + C_{\beta\kappa}\delta_{\alpha\gamma} + C_{\gamma\kappa}\delta_{\alpha\beta}\right) + \frac{298}{105}\left(12R + \theta P\right)\Delta_{\alpha\beta\gamma\kappa}, \tag{4.39}$$

with $C_{\alpha\beta} = \left(\overline{R}_{\alpha\beta} - \theta\sigma_{\alpha\beta}\right)$ and the fifth order moment closure reads as:

$$\overline{N}_{\alpha\beta\gamma} = 9\theta\overline{Q}_{\alpha\beta\gamma}, \qquad n_\alpha = 28\theta q_\alpha. \tag{4.40}$$

Using the above procedure, one can solve the set of semi-linearized transport equations and the predicted velocity profile is:

$$u_x = \frac{1}{\rho\theta^2}\left[A_1 \sinh(\lambda y) + A_2 \cosh(\lambda y)\right] - \frac{1}{\rho\theta\tau}\left(\rho g_x y^2 + K_1 y + K_2\right). \tag{4.41}$$

It can be seen that the velocity profile for this doesn't change with the additional moment and it predicts the boundary layer.

Chapter 5
Lattice Boltzmann Method

5.1 Introduction

Lattice Boltzmann method (LBM) aims to construct simplified kinetic picture on a lattice which captures the physics of macroscopic flow through simple local micro-scale operations. It is highly efficient and easily parallelizable on modern distributed computing hardware (Succi *et al.*, 1992; Chen & Doolen, 1998*b*; Succi, 2001*a*; Aidun & Clausen, 2010*a*). It may be argued that kinetic descriptions are inherently better suited for both complex flow phenomena such as turbulence and for modeling complex flow physics (Chen *et al.*, 2004; Ansumali *et al.*, 2007*b*; Ladd, 1993; Adhikari *et al.*, 2005). Therefore, it is widely used as an alternative numerical method for applications as wide-ranging as fluid turbulence, gaseous microflow, soft matter, polymer dynamics etc. (Chen *et al.*, 2003; Thantanapally *et al.*, 2013*a*; Singh *et al.*, 2013*b*; Thampi *et al.*, 2013; Mendoza *et al.*, 2010*b*; Benzi *et al.*, 2013; Mendoza *et al.*, 2010*a*; Chen *et al.*, 2004; Ansumali *et al.*, 2007*b*; Succi, 2001*b*; Chen *et al.*, 1992; Qian *et al.*, 1992; Lallemand & Luo, 2000; Chen & Doolen, 1998*a*; Aidun & Clausen, 2010*b*; Benzi *et al.*, 1992; Higuera *et al.*, 1989; Yu & Girimaji, 2005; Succi, 2001*a*; Succi *et al.*, 2002*b*; Namburi *et al.*, 2016; Yudistiawan *et al.*, 2010). The kinetic theory background of the method is widely discussed and is known that the method is low Mach number discretization of the Boltzmann equation with model collision terms such as BGK model (Abe, 1997; He & Luo, 1997*a*,*b*; Shan & He, 1998; Ansumali *et al.*, 2003; Yudistiawan *et al.*, 2010). Similarly, it is understood that the method approximates the continuous equilibrium distribution function via projection of Maxwell-Boltzmann onto the Hermite basis which allows conservation in discrete form (Shan & He, 1998). Subsequently, it was known that the thermodynamics inherent in the original Boltzmann description could be restored by working with discrete H-function and (similar to the continuous formulation of the Boltzmann equation) obtaining discrete equilibrium as the minimum of this discrete H-function (Karlin *et al.*, 1998; Boghosian *et al.*, 2003; Wagner, 1998; Chen & Teixeira, 2000; Karlin *et al.*, 1999; Succi *et al.*, 2002*b*; Ansumali *et al.*, 2003; Ansumali & Karlin, 2005). The entropic formulation where the thermodynamically correct description of equilibrium is used and H-theorem is restored in discrete time leads to non-linear stabilization of standard LBM in context of flows with sharp gradients and highly non-equilibrium situations. Moreover, another important progress in the field was the realization that although the hydrodynamic limit of different collision models can be same, they might show quite different numerical stability behavior. Thus, a great deal of effort is made to identify collision models with better numerical stability.

The chapter is organized as follows: in section 5.2 the general idea behind the LBM will be presented, in section 5.3 the principles in choosing the discretization of velocity space will be described, in section 5.4 the process of discretization of space and time will be discussed, finally, in the section 5.5 different collision models are presented.

5.2 Lattice Boltzmann Method

For Lattice Boltzmann Method, the velocities of the particles in D-dimensions are restricted to a discrete velocity set $\mathcal{C}$ with N_d number of velocities in the set. Here, each component $\mathbf{c}_i \in \mathcal{C}$, defines a set of discrete populations $f_i \in \mathbf{f}$. The set $\mathcal{C}$ is chosen to satisfy an appropriate set of symmetries needed to recover hydrodynamics in the long–time limit from the evolution equation of discrete populations f_i (Yudistiawan *et al.*, 2010). The hydrodynamic quantities such as mass

density ρ, the momentum density $j_\alpha = \rho u_\alpha$ with u_α as fluid velocity and energy E are defined as the moments of the distribution function as

$$\sum_{i=1}^{N_d} f_i = \rho, \qquad \sum_{i=1}^{N_d} f_i c_{i\alpha} = j_\alpha = \rho u_\alpha, \qquad \sum_{i=1}^{N_d} f_i c_i^2 = E = \rho u^2 + 3\rho\theta, \tag{5.1}$$

where θ is temperature measured in units of k_B/m with k_B as the Boltzmann constant and m being the mass of the molecule. Typically, the discrete version of the evolution equation for f_i with the Boltzmann-BGK collision term is written as

$$f_i(\mathbf{x} + \mathbf{c}_i\Delta t, t + \Delta t) = f_i(\mathbf{x}, t) + 2\beta[f_i^{\mathrm{eq}}(\rho(\mathbf{f}), \mathbf{u}(\mathbf{f})) - f_i(\mathbf{x}, t)], \tag{5.2}$$

where Δt is the chosen time step and $\beta = \Delta t/(2\tau + \Delta t)$ denotes the discrete dimensionless relaxation parameter related to the relaxation time τ towards the equilibrium. This discrete in space and time representation can be understood as discretized version of the partial differential equation (Boltzmann equation with BGK collision term)

$$\partial_t f_i + c_{i\alpha}\partial_\alpha f_i = -\frac{1}{\tau}\left[f_i - f_i^{\mathrm{eq}}\right]. \tag{5.3}$$

Here, the choice of the discrete version of equilibrium distribution f_i^{eq} is crucial for recovering the correct hydrodynamic limit and different formulations of lattice Boltzmann differ from each other mainly in choice of this discrete equilibrium. A common choice is to project the Maxwell-Boltzmann on the Hermite basis to get a computationally attractive polynomial expression of the equilibrium as (Chen *et al.*, 1992; Qian *et al.*, 2007; Benzi *et al.*, 1992; Shan & He, 1998)

$$f_i^{\mathrm{eq}}(\rho, \mathbf{u}) = w_i\rho\left[1 + \frac{u_\alpha c_{i\alpha}}{\theta_0} + \frac{u_\alpha u_\beta}{2\,\theta_0^2}\left(c_{i\alpha}c_{i\beta} - \theta_0\delta_{\alpha\beta}\right)\right], \tag{5.4}$$

where θ_0 is some reference temperature associated with the chosen lattice and w_i are the weights chosen in such a way that the mass and momentum constraints are ensured, i.e.,

$$\sum_{i}^{N_d} f_i^{\mathrm{eq}} = \rho, \qquad \sum_{i}^{N_d} f_i^{\mathrm{eq}} c_{i\alpha} = \rho u_\alpha. \tag{5.5}$$

Furthermore, in order to get correct hydrodynamic limit for isothermal low Mach number dynamics it is important to ensure that the second moment of the discrete equilibrium is same as that obtained from the Maxwell-Boltzmann distribution, i.e.,

$$\sum_{i}^{N_d} f_i^{\mathrm{eq}} c_{i\alpha}c_{i\beta} = \rho u_\alpha u_\beta + \rho\theta_0\delta_{\alpha\beta}. \tag{5.6}$$

The rationale for adding Eq. (5.6) can be understood by writing the momentum balance equation and evolution equation for the pressure tensor($P_{\alpha\beta} = \sum_i f_i c_{i\alpha}c_{i\beta}$) using Eq.(5.3) and Eq.(5.6) as

$$\begin{gathered}\partial_t j_\alpha + \partial_\beta P_{\alpha\beta} = 0, \\ \partial_t P_{\alpha\beta} + \partial_\beta\left(\sum_i^{N_d} f_i c_{i\alpha}c_{i\beta}c_{i\gamma}\right) = \frac{1}{\tau}\left(\rho u_\alpha u_\beta + \rho\theta_0\delta_{\alpha\beta} - P_{\alpha\beta}\right),\end{gathered} \tag{5.7}$$

from which it is evident that as expected in the limit of $\tau \to 0$, the zeroth order hydrodynamic equation is Euler equation. The Navier-Stokes hydrodynamics is correct provided

$$\sum_i^{N_d} f_i^{\mathrm{eq}} c_{i\alpha} c_{i\beta} c_{i\gamma} = \rho u_\alpha u_\beta u_\gamma + \rho\theta_0 \left(u_\alpha \delta_{\beta\gamma} + u_\beta \delta_{\alpha\gamma} + u_\gamma \delta_{\alpha\beta}\right). \tag{5.8}$$

Due to the absence of the cubic term in the equilibrium, this condition is satisfied only up to linear order by widely used lower order lattice Boltzmann models (Qian & Zhou, 1998). These constraints imply that the discrete velocity set and associated weights have to satisfy following conditions:

$$\sum_i^{N_d} w_i = 1, \quad \sum_i^{N_d} w_i c_{i\alpha} c_{i\beta} = \theta_0 \delta_{\alpha\beta}, \quad \sum_i^{N_d} w_i c_{i\alpha} c_{i\beta} c_{i\gamma} c_{i\zeta} = \theta_0^2 \Delta_{\alpha\beta\gamma\zeta}, \tag{5.9}$$

and all odd order moments are zero, such as

$$\sum_i^{N_d} w_i c_{i\alpha} = 0, \quad \sum_i^{N_d} w_i c_{i\alpha} c_{i\beta} c_{i\gamma} = 0, \quad \sum_i^{N_d} w_i c_{i\alpha} c_{i\beta} c_{i\gamma} c_{i\kappa} c_{i\zeta} = 0. \tag{5.10}$$

These conditions are central to LBM construction for isothermal incompressible hydrodynamics and the procedure to construct model which satisfies these requirements is well understood. Thus, the key points in the method construction are the choice of equilibrium distribution function, velocity space discretization, position and time discretization.

It should be noted here that in case of compressible hydrodynamics, moment chain suggest that one needs to add $O(u^3)$ contribution in the equilibrium distribution so that Eq.(5.8) is satisfied. This adds further restriction on the weights as

$$\sum_i^{N_d} w_i c_{i\alpha} c_{i\beta} c_{i\gamma} c_{i\kappa} c_{i\zeta} c_{i\eta} = \theta_0^3 \Delta_{\alpha\beta\gamma\kappa\zeta\eta}. \tag{5.11}$$

However, only very higher-order on-lattice models are known to satisfy such constraint in 3-dimensions (Chikatamarla & Karlin, 2009). The formulation of LBM where these higher order constraints are satisfied will be the subject of subsequent chapters. In practice, it is easier to satisfy the contracted version of this condition

$$\sum_i^{N_d} f_i^{\mathrm{eq}} c_i^2 c_{i\alpha} = \rho u_\alpha u^2 + (D+2)\,\rho\theta\, u_\alpha, \tag{5.12}$$

which implies

$$\sum_i^{N_d} w_i c_i^2\, c_{i\alpha} c_{i\beta} c_{i\gamma} c_{i\kappa} = 7\theta_0^3 \Delta_{\alpha\beta\gamma\kappa}. \tag{5.13}$$

This condition ensures that the energy conserving compressible hydrodynamics is correct to the leading order. In subsequent chapters, models which satisfy this constraint will be formulated.

5.3 Discrete velocity set

The isotropy requirement up to fourth order (Eq.5.9) forms central requirement for construction of discrete velocity model on a lattice which is suitable for modeling hydrodynamics. It was first shown in (Frisch *et al.*, 1986) that it is indeed possible to recover Navier-Stokes hydrodynamics by a two-dimensional discrete velocity model with six velocities on a hexagonal lattice. Later, it

was shown that Eq.(5.9) is satisfied on a hexagonal lattice provided a rest particle is also added to the system (Chen *et al.*, 1992). Here onwards, we will follow the naming convention used in LBM, where an N dimensional model with the M number of discrete velocities is termed as the $DNQM$ model. Ref.(d'Humieres *et al.*, 1986) showed that on a three-dimensional simple cubic lattice, a discrete velocity model with 19 velocities is sufficient to recover hydrodynamics. Other than this $D3Q19$ model, two other widely used alternative models for three-dimensional hydrodynamics are $D3Q15$ and $D3Q27$.

In this section, we review the construction procedures for such discrete velocity models which also satisfy Eq.(5.9). As a fundamental building block for the discrete velocity model, one begins with the velocity set which forms lattice structure and thus as explained in the chapter 2, section 2.6, form closed group under inversion and reflection. As shown in that chapter, basic lattices do not satisfy the fourth order isotropy condition. However, the structure of the fourth moment suggests that a combination of two lattices can satisfy the isotropy condition. In this section, we show a few examples to illustrate the principles.

As for an example, let us consider the simple cubic lattice in two dimensions. On such a lattice, two possible link vectors are shown in the Fig. 5.1. As shown in this figure, these two models separately do not follow the fourth order isotropic moment condition. However, the weighted combination of the two models (as shown in Fig. 5.2) can satisfy the isotropy condition. For this kind of discrete velocity set, the fourth order moment has the form

$$\sum_i w_i c_{i\alpha} c_{i\beta} c_{i\gamma} c_{i\kappa} = w_2 4c^4 \left[\Delta_{\alpha\beta\gamma\kappa}\right] + (2w_2 - 8w_1) c^4 \delta_{\alpha\beta\gamma\kappa}, \tag{5.14}$$

where w_1 and w_2 are the weights corresponding to lattice-A and lattice-B respectively. This moment is isotropic if we have

$$w_2 = 4w_1. \tag{5.15}$$

This multi-speed model termed as $D2Q9$ model satisfies Eq.(5.9) if

$$w_0 = \frac{16}{36}, \quad w_1 = \frac{4}{36}, \quad w_2 = \frac{1}{36}, \quad \theta_0 = \frac{c^2}{3}. \tag{5.16}$$

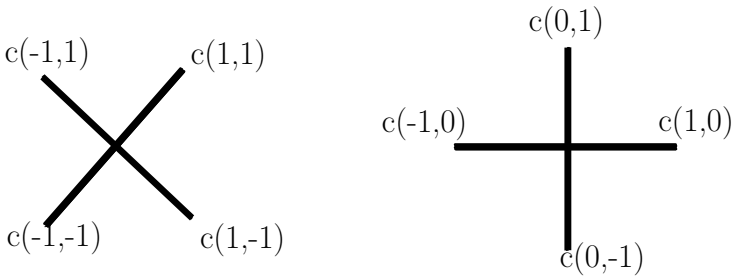

$\Sigma_i\, c_{i\alpha} c_{i\beta} c_{i\gamma} c_{i\kappa} = 4c^4 \left[\Delta_{\alpha\beta\gamma\kappa} - 2\delta_{\alpha\beta\gamma\kappa}\right]$ $\quad$ $\Sigma_i\, c_{i\alpha} c_{i\beta} c_{i\gamma} c_{i\kappa} = 2c^4 \delta_{\alpha\beta\gamma\kappa}$

Figure 5.1: The velocity sets that satisfy the ansatzes in 2-dimensions

Similarly, in 3-dimensions we can see that the fourth moment for discrete velocity set which form SC, FCC or BCC structure is (see Fig. 5.3)

$$\sum_i c_{i\alpha} c_{i\beta} c_{i\gamma} c_{i\kappa} = \Delta_{\alpha\beta\gamma\kappa} \left[8c^4 w_b + 4c^4 w_f\right] + \delta_{\alpha\beta\gamma\kappa} \left[2c^4 w_s - 16c^4 w_b - 4c^4 w_f\right], \tag{5.17}$$

where w_s, w_f, w_b are the weights corresponding to SC, FCC or BCC structures.

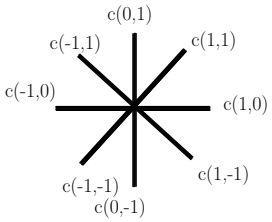

Figure 5.2: The velocity set satisfying the 4th order isotropy of moments in 2-dimensions

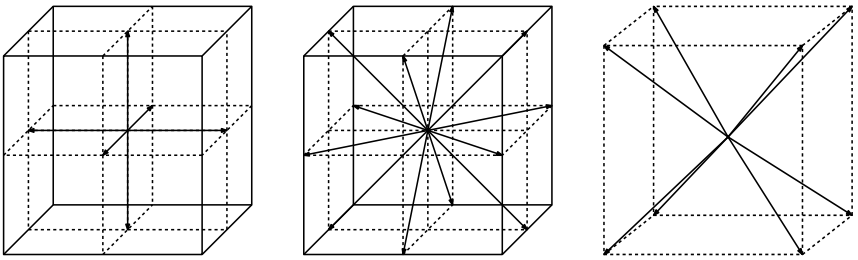

(a) SC (b) FCC (c) BCC

Figure 5.3: General discrete velocity forms in 3-dimensions

As shown in chapter 2, we have on SC lattice

$$\sum_i c_{i\alpha} c_{i\beta} c_{i\gamma} c_{i\kappa} = 2\, c^4\, \delta_{\alpha\beta\gamma\kappa}. \tag{5.18}$$

Similarly, on BCC lattice, we have

$$\sum_i c_{i\alpha} c_{i\beta} c_{i\gamma} c_{i\kappa} = 8\, c^4\, \Delta_{\alpha\beta\gamma\kappa} - 16\, c^4\, \delta_{\alpha\beta\gamma\kappa}. \tag{5.19}$$

A very similar computation reveals that for FCC lattice we have

$$\sum_i c_{i\alpha} c_{i\beta} c_{i\gamma} c_{i\kappa} = 4\, c^4\, \Delta_{\alpha\beta\gamma\kappa} - 4\, c^4\, \delta_{\alpha\beta\gamma\kappa}. \tag{5.20}$$

It is easy to see that a combination of SC and BCC lattice, termed as $D3Q15$ model, forms an isotropic structure and satisfy Eq.(5.9), if

$$w_s = \frac{1}{9}, \qquad w_b = \frac{1}{72}, \qquad w_0 = \frac{2}{9}, \quad \theta_0 = \frac{c^2}{3}. \tag{5.21}$$

This model is widely used in lattice Boltzmann literature for advection-diffusion model (Ginzburg *et al.*, 2010). For simulation of hydrodynamics, this model is mostly replaced with $D3Q19$ model, which shows better stability in numerical simulations. This $D3Q19$ model is formed by combining SC and FCC lattice. It is easy to see that this combination of SC and FCC lattice termed as $D3Q19$ model forms an isotropic structure and satisfies Eq.(5.9) if

$$w_s = \frac{1}{18}, \qquad w_f = \frac{1}{36}, \qquad w_0 = \frac{1}{3}, \qquad \theta_0 = \frac{c^2}{3}. \tag{5.22}$$

This model is widely used in lattice Boltzmann literature for simulation of hydrodynamics such as flow-through porous media and polymer dynamics (Chen & Doolen, 1998*a*; Aidun & Clausen, 2010*b*; Tölke, 2002; Singh *et al.*, 2013*b*).

In recent years, it has been recognized that a more detailed model, termed as $D3Q27$ shows much better stability behavior and is more accurate than $D3Q15$ or $D3Q19$. This $D3Q27$ model

can be constructed by considering SC, FCC and BCC lattices together. This lattice has more degree of freedom than that required to impose conditions on the fourth moment. Thus, on this lattice one imposes the constraint

$$\sum_i w_i c_{ix}^2 c_{iy}^2 c_{iz}^2 \quad = \theta_0^3 \tag{5.23}$$

on the contracted 6th order moments. If we impose Eq.(5.9) along with the above constraint, it is easy to see that $D3Q27$ model has solution

$$w_f = \frac{1}{54}, \qquad w_b = \frac{1}{216}, \qquad w_s = \frac{2}{27}, \qquad w_0 = \frac{8}{27}, \qquad \theta_0 = \frac{c^2}{3}. \tag{5.24}$$

This model has an added advantage that it is possible to derive thermodynamically correct equilibrium needed for entropic formulation exactly (Ansumali *et al.*, 2003). To conclude, as shown in Table. 5.1, we can say that all commonly used 3-D models ($D3Q15$ or $D3Q19$ or $D3Q27$) emerges as weighted average of SC, FCC, BCC lattice for discrete velocity model.

Model	w_{SC}	w_{FCC}	w_{BCC}	w_0	θ_0
D3Q15	$\frac{1}{9}$	0	$\frac{1}{72}$	$\frac{2}{9}$	$\frac{1}{3}$
D3Q19	$\frac{1}{18}$	$\frac{1}{36}$	0	$\frac{1}{3}$	$\frac{1}{3}$
D3Q27	$\frac{2}{27}$	$\frac{1}{54}$	$\frac{1}{216}$	$\frac{8}{27}$	$\frac{1}{3}$

Table 5.1: Widely used discrete velocity models in 3-dimensions.

5.4 Space and time discretization

In this section, we show how discrete time and space formulation of LBM emerges from the Partial Differential Equation (PDE) form (Eq.(5.3)). By integrating Eq.((5.3)) along the characteristics, we have

$$f_i\left(\mathbf{x} + \mathbf{c}_i\Delta t, t + \Delta t\right) = f_i\left(\mathbf{x}, t\right) + \int_{s=0}^{s=\Delta t} ds\ \Omega_i(f_i\left(\mathbf{x} + \mathbf{c}_i s, t + s\right)), \tag{5.25}$$

where Ω_i is the discrete collision operator and Δt is the time step. For BGK collision operator we have

$$\Omega_i = \frac{1}{\tau}\left(f_i^{\mathrm{eq}}\left(M^{\mathrm{slow}}(\mathbf{f})\right) - f_i\right), \tag{5.26}$$

where $M^{\mathrm{slow}} = \{\rho, \mathbf{u}\}$ for isothermal dynamics and $M^{\mathrm{slow}} = \{\rho, \mathbf{u}, \theta\}$ for energy conserving dynamics. Using second order trapezoidal scheme for the discretization, integral term can be approximated as

$$f_i\left(\mathbf{x} + \mathbf{c}_i\Delta t, t + \Delta t\right) = f_i\left(\mathbf{x}, t\right) + \frac{\Delta t}{2}\left[\Omega_i(f_i(\mathbf{x}, t)) + \Omega_i(f_i\left(\mathbf{x} + \mathbf{c}_i\Delta t, t + \Delta t\right))\right]. \tag{5.27}$$

In order to get the explicit expression for the efficient numerical scheme, we introduce the transformation of variable as,

$$g_i = f_i - \frac{\Delta t}{2\tau}\left(f_i^{\mathrm{eq}}(M^{\mathrm{slow}}(\mathbf{f})) - f_i\right). \tag{5.28}$$

As by definition $M^{\text{slow}}(\mathbf{f})$ is conserved by the collision term, we have

$$M^{\text{slow}}(\mathbf{g}) = M^{\text{slow}}(\mathbf{f}), \tag{5.29}$$

which suggest that there is no need to distinguish between f_i^{eq} and g_i^{eq}. Thus, using Eq.((5.28)) we have

$$\left(g_i^{\text{eq}}(M^{\text{slow}}(\mathbf{f})) - g_i\right) = \left(1 + \frac{\Delta t}{2\tau}\right)\left(f_i^{\text{eq}}(M^{\text{slow}}(\mathbf{f})) - f_i\right). \tag{5.30}$$

Using this expression, the Eqn. (5.27) can be re-written as

$$g_i\left(\mathbf{x} + \mathbf{c}_i\Delta t, t + \Delta t\right) = g_i\left(\mathbf{x}, t\right) + 2\beta\left[g_i^{\text{eq}}(\rho(\mathbf{g}), \mathbf{u}(\mathbf{g})) - g_i(\mathbf{x}, t)\right], \tag{5.31}$$

where $\beta = \Delta t/(2\tau + \Delta t)$. Analogous to the continuous Boltzmann description, we can decompose the Eqn (5.31) into two steps of collision and streaming

- **Collision**: This step represent local relaxation towards equilibrium distribution as

$$g_i^*\left(\mathbf{x}, t\right) = g_i\left(\mathbf{x}, t\right) + 2\beta\left[g_i^{\text{eq}}(\rho, \mathbf{u}) - g_i(\mathbf{x}, t)\right]. \tag{5.32}$$

  It is evident that in this local step, no space discretization is needed.

- **Streaming or advection**: This step propagates the molecules from the position $\mathbf{x}$ to $\mathbf{x} + \mathbf{c}_i\Delta t$ as

$$g_i\left(\mathbf{x} + \mathbf{c}_i\Delta t, t + \Delta t\right) = g_i^*\left(\mathbf{x}, t\right). \tag{5.33}$$

  As this step is non-local, one would need spatial interpolation. However, for all lattice Boltzmann models considered in this chapter, if the position space is chosen in such a way that $\Delta x = c\Delta t$, then the discrete velocity set is mapped onto a spatial lattice and no spatial interpolations are needed. This can be seen for a simple 2-dimensional set-up in Fig: 5.4.

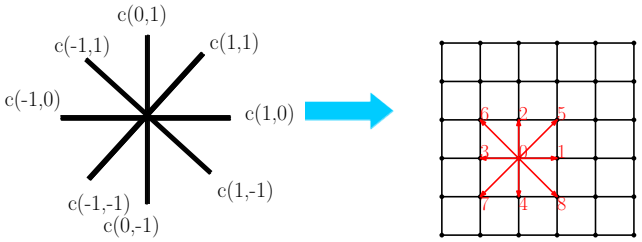

Figure 5.4: The schematic of discrete velocity on the space discretization.

5.5 Collision models in LBM

Similar to the continuous kinetic theory, various approximations for collision operator are available in the literature to adjust the values of the transport coefficient (Chen *et al.*, 2010; Soe *et al.*, 1998; Luo & Girimaji, 2002; Asinari & Karlin, 2010; Luo & Girimaji, 2003; Ansumali *et al.*, 2007*a*; Thantanapally *et al.*, 2013*b*; Arcidiacono *et al.*, 2007). Such models are needed if the flow being modeled is dependent on parameters such as Prandtl number, Schmidt number, etc. However, an important progress in the field was the realization that although the hydrodynamic limit of different collision models can be same, they might show quite different numerical stability behavior. Thus, a great deal of effort was made to identify collision models with better numerical stability(d'Humières, 2002; McCracken & Abraham, 2005; Lallemand & Luo, 2000; Thantanapally *et al.*, 2013*b*; Karlin *et al.*, 2014).

Another important realization in the field was that non-linear stability in the method could be enforcing the thermodynamics inherent in the original Boltzmann description. The same is true in the discrete formulation as well (Karlin *et al.*, 1998; Wagner, 1998; Karlin *et al.*, 1999; Succi *et al.*, 2002*b*; Ansumali *et al.*, 2003; Ansumali & Karlin, 2005). The basic idea was to work out the discrete H-function and introduce variable path-length for ensuring second law of thermodynamics. In this formulation, similar to the continuous formulation of the Boltzmann equation, one obtains the discrete equilibrium as a minimum of this discrete H-function and path-length is chosen to ensure the second law of thermodynamics in discrete time (Karlin *et al.*, 1998; Boghosian *et al.*, 2003; Wagner, 1998; Chen & Teixeira, 2000; Karlin *et al.*, 1999; Succi *et al.*, 2002*b*; Ansumali *et al.*, 2003; Ansumali & Karlin, 2005). The entropic formulation leads to non-linear stabilization of standard LBM in context of flows with sharp gradients and highly non-equilibrium situations (Succi *et al.*, 2002*b*; Aidun & Clausen, 2010*b*). Thus, the Entropic Lattice Boltzmann Model (ELBM) is a discrete space-time kinetic theory which ensures non-linear stability via the discrete time version of the second law of thermodynamics (the H-theorem). In this section, we briefly review such modifications to the collision models often used for LBM simulations.

5.5.1 Entropic Lattice Boltzmann Method (ELBM)

The Entropic Lattice Boltzmann Model (ELBM) restores the H-theorem for discrete space-time evolution (Karlin *et al.*, 1999; Boghosian *et al.*, 2001; Ansumali *et al.*, 2003; Karlin *et al.*, 1998; Boghosian *et al.*, 2003; Wagner, 1998; Chen & Teixeira, 2000; Succi *et al.*, 2002*b*). In this method, one starts with a given H-function, typically taken in Boltzmann form as

$$H(\mathbf{f}) = \sum_i f_i \left[\log\left(\frac{f_i}{w_i}\right) - 1 \right]. \tag{5.34}$$

Similar to the Boltzmann equation, the equilibrium distribution is defined to be minimum of the H-function under constraint that the slow moments M^{slow} are kept fixed (conserved). The slow moments are $M^{\text{slow}} = \{\rho, \mathbf{u}\}$ for the isothermal dynamics and $M^{\text{slow}} = \{\rho, \mathbf{u}, \theta\}$ for the energy conserving dynamics. The equilibrium distribution obtain as solution of the minimization has Maxwell-Boltzmann form

$$f_i^{\text{eq}} = w_i \, \rho \exp\left[-\left(\alpha + \beta_\kappa c_{i\kappa} + \gamma c_i^2\right)\right], \tag{5.35}$$

where α, β_κ and γ are the Lagrange multipliers associated with the mass, momentum and energy conservation, respectively. In case of isothermal dynamics $\gamma = 0$. The explicit form of the equilibrium distribution is typically difficult to obtain, but the series form is known to a very high accuracy. This series form matches with the polynomial form up to order $O(u^2)$. For a few widely used models such as $D2Q9$ and $D3Q27$ the exact equilibrium is known analytically (Ansumali *et al.*, 2003).

ELBM introduces the concept of state-dependent path length α for the discrete collision step (Karlin *et al.*, 1999) and changes the the form of kinetic equation to be solved as

$$f_i^*(\mathbf{x}, t) = f_i(\mathbf{x}, t) + \alpha\beta \left[f_i^{\text{eq}}\left(M^{\text{slow}}\right) - f_i(\mathbf{x}, t) \right], \tag{5.36}$$

such that α is the root of entropy estimate

$$\Delta H \equiv H\left(\mathbf{f}^{\text{mirror}}\right) - H(\mathbf{f}) = 0, \tag{5.37}$$

where

$$\mathbf{f}^{\text{mirror}} = \mathbf{f} + \alpha\left(\mathbf{f}^{\text{eq}} - \mathbf{f}\right). \tag{5.38}$$

Thus, the H-theorem in ELBM requires an additional step of numerically searching for the maximal discrete path-length which corresponds to a jump to a mirror state on the iso-entropy surface (zero dissipation state). This is explained geometrically in Fig. 5.5, where the circles represent entropy levels and the triangle represents the section of phase space inside which the populations are positive. Here, $\mathbf{f}$ is the initial state and $\mathbf{f}^{\text{mirror}}$ is the equal entropy zero dissipation state. As $\beta < 1$ the compliance with H-theorem, i.e., $H(\mathbf{f}^*) < H(\mathbf{f})$ is guaranteed.

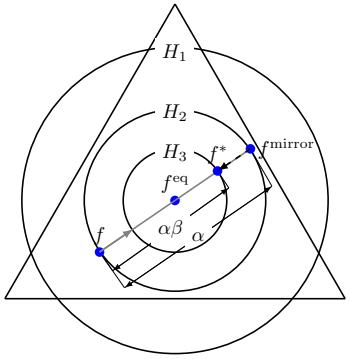

Figure 5.5: Jump to an equal entropy mirror state $H(\mathbf{f}) = H(\mathbf{f}^{\text{mirror}})$. Here $H_1 > H_2 > H_3$

This procedure requires solving a set of the non-linear equation at every point in space. Thus, in contrast to standard LBM floating point operations are quite high. Considerable efforts have been made to ensure the correctness and efficient implementation of this step (Tosi *et al.*, 2006; Chikatamarla *et al.*, 2006*a*; Ansumali & Karlin, 2002*a*; Brownlee *et al.*, 2007; Gorban & Packwood, 2012). ELBM is used successfully used by many groups to perform high Reynolds number flows and multiphase flow simulations (Chikatamarla & Karlin, 2013; Chikatamarla *et al.*, 2015).

5.5.2 Quasi-equilibrium collision

BGK approximation is quite widely used in kinetic theory as well as LBM due to its simplicity and effectiveness in mimicking Boltzmann dynamics. However, it is also well understood that due to the single relaxation time approximation in the model, the agreement cannot be quantitative if temperature dynamics are involved. This is due to the fact that Prandtl number predicted by BGK model is unity as opposed to 2/3 (value predicted by Boltzmann equation). A similar defect exists for the gaseous mixture, where Schmidt number gets the wrong value. This defect can be cured if higher order moments relaxation rate is not same as stress relaxation rate. This can be achieved in a thermodynamically consistent manner by using the concept of quasi-equilibrium distribution which assumes the existence of time-scale hierarchy. The main idea is to divide the set of independent moments into three parts

$$M = \{M^{\text{Slow}}, M^{\text{Quasi-Slow}}, M^{\text{Fast}}\}, \tag{5.39}$$

where M^{Slow} are the set of conserved moments and $M^{\text{Quasi-Slow}}$ are the set of variables which are not conserved, but their relaxation rate is slower than other moments which are termed as M^{Fast} (Gorban & Karlin, 1994). The precise choice of the quasi-slow moment depends on the physical context and for some examples see Ref (Ansumali *et al.*, 2007*a*). The first step in this model is to define the quasi-equilibrium based on the given set of slow and quasi-slow variables as the minimum of the H-function with slow and quasi-slow moment being kept constant. Once this state is defined, the collision term is modeled by two-step relaxation as

$$\Omega_i = \frac{1}{\tau}\left(f_i^*\left(M^{\text{Quasi-Slow}}\right) - f_i\right) + \frac{1}{\tau_1}\left(f_i^{\text{eq}}\left(\rho, \mathbf{u}, \theta\right) - f_i^*\left(M^{\text{Quasi-Slow}}\right)\right), \tag{5.40}$$

where τ and τ_1 are two relaxation times which allows fixing two independent transport coefficients. For this model, thermodynamic consistency in terms of H-theorem requires that $\tau \leq \tau_1$.

As a specific example, if we consider the case of variable Prandtl number model with $\mathrm{Pr} < 1$, we have $M^{\mathrm{Slow}} = q_\alpha^{\mathrm{neq}}$ where the non-equilibrium part of the heat flux is defined as $q_\alpha^{\mathrm{neq}} = \sum_i^{N_d} (f_i - f_i^{\mathrm{eq}}) c_i^2 c_{i\alpha}$. In this case, the discrete evolution equation similar to Eq. (5.31) for multi-relaxation collision operator becomes (Thantanapally *et al.*, 2013*b*)

$$g_i(\mathbf{x} + \mathbf{c}\Delta t, t + \Delta t) = g_i(\mathbf{x}, t)(1 - 2\beta) + 2\beta \left[\left(1 - \frac{\tau}{\tau_1}\right) g^*(\rho, \mathbf{u}, \theta, \mathbf{q}^\star) + \frac{\tau}{\tau_1} g_i^{\mathrm{eq}}(\rho, \mathbf{u}, \theta) \right] \quad (5.41)$$

where the change of variables has been made as

$$g(\mathbf{x}, t) = f(\mathbf{x}, t) - \frac{\Delta t}{2} \Omega_i(f(\mathbf{x}, t)), \quad (5.42)$$

and $\beta = \Delta t/(2\tau + \Delta t)$ and the moments in both representations are related by

$$q_\alpha^\star = q_\alpha^{\mathrm{eq}} + q_\alpha(\mathbf{f}) \left(1 + \frac{\Delta t}{2\tau_1}\right). \quad (5.43)$$

The pictorial representation of this procedure is as shown in Fig. 5.6 where the curved path denotes the relaxation trajectory under the effect of the actual Boltzmann collision integral.

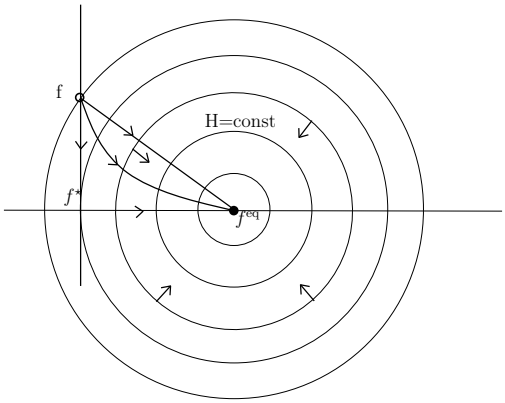

Figure 5.6: Pictorial representation of multi-relaxation process with Quasi-equilibrium.

It can be seen from Chapman Enskog analysis determines the momentum diffusivity and the ratio of the relaxation times define the Prandtl number (Ansumali *et al.*, 2007*a*).

5.5.3 Multiple Relaxation Time (MRT) collision

In typical LBM, we use the BGK collision model which has a Single Relaxation Time(SRT) hence only one time scale. The presence of only one time scale restricts the relaxation of all the moments to the same rate. Unlike the Lattice Boltzmann BGK formulation, in a multi-relaxation model, each of the higher order moment has its own time scale for the relaxation. As most of these relaxation time has no physical significance in the context of an incompressible hydrodynamics, many of these rates can be set arbitrarily. In MRT formulation of LBM one improves the numerical stability and reduces the unphysical oscillations by appropriate choices for these kinetic relaxation parameters (Lallemand & Luo, 2000).

The evolution of populations is written as (d'Humières, 2002)

$$\tilde{f}(\mathbf{x} + \mathbf{c}\Delta t, t + \Delta t) - \tilde{f}(\mathbf{x}, t) = -M^{-1} \hat{S} \left[\tilde{m}(\mathbf{x}, t) - \tilde{m}^{\mathrm{eq}}(\mathbf{x}, t) \right], \quad (5.44)$$

where M is a transformation matrix mapping vector $\tilde{f}$ in velocity space to a vector $\tilde{m}$ in moment

space and $\hat{S} = M \cdot S \cdot M^{-1}$ is a collision matrix diagonal in moment space whose eigen values are the inverse of the relaxation time which lie between 0 to 2. Hence, $\tilde{m} = M\tilde{f}$ and $\tilde{f} = M^{-1}\tilde{m}$. The size of the vector $\tilde{m}$ is dictated by the number of moments corresponding to the discrete velocity model in consideration.

Here, the streaming takes place in the velocity space, and the collision is executed in moment space by mapping the populations onto it. The eigenvalues of $\hat{S}$ are such that non-conserved moments relax faster than the conserved ones. Due to better stability behavior of these models, they are regularly used in numerical simulations(Aidun & Clausen, 2010*b*).

5.5.4 Karlin-Bösch-Chikatamarla (KBC) collision

This model exploits Gibb's principle for constructing the equilibrium state and does not require the tunable parameter setting (Karlin *et al.*, 2014). The kinetic equation to be solved in this model has the form

$$f_i\left(\mathbf{x} + \mathbf{c_i}, t+1\right) = (1-\beta)\, f_i\left(\mathbf{x}, t\right) + \beta f_i^{\text{mirror}}\left(\mathbf{x}, t\right). \tag{5.45}$$

The mirror state is written as a combination of kinematic part (k_i), shear part (s_i) and the linear combination of remaining higher order moments (h_i). The mirror state can be written explicitly as

$$f_i^{\text{mirror}} = k_i + (2s_i^{\text{eq}} - s_i) + \left[(1-\gamma)\, h_i + \gamma h_i^{\text{eq}}\right], \tag{5.46}$$

where the relaxation parameter γ is computed by maximizing entropy in the post collision state as the root of

$$\sum_i \Delta h_i \ln\left[1 + \frac{(1-\beta\gamma)\,\Delta h_i - (2\beta - 1)\,\Delta s_i}{f_i^{\text{eq}}}\right] = 0, \tag{5.47}$$

with $\Delta h_i = h_i - h_i^{\text{eq}}$ and $\Delta s_i = s_i - s_i^{\text{eq}}$. This model shows remarkable improvement in the stability behavior and thus in recent years is increasingly being used for the turbulence simulations(Chikatamarla & Karlin, 2013)

Chapter 6
Crystallographic Boltzmann Method

6.1 Introduction

Applications of Computational Fluid Dynamics (CFD) to the physics of complex flows requires highly accurate and adaptive methods for complex geometries. LBM is used for this purpose due to its high parallel efficiency and ease of use. Indeed, often it is argued that kinetic descriptions are inherently better suited for both complex flow phenomena such as turbulence and for modeling complex flow physics (Chen *et al.*, 2004; Ansumali *et al.*, 2007*b*; Ladd, 1993; Adhikari *et al.*, 2005). However, in order to achieve accuracy that higher order method such as pseudo-spectral(PS) method can achieve, LBM requires an order-of-magnitude (2 to 3 times in each direction) more number of grid points in 3D as compared to the pseudo-spectral method. Nevertheless, in practice, LBM is competitive with respect to PS due to very high parallel efficiency and flexibility in handling complex geometries. Indeed, in a heterogeneous computing environment, LBM and PS are able to perform DNS at comparable Reynolds Numbers for simple flows (Thantanapally *et al.*, 2013*a*; Chikatamarla *et al.*, 2010). However, similar to other structured grid based method LBM needs very high grid resolution to represent the boundaries accurately(for instance see Fig.2.9b in chapter 2).

Historically, the lattice chosen for LBM has been the Simple Cubic (SC) cell which demands that the grid is refined near the solid body or in zones of extreme flow variations (Filippova & Hänel, 1998; Succi *et al.*, 2002*a*). A fundamental problem with such refinements is that the local accuracy of the method remains unchanged and optimization is done only with respect to the global distribution of grid points. For example, for decaying turbulence in a periodic geometry, local grid refinements cannot improve the accuracy of LBM. Thus improving the accuracy and ability to capture local curvatures, while keeping its parallel efficiency intact is an important challenge in LBM.

Further, most lower order LBM models have artificial closure on third order moments which results in the inability to capture the high Knudsen effects accurately in micro-flows(Ansumali *et al.*, 2007*b*). In order to overcome these limitations, we developed a new class of LBM model where the SC grid for position discretization is replaced with a BCC grid. We show that this invertion of the argument of LBM and making of spatial discretization the central point indeed provides lot more freedom and accuracy in the velocity space discretization. As BCC grid has efficient packing density, we show that it can represent the boundaries well.

The chapter is organized as follows, section 6.2 explains the limitations of the standard LB method, section 6.3 describes the Crystallographic LB method which we developed to improve the accuracy and efficiency of LBM, section 6.4 illustrate the application of this method for turbulent flow simulations like Kida flow simulations. section 6.5 describes the moment chain closure for different LB models and finding the minimal condition for predicting the Knudsen boundary layer effect. Then, we will apply the present model to microflows and section 6.6 describes the application of this model to the classical problem of flow past sphere at high Reynolds number and in capturing the drag crisis problem.

6.2 Limitations of standard LBM

Though, LBM is an efficient numerical technique to solve the fluid flows on a structured grid, as discussed above it had a set of technical problems largely related to use of simple cubic lattice

for spatial discretization. In this section, we briefly present some of the accuracy and efficiency related issues.

- **Geometry representation**: It is well understood that the representation of a complex shape on the structured grid is not very accurate. Indeed, it can be seen from the Fig. 6.1 that even the representation of simple shape such as a circle on the structured grid is highly inaccurate. The only working methodology for improving the accuracy of LBM for such cases is to refine the grid near the solid body or in zones of extreme flow variations (Filippova & Hänel, 1998; Succi *et al.*, 2002*a*). A fundamental problem with such approaches is that the local accuracy of the method remains unchanged and optimization is done only with respect to the global distribution of grid points.

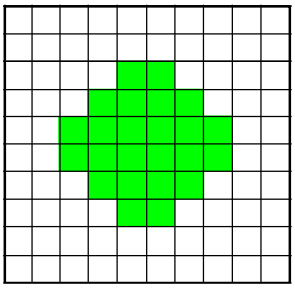

Figure 6.1: The representation of a circle on the Structured grid.

- **Spectral accuracy**: For DNS of homogeneous turbulence, the most accepted methodology is Pseudo-Spectral (PS) method, which has spectral accuracy unmatched by alternative methods. However, it has relatively poor parallel scaling and is largely limited to periodic domains and to a few other simple geometries such as channel flow (Hussaini & Zang, 1987). Thus, in the last two decades, a number of algorithms such as LBM were developed for accelerating hydrodynamic simulation. Indeed, in a heterogeneous computing environment, LBM and PS are able to perform DNS at comparable Reynolds Numbers for simple flows (Thantanapally *et al.*, 2013*a*; Chikatamarla *et al.*, 2010). However, unlike the pseudo-spectral methods, lower order models such as LBM often require more than twice number of grid points in every direction and thus, they require an order-of-magnitude (2 to 2.5 times in each direction) number of grid points in 3D for the same accuracy. This lack of accuracy for LBM is demonstrated here via simulation of Kida-Pelz flow at Re = 1000(Thantanapally *et al.*, 2013*a*). In this set-up, Re = $\rho \mathrm{U_0 L}/\nu$, where in a box of length 2π, it is customary to consider $L = 1$. Enstrophy, which provides a measure of the extent of vortex stretching provides a simple scalar measure to contrast different numerical schemes(Thantanapally *et al.*, 2013*a*). In this flow, starting with a smooth initial condition, the enstrophy(Ω) and the maximum vorticity show very rapid growth. Thus it is not surprising that, for this set-up, the standard D3Q27 lattice Boltzmann model fails to make accurate predictions unless the number of grid points per direction is substantially higher than an equivalent spectral simulation. In Fig. 6.2, it is indeed visible that LBM requires an order of magnitude more points to reach the spectral accuracy.

- **Knudsen boundary layer**: For the models with discrete velocity components being unity ($D3Q19$ or $D3Q27$), the lattice structure introduces the artificial closure on the third order moments.

$$\sum_i^{N_d} f_i c_{ix}^3 = c^2 \sum_i^{N_d} f_i c_{ix}, \quad \sum_i^{N_d} f_i c_{iy}^3 = c^2 \sum_i^{N_d} f_i c_{iy}, \quad \sum_i^{N_d} f_i c_{iz}^3 = c^2 \sum_i^{N_d} f_i c_{iz}. \tag{6.1}$$

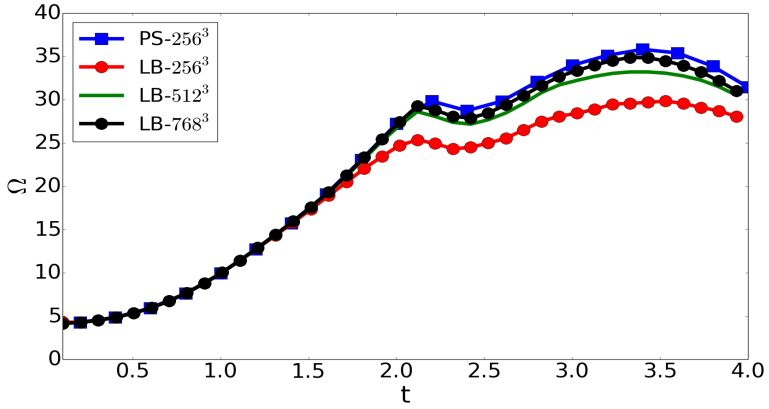

Figure 6.2: Comparison of LB results with Pseudo Spectral for kida flow at Re=1000.

Thus, for third order moments defined as

$$Q_{\alpha\beta\gamma} = \sum_{i}^{N_d} f_i c_{i\alpha} c_{i\beta} c_{i\gamma}, \tag{6.2}$$

the standard LBM models such as $D2Q9$ or the $D3Q27$ model introduces the artificial closure for components such as

$$Q_{xxx} = 3\theta_0 j_x, \quad Q_{yyy} = 3\theta_0 j_y, \quad Q_{zzz} = 3\theta_0 j_z. \tag{6.3}$$

Similarly, the lattice structure introduces artificial closures at the fourth order too. i.e.,

$$\sum_{i}^{N_d} f_i c_{ix} c_{iy}^3 = c^2 \sum_{i}^{N_d} f_i c_{ix} c_{iy} = 3\theta_0 P_{xy} \Rightarrow R_{xyyy} = 3\theta_0 P_{xy}. \tag{6.4}$$

Due to this artificial closure, in the case of the unidirectional flow with the lower order velocity models, the moment chain terminates at the third order and these models fail to capture the Knudsen boundary layer(Ansumali *et al.*, 2007*b*). This further can be seen from the moment chain solution as follows;

$$\partial_y P_{xy} = \rho g_x, \tag{6.5}$$

which is coupled with the off-diagonal part of the pressure tensor as

$$\partial_y Q_{xyy} = -\frac{P_{xy}}{\tau}. \tag{6.6}$$

This system of equations can be solved to obtain

$$Q_{xyy} = \frac{1}{\tau}\left[\rho g_x \frac{y^2}{2} + C_1 y + C_2\right] \tag{6.7}$$

Where the transport equation for Q_{xyy} is,

$$\partial_y R_{xyyy} = -\frac{1}{\tau}\left[j_x \theta_0 - Q_{xyy}\right]. \tag{6.8}$$

However, the closure Eq. (6.4), implies that the solution of velocity profile has the form

$$j_x = \frac{-1}{\tau\theta_0}\left[\rho g_x \frac{y^2}{2} + C_1 y + C_2\right] - 3\tau\rho g_x. \tag{6.9}$$

The form of the velocity profile suggests that the effect of Knudsen boundary layer is artificially supressed for the lower order LBM models.

6.3 Crystallographic LBM

In this section, we introduce our new grid structure which drastically improves the representation of the body and accuracy without compromising the Lagrangian nature or the computational efficiency of LBM. In this new methodology, we invert the argument of standard LBM and choose the discrete space lattice first. Then we choose the appropriate discrete velocity set that follows the principles of closure and isotropy of the moments. Finally, the discrete velocity set is projected on to the discrete space lattice for further calculations. As shown in Fig. 6.3, the introduction of the staircase geometry in LBM is similar to the creation of a Wigner-Seitz cell for a given lattice structure (Ladd, 1994). With this point of view, and considering the Crystallographic principles discussed in Chapter 2 it becomes apparent that, out of all possible space-filling arrangements, the BCC Lattice is most appropriate for space discretization. To illustrate this point, we consider a 2D projection of SC and BCC grids. Fig. 6.3 and Fig. 6.4 show that the discrete approximation of a circle is more accurate on BCC grid than on an SC grid. In fact, the total number of boundary points are almost doubled. The similar representation of a sphere in 3-dimensions on SC and BCC grid can be seen in Fig. 6.5.

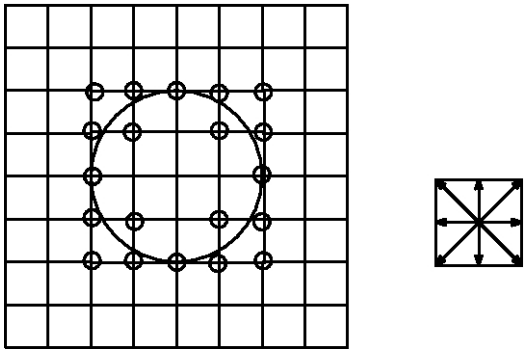

Figure 6.3: Left: grid points near the boundary on the SC grid. Right:Links on the SC grid.

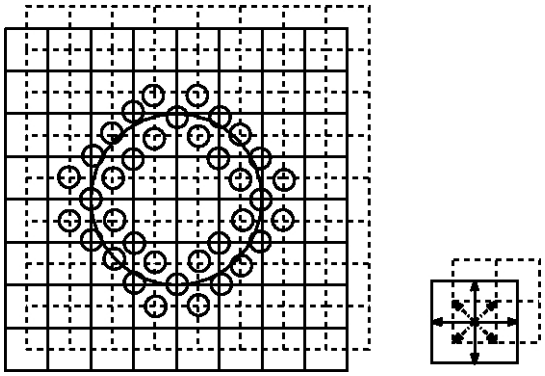

Figure 6.4: Left: grid points near the boundary on the BCC grid. Right:Links on the BCC grid.

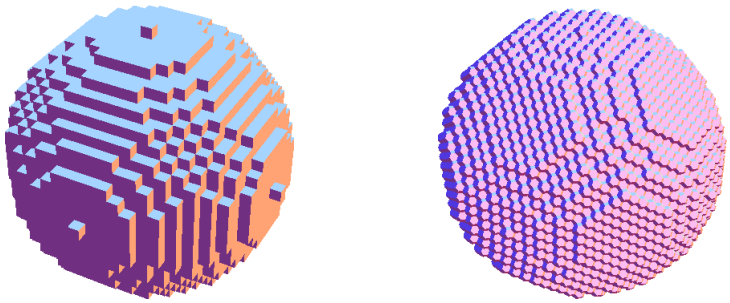

(a) SC (b) BCC

Figure 6.5: The representation of sphere in 3-dimensions on SC and BCC grid.

For any given lattice, the links on the grid in Fig. 6.4 act as discrete velocities in LBM. It is also clear from Fig. 6.4 that, unlike previous attempts to design body-fitted grids, we achieve better space coverage and also a unification of the discretization of space and velocities with this lattice. Indeed, the presence of velocity vector with magnitude half provides new flexibility in model creation for LBM. This can be seen by looking at 2-dimensional projection of BCC lattice. On such a lattice, two possible link vectors are shown in the Fig. 6.6. As shown in this

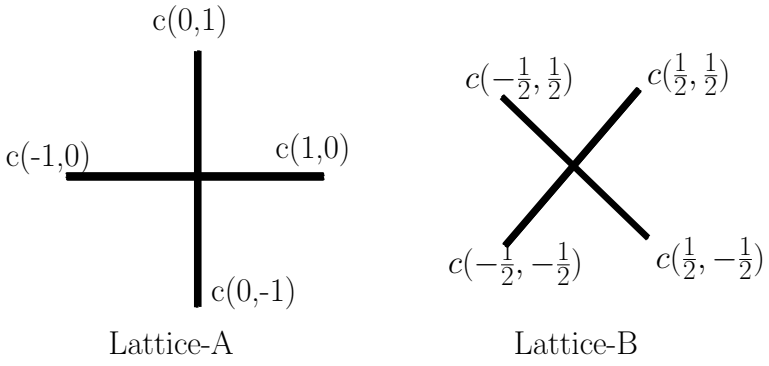

Figure 6.6: The velocity sets on 2D projection of BCC lattice

figure, these two models separately don't follow the fourth order isotropic moment condition. However, the weighted combination of the two models (as shown in Fig. 6.6) can satisfy the isotropy condition. For this kind of discrete velocity set, the fourth order moment has the form,

$$\sum_i w_i c_{i\alpha} c_{i\beta} c_{i\gamma} c_{i\kappa} = w_2 \frac{c^4}{4} \Delta_{\alpha\beta\gamma\kappa} + \left(2w_1 - \frac{w_2}{2}\right) c^4 \delta_{\alpha\beta\gamma\kappa}, \tag{6.10}$$

where w_1 and w_2 are the weights corresponding to lattice-A and lattice-B respectively. This moment is isotropic, if we have

$$w_1 = \frac{w_2}{4}. \tag{6.11}$$

Here onwards, crystallographic LB model in N-dimensions with the M number of discrete velocities is termed as $RDNQM$ model. Thus in $2D$ multispeed model, termed as $RD2Q9$ model, satisfies the isotropy condition on fourth order moment, $\sum_i^{N_d} w_i c_{i\alpha\beta\gamma\kappa} = \Delta_{\alpha\beta\gamma\kappa}\theta_0^2$ if

$$w_0 = \frac{4}{9}, \quad w_1 = \frac{1}{36}, \quad w_2 = \frac{1}{9}, \quad \theta_0 = \frac{c^2}{6}. \tag{6.12}$$

In 3-dimensions, we generalize the $D3Q27$ model on a BCC lattice by changing velocity vectors of type $\{\pm1, \pm1, \pm1\}$ to $\{\pm1/2, \pm1/2, \pm1/2\}$. Hereafter, this model will be referred as the $RD3Q27$ model. Here, in addition to the fourth order isotropy of the moments one of the

6th order constraint is applied on the moments as,

$$\sum_{i}^{N_d} w_i c_i^2 c_{ix}^4 = 3 \sum_{i}^{N_d} w_i c_i^2 c_{ix}^2 c_{iy}^2 \tag{6.13}$$

These constraints gives the solution of the model to be

$$w_s = \frac{1}{30}, \qquad w_f = \frac{1}{300}, \qquad w_b = \frac{4}{75}, \qquad w_0 = \frac{1}{3}, \qquad \theta_0 = \frac{c^2}{5}. \tag{6.14}$$

The set of discrete velocities and corresponding weights are listed in Table 6.2. This procedure also removes artifacts associated with the closure of the third order moment in in LBM.

Shells	Discrete Velocities(c_i)	Weight(w_i)
SC	$(\pm1,0,0)\,,(0,\pm1,0)\,,(0,0,\pm1)$	$\frac{1}{30}$
FCC	$(\pm1,\pm1,0)\,,(\pm1,0,\pm1)\,,(0,\pm1,\pm1)\,,$	$\frac{1}{300}$
BCC	$(\pm1/2,\pm1/2,\pm1/2)$	$\frac{4}{75}$

Table 6.1: Energy shells and their corresponding velocities with weights for $RD3Q27$.

After choosing the appropriate discrete velocity set, it is projected on to the BCC lattice. In 2-dimensions the projection of discrete vlocity set on to the position space (BCC lattice) is shown in Fig. 6.7.

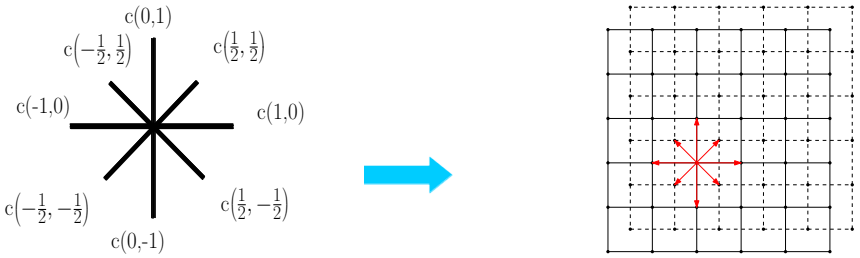

Figure 6.7: The projection of velocity set on to the BCC grid (2d-projection) in 2-dimensions.

6.3.1 Equilibrium distribution function

Following Ansumali et.al (Ansumali & Karlin, 2005), we choose to construct energy the conserving equilibrium as the minimizer of the H-function. The choice of energy the conserving equilibrium is dictated mainly by the increased stability of those models (Singh *et al.*, 2013*a*; Thantanapally *et al.*, 2013*b*). The explicit expression for the energy conserving equilibrium distribution function for $RD3Q27$ model with the $O(u^3)$ is

$$f_i^{\mathrm{eq}} = w_i \rho \left[1 + \frac{\Delta\theta}{2}\left(\frac{c_i^2}{\theta_0} - 3\right)\right]\left[1 + \frac{u_\alpha c_{i\alpha}}{\theta} - \frac{u^2}{2\theta} + \frac{1}{2}\left(\frac{u_\alpha c_{i\alpha}}{\theta}\right)^2 + \frac{u^2}{2\theta}\left(1 - \frac{c_i^2}{\theta}\right)\hat{h}_4 + \frac{1}{6}\left(\frac{u_\alpha c_\alpha}{\theta}\right)^3 - \frac{u^2 u_\alpha c_{i\alpha}}{2\theta^2}\left(1 - \frac{7}{12}\Delta\theta\left(\frac{\theta_0}{\theta}\right)^2\right) + \frac{u^2 u_\alpha c_{i\alpha}}{6\theta^2}\left(5 - \frac{35}{12}\Delta\theta\left(\frac{\theta_0}{\theta}\right)^2 - \frac{c_i^2}{\theta}\right)\hat{h}_4\right], \tag{6.15}$$

where,

$$\hat{h}_4 = \frac{35\Delta\theta\left(\frac{\theta_0}{\theta}\right)^2}{24 + 35\Delta\theta\left(\frac{\theta_0}{\theta}\right)^2}. \tag{6.16}$$

This ensures the conservation of density (ρ), momentum density (ρu_α) and energy density ($\rho u^2 + 3\rho\theta$) during collision. For isothermal case, where $\theta = \theta_0$, the explicit expression for the equilibrium distribution function can be written as ;

$$f_i^{\mathrm{eq}} = w_i\rho\left[1 + \frac{u_\alpha c_{i\alpha}}{\theta_0} - \frac{u^2}{2\theta_0} + \frac{1}{2}\left(\frac{u_\alpha c_{i\alpha}}{\theta_0}\right)^2 + \frac{1}{6}\left(\frac{u_\alpha c_\alpha}{\theta_0}\right)^3 - \frac{u^2 u_\alpha c_{i\alpha}}{2\theta_0^2}\right]. \tag{6.17}$$

The corresponding equilibrium stress tensor and heat flux vector are given by,

$$P_{\alpha\beta}^{\mathrm{eq}} = \rho u_\alpha u_\beta + \rho\theta_0\delta_{\alpha\beta}, \qquad q_\alpha^{\mathrm{eq}} = 5\rho u_\alpha\theta_0 + \frac{5}{12}\rho u^2 u_\alpha. \tag{6.18}$$

This set-up provides a good indication of the convergence of the discrete velocity model towards the Boltzmann equation.

6.3.2 Moment-chain

The governing equation for the discrete population density evolution is

$$\partial_t f_i + c_{i\alpha}\partial_\alpha f_i - F_i = \frac{1}{\tau}\left(f_i^{\mathrm{eq}} - f_i\right). \tag{6.19}$$

Here $c_{i\alpha}$ is the lattice velocity and f_i^{eq} is the equilibrium distribution. We model the external forcing term(F_i) by using the lowest order Hermite-projection of the gradient in the velocity space as (He *et al.*, 1998),

$$F_i = g_\alpha\frac{\partial f}{\partial c_\alpha} = g_\alpha\frac{(c_{i\alpha} - u_\alpha)}{\theta_0}f_i^{\mathrm{eq}}. \tag{6.20}$$

The better representation of extended hydrodynamics by present model can be seen by writing discrete moment chain. The basic set of independent moments for this model are

$$M = \{\rho, j_\alpha, P_{\alpha\beta}, Q_{\alpha\beta\gamma}, R_{\alpha\beta}, \Phi\} \tag{6.21}$$

where

$$Q_{\alpha\beta\gamma} = \sum_i^{N_d} f_i c_{i\alpha}c_{i\beta}c_{i\gamma}, \quad R_{\alpha\beta} = \sum_i^{N_d} f_i c_i^2 c_{i\alpha}c_{i\beta}, \quad \Phi = \sum_i^{N_d} f_i c_i^2 c_i^2 c_i^2. \tag{6.22}$$

The moment-chain by taking the appropriate moments of f_i in the Eq. (6.19) can be written as,

$$\begin{aligned}
\partial_t\rho + \partial_\alpha j_\alpha &= 0,\\
\partial_t j_\alpha + \partial_\beta P_{\alpha\beta} &= \rho g_\alpha,\\
\partial_t P_{\alpha\beta} + \partial_\gamma Q_{\alpha\beta\gamma} &= \frac{1}{\tau}\left(P_{\alpha\beta}^{\mathrm{eq}} - P_{\alpha\beta}\right),\\
\partial_t Q_{\alpha\beta\gamma} + \partial_\gamma R_{\alpha\beta\gamma\kappa} &= \frac{1}{\tau}\left(Q_{\alpha\beta\gamma}^{\mathrm{eq}} - Q_{\alpha\beta\gamma}\right),\\
\partial_t R_{\alpha\beta} + \partial_\gamma N_{\alpha\beta\gamma} &= \frac{1}{\tau}\left(R_{\alpha\beta}^{\mathrm{eq}} - R_{\alpha\beta}\right),\\
\partial_t\Phi + \partial_\gamma S_\gamma &= \frac{1}{\tau}\left(\Phi^{\mathrm{eq}} - \Phi\right),
\end{aligned} \tag{6.23}$$

where

$$N_{\alpha\beta\gamma} = \sum_i f_i c_i^2 c_{i\alpha} c_{i\beta} c_{i\gamma} \quad S_\alpha = \sum_i f_i c_i^2 c_i^2 c_i^2 c_{i\alpha}. \tag{6.24}$$

The closure relations for the higher order moments $R_{\alpha\beta\gamma\kappa}$, $N_{\alpha\beta\gamma}$ and S_α written in terms of other lower order moments as

$$\begin{aligned} R_{\alpha\beta\gamma\kappa} =& \frac{1}{5}\left(R_{\alpha\beta}\delta_{\gamma\kappa} + R_{\alpha\gamma}\delta_{\beta\kappa} + R_{\alpha\kappa}\delta_{\beta\gamma} + R_{\beta\gamma}\delta_{\alpha\kappa} + R_{\beta\kappa}\delta_{\alpha\gamma} + R_{\gamma\kappa}\delta_{\alpha\beta}\right) \\ & - \frac{\theta_0}{3}\left(P_{\alpha\beta}\delta_{\gamma\kappa} + P_{\alpha\gamma}\delta_{\beta\kappa} + P_{\alpha\kappa}\delta_{\beta\gamma} + P_{\beta\gamma}\delta_{\alpha\kappa} + P_{\beta\kappa}\delta_{\alpha\gamma} + P_{\gamma\kappa}\delta_{\alpha\beta}\right) + \frac{1}{3}\Phi\Delta_{\alpha\beta\gamma\kappa}, \\ N_{\alpha\beta\gamma} =& \frac{1}{4}\Delta^{(6)}_{\alpha\beta\gamma\kappa\eta\zeta} Q_{\kappa\eta\zeta} c^2 + \frac{5}{12}\Delta_{\alpha\beta\gamma\kappa}\left(q_\kappa c^2 - j_\kappa c^4\right), \\ S_\alpha =& \frac{1}{16}\left[-71 j_\alpha c^6 + 25\delta_{\alpha\beta\gamma\kappa} Q_{\beta\gamma\kappa} c^4\right] + 7 q_\alpha c^4. \end{aligned} \tag{6.25}$$

This moment chain is very similar to Grad's equation of the form (Ansumali *et al.*, 2007*b*; Shi *et al.*, 2015; Harting *et al.*, 2006): It should be noted that unlike usual $D3Q27$ LBM, for the present model, $Q_{xxx}, Q_{yyy}, Q_{zzz}$ are independent variables, and artificial closures do not exist. This happens, since the velocity component in the diagonal direction $|c_{ix}|$ is $1/2$ rather than 1. Also the closure for $R_{\alpha\beta\gamma\kappa}$ depends on $P_{\alpha\beta}$ along with the higher order moment $R_{\alpha\beta}$. This ensures the effect of higher order moments also in the solution of the moment chain. Thus one can expect that RD3Q27 should show enhanced accuracy for finite Knudsen flows as compared to D3Q27 (Qian & Zhou, 1998).

6.3.3 Time discretization

Finally, following the standard route of discretization along characteristic directions using trapezoidal rule (Succi, 2001*a*), we can write a fully discrete version of the kinetic Eq. (5.3) as

$$f_i\left(\mathbf{x} + c\Delta t, t + \Delta t\right) = f_i\left(\mathbf{x}, t\right) + 2\beta\left[f_i^{\mathrm{eq}}\left(\mathbf{x}, t\right) - f_i\left(\mathbf{x}, t\right)\right], \tag{6.26}$$

where β is the discrete relaxation time.

Notice that similar to D3Q27 model, if we choose $\Delta t = \Delta x$, the advection happens from one lattice point to another and consequently, the method does not require any spatial interpolation. The numerical implementation can be done efficiently by noting that the BCC grid in 3D has an alternate interpretation in terms of replica of simple cubic grids displaced from each other by $\Delta x/2$ in each direction where Δx is the grid spacing. It should be noted that the parallel and serial efficiency of this new model is very similar to the standard D3Q27 model.

6.4 Kida-Pelz flow

To demonstrate the increased accuracy of this new framework, we simulate the Kida vortex initial condition and contrast the result with that of the $D3Q27$ model (Thantanapally *et al.*, 2013*a*; Chikatamarla *et al.*, 2010).

The Fig. 6.8, shows the performance of our new BCC lattice-based RD3Q27 velocity model at Re = 1000 is contrasted with the pseudo-spectral and the D3Q27 model. It is clear that present implementation gives almost order of the same accuracy for the same grid resolution as that of the PS method. Fig. 6.9, shows the further extension of the comparision for Re = $10,000$. In the present model, Re is defined as, $\rho U_0/\nu$, where in the PS method Re = $1/\nu$ as $U_0 = 1$. It is evident from the results shown in Fig. 6.9 that our new method has drastically improved the performance of standard LBM. This gain can be understood in terms of the spectral representation of a bandwidth-limited function (i.e., whose Fourier coefficients are zero above a cut-off wave-number). Essentially, for a fully resolved three-dimensional simulation in

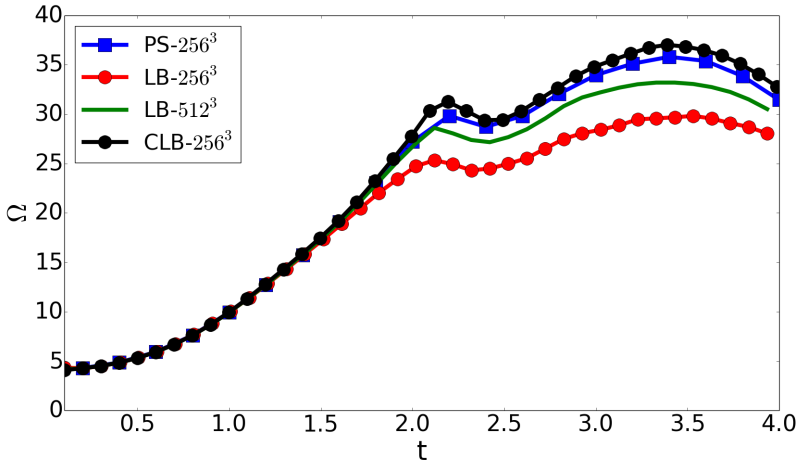

Figure 6.8: Variation of Enstrophy (Ω) with time(t) for Kida-Pelz flow at Re=1000 with different grid resolutions.

a periodic geometry, a reasonable approximation is to assume that the functions to be modeled are isotropic, and the resolution is bandwidth limited. This implies that, in Fourier space, there is no preferred direction and, hence, the efficient distribution of grid points is equivalent to the sphere-packing problem (Petersen & Middleton, 1962; Conway & Sloane, 2013). Thus the most efficient way to distribute points in the Fourier space is to arrange them as an FCC lattice. Consequently, the best sampling lattice in real space is the BCC lattice, which is the dual of the FCC lattice (Petersen & Middleton, 1962; Conway & Sloane, 2013) in the Fourier space. It can be seen from the Fig. 6.10 that, the sphere is packed most efficiently on the BCC lattice. Thus the numerical gain in simulation accuracy is associated with the efficient choice of the lattice.

Although RD3Q27 uses a grid of size $2N^3$ as compared to the standard case of N^3, the performance gain is almost an order-of-magnitude. This happens because, for the same accuracy of simulation, the usual D3Q27 model requires a grid size of $(MN)^3$, where M ranges from $2-3$. This implies that the saving in the number of grid points is in the range of $(MN)^3/2(N)^3$, which is $4-8$ times. Hence the saving in time is $(MN)^4/2(N)^4$ i.e., at least eight times (on a coarser grid, the time steps are larger).

6.5 Unidirectional flow

Similar to the $D3Q27$ model, the moment chain can be solved analytically in case of unidirectional steady flow[1]. Following Ansumali *et al.* (2007*b*), the moment chain is first written for the unidirectional steady flow set-up. Similar to the $D3Q27$ model, momentum balance equation in case of the steady unidirectional flow reduces to

$$\partial_y P_{xy} = \rho g_x, \tag{6.27}$$

which is coupled with the evolution equation of the off-diagonal part of the pressure tensor as

$$\partial_y Q_{xyy} = -\frac{P_{xy}}{\tau}. \tag{6.28}$$

[1]This work is done in collaboraton with Dr.V.K. PonnuLakshmi

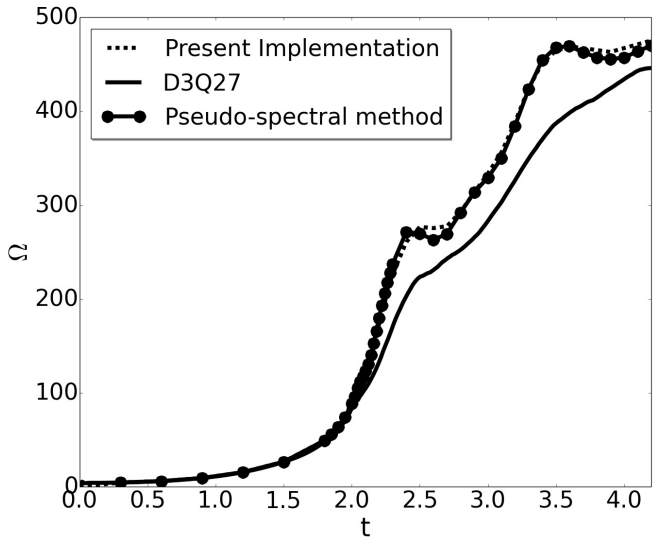

Figure 6.9: Variation of Enstrophy (Ω) with time(t) for Kida-Pelz flow at Re=10,000 on 1200^3 grid.

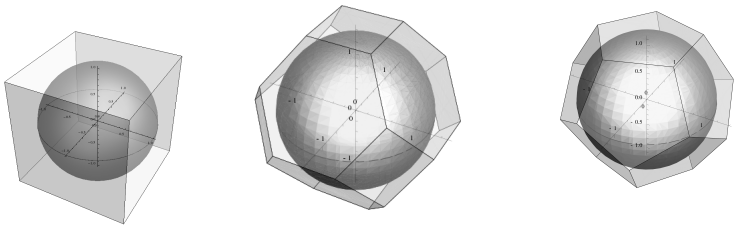

Figure 6.10: Representation of a sphere on (Left to right) SC, FCC and BCC lattice in Fourier space.

This system of equation can be again solved to obtain

$$Q_{xyy} = \frac{1}{\tau}\left[\rho g_x \frac{y^2}{2} + C_1 y + C_2\right]. \tag{6.29}$$

The evolution equation for Q_{xyy} is again

$$\partial_y R_{xyyy} - \rho g_x \theta_0 = \frac{1}{\tau}\left[j_x \theta_0 - Q_{xyy}\right]. \tag{6.30}$$

It should be noted that moment chain is so far identical with that of $D3Q27$ model. However, due to form of closure for R_{xyyy} which is:

$$R_{xyyy} = \frac{3}{5} R_{xy} - \theta_0 P_{xy}, \tag{6.31}$$

It should be noted that the fourth order moment depends on higher order moments R_{xy}, which gets coupled to the lower moments and thus the kinetic boundary layer emerges. Using Eq. (6.25), we have

$$\frac{3}{5}\partial_y R_{xy} - \theta_0 \partial_y P_{xy} - \rho g_x \theta_0 = \frac{1}{\tau}\left[j_x \theta_0 - Q_{xyy}\right]. \tag{6.32}$$

$$-2\theta_0\partial_y P_{xy} + \frac{3}{5}\partial_y R_{xy} = \frac{1}{\tau}\left[3j_x\theta_0 - Q_{xxx}\right]. \tag{6.33}$$

$$\partial_y R_{xy} = \frac{1}{\tau}\left(5\theta_0 j_x - q_x\right) \tag{6.34}$$

The evolution equation for the contracted fourth order moment is:

$$\partial_y N_{xyy} = -\frac{R_{xy}}{\tau}. \tag{6.35}$$

Similarly, using Eq. (6.25) the closure for fifth order moment is

$$N_{xyy} = \left(-\frac{125}{12}\theta_0^2 j_x + \frac{25}{12}\theta_0 Q_{xxx} + 10\theta_0 Q_{xyy}\right). \tag{6.36}$$

Eq. (6.30)- (6.35) can be simplified to obtain

$$\partial_y^2 R_{xy} - \left(\frac{4}{15\theta_0\tau^2}\right) R_{xy} = -\frac{14}{9}\frac{P_{xy}}{\tau^2}, \tag{6.37}$$

which can be solved to obtain R_{xy} as

$$R_{xy} = A_1 \sinh\left(\frac{2}{\sqrt{15\theta_0}\tau}y\right) + A_2 \cosh\left(\frac{2}{\sqrt{15\theta_0}\tau}y\right) + \frac{35}{6}P_{xy}\theta_0. \tag{6.38}$$

The velocity profile using this expression for the fourth order moment is predicted to have form:

$$j_x\theta_0 = -\rho g_x\left(\frac{y^2}{\tau}\right) + C_1 y + C_2 + \frac{6}{5\sqrt{15\theta_0}}\left[A_1 \cosh\left(\frac{2}{\sqrt{15\theta_0}\tau}y\right) + A_2 \sinh\left(\frac{2}{\sqrt{15\theta_0}\tau}y\right)\right]. \tag{6.39}$$

The unknown constants A_1,A_2,C_1 and C_2 can be calculated by applying the boundary conditions, which will be explained in detail in the next section.

Boundary conditions

It was shown by Ansumali *et al.* (2007*b*) that for gaseous microflow modeling via LBM one needs to use the discrete version of the diffuse boundary boundary condition (Ansumali & Karlin, 2002*b*). In this sub-section, following Ansumali *et al.* (2007*b*) we construct boundary condition for moments from diffuse boundary condition for the populations. Diffusive boundary condition states that the population coming from the wall are equilibrated population at wall velocity and temperature as

$$f_i\left(\mathbf{c_i}, t\right) = B\, f_i^{\mathrm{eq}}\left(\rho_w, \mathbf{U}_w, \theta_w\right) \tag{6.40}$$

where, the scattering probability B can be written in term of the outgoing flux as (Ansumali & Karlin, 2002*b*):

$$B = \frac{\sum\limits_{c_i.\mathbf{n}<0} |\mathbf{c}_i.\mathbf{n}| f_i\left(\rho, \mathbf{u}, \theta\right)}{\sum\limits_{c_i.\mathbf{n}<0} |\mathbf{c}_i.\mathbf{n}| f_i^{\mathrm{eq}}\left(\rho_w, \mathbf{U}_w, \theta_w\right)}. \tag{6.41}$$

Here, $\mathbf{n}$ is the normal vector at the wall, ρ_w is the wall density, $\mathbf{U}_w$ is the wall velocity and the wall temperature is θ_w. This definition of scattering probability ensures that the no-flux condition at the wall is satisfied. It should be noted the density of the wall ρ_w doesn't contribute as both numerator and denominator contains wall density and can be factored out. For simplicity, we

take ρ_w to be unity and the above equation reduce to:

$$f_i\left(\mathbf{c_i}, t\right) = \frac{\sum\limits_{c_i.\mathbf{n}<0} |\mathbf{c}_i.\mathbf{n}| f_i\left(\rho, \mathbf{u}, \theta\right)}{\sum\limits_{c_i.\mathbf{n}<0} |\mathbf{c}_i.\mathbf{n}| f_i^{\mathrm{eq}}\left(1, \mathbf{U}_w, \theta_w\right)} f_i^{\mathrm{eq}}\left(1, \mathbf{U}_w, \theta_w\right). \tag{6.42}$$

In present work, it is assumed that the walls and the medium are at the same temperature θ_0. For the present case of straight wall, we write down the equilibrium population corresponding to the wall velocity (U_w) along x direction to be U_1 and U_2 at the bottom and top wall.

$$f_i^{\mathrm{eq}}(1, U_w) = w_i \left(1 + \frac{c_{ix} U_w}{\theta_0}\right). \tag{6.43}$$

With this distribution function, we can calculate the denominator as:

$$\sum_{c_{iy}>0} |c_{iy}| f_i^{\mathrm{eq}}(1, U_w) = \sum_{c_{iy}<0} |c_{iy}| f_i^{\mathrm{eq}}(1, U_w) = c \sum_{c_{iy}<0} \frac{|c_{iy}|}{c} w_i = \frac{23}{150}\sqrt{5\theta_0}. \tag{6.44}$$

Similarly, out-flux for unidirectional flow ($j_y = 0$) can be computed as,

$$\sum_{c_{iy}>0} |c_{iy}| f_i = \sum_{c_{iy}<0} |c_{iy}| f_i = \frac{\sqrt{5\theta_0}}{3750\theta_0^3}\left(16\Phi + 800P\theta_0^2 + 275P_{yy}\theta_0^2 - 240R\theta_0\right), \tag{6.45}$$

where R is $R_{xx} + R_{yy} + R_{zz}$ and $P = P_{xx} + P_{yy} + P_{zz}$. Hence, the scattering probability B is:

$$B = \frac{1}{575}\frac{\left(16\Phi + 800P\theta_0^2 + 275P_{yy}\theta_0^2 - 240R\theta_0\right)}{\theta_0^3}. \tag{6.46}$$

Finally, we follow Ansumali *et al.* (2007*b*) to divide the moments $\mathcal{M}$ into sub-parts

$$\mathcal{M} = M^+ + M^- + M^0 \tag{6.47}$$

where, M^+ and M^- are the moments calculated using the discrete population with $c_i.\mathbf{n} > 0$ and $c_i.\mathbf{n} < 0$ and M^0 corresponds to $c_i.\mathbf{n} = 0$ at the boundaries. The corresponding half moments at the top wall and the bottom walls with weights can be computed and are tabulated in Table 6.2. Next, we write down the half moments for the important physical quantities from the medium to the top and the bottom wall: First, for the top wall we need $\mathcal{M}^+$ half moments which can be calculated from the constructed distribution function and are written as,

$$\begin{aligned}
\rho^+ &= \frac{1}{30}(48\Phi + 96P_{xx} + 111P_{yy} + 96P_{zz} - 20Q_{yyy} - 144R) \\
j_x^+ &= \frac{1}{10}(5j_x + 13P_{xy} - 5Q_{xxx} + 5Q_{xyy} - 4R_{xy}) \\
P_{xy}^+ &= \frac{1}{6}(j_x + 3P_{xy} - Q_{xxx} + 3Q_{xyy}) \\
Q_{xyy}^+ &= \frac{1}{10}(P_{xy} + 5Q_{xyy} + 2R_{xy})
\end{aligned} \tag{6.48}$$

half moment	Top wall ($c_y > 0$)	Bottom wall ($c_y < 0$)	$c_y = 0$
$\sum w_i$	$\frac{13}{50}$	$\frac{13}{50}$	$\frac{12}{25}$
$\sum w_i c_{ix}$	0	0	0
$\sum w_i c_{iy}$	0.342789 $\sqrt{\theta_0}$	- 0.342789 $\sqrt{\theta_0}$	0
$\sum w_i c_{ix} c_{iy}$	0	0	0
$\sum w_i c_{ix}^2 c_{iy}$	0.37267 $\theta_0^{\frac{3}{2}}$	- 0.37267 $\theta_0^{\frac{3}{2}}$	0
$\sum w_i c_{ix} c_{iy}^2$	$\frac{1}{2}\,\theta_0^2$	$\frac{1}{2}\,\theta_0^2$	0
$\sum w_i c_{ix}^2 c_{iy}^2$	0	0	0
$\sum w_i c_i^2 c_{ix} c_{iy}$	0	0	0

Table 6.2: The half moments with respect to weights at the top and bottom wall.

Similarly one can obtain the necessary $\mathcal{M}^-$ half moments at the bottom wall to be as follows:

$$\begin{aligned}
\rho^- =& \frac{1}{30}(48\Phi + 96P_{xx} + 111P_{yy} + 96P_{zz} + 20Q_{yyy} - 144R) \\
j_x^- =& \frac{1}{10}(5j_x - 13P_{xy} - 5Q_{xxx} + 5Q_{xyy} + 4R_{xy}) \\
P_{xy}^- =& \frac{1}{6}(-j_x + 3P_{xy} + Q_{xxx} - 3Q_{xyy}) \\
Q_{xyy}^- =& \frac{1}{10}(-P_{xy} + 5Q_{xyy} - 2R_{xy})
\end{aligned} \tag{6.49}$$

Here, we followed the same convention as defined earlier for M^+ and M^-. Similarly, the contribution for the half moments from the velocity components where $c_i.\mathbf{n} = 0$ is written as:

$$\begin{aligned}
\rho^0 =& \frac{1}{5}(-16\Phi - 32P_{xx} - 37P_{yy} - 32P_{zz} + 48R) + \rho \\
j_x^0 =& Q_{xxx} - Q_{xyy} \\
P_{xy}^0 =& 0 \\
Q_{xyy}^0 =& 0
\end{aligned} \tag{6.50}$$

With these, the moments ρ, j_x, P_{xy} and Q_{xyy} at the boundaries become,

$$\begin{aligned}
\rho =& \rho^{\pm} + \frac{13B}{50} + \rho^0 \\
j_x =& j_x^{\pm} + \frac{3B}{10} j_x|_w + j_x^0 \\
P_{xy} =& P_{xy}^{\pm} \mp \frac{5B}{6} j_x|_w + P_{xy}^0 \\
Q_{xyy} =& Q_{xyy}^{\pm} + \frac{B\theta_0}{2} j_x|_w + Q_{xyy}^0
\end{aligned} \tag{6.51}$$

Now, we will calculate the value of B by substituting the value for P, R and Φ from the energy conservation and their evolution equation. The solution for the above quantities can be written

as:

$$P = P_{xx} + P_{yy} + P_{zz} = 3\rho\theta_0 + 2g_x j_x \tau \tag{6.52}$$
$$R = 5\theta_0 \left[\tfrac{1}{12}\left(-5P_{yy} + 41\rho\theta_0\right) + \tfrac{17}{6} g_x j_x \tau\right] \tag{6.53}$$
$$\Phi = 25\theta_0^2 \left[\tfrac{1}{16}\left(-25P_{yy} + 81\rho\theta_0\right) + \tfrac{37}{8} g_x j_x \tau\right] \tag{6.54}$$

Substituting the above in the scattering probability equation reveals the value of B to be unity. With the scattering probability to be unity, the outgoing population from the wall is set to be its equilibrium value.

To solve the unknown constants, we take the half moments of P_{xy} and Q_{xyy} at both boundaries which results in a system of 4 equations with 4 unknowns(A_1, A_2,C_1, C_2) as:

$$Q_{xyy}|_{y=L/2} = \frac{1}{5}\left(P_{xy}\sqrt{5\theta_0} + \frac{2R_{xy}}{\sqrt{5\theta_0}} + 5\theta_0 U_2\right) \tag{6.55}$$
$$Q_{xyy}|_{y=-L/2} = \frac{1}{5}\left(-P_{xy}\sqrt{5\theta_0} - \frac{2R_{xy}}{\sqrt{5\theta_0}} + 5\theta_0 U_1\right) \tag{6.56}$$
$$P_{xy}|_{y=L/2} = \frac{1}{3}\left(j_x\sqrt{5\theta_0} - \frac{Q_{xxx}}{\sqrt{5\theta_0}} + \frac{3Q_{xyy}}{\sqrt{5\theta_0}} - \sqrt{5\theta_0}U_2\right) \tag{6.57}$$
$$P_{xy}|_{y=-L/2} = \frac{1}{3}\left(-j_x\sqrt{5\theta_0} + \frac{Q_{xxx}}{\sqrt{5\theta_0}} - \frac{3Q_{xyy}}{\sqrt{5\theta_0}} + \sqrt{5\theta_0}U_1\right) \tag{6.58}$$

The solutions for the above equations can be found out and results for Poiseuille and Couette flow will be discussed separately in the next section.

Couette flow

For the Couette flow configuration, we can put $g_x = 0$. The form of the velocity profile remains the same but the shear stress P_{xy} becomes a constant and the integration constants A_1 and C_2 goes to zero and the other constants are:

$$\begin{aligned}
&\mathrm{A1} = 0,\\
&C_2 = 0,\\
&C_1 = \frac{\mathrm{Kn}\sqrt{\theta_0}\Delta U\left(26 + 15\sqrt{3}\coth\left(\frac{2}{\sqrt{5}\mathrm{Kn}}\right)\right)}{-\sqrt{15}\mathrm{Kn}\,\mathrm{csch}\left(\frac{2}{\sqrt{5}\mathrm{Kn}}\right) + \left(33\sqrt{5}\mathrm{Kn} + 26\sqrt{3}\right) + \left(19\sqrt{15}\mathrm{Kn} + 45\right)\coth\left(\frac{2}{\sqrt{5}\mathrm{Kn}}\right)}\\
&A_2 = -\frac{25\mathrm{Kn}\theta_0^{3/2}\Delta U\left(5\tanh\left(\frac{1}{\sqrt{5}\mathrm{Kn}}\right) + 3\sqrt{3}\right)\mathrm{sech}\left(\frac{1}{\sqrt{5}\mathrm{Kn}}\right)}{6\left(9\left(2\sqrt{15}\mathrm{Kn} + 5\right) + \tanh\left(\frac{1}{\sqrt{5}\mathrm{Kn}}\right)\left(66\sqrt{5}\mathrm{Kn} + 5\left(4\sqrt{15}\mathrm{Kn} + 9\right)\tanh\left(\frac{1}{\sqrt{5}\mathrm{Kn}}\right) + 52\sqrt{3}\right)\right)}
\end{aligned} \tag{6.59}$$

Where $\Delta U = (U_1 - U_2)$ and $U = U_1 + U_2$. An important quantity of interest in this set-up is the shear stress (Ansumali *et al.*, 2007*b*) and for this the explicit expression can be written as:

$$\begin{aligned}
P_{xy}^{*} = \frac{P_{xy}}{P_{xy}^{\infty}} &= \frac{6\mathrm{Kn}\sqrt{\theta_0}\left(26\sinh\left(\frac{2}{\sqrt{5}\mathrm{Kn}}\right) + 15\sqrt{3}\cosh\left(\frac{2}{\sqrt{5}\mathrm{Kn}}\right)\right)}{-\sqrt{15}\mathrm{Kn} + \left(33\sqrt{5}\mathrm{Kn} + 26\sqrt{3}\right)\sinh\left(\frac{2}{\sqrt{5}\mathrm{Kn}}\right) + \left(19\sqrt{15}\mathrm{Kn} + 45\right)\cosh\left(\frac{2}{\sqrt{5}\mathrm{Kn}}\right)}\\
P_{xy}^{\infty} &= \frac{\sqrt{5\theta_0}}{6}(U_1 - U_2)
\end{aligned} \tag{6.60}$$

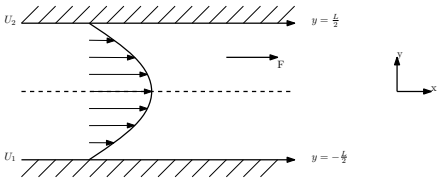

Figure 6.11: The figure shows the schematic of Poiseuille flow set-up where the flow is unidirectional and the flow is due to external applied force g_x.

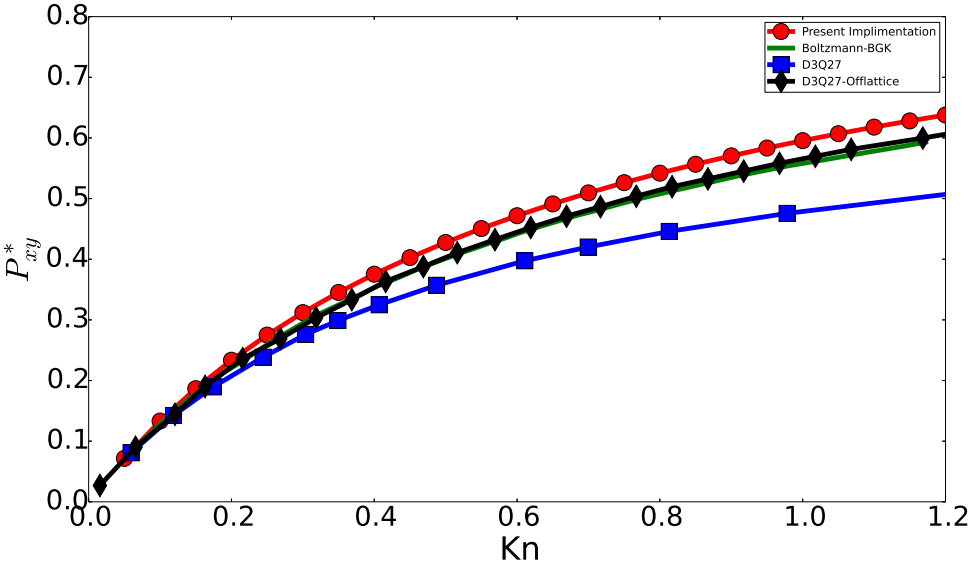

Figure 6.12: Shear stress predicted using equation 6.60 at various Knudsen numbers

The variation of non-dimensional shear stress with Knudsen number is plotted in figure 6.12. The results are compared with continuous Boltzmann equation, standard D3Q27 and D3Q27 with off-lattice (Yudistiawan *et al.*, 2010). It can be seen that the RD3Q27 results are better than standard D3Q27 although off-lattice results are closer to the analytical Boltzmann equation.

Similarly, we compare the slip and the slip length predicted by RD3Q27 with the other models in figure 6.13 and 6.14. It can be seen, the results are in close agreement with the DSMC and continuous Boltzmann equation.

Poiseuille flow

Now we consider the next canonical unidirectional flow between parallel walls at $y = \pm L/2$ and the flow is set-up by the applied external force modeled using equation 6.20. The schematic of the set-up is given in figure 6.11. The quantity of interest is the variation of flow rate with Knudsen number and the prediction of Knudsen minimum. The predicted velocity form is similar to the equation 6.39 and the boundary conditions are that of stationary wall. With

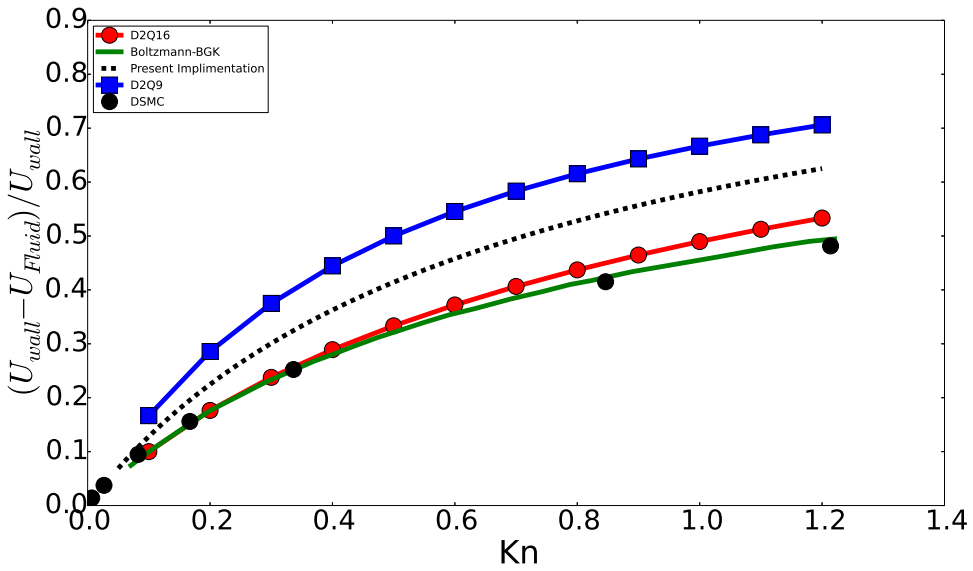

Figure 6.13: The figure shows the comparison of normalized slip velocity (ratio of velocity difference between the wall and the medium to the velocity difference between the top and bottom boundaries) with Knudsen number with the previous studies. The solution obtained using DSMC (Willis, 1962), Boltzmann equation, moment chain model for D2Q16 (Ansumali *et al.*, 2007*b*) are used for comparison.

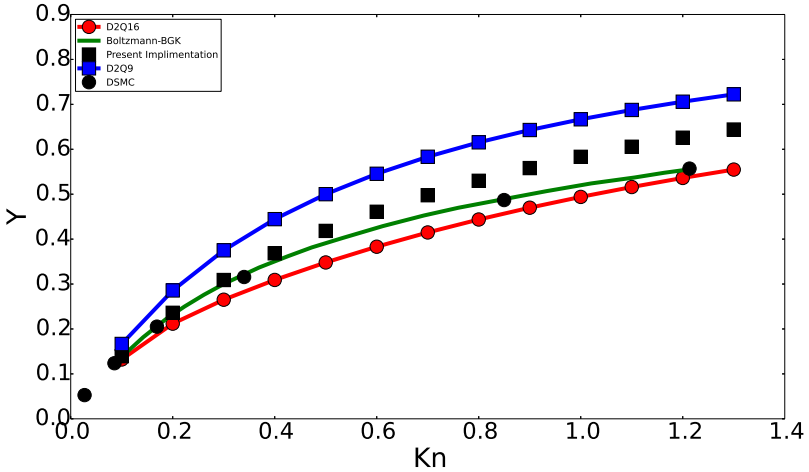

Figure 6.14: The figure shows the comparison of normalized slip length (defined as $Y = \Delta U^{-1}(dU_x/dy)|_{y=0} - 1$) with Knudsen number with the previous studies. The solution obtained using DSMC (Willis, 1962), Boltzmann equation, moment chain model for D2Q16 (Ansumali *et al.*, 2007*b*) are used for comparison.

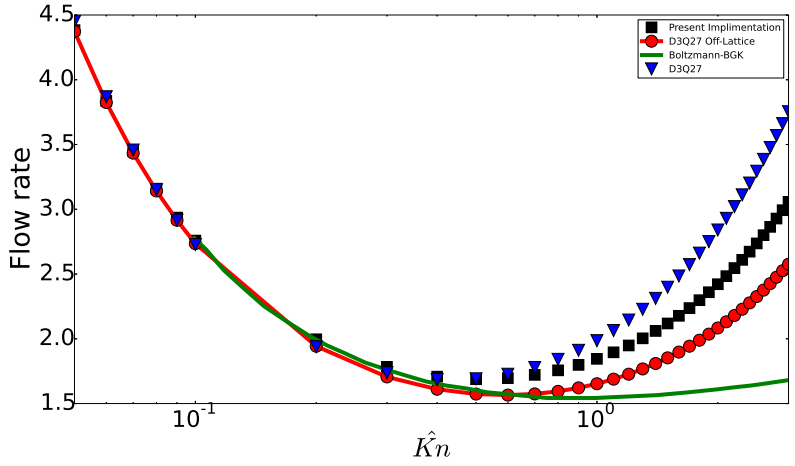

Figure 6.15: The figure shows the comparison of non-dimensional flow rate calculated using equation 6.62 as a function of Knudsen number with the previous studies. The solution obtained using D3Q27 with off-lattice (Yudistiawan *et al.*, 2010), Boltzmann equation, moment chain model for standard D3Q27 (Yudistiawan *et al.*, 2008) are used for comparison.

these conditions,the constants A_2 and C_1 go to zero and the other constants can be written as:

$$C_2 = \frac{\rho g_x \tau \left(\sinh\left(\frac{\sqrt{\frac{2}{15}}}{\widehat{\mathrm{Kn}}}\right)\left(5\left(42\widehat{\mathrm{Kn}}^2 - 6\sqrt{10}\widehat{\mathrm{Kn}} + 1\right)\tau\theta_0 - 8\widehat{\mathrm{Kn}}^2(\tau+3)\right) - 5\sqrt{3}\left(4\sqrt{10}\widehat{\mathrm{Kn}} + 3\right)\tau\theta_0\cosh\left(\frac{\sqrt{\frac{2}{15}}}{\widehat{\mathrm{Kn}}}\right)\right)}{20\widehat{\mathrm{Kn}}^2\left(5\sinh\left(\frac{\sqrt{\frac{2}{15}}}{\widehat{\mathrm{Kn}}}\right) + 3\sqrt{3}\cosh\left(\frac{\sqrt{\frac{2}{15}}}{\widehat{\mathrm{Kn}}}\right)\right)}$$

$$A_1 = \frac{\sqrt{5\theta_0}\rho g_x \mathrm{csch}\left(\frac{\sqrt{\frac{2}{15}}}{\widehat{\mathrm{Kn}}}\right)\left(5\left(\widehat{\mathrm{Kn}}\left(63\widehat{\mathrm{Kn}} + \sqrt{10}\right) + 9\right)\tau\theta_0 - 12\widehat{\mathrm{Kn}}^2(\tau+3)\right)}{12\widehat{\mathrm{Kn}}^2\left(3\sqrt{3}\coth\left(\frac{\sqrt{\frac{2}{15}}}{\widehat{\mathrm{Kn}}}\right) + 5\right)} \tag{6.61}$$

Where $\widehat{\mathrm{Kn}} = \mathrm{Kn}\sqrt{2/3}$.

The non-dimensional flow rate is defined as:

$$Q = -\frac{1}{L^2} g_x^{-1} \sqrt{\frac{2K_B T}{m}} \int_{-L/2}^{L/2} j_x \, dy. \tag{6.62}$$

The non-dimensional flow rate calculated using the velocity profile predicted by RD3Q27 model is:

$$Q = \frac{6\sqrt{3}\left(9\widehat{\mathrm{Kn}}^2 + 2\sqrt{10}\widehat{\mathrm{Kn}} + 1\right)\coth\left(\frac{\sqrt{\frac{2}{15}}}{\widehat{\mathrm{Kn}}}\right) + \left(3\widehat{\mathrm{Kn}}\left(5\widehat{\mathrm{Kn}}\left(2 - 3\sqrt{10}\widehat{\mathrm{Kn}}\right) + 6\sqrt{10}\right) + 10\right)}{12\widehat{\mathrm{Kn}}\left(5 + 3\sqrt{3}\coth\left(\frac{\sqrt{\frac{2}{15}}}{\widehat{\mathrm{Kn}}}\right)\right)} \tag{6.63}$$

The figure 6.15 shows the variation of flow rate with Knudsen number. It can be seen that the model predicts a minimum in flow rate at a Knudsen number around 0.5 closer to the previously reported value by (Yudistiawan *et al.*, 2008) 0.58 and it is accurate than the standard D3Q27 model.

6.6 Flow past sphere

In order to demonstrate the capability of present model, the classical problem of viscous fluid flow past a sphere is investigated in this chapter(Achenbach, 1972; Tomboulides & Orszag, 2000; Spalart, 2009; Johnson & Patel, 1999). The flow past a sphere exhibits non-trivial change in behaviors as a function of Reynolds number, $\mathrm{Re} = \mathrm{U}_\infty \mathrm{D}/\nu$, with D as the diameter of the sphere and U_∞ being velocity at inlet. A set of simulations were performed for various values of Re with $\mathrm{Ma} = 0.05$ for $D3Q27$ and $RD3Q27$ models.

For low Reynolds number case, two representative case of $\mathrm{Re} = 50$ and $\mathrm{Re} = 200$ are reported here. The domain size, in terms of diameter D (measured in lattice unit), of $16D \times 8D \times 8D$ was used for $\mathrm{Re} = 50$ and $20D \times 10D \times 10D$ for $\mathrm{Re} = 200$. The simulations were performed on an Intel Xeon based system (CPU Model: E5-2670) with 16 cores. Fig. 6.16 shows the percentage error (ϵ) in the mean value of $C_\mathrm{D} = F/\left[\frac{1}{2}\rho u_\infty^2 \pi D^2\right]$ from the experimental value of $C_\mathrm{D} = 1.59$ for $\mathrm{Re} = 50$ and $C_\mathrm{D} = 0.78$ for $\mathrm{Re} = 200$ (Johnson & Patel, 1999). From this figure, it is evident that $RD3Q27$ performs an order-of-magnitude better than $D3Q27$. This gain in performance can be seen more conveniently in Fig.6.17, where percentage error (ϵ) is plotted against CPU-time(t in seconds). In this plot, one can see that for the same error, present method requires an order-of-magnitude less time when compared to $D3Q27$ LBM.

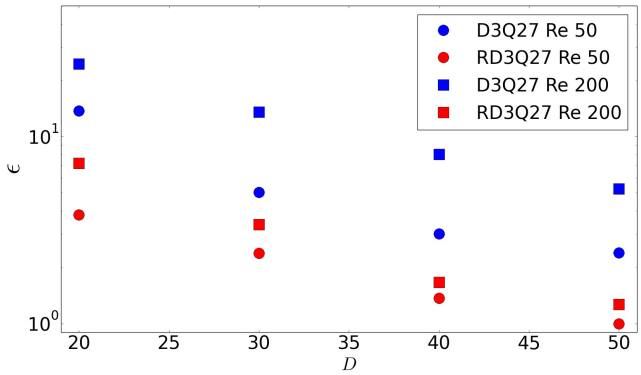

Figure 6.16: Comparison of percentage error (ϵ) in the mean value of C_D with increasing diameter (in lattice points) for flow past sphere between D3Q27 (in blue colour) and RD3Q27 (in red colour) at $\mathrm{Re} = 50$ and 200.

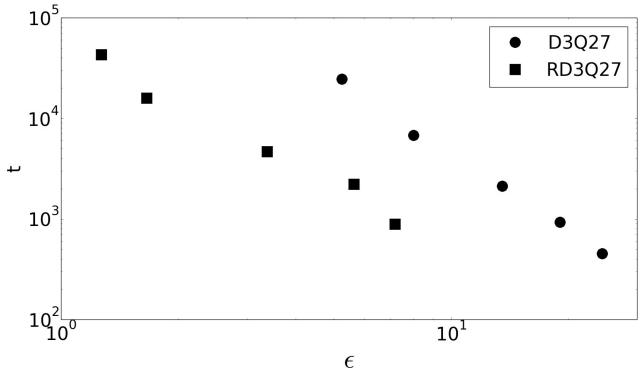

Figure 6.17: Simulation cost (t in seconds) for one convection with respect to the percentage error (ϵ) for flow past sphere at $\mathrm{Re} = 200$. Simulations were performed for one convection time ($\frac{D}{U_0}$, where U_0 is the free stream velocity) on an Intel Xeon based system (CPU Model: E5-2670) with 16 cores.

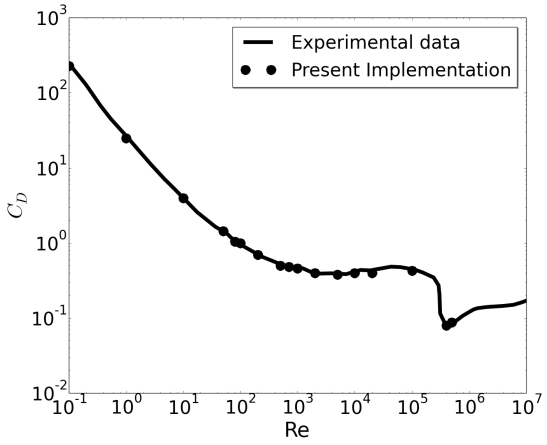

Figure 6.18: Variation of drag coefficient(C_D) with Re for flow past a sphere compared with experimental data (Achenbach, 1972).

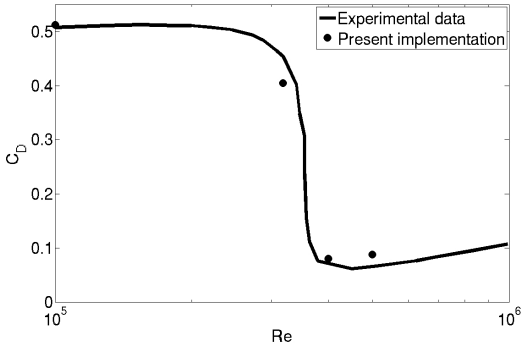

Figure 6.19: Drag coefficient(C_D) zoomed into the range of Re = 10^5 to 10^6 with linear scaling.

As the result for Re = 200 suggests that the computing requirement for the present model is substantially lower than LBM, we performed this simulation of flow past sphere for a wide range of Reynolds numbers. To the best of our knowledge, none of the existing methods can predict the drag behavior over the wide range of Reynolds Numbers for which experimental data is available. In Fig.6.18 and Fig.6.19 the drag coefficient C_D, predicted by present model is contrasted with the experimental result in Achenbach et al, 1972 (Achenbach, 1972) and Bakic et al, 2002 (Bakic, 2002) with Re = UD/ν where D and U are the diameter and speed of the sphere in lattice units. The values of C_{D} for Re = 10^5 and 3.18×10^5 are depicted in Table6.3. Fig. 6.22 shows the variation of drag coefficient C_{D} with time at Re = 3.18×10^5. We have implemented a version of the diffuse bounce-back rule as described in Krithivasan et.al, (Krithivasan *et al.*, 2014) for the solid-fluid interface at the body. For inlet-outlet, we have used Grad's closure approximation as described in Chikatamarla et.al, (Chikatamarla *et al.*, 2006*b*). To highlight the reliability and robustness of our approach, the angular distribution of pressure coefficient $C_P = (P - P_0) \,/\, \left(\frac{1}{2}\rho u_\infty^2\right)$ on the surface of the sphere for Re = 10^5 and Re = 1.62×10^5 are presented in Fig. 6.20, Fig. 6.21 and these are compared with the experimental data. It is evident from the plot that the quality of C_P prediction remains very good even with a sphere size of D = 160 (lattice points). Even for this size of grid, the error in mean value of $\mathrm{C_D}$ is only around 8%. Fig. 6.23 shows a snapshot of the azimuthal component of vorticity. This also shows that our model captures the flow separation clearly. We believe that the reason for such good accuracy without a well-resolved boundary layer is largely due to the fact that the

drag for flow past sphere is largely dominated by form drag, which does not crucially depend on boundary-layer resolution. Thus, with moderate resolution requirement, our approach is able to predict quantities of engineering interest quite accurately. This improvement in LBM is remarkable as typical LBM simulations for high Reynolds Numbers for any setup require the use of turbulence models (Chen *et al.*, 2003; Teixeira, 1998; Girimaji, 2007; Premnath *et al.*, 2009) but the present RD3Q27 model does not require any explicit model for turbulence.

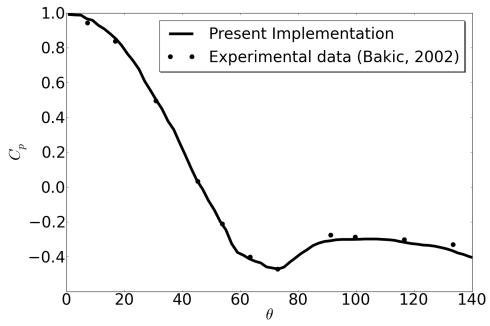

Figure 6.20: Distribution of pressure coefficient(C_P) on the surface of the sphere at Re= 10^5 .

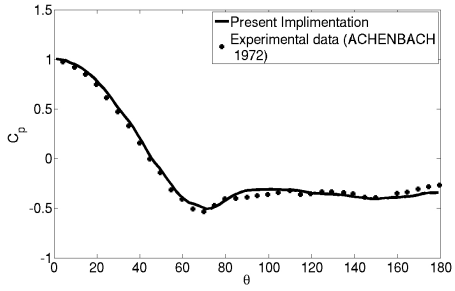

Figure 6.21: Distribution of pressure coefficient(C_P) on the surface of the sphere at Re = 1.62×10^5 .

Re	C_D(expt,Achenbach)	C_D (present)
10^5	0.4-0.5	0.4957
3.18×10^5	0.453	0.4044

Table 6.3: Comparison of C_D values obtained using the present RD3Q27 model with experimental data (Achenbach, 1972).

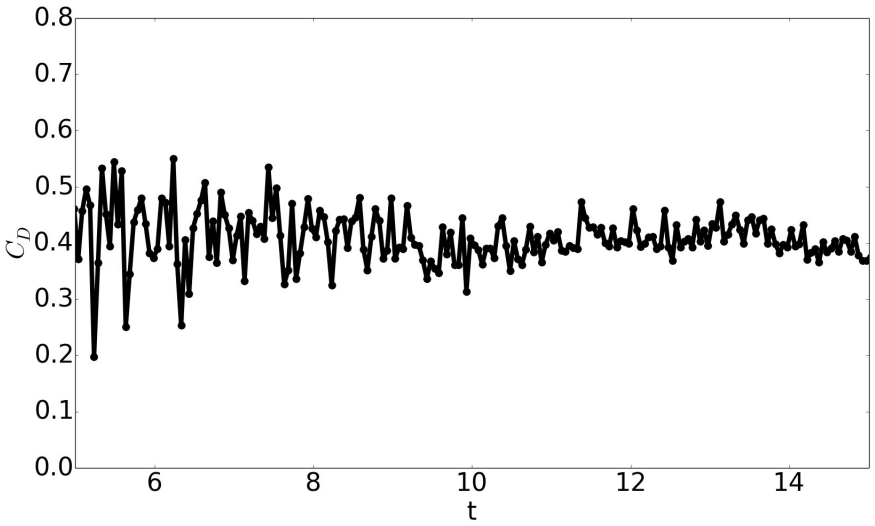

Figure 6.22: Variation of the drag coefficient(C_D) with time for the flow past sphere at Re $= 3.18 \times 10^5$.

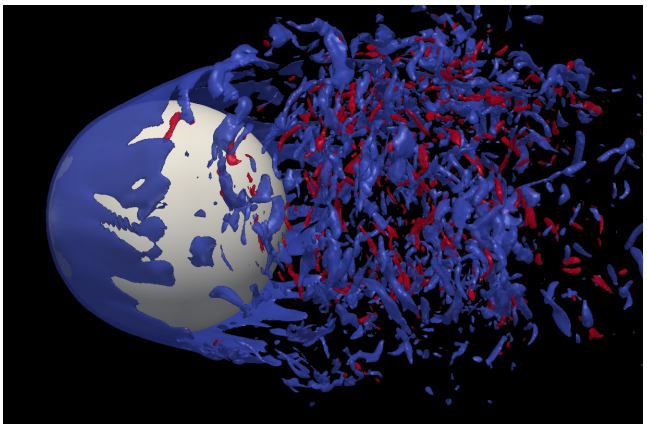

Figure 6.23: The snapshot of ω_ϕ for flow past sphere at Re $= 10^5$.

Chapter 7
Higher order Crystallographic Lattice Boltzmann Method

7.1 Introduction

Lower order Lattice Boltzmann Method has been a successful methodology for incompressible isothermal hydrodynamics and gaseous microflow in slip flow regime. However, an extension of LB method to strong thermal flows and strong flow regimes characterized by high Mach number or high Knudsen regime has been a nontrivial task so far. It has been shown that for modeling gaseous microflows the accuracy of velocity space discretization is very important and it is important to include larger number of velocities. Such discrete velocity models with larger number of velocity shells are termed as higher order Lattice Boltzmann (hereafter referred as HOLB) models. For example, in order to describe the Knudsen layer in $3D$ one needs at least 64 velocities if the velocity set is constructed via Gauss-Hermite quadrature(Ansumali *et al.*, 2007*b*). Based on the entropic formulation of LBM, higher order models have been created to extend the LBM to compressible flow domain and finite Knudsen regime (Chikatamarla & Karlin, 2009, 2006; Chikatamarla *et al.*, 2010; Yudistiawan *et al.*, 2010; Pareschi *et al.*, 2016). It was found that while the lower order LB models were able to represent slip flow effect correctly, only higher order models could predict the Knudsen boundary layer correctly (Kim *et al.*, 2008*b*). Similarly, the best-known model for $3D$ hydrodynamics for fully compressible flow requires 343 velocities on simple cubic lattice(Frapolli *et al.*, 2016).

In this chapter, we will discuss the higher order Lattice Boltzmann Methods on BCC grid. The result shows that use of BCC grid allows construction of higher order LBM with less number of discrete velocities. We use this formulation to create models for thermal flows and trans-sonic flows.

The chapter is organized as follows, In section 7.2, the conditions on the discrete velocity selection for application of LBM to compressible flows are defined. Section 7.3 describes the model that can be applicable for compressible flows i.e., RD3Q67 model with its weights has been defined. Finally in section 7.4, the conditions on the discrete velocity selection for application of LBM to fully compressible and thermal flows are defined.

7.2 LBM for Compressible Hydrodynamics

As discussed in the previous chapters, the discrete equilibrium must satisfy following constraints

$$\sum_{i=1}^{N_d} f_i^{\mathrm{eq}} = \rho, \qquad \sum_{i=1}^{N_d} f_i^{\mathrm{eq}} c_{i\alpha} = \rho u_\alpha, \quad \sum_{i=1}^{N_d} f_i^{\mathrm{eq}} c_{i\alpha} c_{i\beta} = \rho u_\alpha u_\beta + \rho\theta_0 \delta_{\alpha\beta} \tag{7.1}$$

It is typical to write a second order polynomial expression of the equilibrium using the projection of the Maxwell-Boltzmann on the Hermite basis (Chen *et al.*, 1992; Qian *et al.*, 2007; Benzi *et al.*, 1992; Shan & He, 1998). However, these conditions do not ensure that third order moment of the discrete equilibrium is same as that of Maxwell-Boltzmann.

$$\sum_{i=1}^{N_d} f_i^{\mathrm{eq}} c_{i\alpha} c_{i\beta} c_{i\gamma} = \rho u_\alpha u_\beta u_\gamma + \rho\theta_0 \left(u_\alpha \delta_{\beta\gamma} + u_\beta \delta_{\alpha\gamma} + u_\gamma \delta_{\alpha\beta} \right). \tag{7.2}$$

Due to the absence of the cubic term in the equilibrium, this condition is satisfied only up to linear order by widely used lower order lattice Boltzmann models (Qian & Zhou, 1998). This condition on third moment can be fullfiled only if the discrete equilibrium distribution is of the form (Chikatamarla & Karlin, 2009),

$$f_i^{\mathrm{eq}} = w_i \left(1 + \frac{u_\alpha c_{i\alpha}}{\theta_0} + \frac{u_\alpha u_\beta}{2\,\theta_0^2}\left(c_{i\alpha}c_{i\beta} - \theta_0\delta_{\alpha\beta}\right) + \frac{u_\alpha u_\beta u_\gamma c_{i\gamma}}{6\,\theta_0^3}\left(c_{i\alpha}c_{i\beta} - 3\theta_0\delta_{\alpha\beta}\right)\right), \tag{7.3}$$

In case of the entropic lattice Boltzmann method, the series expansion of the true equilibrium at reference temperature θ_0 must reduce to this form. These constraints imply that the discrete velocity set and associated weights have to satisfy following conditions:

$$\sum_{i=1}^{N_d} w_i = 1,\ \sum_{i=1}^{N_d} w_i c_{i\alpha}c_{i\beta} = \theta_0\delta_{\alpha\beta},\ \sum_{i=1}^{N_d} w_i c_{i\alpha}c_{i\beta}c_{i\gamma}c_{i\zeta} = \theta_0^2\Delta_{\alpha\beta\gamma\zeta},\ \sum_{i=1}^{N_d} w_i c_{i\alpha}c_{i\beta}c_{i\gamma}c_{i\kappa}c_{i\zeta}c_{i\eta} = \theta_0^3\Delta_{\alpha\beta\gamma\kappa\zeta\eta}. \tag{7.4}$$

and odd order (till 5th order) moments are zero. It should be noted that as shown in the earlier chapter, odd order moments are zero by construction.

The rationale for adding a cubic term in the equilibrium can be understood by writing the mass and the momentum balance equation and evolution equation for the pressure tensor and flux of pressure tensor term

$$\begin{aligned}
\partial_t\rho + \partial_\alpha j_\alpha &= 0,\\
\partial_t j_\alpha + \partial_\beta P_{\alpha\beta} &= 0,\\
\partial_t P_{\alpha\beta} + \partial_\beta Q_{\alpha\beta\gamma} &= \frac{1}{\tau}\left(\rho u_\alpha u_\beta + \rho\theta_0\delta_{\alpha\beta} - P_{\alpha\beta}\right),\\
\partial_t Q_{\alpha\beta\gamma} + \partial_\kappa R_{\alpha\beta\gamma\kappa} &= \frac{1}{\tau}\left(\rho u_\alpha u_\beta u_\gamma + \rho\theta_0\left(u_\alpha\delta_{\beta\gamma} + u_\beta\delta_{\alpha\gamma} + u_\gamma\delta_{\alpha\beta}\right) - Q_{\alpha\beta\gamma}\right)
\end{aligned} \tag{7.5}$$

from which it is evident that as expected in the limit of $\tau \to 0$, the zeroth order hydrodynamic equation is Euler equation and the first order term lead to correct Navier-Stokes hydrodynamics needed for the compressible dynamics. These conditions are central to LBM construction for isothermal hydrodynamics and the procedure to construct a model which satisfies these requirements is well understood (Chikatamarla & Karlin, 2009; Frapolli *et al.*, 2016).

However, a correct compressible model must have energy conservation and kinetic formulation must ensure that Navier-Stokes-Fourier dynamics is the first order hydrodynamic description. This needs the moment chain to have form

$$\begin{aligned}
\partial_t\rho + \partial_\alpha j_\alpha &= 0,\\
\partial_t j_\alpha + \partial_\beta P_{\alpha\beta} &= 0,\\
\partial_t P_{\alpha\beta} + \partial_\beta Q_{\alpha\beta\gamma} &= \frac{1}{\tau}\left(\rho u_\alpha u_\beta + \rho\theta\delta_{\alpha\beta} - P_{\alpha\beta}\right),\\
\partial_t Q_{\alpha\beta\gamma} + \partial_\kappa R_{\alpha\beta\gamma\kappa} &= \frac{1}{\tau}\left(\rho u_\alpha u_\beta u_\gamma + \rho\theta\left(u_\alpha\delta_{\beta\gamma} + u_\beta\delta_{\alpha\gamma} + u_\gamma\delta_{\alpha\beta}\right) - Q_{\alpha\beta\gamma}\right),\\
\partial_t R_{\alpha\beta\gamma\kappa} + \partial_\zeta R_{\alpha\beta\gamma\kappa\zeta} &= \frac{1}{\tau}\left(R^{\mathrm{eq}}_{\alpha\beta\gamma\kappa} - R_{\alpha\beta\gamma\kappa}\right)
\end{aligned} \tag{7.6}$$

with the equilibrium fourth order moment in the Maxwell-Boltzmann form

$$\begin{aligned}
R^{\mathrm{eq}}_{\alpha\beta\gamma\kappa} = \sum_i^{N_d} f_i^{\mathrm{eq}} c_{i\alpha}c_{i\beta}c_{i\gamma}c_{i\kappa} &= \rho\theta^2\left(\delta_{\alpha\beta}\delta_{\gamma\kappa} + \delta_{\alpha\gamma}\delta_{\beta\kappa} + \delta_{\alpha\kappa}\delta_{\beta\gamma}\right)\\
&+ \rho\theta\left(u_\alpha u_\beta\delta_{\gamma\kappa} + u_\alpha u_\gamma\delta_{\beta\kappa} + u_\alpha u_\kappa\delta_{\beta\gamma} + u_\beta u_\gamma\delta_{\alpha\kappa} + u_\beta u_\kappa\delta_{\alpha\gamma}\right) + \rho u_\alpha u_\beta u_\gamma u_\kappa.
\end{aligned} \tag{7.7}$$

With cubic equilibrium, one would like to satisfy this equation till $O(u^3)$ at $\theta = \theta_0$ and at arbitrary temperature θ at least be quadratically correct in terms of departure from θ_0. Thus, we need to ensure that

$$R^{\rm eq}_{\alpha\beta\gamma\kappa}\left(\mathbf{u}=0\right) = \rho\theta^2\left(\delta_{\alpha\beta}\delta_{\gamma\kappa} + \delta_{\alpha\gamma}\delta_{\beta\kappa} + \delta_{\alpha\kappa}\delta_{\beta\gamma}\right). \tag{7.8}$$

is true till $O(\Delta\theta^2)$ at least. In practice, we only need to ensure that trace of this tensor is in correct form, as only trace appears in the balance equation for the heat flux.

$$R^{\rm eq}_{\alpha\beta}\left(\mathbf{u}=0\right) = 5\rho\theta^2\delta_{\alpha\beta}. \tag{7.9}$$

This is needed as the correct form of Fourier law via Chapman-Enskog procedure requires that evolution equation for the energy flux

$$\partial_t q_\alpha + \partial_\beta R_{\alpha\beta} = \frac{1}{\tau}\left(q^{\rm eq}_\alpha - q_\alpha\right) \tag{7.10}$$

is correct at the leading order

$$\partial^{(0)}_t q^{\rm eq}_\alpha + \partial_\beta R^{\rm eq}_{\alpha\beta} = \frac{1}{\tau}\left(-q^{\rm neq}_\alpha\right) \tag{7.11}$$

In order to ensure correct form of fourth moment $R_{\alpha\beta}$, we need to write the zero velocity equilibrium at finite temperature. In next chapter, starting from Boltzmann form of the H-function, for models which have fourth and sixth order isotropy the equilibrium function with zero velocity at finite temperature θ is derived upto $O(\Delta\theta^2)$ as

$$\tilde{f}_i = w_i\rho\left[1 + \frac{\Delta\theta}{2}\left(\frac{c_i^2}{\theta_0} - 3\right) + \frac{\Delta^2\theta}{8}\left(\frac{c_i^4}{\theta_0^2} - 10\frac{c_i^2}{\theta_0} + 15\right)\right], \tag{7.12}$$

where $\Delta\theta = \theta/\theta_0 - 1$. Thus, for such models

$$R^{\rm eq}_{\alpha\beta}\left(\mathbf{u}=0\right) = 5\rho\theta_0^2\delta_{\alpha\beta}\left(1 + 2\Delta\theta + \Delta\theta^2\right) = 5\rho\theta^2\delta_{\alpha\beta} \tag{7.13}$$

provided

$$\sum_i w_i c_i^8 = 945\theta_0^4. \tag{7.14}$$

If, one also imposes

$$\sum_i w_i c_i^{10} = 10395\theta_0^5, \tag{7.15}$$

the equilibrium function with zero velocity at finite temperature θ is derived upto $O(\Delta\theta^3)$ as

$$\tilde{f}_i = w_i\rho\left[1 + \frac{\Delta\theta}{2}\left(\frac{c_i^2}{\theta_0} - 3\right) + \frac{\Delta^2\theta}{8}\left(\frac{c_i^4}{\theta_0^2} - 10\frac{c_i^2}{\theta_0} + 15\right) + \frac{\Delta^3\theta}{48}\left(\frac{c_i^6}{\theta_0^3} + 21\frac{c_i^4}{\theta_0^2} + 105\frac{c_i^2}{\theta_0} - 105\right)\right], \tag{7.16}$$

which ensures that $R_{\alpha\beta}$ at zero velocity is accurate till $O(\Delta\theta^3)$.

7.3 $RD3Q67$ model for Thermo-hydrodynamics

In last section, conditions for correct thermo-hydrodynamics till $O(u^3)$ and $O(\Delta\theta^3)$ was discussed. To summerize, the weights have to follow the constraints:

$$\begin{aligned}\sum_i w_i = 1, \quad \sum_i w_i c_{i\alpha} c_{i\beta} = \theta_0 \delta_{\alpha\beta},\\ \sum_i w_i c_{i\alpha} c_{i\beta} c_{i\gamma} c_{i\kappa} = \theta_0^2 \Delta_{\alpha\beta\gamma\kappa},\\ \sum_i w_i c_{i\alpha} c_{i\beta} c_{i\gamma} c_{i\kappa} c_{i\eta} c_{i\zeta} = \theta_0^3 \Delta_{\alpha\beta\gamma\kappa\eta\zeta}.\end{aligned} \tag{7.17}$$

and

$$\sum_i w_i c_i^8 = 945\theta_0^4, \qquad \sum_i w_i c_i^{10} = 10395\theta_0^4. \tag{7.18}$$

Along with the above conditions, an additional constraint at 8th order

$$\sum_i w_i c_i^4 c_{ix}^4 = 189\theta_0^4, \tag{7.19}$$

allows us to construct one such higher order Lattice Boltzmann models on BCC lattice with higher order isotropy. As discussed in previous chapters, on basic lattices 4th and 6th order moment have structure

$$\begin{aligned}M^{(4)}_{i_1 i_2 i_3 i_4} &= C_1^{(4)} \Delta^{(4)}_{i_1 i_2 i_3 i_4} + C_2^{(4)} \delta_{i_1 i_2 i_3 i_4},\\ M^{(6)}_{i_1 i_2 i_3 i_4 i_5 i_6} &= C_1^{(6)} \Delta^{(6)}_{i_1 i_2 i_3 i_4 i_5 i_6} + C_2^{(6)} \delta^{(6)}_{i_1 i_2 i_3 i_4 i_5 i_6} + C_3^{(6)} \delta^{(4,2)}_{i_1 i_2 i_3 i_4 i_5 i_6}.\end{aligned} \tag{7.20}$$

This form along with values of coefficients suggest that we need at-least 1 FCC and 1 BCC cells. Indeed, it is evident that the number of independent constraint are 10 and in explicit form they are

$$\begin{aligned}\sum_i w_i = 1, \qquad \sum_i w_i c_i^2 = 3\theta_0, \qquad \sum_i w_i c_x^4 = 3\theta_0^2, \qquad \sum_i w_i c_x^2 c_y^2 = \theta_0^2,\\ \sum_i w_i c_x^2 c_y^2 c_z^2 = \theta_0^3, \qquad \sum_i w_i c_x^2 c_y^4 = 3\theta_0^3, \qquad \sum_i w_i c_x^6 = 15\theta_0^3,\\ \sum_i w_i c_i^8 = 945\theta_0^4, \qquad \sum_i w_i c_i^4 c_{ix}^4 = 189\theta_0^4, \qquad \sum_i w_i c_i^{10} = 10395\theta_0^5.\end{aligned} \tag{7.21}$$

We have chosen 3 SC, 2 FCC and 3 BCC energy shells for this purpose. The set of equations has many solutions. We have chosen the ones which satisfy the condition that $w_i > 0$ and real. The magnitude of the energy shells, coordinates of discrete velocity set and the corresponding weights are given the Table 7.1 and the relevant energy shells are shown in Fig. 7.1. In subsequent chapters this model will be used to simulate thermo-hydrodynamics.

7.4 LBM for fully compressible hydrodynamics flows

In the previous section, we have considered the applicability of LBM to compressible thermal flows. However, the application of LBM to high Ma thermal flows is a more challenging problem. The difficulty arises due to the fact that one needs 8th order isotropy on the lattice. This can

Shells	Discrete Velocities(c_i)	Weight(w_i)
SC - 1	$(\pm1,0,0)\,,(0,\pm1,0)\,,(0,0,\pm1)$	0.0707815774
SC - 2	$(\pm2,0,0)\,,(0,\pm2,0)\,,(0,0,\pm2)$	0.0184771812
SC - 3	$(\pm3,0,0)\,,(0,\pm3,0)\,,(0,0,\pm3)$	0.0011597253
FCC-2	$(\pm2,\pm2,0)\,,(0,\pm2,\pm2)\,,(\pm2,\pm2,0)$	0.0030160186
FCC-3	$(\pm3,\pm3,0)\,,(0,\pm3,\pm3)\,,(\pm3,\pm3,0)$	0.0000231150
BCC-1	$(\pm1/2,\pm1/2,\pm1/2)$	0.0050428593
BCC-2	$(\pm1,\pm1,\pm1)$	0.0385423174
BCC-3	$(\pm3/2,\pm3/2,\pm3/2)$	0.0012157288

Table 7.1: Energy shells and their corresponding velocities with weights for RD3Q67 model.

be seen by writing the equilibrium distribution at $\theta=\theta_0$ and correct up to $O(u^4)$ as

$$f_i^{\rm eq} = w_i\left\{1+\frac{u_\alpha c_{i\alpha}}{\theta}-\frac{u^2}{2\theta}+\frac{\left(u_\alpha c_{i\alpha}\right)^2}{2\theta^2}+\frac{\left(u_\alpha c_{i\alpha}\right)^3}{\theta^3}-\frac{u^2u_\alpha c_{i\alpha}}{2\theta^2}+\frac{\left(u_\alpha c_{i\alpha}\right)^4}{24\theta^4}-\left(\frac{u_\alpha c_{i\alpha}}{\theta}\right)^2\frac{u^2}{4\theta}+\frac{u^4}{8\theta^2}\right\}. \tag{7.22}$$

This shows that $R_{\alpha\beta\gamma\kappa}$ will have correct form only if

$$\sum_i w_i c_{i\alpha}c_{i\beta}c_{i\gamma}c_{i\kappa}c_{i\eta}c_{i\zeta}c_{i\xi}c_{i\phi}=\theta_0^4\Delta_{\alpha\beta\gamma\kappa\eta\zeta\xi\phi}. \tag{7.23}$$

The same at finite temperature requires that at least

$$\sum_i w_i c_i^2 c_{i\alpha}c_{i\beta}c_{i\gamma}c_{i\kappa}c_{i\eta}c_{i\zeta}c_{i\xi}c_{i\phi}=\theta_0^5\Delta_{\alpha\beta\gamma\kappa\eta\zeta\xi\phi}. \tag{7.24}$$

Thus, the weights has the following set of constraints

$$\begin{aligned}\sum_i w_i=1,\quad \sum_i w_i c_{i\alpha}c_{i\beta}=\theta_0\delta_{\alpha\beta},\quad \sum_i w_i c_{i\alpha}c_{i\beta}c_{i\gamma}c_{i\kappa}=\theta_0^2\Delta_{\alpha\beta\gamma\kappa},\\ \sum_i w_i c_{i\alpha}c_{i\beta}c_{i\gamma}c_{i\kappa}c_{i\eta}c_{i\zeta}=\theta_0^3\Delta_{\alpha\beta\gamma\kappa\eta\zeta},\\ \sum_i w_i c_{i\alpha}c_{i\beta}c_{i\gamma}c_{i\kappa}c_{i\eta}c_{i\zeta}c_{i\xi}c_{i\phi}=\theta_0^4\Delta_{\alpha\beta\gamma\kappa\eta\zeta\xi\phi},\\ \sum_i w_i c_i^2 c_{i\alpha}c_{i\beta}c_{i\gamma}c_{i\kappa}c_{i\eta}c_{i\zeta}c_{i\xi}c_{i\phi}=\theta_0^5\Delta_{\alpha\beta\gamma\kappa\eta\zeta\xi\phi}.\end{aligned} \tag{7.25}$$

In addition to these, we add one more constraint as

$$\sum_i w_i c_i^{12}=135135\theta_0^6, \tag{7.26}$$

which ensures that thermal dynamics is correct to all leading orders.

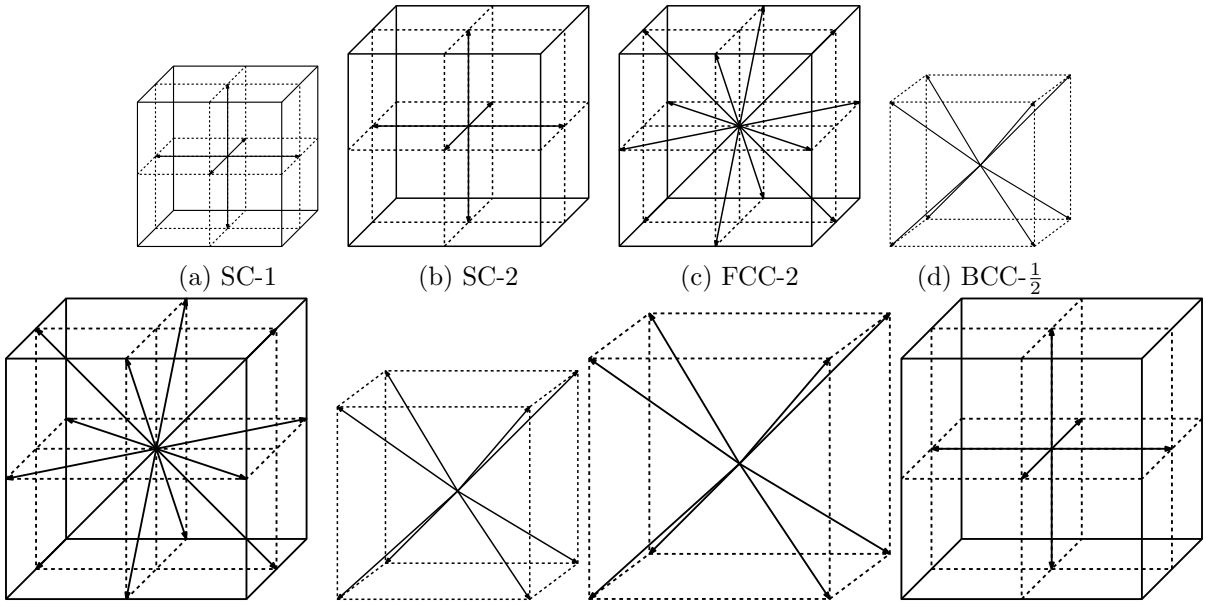

(a) SC-1 (b) SC-2 (c) FCC-2 (d) BCC-$\frac{1}{2}$

(e) FCC-3 (f) BCC-1 (g) BCC-$\frac{3}{2}$ (h) SC-3

Figure 7.1: The energy shells in $RD3Q67$ model.

In the traditional energy shell representation, it is difficult to impose the conditions on the 8th order moments such as $\sum_i w_i c_i^2 c_{ix}^6 c_{iy}^2$ and $\sum_i w_i c_i^2 c_{ix}^4 c_{iy}^4$ together if the velocities in the all directions are of same magnitude. In order to resolve this problem, we introduced an energy shell with the non-identical magnitude of velocities in each direction. In this case, we introduced 2 BCC with the energies 9/4, 5 and one FCC shell with the energy 5. The weights and velocities are tabulated in Table: 7.2. The detailed expression for equilibrium and the moments will be calculated in the next chapter. This model has the applicability to transonic flows with a very high Ma and can handle the strong thermal variations.

Shells	Discrete Velocities(c_i)	Weight(w_i)
SC - 1	$(\pm1,0,0)\,,(0,\pm1,0)\,,(0,0,\pm1)$	0.0111443971
SC - 2	$(\pm3,0,0)\,,(0,\pm3,0)\,,(0,0,\pm3)$	0.0009925820
SC - 3	$(\pm4,0,0)\,,(0,\pm4,0)\,,(0,0,\pm4)$	0.0004322964
FCC-1	$(\pm1,\pm1,0)\,,(0,\pm1,\pm1)\,,(\pm1,\pm1,0)$	0.0078020595
FCC-2	$(\pm2,\pm2,0)\,,(0,\pm2,\pm2)\,,(\pm2,\pm2,0)$	0.0008848260
FCC-3	$(\pm3,\pm3,0)\,,(0,\pm3,\pm3)\,,(\pm3,\pm3,0)$	6.6974×10^{-6}
BCC-1	$(\pm1,\pm1,\pm1)$	0.0071479427
BCC-2	$(\pm2,\pm2,\pm2)$	0.0000121756
BCC-h	$(\pm1/2,\pm1/2,\pm1/2)$	0.0447801239
BCC-3h	$(\pm3/2,\pm3/2,\pm3/2)$	0.0026467301
BCC-5h	$(\pm5/2,\pm5/2,\pm5/2)$	4.8164×10^{-6}
offdiagonal BCC- h	$(\pm1/2,\pm1,\pm1)\,,\ (\pm1,\pm1/2,\pm1),\ (\pm1,\pm1,\pm1/2)$	0.0103828723
offdiagonal BCC-1	$(\pm2,\pm1,\pm1)\,,\ (\pm1,\pm2,\pm1),\ (\pm1,\pm1,\pm2)$	0.0002149798
offdiagonal FCC	$(\pm2,\pm1,0)\,,(0,\pm2,\pm1)\,,(\pm2,\pm1,0)$	
	$(\pm1,\pm2,0)\,,(0,\pm1,\pm2)\,,(\pm1,\pm2,0)$	0.0041472523

Table 7.2: Energy shells and their corresponding velocities with weights for $RD3Q167$ model.

Chapter 8
Discrete Equilibrium Distribution

8.1 Introduction

In last few decades, the Lattice Boltzmann Model (LBM) has emerged as a powerful tool for hydrodynamics and gaseous microflow simulations (Succi, 2001*a*; Succi *et al.*, 2002*b*; Namburi *et al.*, 2016; Yudistiawan *et al.*, 2010). In the previous chapter, the form of equilibrium distribution function under the constraints of mass, momentum and energy is described. However, the computational simplifications involved are responsible for the loss of many desirable features inherent in microscopic Boltzmann dynamics such as positivity of the equilibrium distribution and finally H-theorem (Karlin *et al.*, 1999; Succi *et al.*, 2002*b*). The absence of discrete time H-theorem results in the growth of numerical instabilities in standard LBM. This makes low viscosity and/or large spatial gradients for hydrodynamics or large density ratios in multiphase flows often unattainable (Karlin *et al.*, 1999; Succi *et al.*, 2002*b*; Chikatamarla *et al.*, 2015).

The Entropic Lattice Boltzmann Model (ELBM) has emerged as an alternative to the conventional LBM by ensuring the positivity of the equilibrium distribution and restoration of the H-theorem for discrete space-time evolution (Karlin *et al.*, 1999; Boghosian *et al.*, 2001; Ansumali *et al.*, 2003; Karlin *et al.*, 1998; Boghosian *et al.*, 2003; Wagner, 1998; Chen & Teixeira, 2000; Succi *et al.*, 2002*b*). This methodology due to its non-linear stability is quite successful in performing hydrodynamic simulations for high Reynolds number flows where gradients are too sharp for standard LBM. Recently, it was also shown that the same non-linear stability of ELBM can also improve the quality of multiphase simulations. However, this methodology introduces extra computational cost at every grid point for evaluating exact equilibrium, which is supposed to be the minimum of H-function and evaluation of the variable path length which ensures discrete time H-theorem. For evaluation of variable path length, which requires solving a non-linear equation at every grid point, numerical optimization procedures have matured to make method computationally attractive. However, for equilibrium computation numerical procedures have not matured. In case of few important lattices such as D3Q27 and D2Q9, we know the exact solution which alleviates the need of numerical minimization procedure for finding equilibrium. For a general lattice, perturbation method for Lagrange multipliers has been proposed for efficient evaluation of the equilibrium. However, the existing methodology of finding perturbative equilibrium is not expected to work efficiently for the case of strong flow characterized by either finite Mach number (Ma) or finite temperature variations (where one writes energy conserving equilibrium). Thus, for higher order LBM one often employs iterative algorithms to find equilibrium.

In this chapter, we provide a hybrid methodology to compute discrete equilibrium in an efficient fashion. The basic idea is to derive the Lagrange multipliers for discrete equilibrium at high precision for a general discrete velocity model and then use this expression in a Newton-like iterative scheme. We provide examples to illustrate that such a method converges in very few iterations. As the number of iterations required is very few, the use of "if" condition branching such as to check convergence can be completely eliminated in numerical implementations. In particular, we observe that for $\mathrm{Ma} < 0.5$ the scheme converges in a single iteration. Thus, even for low Mach number case, the current methodology provides an attractive option for computing discrete equilibrium. For higher order LBM, where Ma can be of order one, present scheme provides a numerically viable extension of LBM.

The chapter is organized as follows: In section 8.2, the ansatzes for the selection of discrete

velocity set and discrete $H-$ function are described. In section 8.3, the general discrete equilibrium distribution derivation into perturbative series of velocity and temperature θ around a reference state is presented and calculated the general expression for some moments. In section 8.4, the efficient hybrid numerical method of deriving equilibrium distribution is presented. Finally, in section 8.6, the application of the numerical solution of equilibrium distribution for different models and the convergence of equilibrium moments are calculated.

8.2 Discrete H-function

Entropic Lattice Boltzmann method is formulated assuming the existence of a convex entropy functional whose minimum defines the discrete equilibrium (Karlin *et al.*, 1999; Ansumali *et al.*, 2003; Chikatamarla *et al.*, 2006*a*) . It was shown by (Karlin *et al.*, 1999) that for recovering Navier-Stokes hydrodynamics the form of H-function is the Boltzmann form. This was later confirmed that other form of entropy does not lead to a correct form of stress tensor (Boghosian *et al.*, 2001). Following these results, one begins with the discrete H-function of the form

$$H = \sum_{i=1}^{N_d} f_i \left(\ln \left(\frac{f_i}{w_i} \right) - 1 \right), \tag{8.1}$$

where the discrete weights w_i are unknown positive numbers such that

$$w_i > 0 \text{ and } \quad \sum_{i=1}^{N_d} w_i = 1. \tag{8.2}$$

Further, w_i are the discrete weights corresponding to the each energy shell of a lattice. Similar to all existing LB models, it is assumed that discrete weights are the function of c_i^2 only. Essentially, this condition sets zero velocity equilibrium to be independent of velocity direction. This condition is motivated from Maxwell-Boltzmann expression at zero velocity and reference temperature θ_0, $f_i^{\text{eq}} = w_i \rho$. Most of the existing models such as D3Q15, D3Q19, and D3Q27 satisfy this constraint.

The symmetry of the discrete velocities also implies that second order moment is an isotropic tensor

$$\sum_{i=1}^{N_d} w_i c_{i\alpha} c_{i\beta} = \theta_0 \delta_{\alpha\beta}. \tag{8.3}$$

These ansatzes reduce the available degree of freedom available in search of discrete velocity models (Yudistiawan *et al.*, 2010). In this thesis, attention is further restricted to discrete velocity models satisfying isotropy constraints on fourth order tensor as

$$\sum_{i=1}^{N_d} w_i c_{i\alpha} c_{i\beta} c_{i\gamma} c_{i\kappa} = A \theta_0^2 \Delta_{\alpha\beta\gamma\kappa}. \tag{8.4}$$

where, the value of A is 7 for Maxwell-Boltzmann distribution. This condition on fourth order moment ensures that the fourth order moments of equilibrium at zero velocity and reference temperature θ_0 is same as that of Maxwell-Boltzmann model. Eqs (8.2)-(8.4) ensures that polynomial form of equilibrium satisfy Maxwell-Boltzmann form on second and fourth moments at finite velocity. Thus, widely used models such as D3Q19 and D3Q27 satisfy these constraints. However, these conditions do not ensure that third order moment of the discrete equilibrium is same as that of Maxwell-Boltzmann. This condition on third moment can be fullfiled only if the

discrete equilibrium distribution is of the form (Chikatamarla & Karlin, 2009).

$$f_i^{\mathrm{eq}} = \tilde{f}_i \left(1 + \frac{u_\alpha c_{i\alpha}}{\theta_0} + \frac{u_\alpha u_\beta}{2\,\theta_0^2} \left(c_{i\alpha} c_{i\beta} - \theta_0 \delta_{\alpha\beta} \right) + \frac{u_\alpha u_\beta u_\gamma c_{i\alpha} c_{i\beta} c_{i\gamma}}{6\,\theta_0^3} \right), \tag{8.5}$$

In case of the entropic lattice Boltzmann method, the series expansion of the true equilibrium at reference temperature θ_0 must reduce to this form. It can be easily verified that in order to get third moment same as Maxwell-Boltzmann, a necessary condition to be imposed on any higher order LB models is an isotropy condition on contracted sixth order moment of the weight as

$$\sum_{i=1}^{N_d} w_i c_i^2 c_{i\alpha} c_{i\beta} c_{i\gamma} c_{i\kappa} = 7\theta_0^3 \Delta_{\alpha\beta\gamma\kappa}. \tag{8.6}$$

In this chapter, the discrete equilibrium for the higher order lattice Boltzmann models satisfying these constraints will be derived using the entropic lattice Boltzmann formulation. Here, we remind that the entropic lattice Boltzmann can be used to derive the energy conserving equilibrium. Thus, we will derive the equilibrium at arbitrary temperature θ.

8.3 Evaluation of Discrete Equilibrium Distribution

In this section, we derive the equilibrium distribution for discrete velocity models satisfying ansatzes described in the previous section. Similar to the continuous kinetic theory, the equilibrium distribution function f_i^{eq} is the minimizer of the H-function (Eq. (8.1)) subjected to the constraints of mass, momentum and energy conservation. The equilibrium distribution obtain as solution of the minimization has Maxwell-Boltzmann form

$$f_i^{\mathrm{eq}} = w_i\, \rho \exp\left[- \left(\alpha + \beta_\kappa c_{i\kappa} + \gamma c_i^2 \right) \right], \tag{8.7}$$

where α, β_κ and γ are the Lagrange multipliers associated with the mass, momentum and energy conservation, respectively. In order to find Lagrange multipliers, one substitutes equilibrium expression in the definition of conserved moments, which are defined as

$$\sum_{i=1}^{N_d} f_i^{\mathrm{eq}} = \rho, \quad \sum_{i=1}^{N_d} f_i^{\mathrm{eq}} c_{i\kappa} = \rho u_\kappa, \quad \sum_{i=1}^{N_d} f_i^{\mathrm{eq}} c_i^2 = E = \rho u^2 + 3\rho\theta. \tag{8.8}$$

In order to do so, the formal expression for the equilibrium is re-written as

$$f_i^{\mathrm{eq}} = w_i \rho A\, \Gamma^{c_i^2/\theta_0}\, B_x^{c_{ix}/\sqrt{\theta_0}}\, B_y^{c_{iy}/\sqrt{\theta_0}}\, B_z^{c_{iz}/\sqrt{\theta_0}}, \tag{8.9}$$

with

$$A = \exp\left(-\alpha\right), \quad B_\kappa = \exp\left(-\beta_\kappa \sqrt{\theta_0} \right), \quad \Gamma = \exp\left(-\gamma\theta_0\right). \tag{8.10}$$

As, for the discrete velocity models under consideration the velocity set is closed under inversion, the constraints in Eq (8.8) can be decomposed as the pair wise sum over opposite velocities (such

as $(c_i, -c_i)$), the moments equations can be re-written as

$$\sum_{i=1}^{N_d} w_i \, \Gamma^{c_i^2/\theta_0} \left(B_x^{c_{ix}/\sqrt{\theta_0}} \, B_y^{c_{iy}/\sqrt{\theta_0}} \, B_z^{c_{iz}/\sqrt{\theta_0}} \right) = \frac{\rho}{A},$$

$$\sum_{i=1}^{N_d/2} w_i \, \Gamma^{c_i^2/\theta_0} \, |c_{i\kappa}| \left(B_x^{c_{ix}/\sqrt{\theta_0}} \, B_y^{c_{iy}/\sqrt{\theta_0}} \, B_z^{c_{iz}/\sqrt{\theta_0}} - B_x^{-c_{ix}/\sqrt{\theta_0}} \, B_y^{-c_{iy}/\sqrt{\theta_0}} \, B_z^{-c_{iz}/\sqrt{\theta_0}} \right) = \frac{\rho u_\kappa}{A}, \quad (8.11)$$

$$\sum_{i=1}^{N_d/2} w_i \, \Gamma^{c_i^2/\theta_0} \, c_i^2 \left(B_x^{c_{ix}/\sqrt{\theta_0}} \, B_y^{c_{iy}/\sqrt{\theta_0}} \, B_z^{c_{iz}/\sqrt{\theta_0}} + B_x^{-c_{ix}/\sqrt{\theta_0}} \, B_y^{-c_{iy}/\sqrt{\theta_0}} \, B_z^{-c_{iz}/\sqrt{\theta_0}} \right) = \frac{E}{A}.$$

These transformed set of equations were earlier used to find exact solution for D3Q27 model of LBM. However, the analytical inversion of Lagrange multiplier in terms of explicit expressions are not possible. For numerical computation, it is possible to build a series expression around a reference solution. At this point, we point out that at the reference state $\theta = \theta_0, u_\kappa = 0$, using Eq.(8.11) the Lagrange multiplier associated with the momentum conservation are known explicitly to be $B_\kappa = 1$ i.e $\beta_\kappa = 0$. Our aim is to build a perturbative solution around this reference state. Typically, this series is written with second order (or in some cases third order) accuracy in Mach number in lattice Boltzmann method. However, in case of entropic lattice Boltzmann model, for every discrete velocity model, one finds the Lagrange multiplier with the high order of accuracy to preserve the positive form of equilibrium (Chikatamarla *et al.*, 2006*a*). This step is also needed for describing higher order thermo-hydrodynamics with discrete velocity models.

In this section, starting from the formal expression for the discrete equilibrium (Eq.8.9), we derive a generic expression for the equilibrium via a perturbative methodology. The detailed step of this perturbative method are

- To build the perturbative series around the reference state, we will expand the Lagrange multipliers in powers of the smallness parameter ϵ (denoting smallness of the Mach number) as

$$\begin{aligned} \alpha &= \alpha^{(0)} + \epsilon\alpha^{(1)} + \epsilon^2\alpha^{(2)} + \cdots, \\ \beta_\kappa &= \beta_\kappa^{(0)} + \epsilon\beta_\kappa^{(1)} + \epsilon^2\beta_\kappa^{(2)} + \cdots, \\ \gamma &= \gamma^{(0)} + \epsilon\gamma^{(1)} + \epsilon^2\gamma^{(2)} + \cdots, \end{aligned} \quad (8.12)$$

  The lowest order contribution, the zero velocity equilibrium distribution function $\tilde{f}_i^{\mathrm{eq}}$ is written as

$$\tilde{f}_i^{\mathrm{eq}} = f_i^{\mathrm{eq}}(\rho, \mathbf{u} = 0, \theta) = w_i \, \rho \exp\left(\alpha^{(0)} + \gamma^{(0)} c_i^2 \right). \quad (8.13)$$

  In this case, the constraints Eq (8.8) simplifies in terms of the departure from the reference temperature $\Delta\theta = (\theta - \theta_0)/\theta_0$ as

$$\sum_i^{N_d} \tilde{f}_i^{\mathrm{eq}} = \rho, \qquad \sum_i^{N_d} \tilde{f}_i^{\mathrm{eq}} c_i^2 = 3\rho\theta = 3\rho\theta_0 (1 + \Delta\theta), \quad (8.14)$$

  It will be convenient to write these constraints in infinite series form using series expansion

of exp as

$$\begin{aligned}\alpha^{(0)}+3\,\gamma^{(0)}\theta_0+\frac{1}{2}\left[\left(\alpha^{(0)}\right)^2+6\alpha^{(0)}\gamma^{(0)}\theta_0+15\,\theta_0^2\left(\gamma^{(0)}\right)^2\right]+\cdots=0,\\ 3\alpha^{(0)}+15\,\gamma^{(0)}\theta_0+\frac{1}{2}\left[3\left(\alpha^{(0)}\right)^2+30\alpha^{(0)}\gamma^{(0)}\theta_0+105\,\theta_0^2(1-m_3)\left(\gamma^{(0)}\right)^2\right]+\cdots=3\Delta\theta,\end{aligned} \tag{8.15}$$

where

$$m_n=1-\frac{\sum_i w_i c_i^{2n}}{\int f^{\mathrm{MB}}\left(\mathbf{u}=0,\theta_0\right)c^{2n}dc}. \tag{8.16}$$

As these constraints are also highly non-linear explicit inversion is not feasible even for this simple case. However, at zero velocity and reference temperature $\theta=\theta_0$ explicit solution is

$$\tilde{f}_i^{\mathrm{eq}}\left(\rho,\mathbf{u}=0,\theta_0\right)=w_i\rho. \tag{8.17}$$

Thus, we can use this reference temperature solution to build a perturbative equilibrium at arbitrary temperature.

- We build a perturbative zero velocity equilibrium by expanding the zero order Lagrange multipliers as a series in terms of $\Delta\theta$ around the reference state as

$$\begin{aligned}\alpha^{(0)}&=\Delta\theta\alpha^{(01)}+\Delta\theta^2\alpha^{(02)}+\cdots,\\ \gamma^{(0)}&=\Delta\theta\gamma^{(01)}+\Delta\theta^2\gamma^{(02)}+\cdots.\end{aligned} \tag{8.18}$$

By comparing the $O\left(\Delta\theta\right)$ terms on the both sides of Eq (8.15) we have;

$$\alpha^{(01)}+\gamma^{(01)}3\theta_0=0,\quad \alpha^{(01)}+5\theta_0\gamma^{(01)}=1. \tag{8.19}$$

Similar, by comparing the $\mathrm{O}\left(\Delta\theta^2\right)$ and $\mathrm{O}\left(\Delta\theta^3\right)$ and so on terms on both sides of Eq (8.15), we can calculate the higher order terms in series of Lagrange multipliers as

$$\begin{aligned}\alpha^{(0)}&=-\Delta\theta\frac{3}{2}+\Delta\theta^2\frac{3}{4}-\Delta\theta^3\frac{1}{2}-\frac{105m_3}{16}\Delta\theta^2+\left(\frac{35m_3}{64}\left(64-105m_3\right)-\frac{315m_4}{32}\right)\Delta\theta^3+\cdots,\\ \gamma^{(0)}&=\frac{1}{2\theta_0}\left(\Delta\theta-\Delta\theta^2+\Delta\theta^3\right)+\frac{1}{\theta_0}\left(\frac{35m_3}{16}\Delta\theta^2+\left(\frac{35m_3}{64}(-24+35m_3)+\frac{105m_4}{32}\right)\Delta\theta^3\right)\cdots.\end{aligned} \tag{8.20}$$

It is noteworthy that in the limit when $m_3=m_4=0$, the series converges to

$$\alpha^{(0)}=-\frac{3}{2}\log\left(1+\Delta\theta\right)\qquad\gamma^{(0)}=\frac{\Delta\theta}{2\theta} \tag{8.21}$$

The distribution function obtained with these Lagrange multipliers in this limiting case is same as the Maxwell-Boltzmann distribution function with the zero velocity condition.

Finally, using these expressions for Lagrange multipliers, the equilibrium function with zero velocity at finite temperature θ is;

$$\tilde{f}_i = w_i\rho\Bigg[1 + \frac{\Delta\theta}{2}\left(\frac{c_i^2}{\theta_0} - 3\right) + \frac{\Delta^2\theta}{8}\left(\frac{c_i^4}{\theta_0^2} - 10\frac{c_i^2}{\theta_0} + 15\right) + \frac{\Delta^3\theta}{48}\left(\frac{c_i^6}{\theta_0^3} + 21\frac{c_i^4}{\theta_0^2} + 105\frac{c_i^2}{\theta_0} - 105\right) + \frac{\Delta^4\theta}{384}\left(\frac{c_i^8}{\theta_0^4} - 36\frac{c_i^6}{\theta_0^3} + 378\frac{c_i^4}{\theta_0^2} - 1260\frac{c_i^2}{\theta_0} + 945\right) + A_i + B_i\Bigg]. \tag{8.22}$$

Where,

$$\begin{aligned}
A_i = {} & \frac{35m_3}{16}\Delta^2\theta\left(\frac{c_i^2}{\theta_0} - 3\right) + \frac{105\Delta^3\theta}{192}\left(2m_3\frac{c_i^4}{\theta_0^2} + \frac{c_i^2}{\theta_0}\left(35m_3^2 - 36m_3\right) - \left(105m_3^2 - 82m_3\right)\right) \\
& + \frac{\Delta^4\theta}{384}\Bigg(\frac{c_i^6}{\theta_0^3}105m_3 + \frac{c_i^4}{\theta_0^2}\left(-3885m_3 + \frac{18375}{4}m_3^2\right) \\
& + \frac{c_i^2}{\theta_0}\left(36330m_3 - \frac{238875}{2}m_3^2 + \frac{643125}{8}m_3^3 + \frac{55125}{2}m_3m_4\right) \\
& + \left(-65520m_3 + \frac{1201725}{4}m_3^2 - \frac{1929375}{8}m_3^3 - \frac{165375}{2}m_3m_4\right)\Bigg), \\
B_i = {} & \frac{105\Delta^3\theta}{192}\left(\frac{c_i^2}{\theta_0}\left(6m_4\right) - \left(18m_4\right)\right) + \frac{\Delta^4\theta}{384}\Bigg(\frac{c_i^4}{\theta_0^2}\left(630m_4\right) + \frac{c_i^2}{\theta_0}\left(-\frac{24885}{2}m_4 + \frac{3465}{2}m_5\right) \\
& + \left(\frac{57645}{2}m_4 - \frac{10395}{2}m_5\right)\Bigg).
\end{aligned} \tag{8.23}$$

From the expressions it is clear that, if the 6th order moment error term m_3 is zero, many of the error terms in $\tilde{f}_i$ disappear.

In order to make the expression exact till $\mathrm{O}(\Delta^2\theta)$, the error term m_3 has to be zero. Similarly for the error in $\mathrm{O}(\Delta^3\theta)$ to be zero, m_4 also should go to zero. If all m_3, m_4 and m_5 are zero, we can achieve the exact equilibrium for the zero velocity model to the $\mathrm{O}(\Delta^4\theta)$.

- The equilibrium distribution at the finite velocity can now be derived by using the perturbative series expansion of the Lagrange multipliers around the zero velocity equilibrium. The series can be written as;

$$\begin{aligned}
f^{\mathrm{eq}} = {} & \tilde{f}_i^{\mathrm{eq}}\Bigg\{1 + \epsilon\left[\alpha^{(1)} + \beta_\kappa^{(1)}c_{i\kappa} + \gamma^{(1)}c_i^2\right] \\
& + \epsilon^2\left[\frac{1}{2}\left(\alpha^{(1)} + \beta_\kappa^{(1)}c_{i\kappa} + \gamma^{(1)}c_i^2\right)^2 + \alpha^{(2)} + \beta_\kappa^{(2)}c_{i\kappa} + \gamma^{(2)}c_i^2\right] \\
& + \epsilon^3\Bigg[\frac{1}{6}\left(\alpha^{(1)} + \beta_\kappa^{(1)}c_{i\kappa} + \gamma^{(1)}c_i^2\right)^3 + \left(\alpha^{(2)} + \beta_\kappa^{(2)}c_{i\kappa} + \gamma^{(2)}c_i^2\right)\left(\alpha^{(1)} + \beta_\kappa^{(1)}c_{i\kappa} + \gamma^{(1)}c_i^2\right) \\
& + \alpha^{(3)} + \beta_\kappa^{(3)}c_{i\kappa} + \gamma^{(3)}c_i^2\Bigg].
\end{aligned} \tag{8.24}$$

and the moments has the form,

$$\sum_{i=1}^{N_d} f_i = \rho, \qquad \sum_{i=1}^{N_d} f_i c_{i\alpha} = j_\alpha, \qquad \sum_{i=1}^{N_d} f_i c_i^2 = E = \rho u^2 + 3\rho\theta, \tag{8.25}$$

Now using this equation in the moment equations Eq.(8.25) and comparing the $\mathrm{O}(\epsilon)$ on both sides of the equations we get,

$$\alpha^{(1)} = 0, \qquad \beta_\kappa^{(1)}\theta = \frac{u_\kappa}{\theta}, \qquad \gamma^{(1)} = 0. \tag{8.26}$$

Similarly by comparing the $\mathrm{O}\left(\epsilon^2\right)$ and $\mathrm{O}\left(\epsilon^3\right)$ terms, we get the series of Lagrange multipliers as;

$$\begin{aligned}
\alpha &= -\epsilon^2 \frac{u^2}{2\theta}\left[\frac{1}{1+5/2M_2}\right] + O(\epsilon^4 u^4) + \cdots, \\
\beta_\kappa &= \frac{\epsilon u_\kappa}{\theta} - \epsilon^3 \frac{u^2 u_\kappa}{6\theta^2}\left[3\left(1-M_2'\right) + 5\left(M_2' - M_2\right)\right] - \frac{u_\kappa}{\theta}\left[\alpha^{(2)} + \gamma^{(2)} 5\theta\left(1-M_2\right)\right] + O(\epsilon^5 u^5) + \cdots, \\
\gamma &= -\epsilon^2 \frac{u^2}{6\theta^2}\left[1 - \frac{1}{1+5/2M_2}\right] + O(\epsilon^4 u^4) + \cdots.
\end{aligned} \tag{8.27}$$

where,

$$\begin{aligned}
M_2 &= \frac{\sum_{i=1}^{N_d} \tilde{f}_i c_i^4 - 15\rho\theta^2}{15\rho\theta^2}, \\
M_2' &= \frac{\rho\theta^2 - \sum_{i=1}^{N_d} \tilde{f}_i c_{ix}^2 c_{iy}^2}{\rho\theta^2}.
\end{aligned} \tag{8.28}$$

Finally, the equilibrium distribution till the $\mathrm{O}\left(u^3\right)$ is;

$$\begin{aligned}
f_i^{\mathrm{eq}} = \tilde{f}_i \Bigg\{ & 1 + \frac{u_\alpha c_{i\alpha}}{\theta} - \frac{u^2}{2\theta}\left(\frac{1}{1+5/2\,M_2}\right) - \frac{u^2 c_i^2}{6\theta^2}\left(1 - \frac{1}{1+5/2\,M_2}\right) + \frac{1}{2}\left(\frac{u_\alpha c_{i\alpha}}{\theta}\right)^2 \\
& + \frac{1}{6}\left(\frac{u_\alpha c_{i\alpha}}{\theta}\right)^3 + \frac{u^2 u_\alpha c_{i\alpha}}{6\theta^2} A_4 - \frac{u^2 c_i^2 u_\alpha c_{i\alpha}}{6\theta^3} \frac{5/2M_2}{1+5/2M_2} \Bigg\},
\end{aligned} \tag{8.29}$$

where

$$A_4 = \left[\frac{5/2M_2}{1+5/2M_2}\left(5\left(1-M_2\right)\right) - \left(3 + M_2' - 5M_2\right)\right]. \tag{8.30}$$

If M_2 and M_2' are zero, we will be able to get the exact thermal equilibrium till the $\mathrm{O}(u^3)$.

8.3.1 Equilibrium Moments

From the knowledge of equilibrium distribution calculated in the previous section, we can calculate the model dependent quantities such as moments of the distribution function. In this section, we will calculate second, third and contracted fourth order moments.

Stress tensor : Using the equation Eq.(8.59) and calculating the equilibrium value of Pressure tensor $P_{\alpha\beta} = \sum_{i=1}^{N_d} f_i^{\text{eq}} c_{i\alpha} c_{i\beta}$ we get;

$$P_{\alpha\beta} = \rho\theta\delta_{\alpha\beta} + \rho u_\alpha u_\beta \left(1 - M_2'\right) + \frac{u^2}{2}\delta_{\alpha\beta}\left[1 + 4M_2' - 5M_2 - \frac{1}{1+\frac{5}{2}M_2}\left(1 + \frac{25}{6}M_2 - \frac{25}{6}M_2^2\right)\right]. \tag{8.31}$$

where as, it goes to $\rho\theta\delta_{\alpha\beta} + \rho u_\alpha u_\beta$ when $M_2, M_2' \to 0$.

3rd order moment: The equilibrium value of heat flux $q_\alpha = \sum_{i=1}^{N_d} f_i^{\text{eq}} c_{i\alpha} c_i^2$ calculated using the equation Eq. (8.59) is,

$$\begin{aligned} q_\alpha = {} & 5\theta u_\alpha \left(1 - M_2\right) + \frac{1}{6}u^2 u_\alpha \Bigg[5A_4\left(1 - M_2\right) - 7\left(1 - \frac{1}{1+\frac{5}{2}M_2}\right)\left(1 - M_3\right) \\ & + 7\left(3 + 2M_3' - 5M_3\right)\Bigg] \end{aligned} \tag{8.32}$$

contracted fourth order moment: The equilibrium value of contracted fourth order tensor $R_{\alpha\beta} = \sum_{i=1}^{N_d} f_i^{\text{eq}} c_i^2 c_{i\alpha} c_{i\beta}$ can be calculated using the equilibrium distribution in Eq. (8.59) is,

$$\begin{aligned} R_{\alpha\beta} = {} & 5\theta^2\delta_{\alpha\beta}\left(1 - M_3\right) - \frac{5u^2\theta}{2}\delta_{\alpha\beta}\frac{1}{1+\frac{5}{2}M_2} - \frac{35u^2\theta}{6}\delta_{\alpha\beta}\left(1 - \frac{1}{1+\frac{5}{2}M_2}\right) \\ & + \frac{7u^2\theta}{2}\delta_{\alpha\beta}\left(1 + 4M_3' - 5M_3\right) + 7u_\alpha u_\beta\theta\left(1 - M_3'\right) \end{aligned} \tag{8.33}$$

where

$$\begin{aligned} M_3 = & \frac{\sum_i^{N_d} \tilde{f}_i^{\text{eq}} c_i^6 - 105\rho\theta^3}{105\theta^3}, \\ M_3' = & 1 - \frac{\sum_i \tilde{f}_i c_i^2 c_x^2 c_y^2}{7\rho\theta^3}. \end{aligned} \tag{8.34}$$

If we consider a model with the discrete velocity set satisfying the condition of $\sum_i w_i c_i^6 = 105\theta_0^3$, then the error term $m_3 = 0$. However, using the isotropy condition on weight Eq (8.6) reduces the error terms of the hydrodynamic variables in lower order discrete velocity models.

8.4 Iterative numerical method for equilibrium distribution

As discussed in the previous section, we will start with the form f^{eq} defined in Eq.(8.7) and find the exact solution of f^{eq} using the iterative method.

Firstly, using the mass conservation constraint $\sum_{i=1}^{N_d} f_i = \rho$,

$$\rho = \sum_{i=1}^{N_d} \rho\ w_i\ e^{(\alpha + \beta_j c_{ij} + \gamma c_i^2)}. \tag{8.35}$$

Therefore, eliminating the Lagrange multiplier α using the above equation we get,

$$f_i^{eq} = \frac{\rho\ w_i\ e^{(\beta_j c_{ij} + \gamma c_i^2)}}{\sum_{i=1}^{N_d} w_i\ e^{(\beta_j c_{ij} + \gamma c_i^2)}}. \tag{8.36}$$

The form of f_i^{eq} given in Eq. (8.36) satisfies the mass conservation constraint.
Now, imposing the energy conservation constraint $E = \rho u^2 + 3\rho\theta = \sum_{i=1}^{N_d} f_i c_i^2$,

$$\sum_{i=1}^{N_d} w_i e^{(\beta_j c_{ij} + \gamma c_i^2)}(c_i^2 - (u^2 + 3\theta)) = 0, \tag{8.37}$$

and imposing the momentum conservation constraint $\sum_{i=1}^{N_d} f^{eq} c_{ik} = \rho u_k$,

$$\sum_{i=1}^{N_d} w_i e^{(\beta_j c_{ij} + \gamma c_i^2)}(c_{ik} - u_k) = 0. \tag{8.38}$$

If the values of the Lagrange multipliers are taken as lower order approximations from power series expansion of equation Eq. (8.36), there will be a correction required to exactly satisfy the conservation conditions. Then, each of the Lagrange multipliers can be rewritten as;

$$\beta_j = \beta_j^{(0)} + \eta\beta_j, \quad \gamma = \gamma^{(0)} + \eta\gamma, \tag{8.39}$$

where the superscript 0 denotes a lower order approximation of the Lagrange multipliers and η is the smallness parameter. Substituting Eq. (8.39) in Eq 8.36 gives,

$$f_i^{\text{eq}} = \frac{\rho\tilde{f}_i\left(1 + \eta\beta_m c_{im} + \eta\gamma c_i^2\right)}{\tilde{\rho} + \eta\beta_m\tilde{j}_m + \eta\gamma\tilde{e}}, \tag{8.40}$$

where,

$$\begin{aligned} \tilde{f}_i &= w_i e^{(\beta_m^{(0)} c_{im} + \gamma^{(0)} c_i^2)}, \\ \tilde{\rho} &= \sum_i \tilde{f}_i, \quad \tilde{j}_m = \sum_i \tilde{f}_i c_{im}, \quad \tilde{e} = \sum_i \tilde{f}_i c_i^2. \end{aligned} \tag{8.41}$$

Substituting Eq. (8.39) in Eq. (8.37) and writing the series expansion of the exponential function up to the first order, we get,

$$\sum_{i=1}^{N_d} w_i(c_i^2 - (u^2 + 3\theta)) e^{(\beta_j^{(0)} c_{ij} + \gamma^{(0)} c_i^2)}(1 + \eta\beta_j c_{ij} + \eta\gamma c_i^2) = 0. \tag{8.42}$$

Similarly, substituting Eq. (8.39) in Eq. (8.38) and expanding the exponential gives;

$$\sum_{i=1}^{N_d} w_i(c_{ik} - u_k) e^{(\beta_j^{(0)} c_{ij} + \gamma^{(0)} c_i^2)}(1 + \eta\beta_j c_{ij} + \eta\gamma c_i^2) = 0. \tag{8.43}$$

For simplification, let us define the moments as;

$$
\begin{aligned}
\rho_T &= \sum_{i=1}^{N_d} w_i e^{(\beta_j^{(0)} c_{ij} + \gamma^{(0)} c_i^2)} \\
v_k &= \sum_{i=1}^{N_d} w_i c_{ik} e^{(\beta_j^{(0)} c_{ij} + \gamma^{(0)} c_i^2)} \\
m_{kj} &= \sum_{i=1}^{N_d} w_i c_{ik} c_{ij} e^{(\beta_j^{(0)} c_{ij} + \gamma^{(0)} c_i^2)} \\
q_k &= \sum_{i=1}^{N_d} w_i c_{ik} c_i^2 e^{(\beta_j^{(0)} c_{ij} + \gamma^{(0)} c_i^2)} \\
r &= \sum_{i=1}^{N_d} w_i c_i^2 c_i^2 e^{(\beta_j^{(0)} c_{ij} + \gamma^{(0)} c_i^2)}
\end{aligned}
\tag{8.44}
$$

Expanding equations (8.42) to (8.43) and using the definitions from equation set (8.44), we obtain the following equations,

$$u_k \rho_T - v_k = (m_{kj} - u_k v_j) \cdot \eta\beta_j + (q_k - u_k m_{jj}) \cdot \eta\gamma, \tag{8.45}$$

$$E\rho_T - m_{jj} = (q_j - E v_j) \cdot \eta\beta_j + (r - E m_{jj}) \cdot \eta\gamma. \tag{8.46}$$

Equations (8.45) and (8.46) together constitute a 4 by 4 system of linear equations which can be solved by any of the available direct or iterative linear system solvers. By substituting the values of $\eta\beta_m$ and $\eta\gamma$ in Eq (8.40), we get the exact solution of f_i^{eq}.

The $\beta_m^{(0)}$ and $\gamma^{(0)}$ are the guess values, which can be taken from the series expansion of equilibrium solution. Once these guess values are known, the procedure is model independent.

8.5 Discrete velocity models

In this section, we will demonstrate the efficiency of the present numerical solution of f_i^{eq} by considering the examples of RD3Q27, RD3Q41, RD3Q67, and RD3Q167 velocity models.

In this section, we will calculate the discrete populations f_i^{eq} at variable Ma and evaluate the moments such as P_{xy}^{eq}, P_{xx}^{eq}, q_x and R and compared with the exact equilibrium solution (completely converged values) at different number of iterations. It is clear that the solution to the discrete populations f_i^{eq} converges in two to three iterations.

8.5.1 RD3Q27 model

One of the widely used models in LBM is the 27 velocity model. In this section, we consider the model with 27 velocities on the BCC grid structure. This model is proved to be efficient than the normal D3Q27 model on the SC grid structure. The detailed, description of this model is given in (Namburi *et al.*, 2016).

The set of discrete velocities and corresponding weights are listed in Table 8.1. For the D3Q27 lattice, the reference temperature is $\theta_0 = 1/5$.

Using the above weights, it is clear that the error term m_3 for this model is $1/6$ and $m_4 = 0.35515$. Using these values, the equations for $\tilde{f}_i^{\text{eq}}$, f_i^{eq} and the equilibrium moments become as

Shells	Discrete Velocities(c_i)	Weight(w_i)
SC	$(\pm1,0,0)\,,(0,\pm1,0)\,,(0,0,\pm1)$	$\frac{1}{30}$
FCC	$(\pm1,\pm1,0)\,,(0,\pm1,\pm1)\,,(\pm1,\pm1,0)\,,$	$\frac{1}{300}$
BCC	$\left(\pm\frac{1}{2},\pm\frac{1}{2},\pm\frac{1}{2}\right)$	$\frac{4}{75}$

Table 8.1: Energy shells and their corresponding velocities with weights for RD3Q27.

follows, The equilibrium function with zero velocity at finite temperature θ is;

$$\begin{aligned}\tilde{f}_i = w_i\rho\Bigg[1 &+ \frac{\Delta\theta}{2}\left(\frac{c_i^2}{\theta_0}-3\right)+\frac{\Delta\theta^2}{8}\left(\frac{c_i^4}{\theta_0^2}-\left(10-\frac{35m_3}{2}\right)\frac{c_i^2}{\theta_0}+\left(15-\frac{105m_3}{2}\right)\right)\\ &+\frac{\Delta\theta^3}{48}\Bigg(\frac{c_i^6}{\theta_0^3}+\frac{21}{2}\frac{c_i^4}{\theta_0^2}(5m_3-2)+\frac{105}{4}\frac{c_i^2}{\theta_0}\left(35m_3^2-36m_3+6m_4+4\right)\\ &-\frac{105}{4}\left(105m_3^2-82m_3+18m_4+4\right)\Bigg)\Bigg].\end{aligned} \tag{8.47}$$

where as, for this model $m_3 = 1/6$ and $m_4 = 0.35515$.

The equilibrium function with finite velocity and finite temperature is;

$$\begin{aligned}f_i^{\mathrm{eq}} =&\tilde{f}_i\Bigg\{1+\frac{u_\alpha c_{i\alpha}}{\theta}-\frac{u^2}{2\theta}\left(\frac{1}{1+5/2\,M_2}\right)-\frac{u^2c_i^2}{6\theta^2}\left(1-\frac{1}{1+5/2\,M_2}\right)+\frac{1}{2}\left(\frac{u_\alpha c_{i\alpha}}{\theta}\right)^2\\ &+\frac{1}{6}\left(\frac{u_\alpha c_{i\alpha}}{\theta}\right)^3+\frac{u^2u_\alpha c_{i\alpha}}{6\theta^2}A_4-\frac{u^2c_i^2u_\alpha c_{i\alpha}}{6\theta^3}\frac{5/2M_2}{1+5/2M_2}\Bigg\},\\ A_4 =&\left[\frac{5/2M_2}{1+5/2M_2}\left(5\left(1-M_2\right)\right)-\left(3+M_2'-5M_2\right)\right]\end{aligned} \tag{8.48}$$

$$\begin{aligned}M_2 &= 3.1467\Delta\theta\left(\Delta\theta^2-1.45655\Delta\theta-2.78069\right),\\ M_2' &= 0.491898\Delta\theta\left(\Delta\theta^2-0.0917647\Delta\theta-1.18588\right).\end{aligned} \tag{8.49}$$

$$P_{\alpha\beta} = \rho\theta\delta_{\alpha\beta}+\rho u_\alpha u_\beta\left(1-M_2'\right)+\frac{u^2}{2}\delta_{\alpha\beta}\left[1+4M_2'-5M_2-\frac{1}{1+\frac{5}{2}M_2}\left(1+\frac{25}{6}M_2-\frac{25}{6}M_2^2\right)\right]. \tag{8.50}$$

Since the constraints used in this model are till all 4th order and one of the 6th order on weights, the error in the second order moment is of $\mathrm{O}(U^2,\Delta\theta)$.

$$\begin{aligned}R_{\alpha\beta} = 5\theta^2\delta\alpha\beta\left(1-M_3\right)&-\frac{5u^2\theta}{2}\delta_{\alpha\beta}\frac{1}{1+\frac{5}{2}M_2}-\frac{35u^2\theta}{6}\delta_{\alpha\beta}\left(1-\frac{1}{1+\frac{5}{2}M_2}\right)\\ &+\frac{7u^2\theta}{2}\delta_{\alpha\beta}\left(1+4M_3'-5M_3\right)+7u_\alpha u_\beta\theta\left(1-M_3'\right)\end{aligned} \tag{8.51}$$

It was shown in (Namburi *et al.*, 2016) that this model can be used efficiently for low mach isothermal flows. This is also evident from the fact that at $\theta = \theta_0$, moments follow Maxwell-

Boltzmann results closely,

$$\begin{aligned} P_{\alpha\beta} &= \rho\theta_0\delta_{\alpha\beta} + \rho u_\alpha u_\beta. \\ q_\alpha &= 5\theta_0 u_\alpha + u^2 u_\alpha, \\ R_{\alpha\beta} &= 5\theta_0^2\delta\alpha\beta - \frac{5u^2\theta_0}{2}\delta_{\alpha\beta} + \frac{7u^2\theta_0}{2}\delta_{\alpha\beta} + 7u_\alpha u_\beta\theta_0 \end{aligned} \tag{8.52}$$

8.5.2 RD3Q41 model

In this model, in addition to the constraints defined in 27 model, we have taken the constraints on 6th order and one of the 8th order isotropy of moments on weights to increase the validity in mach number and the number of energy shells are increased to 5 from 3.

Shells	Discrete Velocities(c_i)	Weight(w_i)
SC - 1	$(\pm1,0,0)\,,(0,\pm1,0)\,,(0,0,\pm1)$	0.04743040745116578
SC - 2	$(\pm2,0,0)\,,(0,\pm2,0)\,,(0,0,\pm2)$	0.00165687664501576
FCC-1	$(\pm1,\pm1,0)\,,(0,\pm1,\pm1)\,,(\pm1,\pm1,0)$	0.00651175327832464
BCC-1	$(\pm1/2,\pm1/2,\pm1/2)$	0.04917980624482672
BCC-2	$(\pm1,\pm1,\pm1)$	0.00454087801154440

Table 8.2: Energy shells and their corresponding velocities with weights

The equilibrium function with zero velocity at finite temperature θ is;

$$\tilde{f}_i = w_i\rho\left[1 + \frac{\Delta\theta}{2}\left(\frac{c_i^2}{\theta_0} - 3\right) + \frac{\Delta\theta^2}{8}\left(\frac{c_i^4}{\theta_0^2} - 10\frac{c_i^2}{\theta_0} + 15\right) + \frac{\Delta\theta^3}{48}\left(\frac{c_i^6}{\theta_0^3} - 21\frac{c_i^4}{\theta_0^2} + 105\frac{c_i^2}{\theta_0} - 105\right)\right]. \tag{8.53}$$

In this model, the equilibrium expression at zero velocity is exact till the $O(\Delta^3\theta)$.

The equilibrium function with finite velocity and finite temperature is;

$$\begin{aligned} f_i^{\mathrm{eq}} =& \tilde{f}_i\Bigg\{1 + \frac{u_\alpha c_{i\alpha}}{\theta} - \frac{u^2}{2\theta}\left(\frac{1}{1+5/2\,M_2}\right) - \frac{u^2c_i^2}{6\theta^2}\left(1 - \frac{1}{1+5/2\,M_2}\right) + \frac{1}{2}\left(\frac{u_\alpha c_{i\alpha}}{\theta}\right)^2 \\ &+ \frac{1}{6}\left(\frac{u_\alpha c_{i\alpha}}{\theta}\right)^3 + \frac{u^2u_\alpha c_{i\alpha}}{6\theta^2}A_4 - \frac{u^2c_i^2u_\alpha c_{i\alpha}}{6\theta^3}\frac{5/2M_2}{1+5/2M_2}\Bigg\}, \\ A_4 =& \left[\frac{5/2M_2}{1+5/2M_2}\left(5\left(1-M_2\right)\right) - \left(3 + M_2' - 5M_2\right)\right] \end{aligned} \tag{8.54}$$

The error terms with respect to zero velocity equilibrium moments are,

$$\begin{aligned}
M_2 &= -0.807953\Delta^3\theta\left(\frac{\theta_0}{\theta}\right)^2, \quad M_2' = -\left[0.520459\Delta^2\theta + 1.41017\Delta^3\theta\right]\left(\frac{\theta_0}{\theta}\right)^2, \\
M_3 &= -\left[0.69253\Delta^2\theta - 2.49925\Delta^2\theta\right]\left(\frac{\theta_0}{\theta}\right)^3, \\
M_3' &= -3.18168\left(\frac{\theta_0}{\theta}\right)^3\left(0.0934743\Delta\theta + 0.636954\Delta^2\theta + \Delta^3\theta\right).
\end{aligned} \tag{8.55}$$

The equilibrium moments for this model becomes,

$$\begin{aligned}
P_{\alpha\beta} &= \rho\theta\delta_{\alpha\beta} + \rho u_\alpha u_\beta\left(1 - M_2'\right) + \frac{u^2}{2}\delta_{\alpha\beta}\left[1 + 4M_2' - 5M_2 - \frac{1}{1+\frac{5}{2}M_2}\left(1 + \frac{25}{6}M_2 - \frac{25}{6}M_2^2\right)\right], \\
q_\alpha &= 5\theta u_\alpha\left(1 - M_2\right) + \frac{1}{6}u^2u_\alpha\left[5A_4\left(1 - M_2\right) - 7\left(1 - \frac{1}{1+\frac{5}{2}M_2}\right)\left(1 - M_3\right) + 7\left(3 + 2M_3' - 5M_3\right)\right], \\
R_{\alpha\beta} &= 5\theta^2\delta\alpha\beta\left(1 - M_3\right) - \frac{5u^2\theta}{2}\delta_{\alpha\beta}\frac{1}{1+\frac{5}{2}M_2} - \frac{35u^2\theta}{6}\delta_{\alpha\beta}\left(1 - \frac{1}{1+\frac{5}{2}M_2}\right) \\
&\quad + \frac{7u^2\theta}{2}\delta_{\alpha\beta}\left(1 + 4M_3' - 5M_3\right) + 7u_\alpha u_\beta\theta\left(1 - M_3'\right)
\end{aligned} \tag{8.56}$$

From the expressions above, it is clear that $P_{\alpha\beta}$ has $\mathrm{O}(u^2\Delta^2\theta)$ error, heat flux q_α has $\mathrm{O}(u\Delta^3\theta)$ error and $R_{\alpha\beta}$ has $\mathrm{O}(\Delta^2\theta)$ error.

It is clear that, in the isothermal thermal of $\theta = \theta_0$, the moments reduce to the Maxwell-Boltzmann limit.

$$\begin{aligned}
P_{\alpha\beta} &= \rho\theta_0\delta_{\alpha\beta} + \rho u_\alpha u_\beta, \\
q_\alpha &= 5\theta_0 u_\alpha + u^2 u_\alpha, \\
R_{\alpha\beta} &= 5\theta_0^2\delta\alpha\beta - \frac{5u^2\theta_0}{2}\delta_{\alpha\beta} + \frac{7u^2\theta_0}{2}\delta_{\alpha\beta} + 7u_\alpha u_\beta\theta_0.
\end{aligned} \tag{8.57}$$

8.5.3 RD3Q67 model

In order to extend the applicability of the model to the compressible flows with the thermal effects, we have imposed some of the 6th and eighth order constraints. The detailed derivation of weights has been discussed in the previous chapter.

Since we have applied all the constraints of 6th and 8th order on weights, $m_3 = m_4 = 0$ for this model. The equilibrium function with zero velocity at finite temperature θ is;

$$\tilde{f}_i = w_i\rho\left[1 + \frac{\Delta\theta}{2}\left(\frac{c_i^2}{\theta_0} - 3\right) + \frac{\Delta\theta^2}{8}\left(\frac{c_i^4}{\theta_0^2} - 10\frac{c_i^2}{\theta_0} + 15\right) + \frac{\Delta\theta^3}{48}\left(\frac{c_i^6}{\theta_0^3} - 21\frac{c_i^4}{\theta_0^2} + 105\frac{c_i^2}{\theta_0} - 105\right)\right]. \tag{8.58}$$

In this model also, we are able to achieve the equilibrium at zero velocity to be exact till $\mathrm{O}(\Delta^3\theta)$.

The equilibrium function with finite velocity and finite temperature is;

$$\begin{aligned} f_i^{\mathrm{eq}} =& \tilde{f}_i \Bigg\{ 1 + \frac{u_\alpha c_{i\alpha}}{\theta} - \frac{u^2}{2\theta} + \frac{1}{2}\left(\frac{u_\alpha c_{i\alpha}}{\theta}\right)^2 + \frac{1}{6}\left(\frac{u_\alpha c_{i\alpha}}{\theta}\right)^3 + \frac{u^2 u_\alpha c_{i\alpha}}{6\theta^2} A_4 \Bigg\}, \\ & A_4 = \left[-\left(3 + M_2'\right) \right], \qquad M2' = -0.256748 \Delta^3 \theta \left(\frac{\theta_0}{\theta}\right)^2 \end{aligned} \tag{8.59}$$

The equilibrium moments for this model are,

$$\begin{aligned} P_{\alpha\beta} &= \rho\theta\delta_{\alpha\beta} + \rho u_\alpha u_\beta \left(1 - M_2'\right) + \frac{u^2}{2}\delta_{\alpha\beta}\left(4M_2'\right), \\ q_\alpha &= 5\theta u_\alpha + u^2 u_\alpha + \frac{1}{6}u^2 u_\alpha \left[-5M_2' + 7\left(2M_3' - 5M_3\right)\right], \\ R_{\alpha\beta} &= 5\theta^2 \delta\alpha\beta \left(1 - M_3\right) - \frac{5u^2\theta}{2}\delta_{\alpha\beta} + \frac{7u^2\theta}{2}\delta_{\alpha\beta}\left(1 + 4M_3' - 5M_3\right) + 7u_\alpha u_\beta \theta \left(1 - M_3'\right), \end{aligned} \tag{8.60}$$

where ,

$$M_3 = 48.4093\Delta^3\theta, \quad M_3' = 1.54049\Delta^2\theta + 8.40758\Delta^3\theta. \tag{8.61}$$

From the expressions above, it is clear that $P_{\alpha\beta}$ has $\mathrm{O}(u^2\Delta^3\theta)$ error, heat flux q_α has $\mathrm{O}(u^3\Delta^3\theta)$ error and $R_{\alpha\beta}$ has $\mathrm{O}(\Delta^3\theta)$ error.

8.5.4 RD3Q167 model

For extending the applicability of the model to high Ma compressible flows with thermal effects, we have applied the 10th order constraints on weights. The weights and corresponding discrete velocity sets are tabulated in the previous chapter.

The values of m_3, m_4 and m_5 for this model are zero. In this model, we are able to reach the exact expression for equilibrium distribution at zero velocity even with the $\mathrm{O}(\Delta^4\theta)$ terms included. By using this values of m_{2n} and calculating the equilibrium distribution at zero velocity and finite temperature θ we get;

$$\begin{aligned} \tilde{f}_i = w_i \rho \Bigg[& 1 + \frac{\Delta\theta}{2}\left(\frac{c_i^2}{\theta_0} - 3\right) + \frac{\Delta\theta^2}{8}\left(\frac{c_i^4}{\theta_0^2} - 10\frac{c_i^2}{\theta_0} + 15\right) + \frac{\Delta\theta^3}{48}\left(\frac{c_i^6}{\theta_0^3} - 21\frac{c_i^4}{\theta_0^2} + 105\frac{c_i^2}{\theta_0} - 105\right) \\ & + \frac{\Delta\theta^4}{384}\left(\frac{c_i^8}{\theta_0^4} - 36\frac{c_i^6}{\theta_0^3} + 378\frac{c_i^4}{\theta_0^2} - 1260\frac{c_i^2}{\theta_0} + 945\right)\Bigg]. \end{aligned} \tag{8.62}$$

From the above expression we can see that $M_2 = M_2' = M_3 = 0$. However, M_3' has the error $O(\Delta^3\theta)$.

Now, the equilibrium function with finite velocity and finite temperature becomes;

$$\begin{aligned} f_i^{\mathrm{eq}} =& \tilde{f}_i \Bigg\{ 1 + \frac{u_\alpha c_{i\alpha}}{\theta} - \frac{u^2}{2\theta} + \frac{1}{2}\left(\frac{u_\alpha c_{i\alpha}}{\theta}\right)^2 + \frac{1}{6}\left(\frac{u_\alpha c_{i\alpha}}{\theta}\right)^3 - \frac{u^2 u_\alpha c_{i\alpha}}{2\theta^2} \\ & + \frac{1}{24}\left(\frac{u_\alpha c_{i\alpha}}{\theta}\right)^4 - \frac{1}{4}\left(\frac{u_\alpha c_{i\alpha}}{\theta}\right)^2 \frac{u^2}{\theta} + \left(\frac{u^2}{\theta}\right)^2 \left(\frac{1}{8} + \frac{7}{24}M_3' - \frac{7}{72}M_3'\frac{c_i^2}{\theta}\right)\Bigg\}. \end{aligned} \tag{8.63}$$

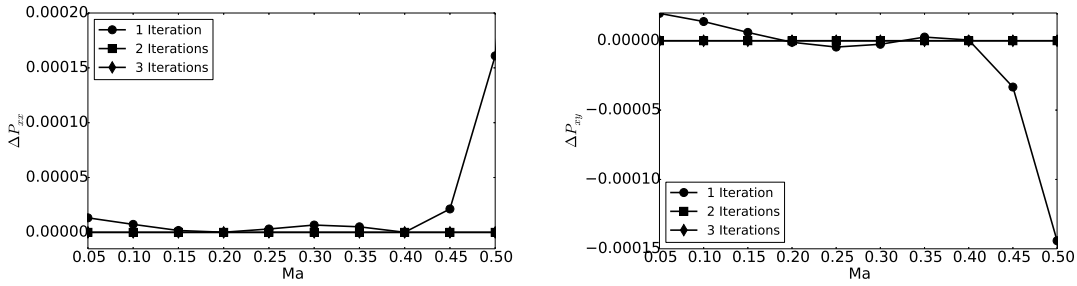

Figure 8.1: The percentage error of Pressure tensor P_{xx} and P_{xy} from the one calculated using exact thermal equilibrium with varying Mach number for 27 velocity model on the BCC grid with $\Delta\theta = -10\%\theta_0$.

The equilibrium pressure tensor, heat flux and $R_{\alpha\beta}$ ar finite velocity are,

$$\begin{aligned} P_{\alpha\beta} &= \rho\theta\delta_{\alpha\beta} + \rho u_\alpha u_\beta, \\ q_\alpha &= 5\theta u_\alpha + u^2 u_\alpha + \frac{7M_3'}{3} u^2 u_\alpha, \\ R_{\alpha\beta} &= 5\theta^2\delta\alpha\beta - \frac{5u^2\theta}{2}\delta_{\alpha\beta} + \frac{7u^2\theta}{2}\delta_{\alpha\beta}\left(1 + 4M_3'\right) + 7u_\alpha u_\beta\theta\left(1 - M_3'\right). \end{aligned} \tag{8.64}$$

It is clear from the above expressions that, the pressure tensor is exact upto O($u^4\Delta^3\theta$) for this model.

However, for isothermal case where $\theta = \theta_0$, all the moments $P_{\alpha\beta}, q_\alpha$ and $R_{\alpha\beta}$ becomes exact as the Maxwell-Boltzmann distribution, this can be seen from the following expressions,

$$\begin{aligned} P_{\alpha\beta} &= \rho\theta_0\delta_{\alpha\beta} + \rho u_\alpha u_\beta, \\ q_\alpha &= 5\theta_0 u_\alpha + u^2 u_\alpha, \\ R_{\alpha\beta} &= 5\theta_0^2\delta\alpha\beta - \frac{5u^2\theta_0}{2}\delta_{\alpha\beta} + \frac{7u^2\theta_0}{2}\delta_{\alpha\beta} + 7u_\alpha u_\beta\theta_0. \end{aligned} \tag{8.65}$$

8.6 Results

The new iterative scheme is more useful for the high Ma simulations, where we have to use higher order models with more number of discrete velocities. The time to calculate the discrete equilibrium distribution reduces and the populations are positive for high Ma simulations also. For higher order models also, the method converges in 3 iterations.

In this section we have considered the widely known model of 27 velocities(D3Q27) and D3Q41 defined in (Chikatamarla & Karlin, 2009) are considered. In addition to those, the models with BCC grid-based methods with high-velocity models such as RD3Q67 and RD3Q167 are also presented. The percentage error in calculation of some of the important moments such as P_{xx}, P_{xy}, q_x and R using iterative method to the calculation using exact equilibrium at varying Ma for different models D3Q27, D3Q41, RD3Q27, RD3Q41, RD3Q67 and RD3Q167 are shown in the figures, Fig 8.1 to Fig 8.24. It is clear from the plot that, the method converges in two iterations for the Ma<0.5. However, the solution converges in 3 iterations for the higher Ma. The velocities for the system are initialized non-uniformly such that, $u_x = u/\sqrt{14}, u_y = 2u_x, u_z = 3u_x$ and Ma=u/c_s.

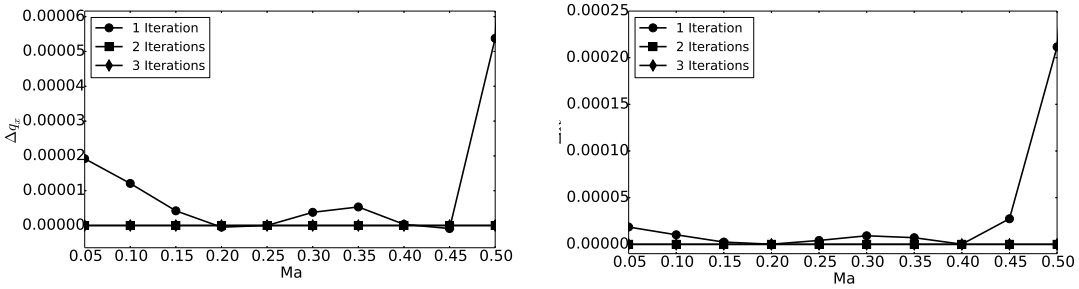

Figure 8.2: The percentage error of heat flux q_x and R from the one calculated using exact thermal equilibrium with varying Mach number for 27 velocity model on the BCC grid with $\Delta\theta = -10\%\theta_0$.

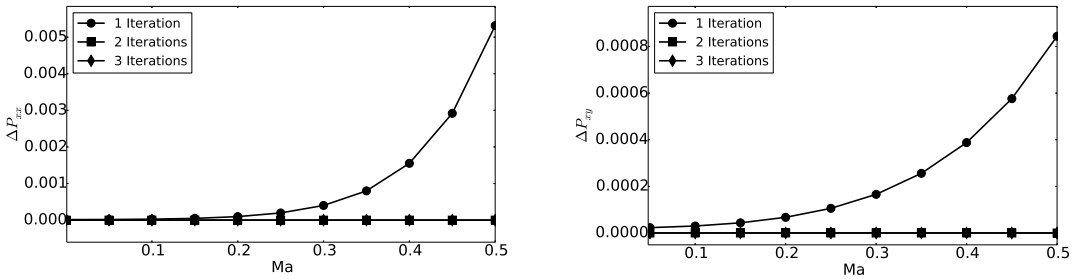

Figure 8.3: The percentage error of Pressure tensor P_{xx} and P_{xy} from the one calculated using exact thermal equilibrium with varying Mach number for 27 velocity model with on the BCC grid $\Delta\theta = 10\%\theta_0$.

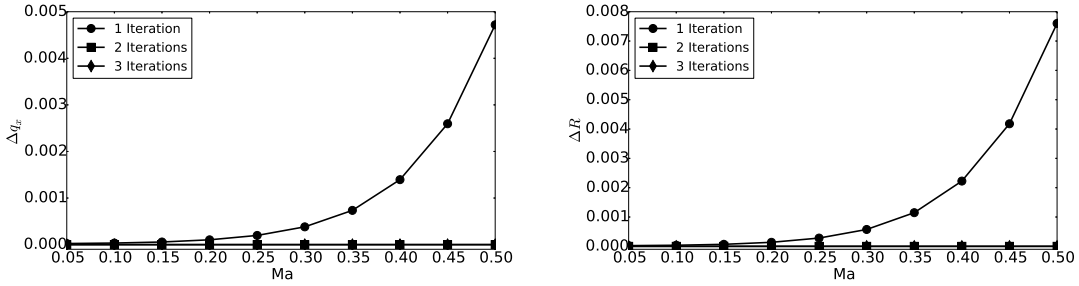

Figure 8.4: The percentage error of heat flux q_x and R from the one calculated using exact thermal equilibrium with varying Mach number for 27 velocity model on the BCC grid with $\Delta\theta = 10\%\theta_0$.

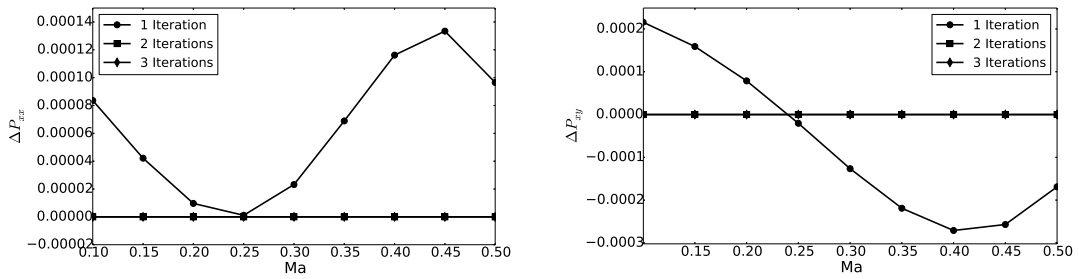

Figure 8.5: The percentage error of Pressure tensor P_{xx} and P_{xy} from the one calculated using exact thermal equilibrium with varying Mach number for 27 velocity model with $\Delta\theta = -10\%\theta_0$.

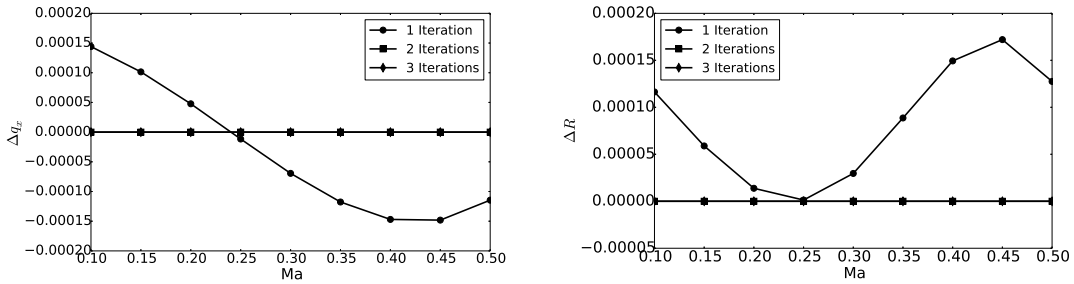

Figure 8.6: The percentage error of heat flux q_x and R from the one calculated using exact thermal equilibrium with varying Mach number for 27 velocity model with $\Delta\theta = -10\%\theta_0$.

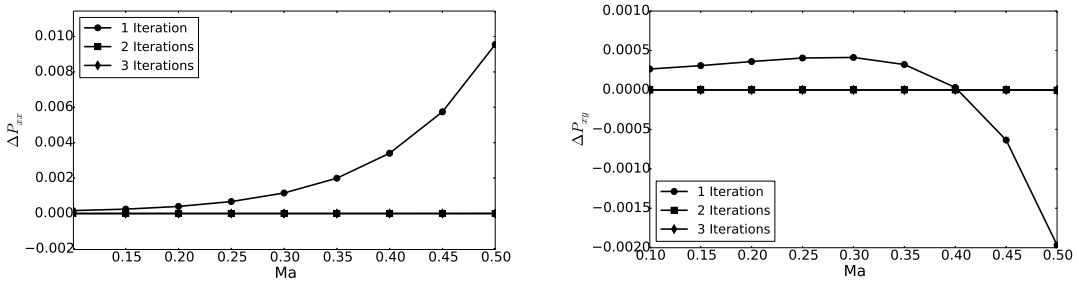

Figure 8.7: The percentage error of Pressure tensor P_{xx} and P_{xy} from the one calculated using exact thermal equilibrium with varying Mach number for 27 velocity model with $\Delta\theta = 10\%\theta_0$.

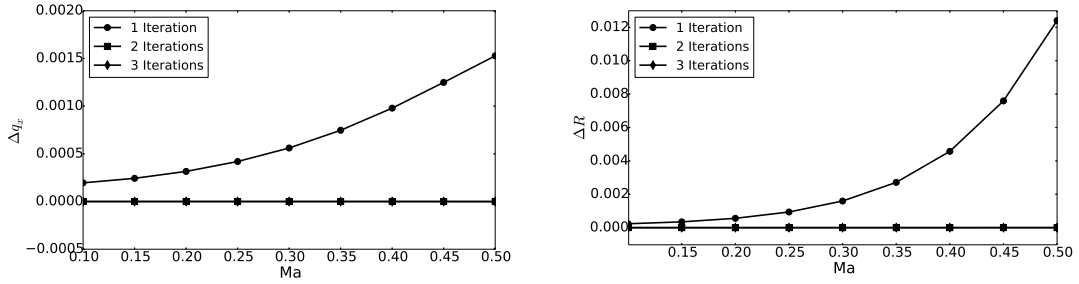

Figure 8.8: The percentage error of heat flux q_x and R from the one calculated using exact thermal equilibrium with varying Mach number for 27 velocity model with $\Delta\theta = 10\%\theta_0$.

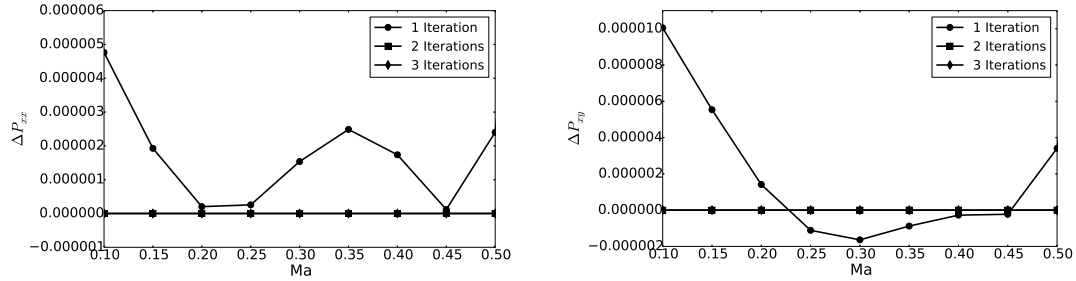

Figure 8.9: The percentage error of Pressure tensor P_{xx} and P_{xy} from the one calculated using exact thermal equilibrium with varying Mach number for 41 velocity model with $\Delta\theta = -10\%\theta_0$.

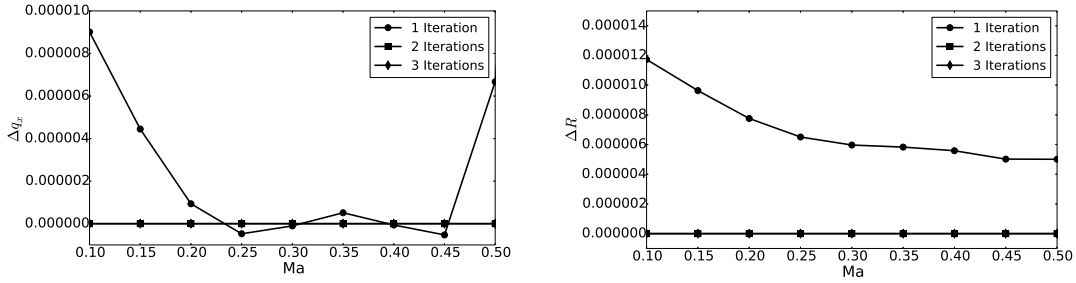

Figure 8.10: The percentage error of heat flux q_x and R from the one calculated using exact thermal equilibrium with varying Mach number for 41 velocity model with $\Delta\theta = -10\%\theta_0$.

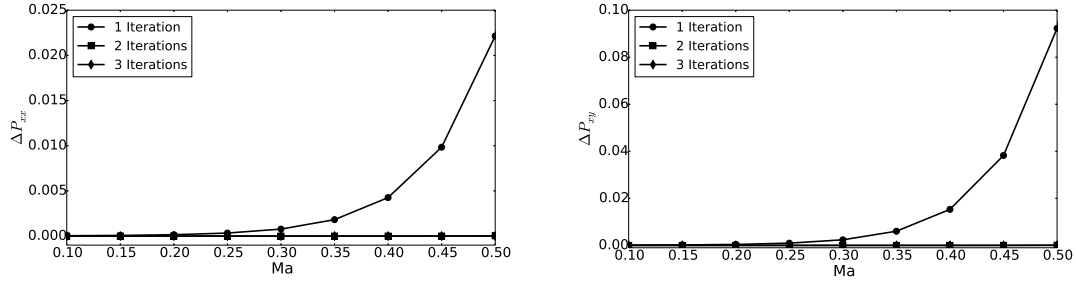

Figure 8.11: The percentage error of Pressure tensor P_{xx} and P_{xy} from the one calculated using exact thermal equilibrium with varying Mach number for 41 velocity model with $\Delta\theta = 10\%\theta_0$.

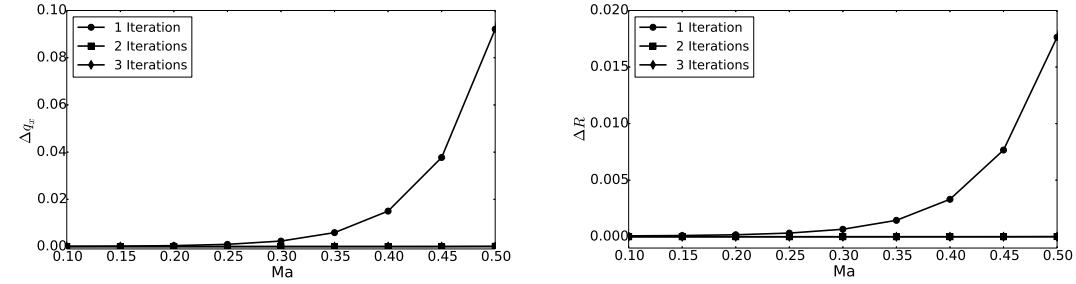

Figure 8.12: The percentage error of heat flux q_x and R from the one calculated using exact thermal equilibrium with varying Mach number for 41 velocity model with $\Delta\theta = 10\%\theta_0$.

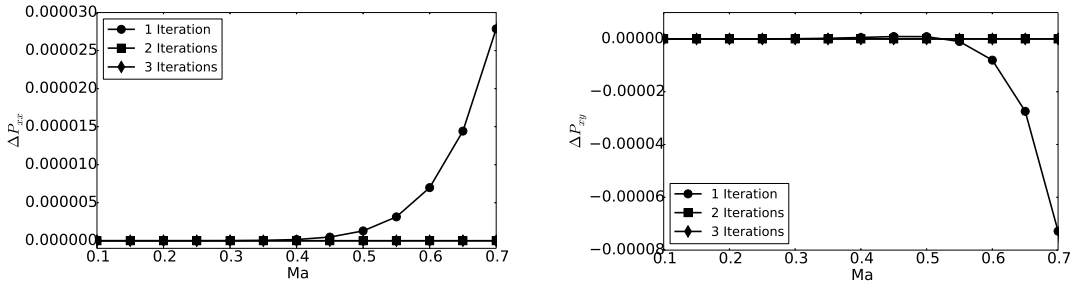

Figure 8.13: The percentage error of Pressure tensor P_{xx} and P_{xy} from the one calculated using exact thermal equilibrium with varying Mach number for 41 on BCC grid velocity model with $\Delta\theta = -10\%\theta_0$.

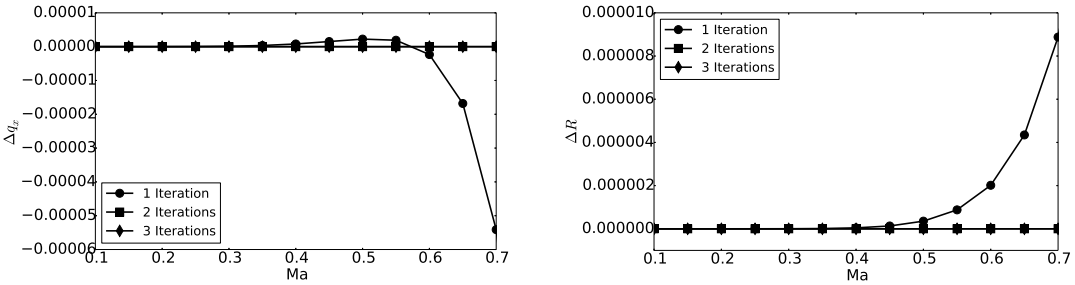

Figure 8.14: The percentage error of heat flux q_x and R from the one calculated using exact thermal equilibrium with varying Mach number for 41 velocity model on BCC grid with $\Delta\theta = -10\%\theta_0$.

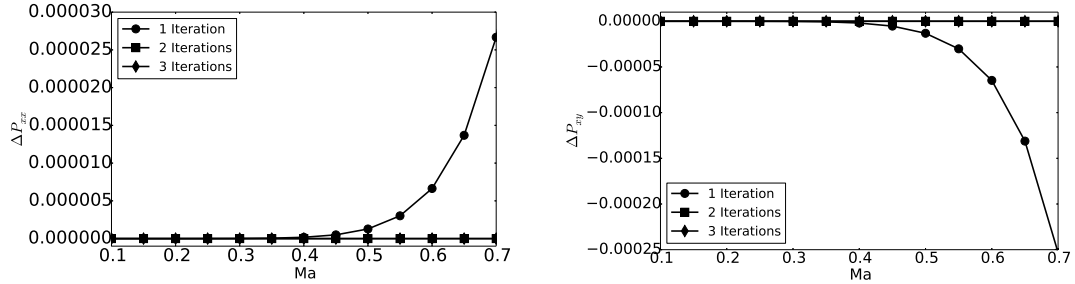

Figure 8.15: The percentage error of Pressure tensor P_{xx} and P_{xy} from the one calculated using exact thermal equilibrium with varying Mach number for 41 velocity model on BCC grid with $\Delta\theta = 10\%\theta_0$.

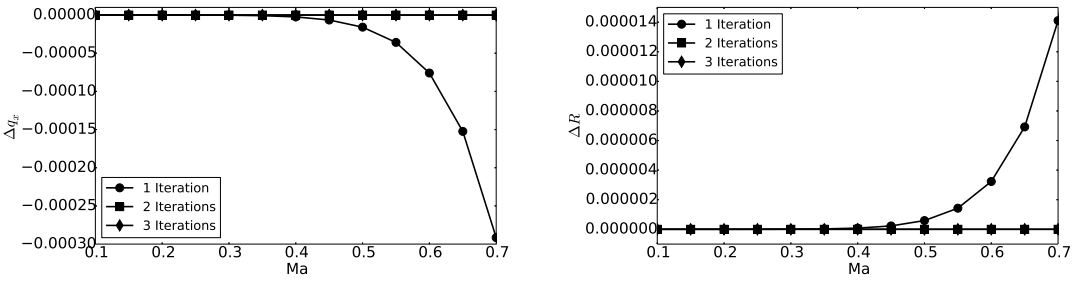

Figure 8.16: The percentage error of heat flux q_x and R from the one calculated using exact thermal equilibrium with varying Mach number for 41 velocity model on BCC grid with $\Delta\theta = 10\%\theta_0$.

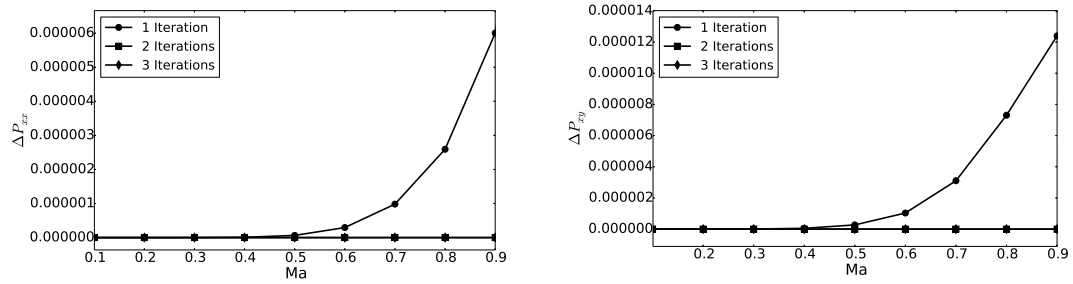

Figure 8.17: The percentage error of Pressure tensor P_{xx} and P_{xy} from the one calculated using exact thermal equilibrium with varying Mach number for 67 velocity model with $\Delta\theta = -10\%\theta_0$.

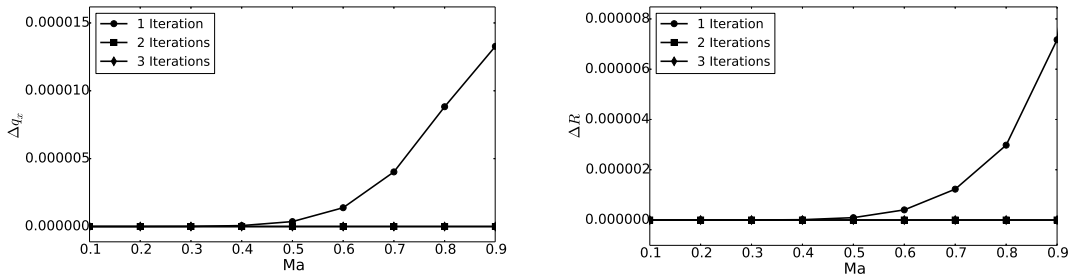

Figure 8.18: The percentage error of heat flux q_x and R from the one calculated using exact thermal equilibrium with varying Mach number for 67 velocity model with $\Delta\theta = -10\%\theta_0$.

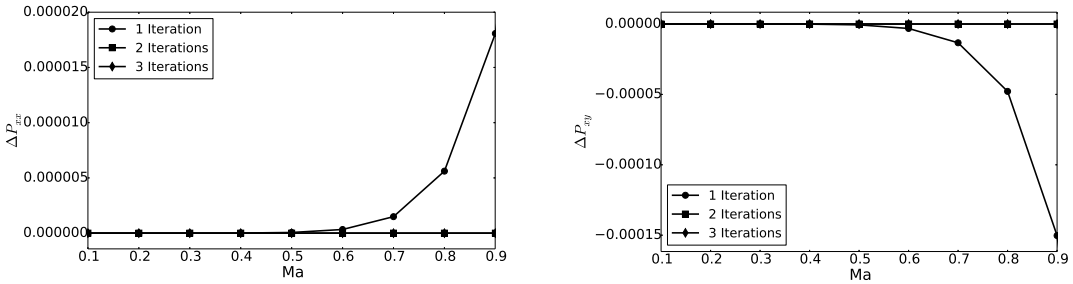

Figure 8.19: The percentage error of Pressure tensor P_{xx} and P_{xy} from the one calculated using exact thermal equilibrium with varying Mach number for 67 velocity model with $\Delta\theta = 10\%\theta_0$.

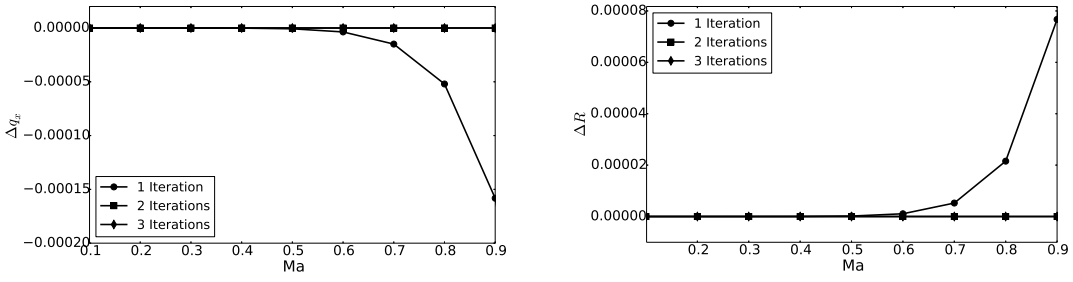

Figure 8.20: The percentage error of heat flux q_x and R from the one calculated using exact thermal equilibrium with varying Mach number for 67 velocity model with $\Delta\theta = 10\%\theta_0$.

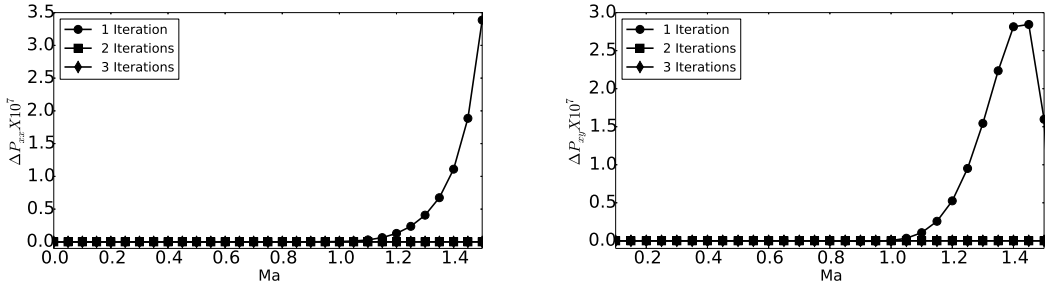

Figure 8.21: The percentage error of Pressure tensor P_{xx} and P_{xy} from the one calculated using exact thermal equilibrium with varying Mach number for 167 velocity model with $\Delta\theta = -10\%\theta_0$.

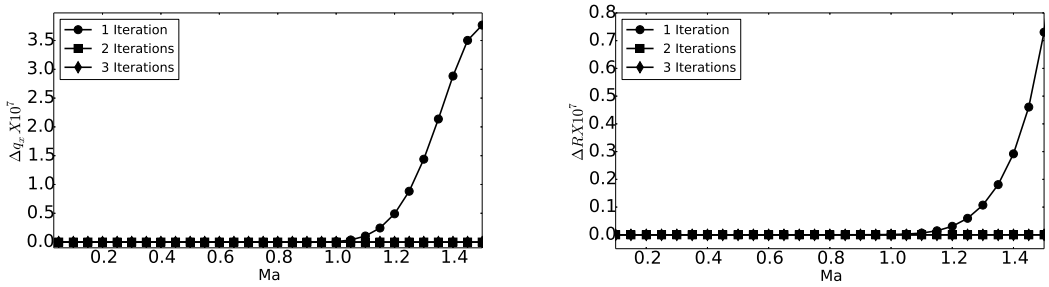

Figure 8.22: The percentage error of heat flux q_x and R from the one calculated using exact thermal equilibrium with varying Mach number for 167 velocity model with $\Delta\theta = -10\%\theta_0$.

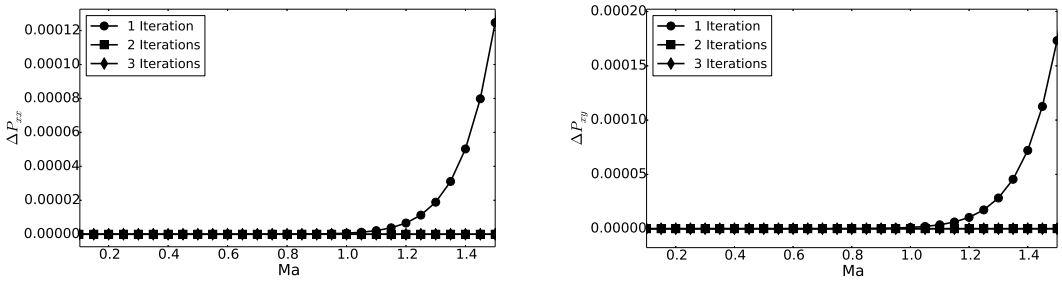

Figure 8.23: The percentage error of Pressure tensor P_{xx} and P_{xy} from the one calculated using exact thermal equilibrium with varying Mach number for 167 velocity model with $\Delta\theta = 10\%\theta_0$.

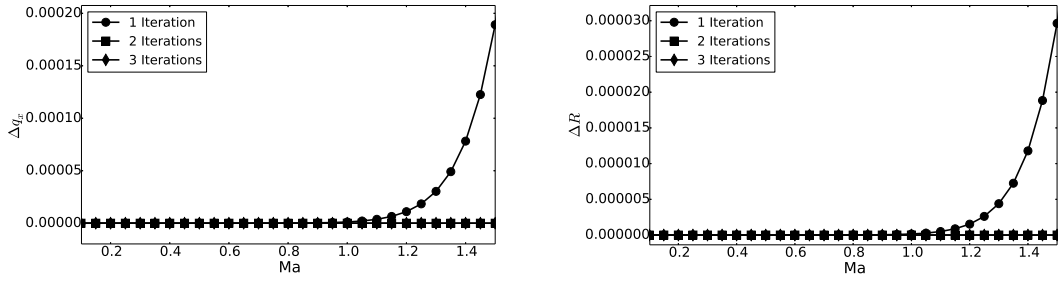

Figure 8.24: The percentage error of heat flux q_x and R from the one calculated using exact thermal equilibrium with varying Mach number for 167 velocity model with $\Delta\theta = 10\%\theta_0$.

In order to check the efficiency of RD3Q167 model we have considered the errors in moments calculated from the iterative equilibrium from the moments calculated using the Maxwell-Boltzmann distribution at different ranges of Ma. It is observed that the method is more accurate even at the Ma as high as 1.8. This is clear from the following plots. Where ΔM is the percentage error of the moment calculated from the iterative equilibrium.

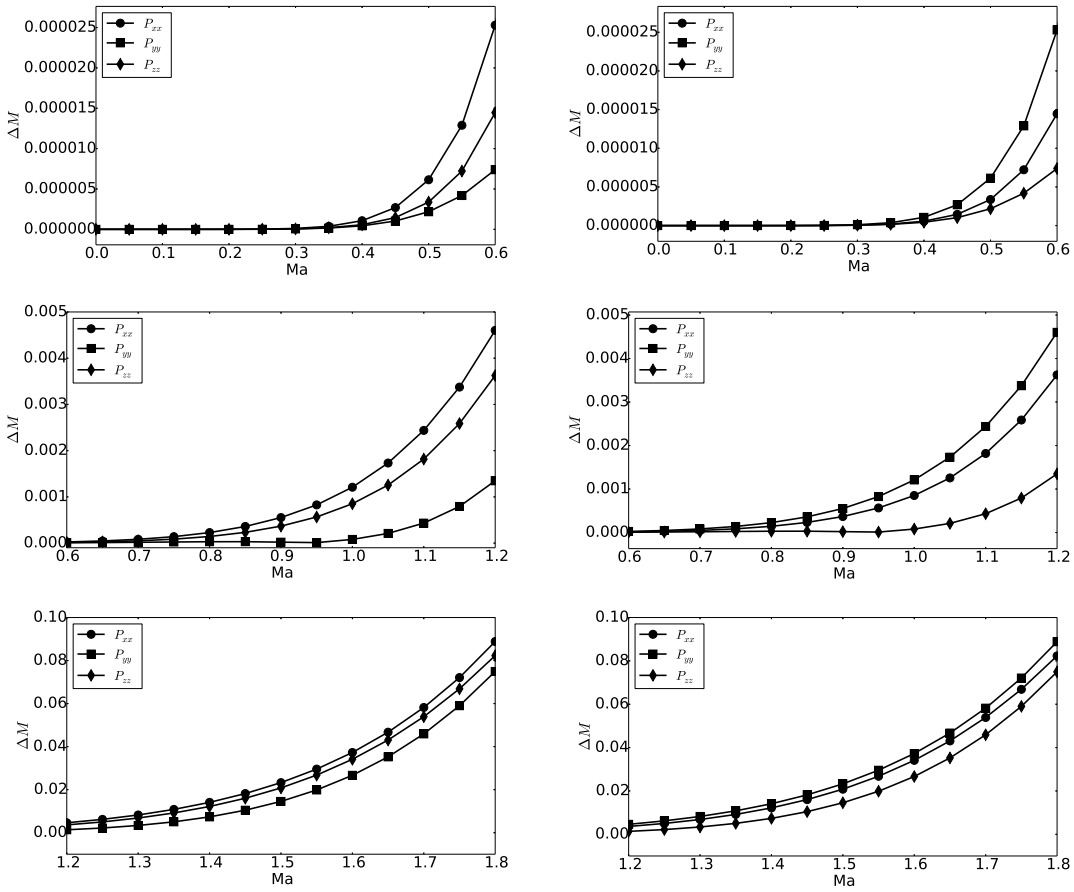

Figure 8.25: The percentage error in the moments P_{xx}, P_{yy} and P_{zz} for the flow with the initial velocity $(u_x, 2u_x, 3u_x)$ on left and $(3u_y, u_y, 2u_y)$ on right from the moments calculated using Maxwell-Boltzmann equilibrium distribution with varying Mach number for 167 velocity model with $\theta = \theta_0$.

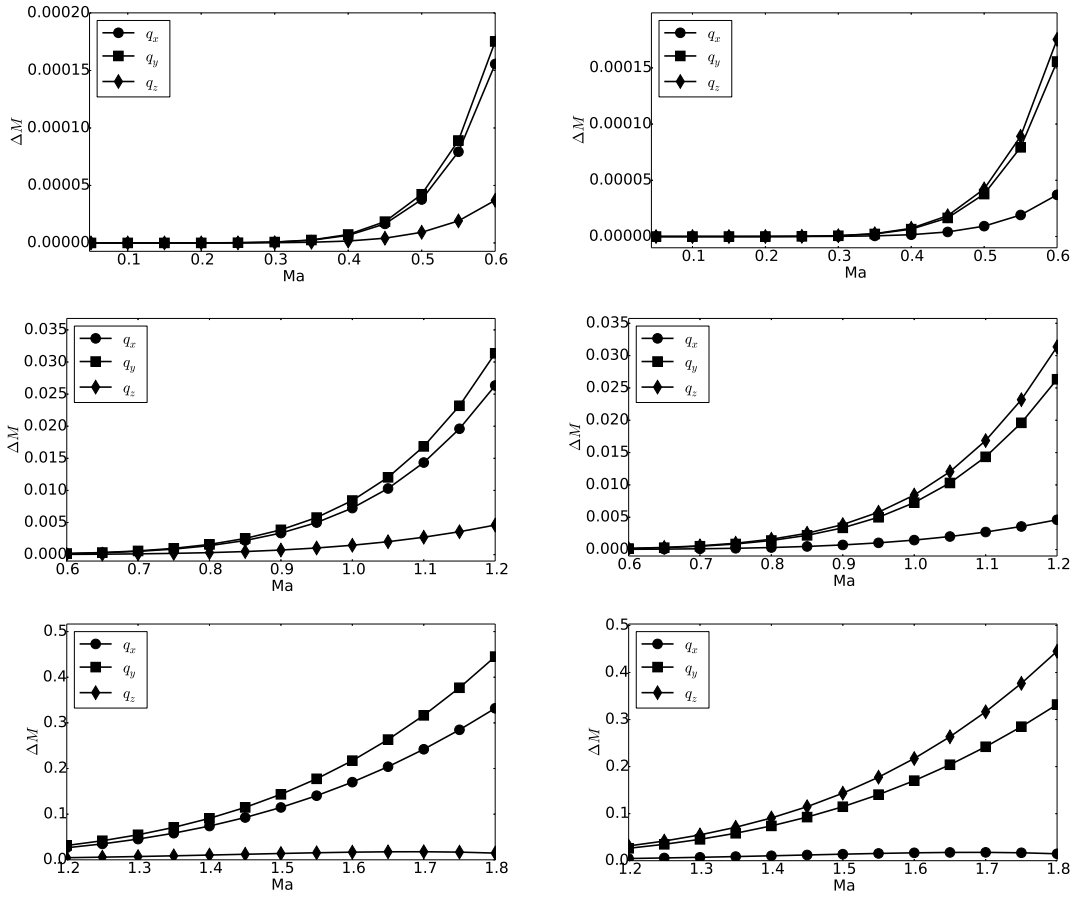

Figure 8.26: The percentage error in the moments q_x, q_y and q_z for the flow with the initial velocity $(u_x, 2u_x, 3u_x)$ on left and $(3u_y, u_y, 2u_y)$ on right from the moments calculated using Maxwell-Boltzmann equilibrium distribution with varying Mach number for 167 velocity model with $\theta = \theta_0$.

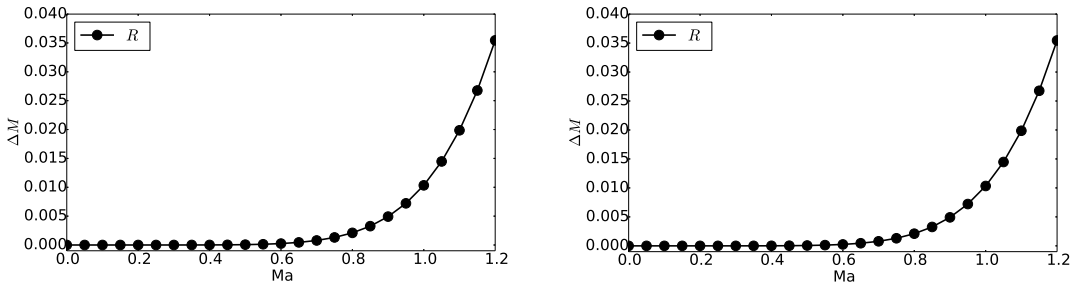

Figure 8.27: The percentage error in the moment R from the moments calculated using Maxwell-Boltzmann equilibrium distribution with varying Mach number for 167 velocity model with $\theta = \theta_0$.

Chapter 9
Higher order Crystallographic Lattice Boltzmann for thermal and transonic flows

In the previous two chapters, higher order models with BCC spatial grid was developed. In chapter 7, a model for compressible thermohydrodynamics with 67 discrete velocities, termed as $RD3Q67$, was developed. So far, almost all working lattice Boltzmann models of thermohydrodynamics are based on two distribution function formulation where one writes LBM models for hydrodynamics and therohydrodynamics separately (Succi, 2001*b*). Though 2D models are available(Frapolli *et al.*, 2015), there are no stable and 3D LBM models for thermohydrodynamics with less than 100 velocities are available so far. The best-known model for 3D hydrodynamics for fully compressible flow requires 343 velocities on simple cubic lattice(Frapolli *et al.*, 2016). In this chapter, we show that the higher order model created in the last chapter is indeed successful in modeling thermohydrodynamics in compressible flow regime. Similarly, for flow with Mach number larger than one, there are no available models other than 343 model. Furthermore, no known LBM model, which are on lattice predict well rarefied gas effect in the regime of Knudsen number one. In chapter 7, a model for trans-sonic flow and high Knudsen flows with 167 discrete velocities, termed as $RD3Q167$, was developed. In this chapter, we present simulation results from a few canonical test cases to show the effectiveness of these models.

The chapter is organized as follows: in section 9.1, we will present simulations of 3-dimensional Rayleigh-Bénard convection and 1-dimensional Riemann problems at high Mach values using $RD3Q67$ model. In section 9.2 the $RD3Q167$ model is applied to Poiseuille flow and 1-dimensional Riemann problems at high Mach values. The simulations exhibit good match with the literature and analytical solutions, therefore the models are found to be accurate and numerically stable for simulations of fluid flows with heat and mass transfer as well as transonic flows.

9.1 $RD3Q67$ Model for thermal simulations

Following McNamara *et al.* (1995), in order to see the effectiveness of the new thermal model, Rayleigh-Bénard flow was simulated. Rayleigh-Bénard convection occurs when a horizontal layer of fluid is heated from the bottom and cooled from the top (Bodenschatz *et al.*, 2000). The schematic for Rayleigh-Bénard setup is depicted in the Fig. 9.1. The flow is caused by the temperature induced unstable density gradients in the presence of external force field (usually gravitational field). The setup consists of a horizontal layer of viscous fluid confined between two thermally well conducting parallel plates at a distance L. The bottom plate is at an excess temperature $T_0 + \Delta T$, while the top plate is maintained at a lower temperature $T_0 - \Delta T$. In this work, Prandtl number ($\Pr = \nu/\hat{\alpha}$) is set to unity $\Pr = 1$.

The dynamics is characterized by non-dimensional parameter, termed as Rayleigh number (Ra), which represents the strength of buoyancy driven inertial force to the viscous force and is defined as

$$Ra = \frac{G\hat{\beta}\Delta T L^3}{\nu\hat{\alpha}}, \tag{9.1}$$

where G is the gravity in the negative y-direction, $\hat{\beta} = -1/\rho(\partial\rho/\partial T)_P$ is the thermal expansion

coefficient, ΔT is the temperature difference between the two walls, ν is the kinematic viscosity and $\hat{\alpha}$ is the thermal diffusivity. Below a certain critical Rayleigh number ($Ra_c = 1708$), a steady solution exists for this problem with the velocity zero everywhere and the temperature a linear function of the vertical coordinate. However, when Ra is increased above a critical value, this solution becomes unstable for any small disturbances and the convection currents are set up. As Ra is increased further, the flow becomes turbulent in nature.

The numerical simulations were carried out for the Rayleigh-Bénard convection, where we considered a temperature difference of 2% from the reference temperature (T_0) for various Rayleigh numbers on a grid size of $256 \times 128 \times 8$ [1]. In our simulations, constant temperature boundary conditions at the top and the bottom walls were imposed using the diffusive wall boundary conditions (Ansumali & Karlin, 2002*b*). In other two directions, periodic boundary conditions were applied. Snapshots of temperature distributions and the isotherms for $Ra = 10^4, 10^5, 10^6, 10^8$ are plotted in the Fig. 9.2a, Fig. 9.2b, Fig. 9.2c and Fig. 9.2d respectively. As is evident from the figure, the plumes become sharper with increased Rayleigh numbers signifying better mixing of hot and cold fluid. At $Ra = 10^8$ the flow has become turbulent. The results are found to be in good agreement with that given in (Shan, 1997; Prasianakis & Karlin, 2007).

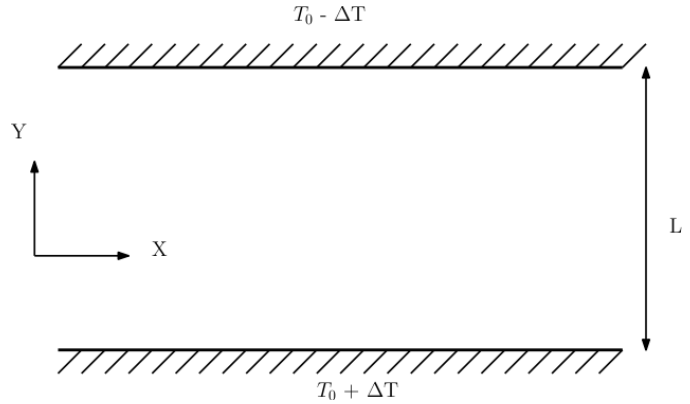

Figure 9.1: Rayleigh-Bénard convection setup.

For quantitative analysis, we calculated the Nusselt number (Nu) which was the measure of heat transfer in the system and represents the ratio of net heat transfer to the conductive heat transfer. The Nusselt number is calculated as

$$\mathrm{Nu} = 1 + \frac{< u_y T > H}{\kappa \Delta T}, \tag{9.2}$$

where the thermal conductivity $\kappa = (1 + D/2)\rho\nu/\mathrm{Pr}$, D is the number of dimensions. Fig. 9.3 shows the Rayleigh vs Nusselt values obtained from current simulations compared with that from (Clever & Busse, 1974) and the empirical power law $\mathrm{Nu} = 1.56\,(\mathrm{Ra}/\mathrm{Ra_{cr}})^{0.296}$.

9.1.1 Compressible flows

In order to study the suitability for sub-sonic compressible flows, we chose a set of Riemann problems to validate the method [2]. The presence of discontinuities in the initial conditions is a challenging task for any numerical simulation (Laney, 1998). In particular, Riemann problem poses difficulties due to the generation of new and faster waves than those present in the initial conditions. Given a sufficient jump in initial conditions across an interface, the resulting flow

[1] This work was done in collaboration with Mohammad Atif, who wrote the code for the simulation

[2] This work was done in collaboration with Chakradhar Thantanapally, SankhyaSutra Labs Pvt. Ltd., Bangalore who wrote the code for the simulation

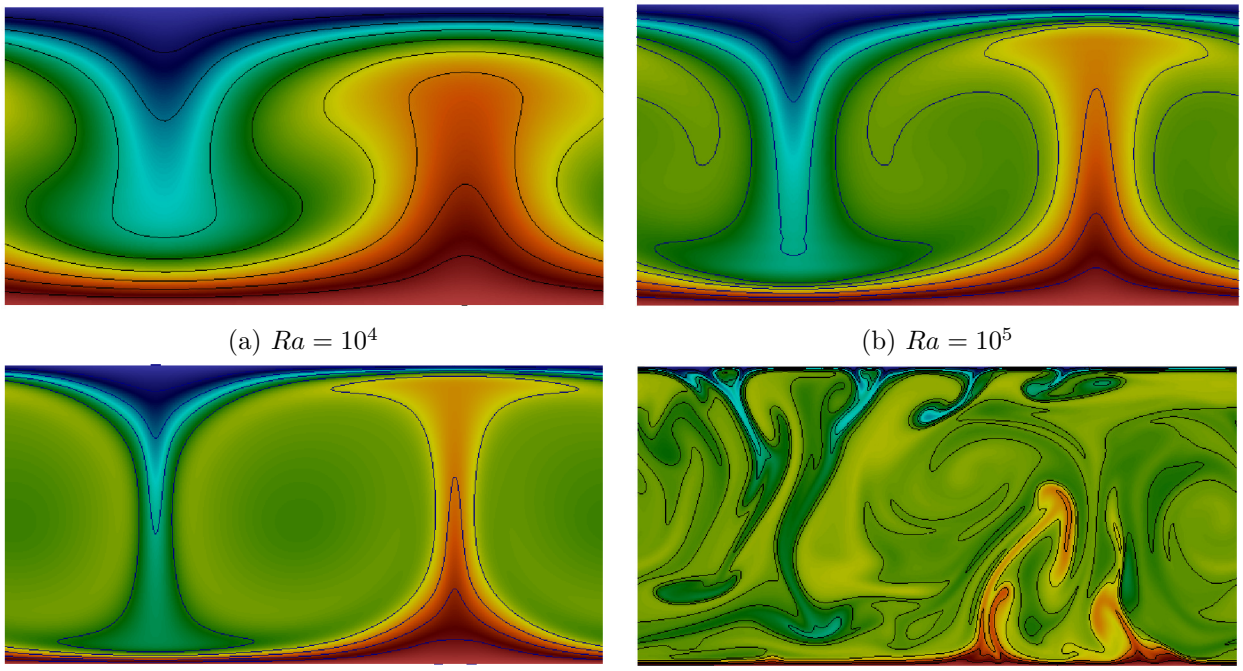

(a) $Ra = 10^4$ (b) $Ra = 10^5$

(c) $Ra = 10^6$ (d) $Ra = 10^8$

Figure 9.2: Snapshots of temperature distribution along with uniformly spaced temperature contours for various Rayleigh numbers.

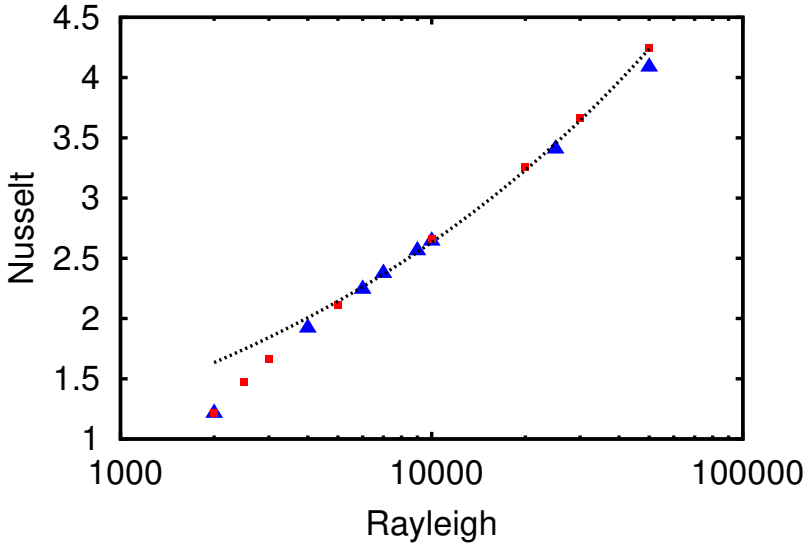

Figure 9.3: Nusselt vs Rayleigh, triangles are from current simulation, squares are from Ref. Clever & Busse (1974), line is empirical power law $\mathrm{Nu} = 1.56(\mathrm{Ra}/\mathrm{Ra_c})^{0.296}$

gives rise to a shock, expansion fan and a contact separating the expansion fan and shock. The three dimensional $RD3Q67$ model was used to solve for Riemann problem solutions with periodic boundary condition in the normal directions. The missing populations at the ends of the domain were copied from the neighboring planes normal to propagation.

The fluid was modeled as hard sphere molecules with the viscosity (μ) proportional to the square-root of temperature (T). Here for the test cases considered the reference viscosity is taken as 10^{-5} corresponding to the minimum temperature in the flow. The viscosity given above is in lattice units, where viscosity $\mu = \tau p$, τ and p being the relaxation time and pressure. The equilibrium function was found iteratively by minimizing the H-function, as the perturbative expansion around the reference temperature is not accurate for higher temperature differences.

The ratio of specific heats (γ) of the fluid is 1.67 for the $RD3Q67$ model. The simulations were performed over a grid size of $(3840 \times 8 \times 8)$. The length of the domain was considered unity and the initial discontinuities in the flow properties (density, velocity and pressure) are introduced at the interface $x = 0.5$. The time scale is chosen based on the length of the domain and speed of sound in the right section of the interface. The flow quantities to the left are indicated by subscript L and to the right by R.

Three Riemann problems are chosen to show the capability of the solver. The first problem is the well known standard Sod's shock tube problem (Sod, 1978) for which exact Euler solutions exist. The second problem is similar to Sod's test but with a finite velocity (Laney, 1998) which gives a stronger shock. The third one is the Roe's test (Einfeldt *et al.*, 1991) with discontinuity only in velocity. In the shock wave propagation setup, different kinds of elementary waves will be formed as are shown in the Fig. 9.4. The density, pressure and Mach number from these

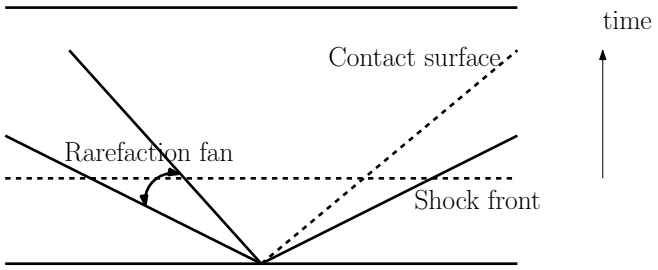

Figure 9.4: Different kinds of elementary waves in the shock tube.

simulation results are compared with the Euler solutions and are discussed below.

Riemann Problem 1: Sod shock tube test

This problem consists of an initially quiescent fluid separated by an interface at $x = 0.5$ across which the density and pressure have a jump. The initial conditions for this case are given by

$$\begin{pmatrix} \rho_L \\ u_L \\ p_L \end{pmatrix} = \begin{pmatrix} 1 \\ 0 \\ 1 \end{pmatrix}, \qquad \begin{pmatrix} \rho_R \\ u_R \\ p_R \end{pmatrix} = \begin{pmatrix} 0.125 \\ 0 \\ 0.1 \end{pmatrix}. \tag{9.3}$$

The density ratio of 8 and pressure ratio of 10 taken here, give rise to a shock moving towards the right and an expansion fan towards left. The maximum Mach number attained in this simulation is around 0.83 between the tail of expansion fan and contact discontinuity as shown in figure 9.5. The speed of the shock is captured accurately by the method as shown against the exact Euler solutions. There is a small discrepancy in the speed with which the tail of the expansion fan travels.

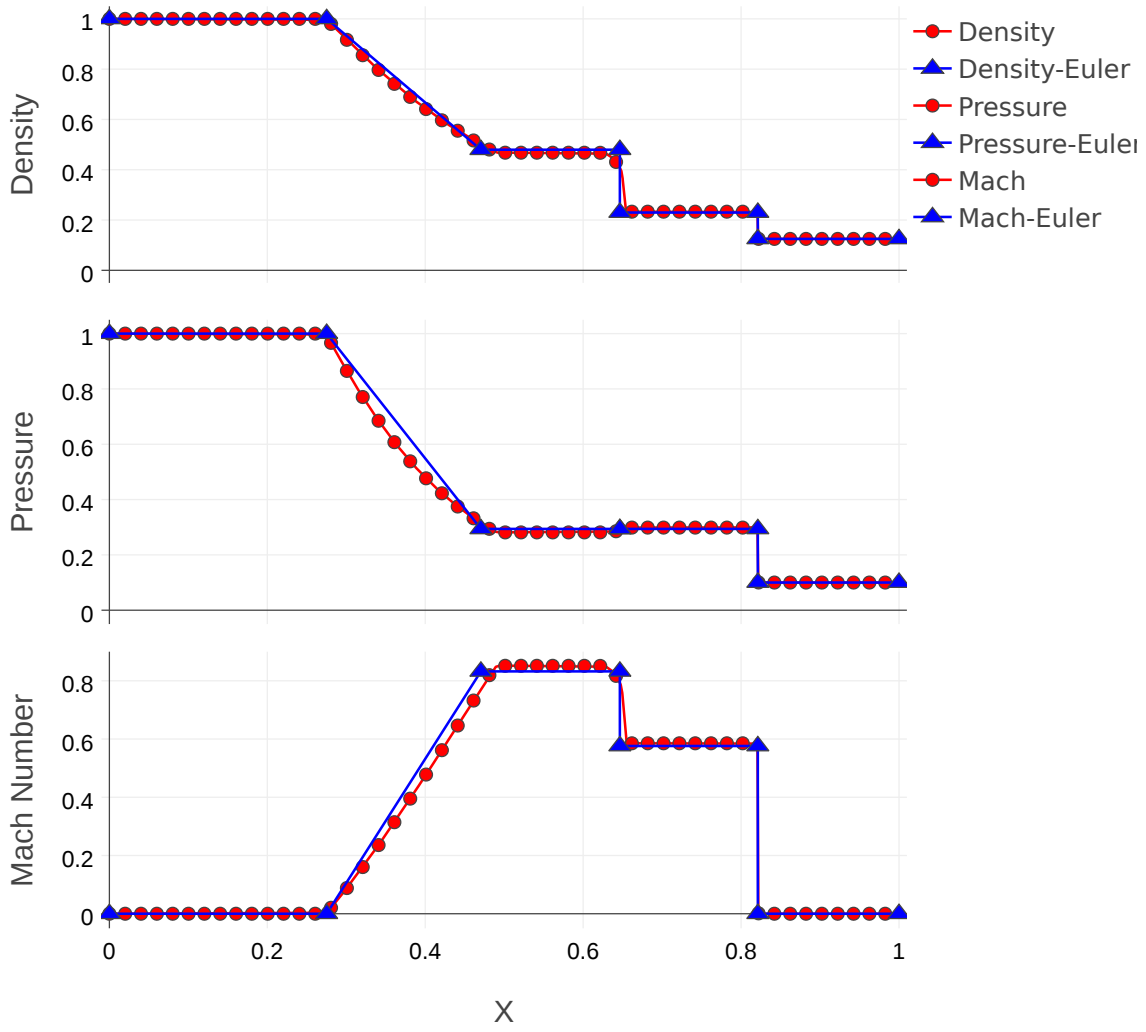

Figure 9.5: The figure shows the variation of density, pressure and Mach number along the length for the Sod's test problem. The plots show a comparison of RD3Q67 result with exact solutions of Euler equations at $t = 0.2$.

Riemann Problem 2: Sod test with finite velocity

This set-up is similar to that of Sod's test described above, except that the fluid has a finite velocity initially on both sides of the interface (Laney, 1998). The initial conditions are given by

$$\begin{pmatrix} \rho_L \\ u_L \\ p_L \end{pmatrix} = \begin{pmatrix} 1 \\ 0.2449 \\ 1 \end{pmatrix}, \qquad \begin{pmatrix} \rho_R \\ u_R \\ p_R \end{pmatrix} = \begin{pmatrix} 0.125 \\ -0.1225 \\ 0.1 \end{pmatrix}. \tag{9.4}$$

This gives rise to a stronger shock and higher contact speeds than that of the previous case as shown in figure 9.6. The comparison with exact Euler solutions show a good match for the shock speed.

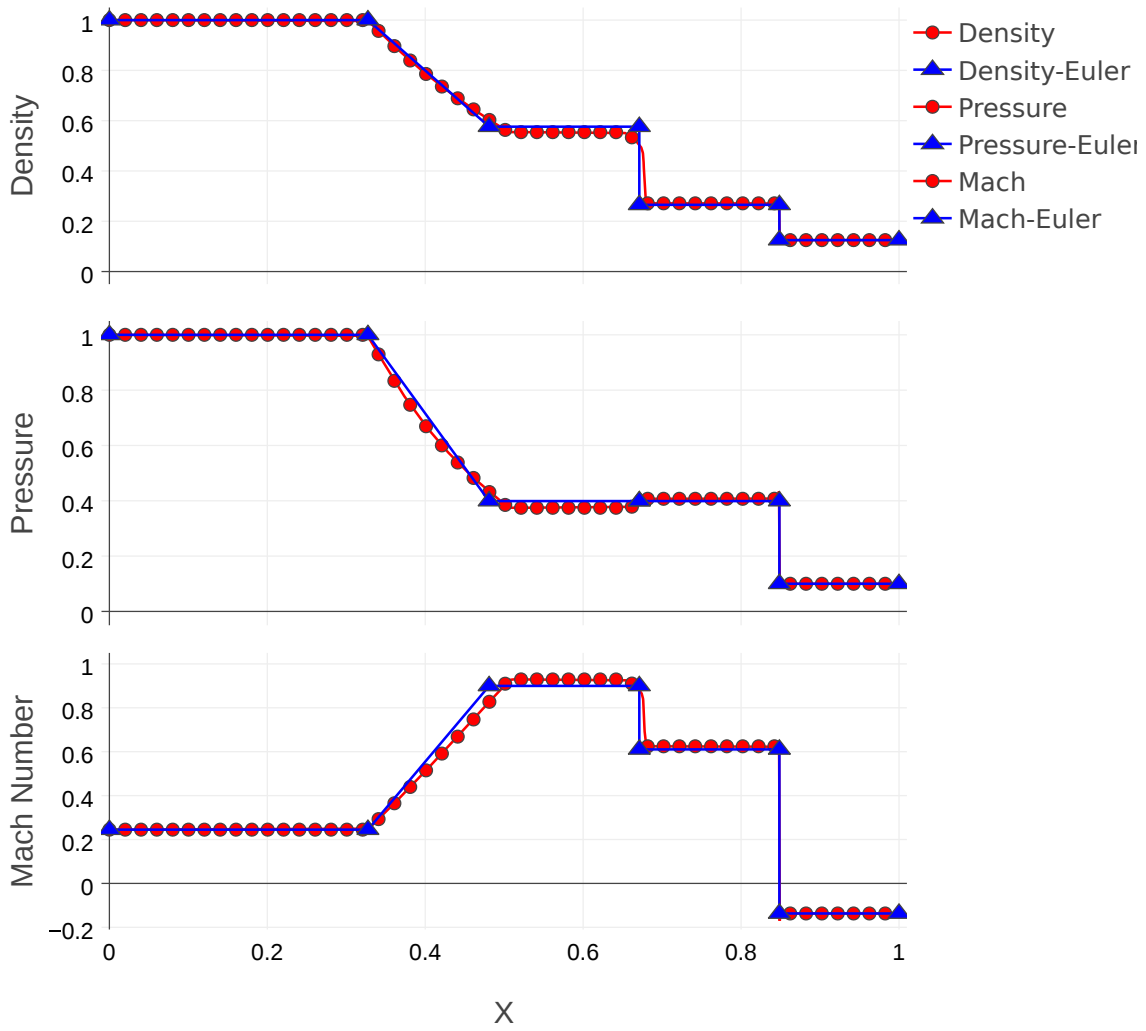

Figure 9.6: The figure shows the variation of density, pressure and Mach number along the length for Sod test with finite velocity. The plots show a comparison of RD3Q67 result with exact solutions of Euler equations at $t = 0.2$.

Riemann Problem 3: Roe test

This initial condition has continuous density and pressure across the interface unlike the previous test cases. There is only a jump in velocity, with the fluid moving away from the interface. The initial conditions for this case are given by

$$\begin{pmatrix} \rho_L \\ u_L \\ p_L \end{pmatrix} = \begin{pmatrix} 1 \\ -1 \\ 1.8 \end{pmatrix}, \qquad \begin{pmatrix} \rho_R \\ u_R \\ p_R \end{pmatrix} = \begin{pmatrix} 1 \\ 1 \\ 1.8 \end{pmatrix}. \tag{9.5}$$

Since the fluid has an initial velocity that moves away from the interface on both sides, it creates a pair of expansion fans moving away from the center. This is a mild test case as there is no shock formed, but the drop in pressure at the interface is highest among all the simulations discussed here.

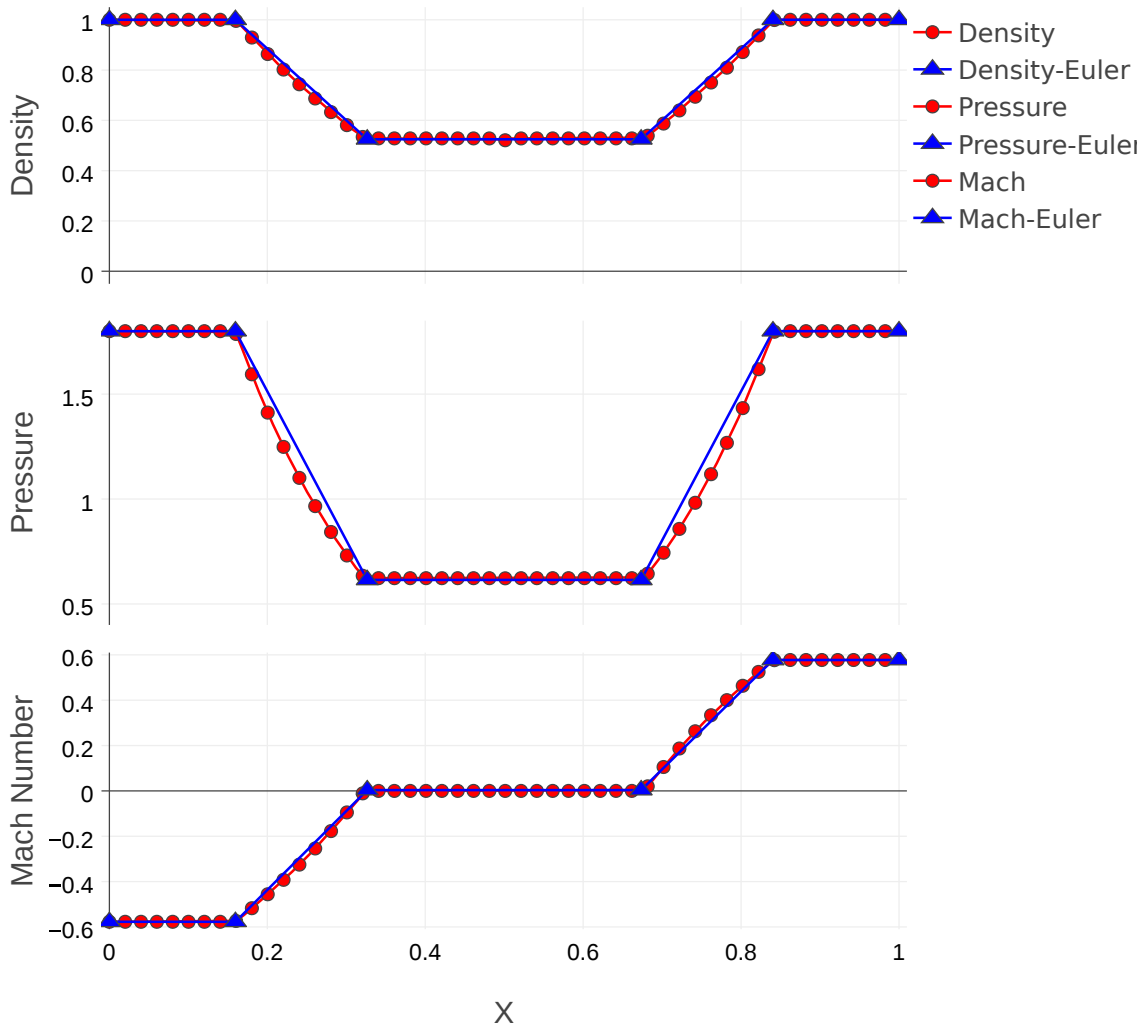

Figure 9.7: The figure shows the variation of density, pressure and Mach number along the length for the Roe's test problem. The plots show a comparison of RD3Q67 result with exact solutions of Euler equations at $t = 0.22$.

9.2 *RD*3*Q*167

To test the efficiency of the present model, a classical test case of Poiseuille flow problem was simulated(Cercignani, 1975; Yudistiawan *et al.*, 2010). Here, the flow is driven by the pressure difference between the two parallel plates separated by a distance h. At the top and bottom walls, the classical diffuse boundary conditions have been applied and periodic boundary conditions were applied in the other two directions. In the Fig 9.8, mass flow rate as a function of Knudsen number (Kn) is plotted and the percentage error from the analytical solution obtained from the Boltzmann-BGK solution is tabulated in the Table 9.1. Though, the flow rate is in good agreement with the BGK results for low Kn, the flow rate has the minimum value at $Kn = 0.7$ unlike the $Kn = 1$ for the Boltzmann-BGK solution.

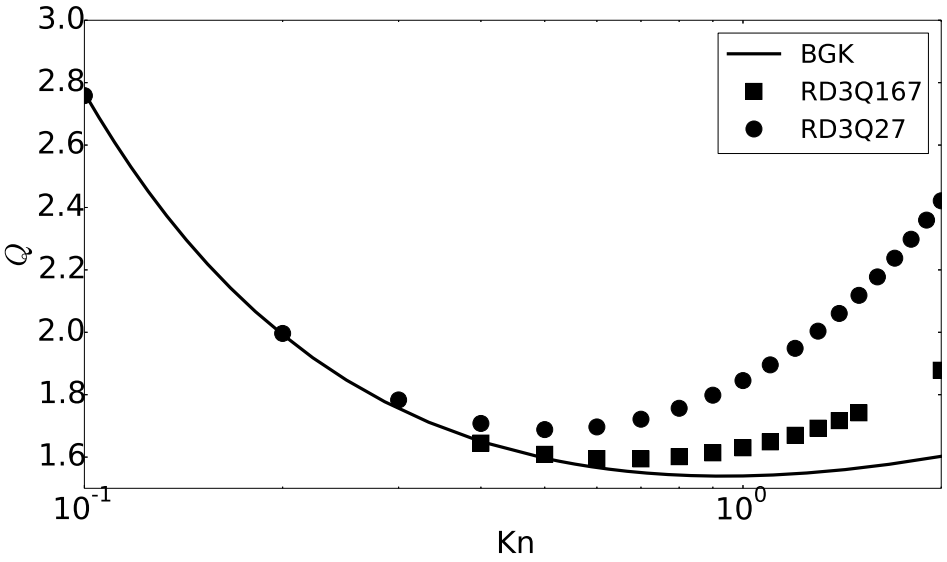

Figure 9.8: Mass flow rate as a funciton of Kn

Finally, we demonstrate trans-sonic flow capabilities of this model by considering the one-dimensional problem of unsteady flow in a shock tube. Two test cases with the same initial conditions as section 9.1.1 are chosen, namely, the classic Sod shock tube test Sod (1978) and the Sod test with finite velocity (Laney, 1998). The density, pressure and Mach number from these simulations results are contrasted with the Euler solutions in Figs. 9.9 and 9.10 respectively. From this result, it can be concluded that this model indeed allows LBM simulations in trans-sonic flow regime.

Kn	% error(RD3Q167)	% error(RD3Q27)
0.4	0.290412	3.525489
0.5	0.790955	5.755810
0.6	1.832461	8.123884
0.7	2.835591	11.14798
0.8	3.829770	13.82321
0.9	4.841172	16.54032
1.0	5.864284	19.85126
1.1	6.909680	22.87353
1.2	7.980879	25.09823
1.3	9.075885	28.44102
1.4	10.191777	31.66072
1.5	11.324215	35.80485

Table 9.1: Percentage error in the mass flow rate calculation with respect to Boltzmann-BGK solution.

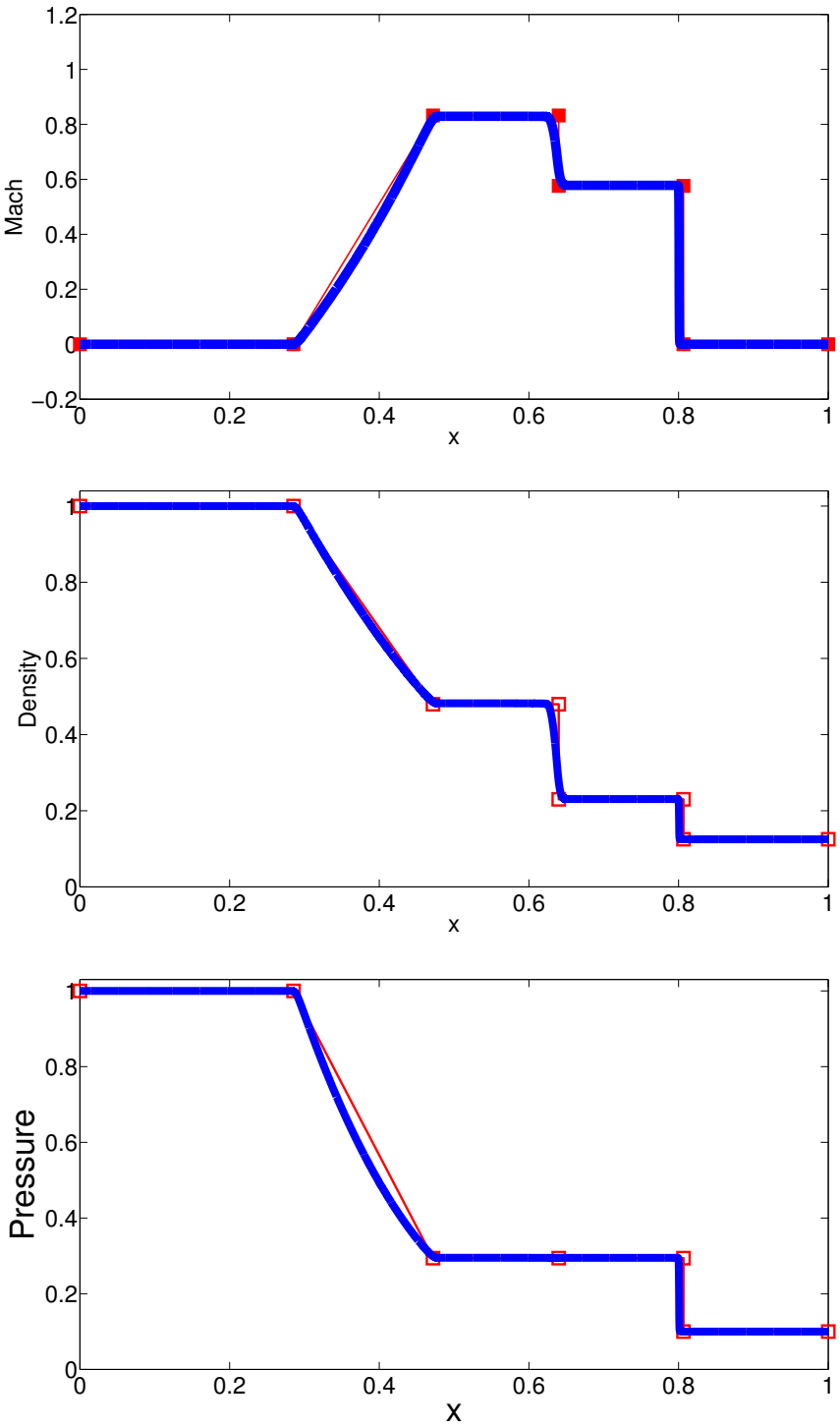

Figure 9.9: The figure shows the variation of Mach number, density and pressure along the length for the Sod's test problem. The plots show a comparison of RD3Q167 result with exact solutions of Euler equations at $t = 0.6$.

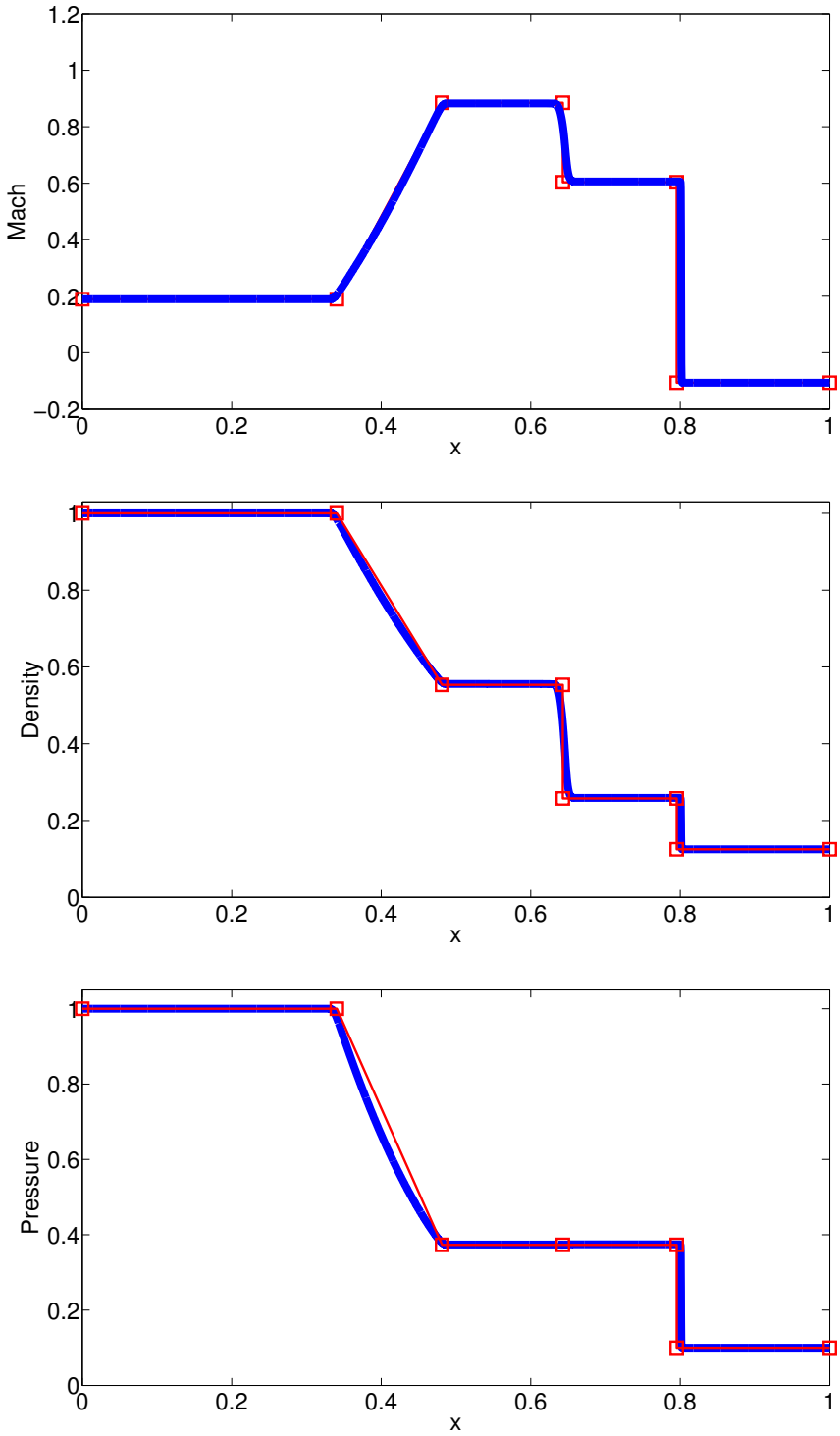

Figure 9.10: The figure shows the variation of Mach number, density and pressure along the length for Sod test with finite velocity. The plots show a comparison of RD3Q167 result with exact solutions of Euler equations at $t = 0.6$.

Chapter 10
Outlook

In this thesis, an inverted argument of the LBM is presented where spatial discretization is made as the central theme. The main hypothesis is that the optimal spatial discretization for LBM is a Body Centered Cubic (BCC) arrangement of grid points. This thesis shows that this inversion of the argument of LBM and making of spatial discretization the central point indeed provides lot more freedom and accuracy in the velocity space discretization. In this thesis, a new class of Lattice Boltzmann Method, based on the BCC space discretization are presented. It has been shown that LBM based on the BCC lattice spatial discretization has an efficiency that is an order-of-magnitude higher than traditional LBM. The gain obtained by using the BCC lattice has been demonstrated by various representative simulations. This new method has been benchmarked for Poiseuille and Couette flow by demonstrating the ability of this method to capture the high Knudsen effects. The usefulness of the method has been shown by considering the simulation of flow past sphere where it is shown that new method can describe flow over a sphere for a wide range of Reynolds number. The flexibility in the velocity space discretization is used to create higher order LBM for compressible and thermal flows. The discrete equilibrium distribution in perturbative series around $u = 0$ is not applicable when Ma number is order one. The numerical solution of discrete equilibrium distribution function has been developed for the applicability to such problems.

The proposed model allows thermohydrodynamic simulations in 3D. So far such models were only available in 2D. The existing LBM simulations in 3D solve an advection-diffusion for temperature dynamics along with LBM for flows (Karlin *et al.*, 2013). Primary studies in the thesis have shown that the model correctly describes the thermohydrodynamics in qualitatively correct fashion. An important use of thermohydrodynamic simulations is combustion modeling. An important feature of such problem is large temperature variations in the domain from the mean temperature. Very often this can be more than O(1) too. However, the model described in the thesis is only $O(\Delta T^4)$ accurate. Therefore, for practical applications of the methodology described in the thesis, further improvements are needed. The limitations of the present methodology are,

- The model is accurate to $O(\Delta T^4)$, which for example at $T = 300K$, implies that when a temperature difference of 20 % from the mean is attained with the error in the range of 10^{-2}. This difference needs to be improved further.
- The Prandtl number for the model is fixed.
- The ratio of specific heats (γ) is fixed to $Pr = 1$.
- The equation of state is restricted to the ideal gas.

In order to resolve these issues, following strategy can be followed:

- Current models have limitations for flows involving high thermal fluctuations. Such models can be further improved by using a correction scheme to the BGK equation (Kang *et al.*, 2013). In particular, one works with a modified kinetic equation,

$$\partial_t f_i + c_{i\alpha}\partial_\alpha f_i = \Omega_i + F_i \tag{10.1}$$

  where F_i is the forcing term designed to cancel all deviations of the model from the desired thermohydrodynamic equations at the macroscopic limit. This enables us to extend the method to applications involving large temperature gradients.

- Quasi-equilibrium LB models can be used to extend the applicability of the present method to variable Prandtl number (Ansumali *et al.*, 2007*a*; Levermore, 1996).
- In hydrodynamic equations, γ appears only in the energy balance equation. The missing term can be added as a force term which is modeled such that it effects only the dynamics of the energy equation.
- LBM for multiphase and phase separation models are well studied (Chikatamarla *et al.*, 2015; Nourgaliev *et al.*, 2003). When the present method is coupled with such models the equation of state can be varied.

Current thermal model with its roots in kinetic theory should allow large-scale simulations at a wide range of Re and finite temperature variations. We can study the hydrodynamics of such flows with the proposed RD3Q67 discrete velocity model.

For example, Entropic LBM with exact time stepper was employed to perform a study of Rayleigh-Benard simulations using the RD3Q67 model at $Ra = 10^8$ with a temperature difference of 20% from the mean value (Atif *et al.*, 2017). Fig. 10.1 shows the temperature contours of the flow. However, the quantitative study has to be done for further understanding of the flow pattern.

The ability to do large-scale simulations of thermohydrodynamics can be used to study open problems in the area of heat transfer. For example, in case of Rayleigh-Benard convection, following questions are considered open (Niemela *et al.*, 2000) ,

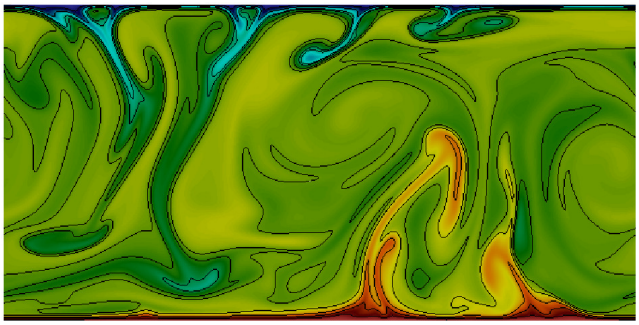

Figure 10.1: Thermal flows with the high Rayleigh number $Ra = 10^8$.

- Whether the empirical power law relating the Nusselt number and the Rayleigh number exists? If so, what is the empirical relation?
- Does the asymptotic state exist?

LBM simulations at very high Rayleigh number might be useful in better understanding of these issues.

Yet another area, where the current method could be useful is that of separated flow in the turbulent regime. For example, numerical simulations of flow separation over an airfoil, airplane wing etc, at high Reynolds numbers is a challenging problem. The proposed methodology coupled with Entropic LBM is a good tool for studying such problems which are of great importance in aerodynamics. Indeed, recently a simulation of viscous flow over a NACA-0012 airfoil at 10° angle of attack (AOA) and a Reynolds number 2.88×10^6 was performed using a higher-order crystallographic LBM (Atif *et al.*, 2017). Fig 10.2 shows a snapshot of instantaneous vorticity field of an airfoil in stall. These studies can be made more realistic.

This thesis has also extended the higher order LBM to transonic as well as transitional rarefied gas flow. In particular, the D3Q167 model developed in this thesis has demonstrated the feasibility of such simulation with LBM. In contrast to DSMC, the present method is quite efficient in the region of $Kn < 1$ and $Ma << 1$. The regime of rarefied gas has the applications in

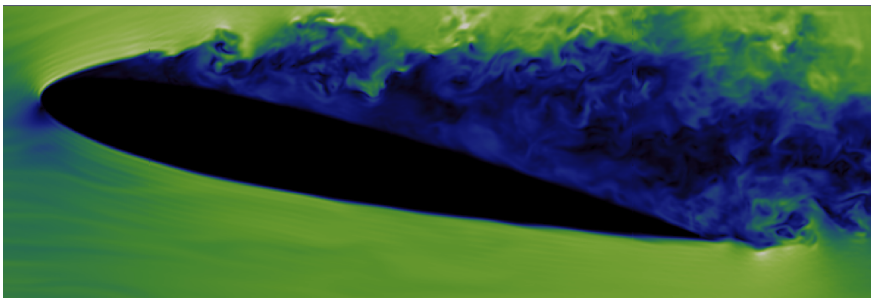

Figure 10.2: snapshot of instantaneous vorticity field of an airfoil in stall

the semiconductor industry to study the heat transfer in semiconductors (Klick & Bernt, 2006).

Finally, a comment on badwidth limited approximation on solution of non-linear PDE such as Navier-Stokes or Boltzmann equation is needed. For example, one can question whether the solutions for Boltzmann equation are bandwidth limited. Indeed, one does not expect PDE solutions to be bandwidth limited. However, one does expect that for non-linear PDEs such as Boltzmann equation, one can find a physically relevant small length scale, beyond which PDE is effectively linear. A fully resolved Direct Numerical Simulation must have grid points to that scale. If that is the case, one would expect bandwidth limited approximation solution will not corrupt the solution at a smaller wavelength.

This issue can be analyzed further, in the hydrodynamics point of view, where, in the low Ma limit the above equation has asymptotic limit of incompressible Navier-Stokes equation,

$$\partial_t \mathbf{u} + \mathbf{u}.\nabla \mathbf{u} = -\nabla p + \nu \nabla^2 \mathbf{u} + \mathbf{f}, \qquad \nabla.\mathbf{u} = 0 \tag{10.2}$$

Fourier transform of the above equation is,

$$\left(\partial_t + \nu k^2\right) \hat{u_i} = -i\mathcal{P}_{ij} \sum_{k_1+k_2=k} \hat{u_i}(k_1)\hat{u_i}(k_2) \tag{10.3}$$

The projection operator $\mathcal{P}_{ij} = \left(\delta_{ij} - \frac{k_i k_j}{k^2}\right)$. Here, we consider, initial condition of the form $u_i\left(k, t=0\right) = \phi_i(k)$, which is not necessarily bandwidth limited.

Suppose the numerical simulation is performed in the range where $0 < k < k_{max}$. This implies that we have approximated the initial condition to a bandwidth limited function

$$u_i\left(k, t=0\right) = \psi_i\left(k\right) \tag{10.4}$$

Where, $\psi_i\left(k\right)$ can written as a bandwidth limited function i.e.,

$$\psi_i\left(k\right) = \begin{cases} \phi(k) & \text{if } k < k_{max} \\ 0 & \text{else} \end{cases} \tag{10.5}$$

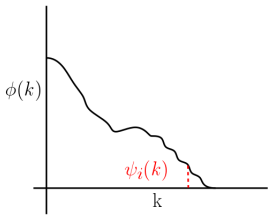

Figure 10.3: The form of initial condition with respect to wave number.

This is illustated in Fig. 10.3, where the original initial condition is denoted by solid line and approximated initial condition is denoted by dotted line.

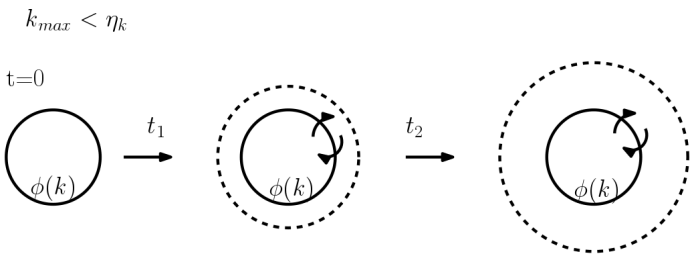

Figure 10.4: Evolution of the initial condition with time for$K_{max} < \eta_k$.

In case of hydrodynamics, it is expected that such cutoff length scale is η. Where η is the Kolmogorov length-scale, $\eta = \left(\frac{\nu^3}{\varepsilon}\right)^{1/4}$ (Frisch, 1995). In the limit of $K_{max} < \eta_k$ as shown in Fig. 10.4 two-way interaction possible with the high wave number and low wave number modes and the the solution does not remain bandwidth limited.

In the limit of $K_{max} > \eta_k$ (shown in the Fig. 10.5) the Eq. (10.3) reduces to

$$\left(\partial_t + \nu k^2\right) \hat{u_i} = 0, \tag{10.6}$$

Thus the higher wavelength does not influence the solution at lower wavelength. Hence the solution approximation is physically plausible.

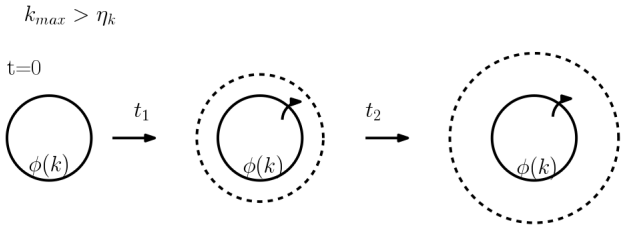

Figure 10.5: Evolution of the initial condition with time for$K_{max} > \eta_k$.

Similarly, for the finite Mach number flows, the relavent smallest length-scale has to the mean free path. Where this is function of Ma and Re as follows,

$$\frac{\eta}{\lambda_{mfp}} \sim \frac{Re^{1/4}}{Ma}. \tag{10.7}$$

To conclude, this new formulation has substantially enhanced the accuracy of the LBM without any loss in the efficiency. Thus, the current approach of formulating LBM on a BCC grid is a step towards the prospect of direct simulations of turbulence without using explicit turbulence models. Here we emphasize that this new route to increase accuracy is not an alternative to building higher order LBM for better accuracy (Chikatamarla *et al.*, 2010). Indeed, by constructing higher-order LB on BCC, the accuracy can be further improved.

References

Abe, T. 1997 Derivation of the lattice Boltzmann method by means of the discrete ordinate method for the Boltzmann equation. *Journal of Computational Physics* **131** (1), 241–246.

Achenbach, E. 1972 Experiments on the flow past spheres at very high reynolds numbers. *J. Fluid Mech* **54** (3), 565–575.

Adhikari, R., Stratford, K., Cates, M. & Wagner, A. 2005 Fluctuating lattice boltzmann. *EPL (Europhysics Letters)* **71** (3), 473.

Aidun, C. & Clausen, J. 2010*a* Lattice-Boltzmann method for complex flows. *Annual Review of Fluid Mechanics* **42**, 439–472.

Aidun, C. K. & Clausen, J. R. 2010*b* Lattice-boltzmann method for complex flows. *Annual Rev. Fluid Mech.* **42**, 439–472.

Alexander, F. J. & Garcia, A. L. 1997 The direct simulation monte carlo method. *Computers in Physics* **11** (6), 588–593.

Ansumali, S., Arcidiacono, S., Chikatamarla, S., Prasianakis, N., Gorban, A. & Karlin, I. 2007*a* Quasi-equilibrium lattice boltzmann method. *The European Physical Journal B* **56** (2), 135–139.

Ansumali, S., Karlin, I., Arcidiacono, S., Abbas, A. & Prasianakis, N. 2007*b* Hydrodynamics beyond navier-stokes: Exact solution to the lattice boltzmann hierarchy. *Physical review letters* **98** (12), 124502.

Ansumali, S. & Karlin, I. V. 2002*a* Entropy function approach to the lattice boltzmann method. *J. Stat. Phys.* **107** (1-2), 291–308.

Ansumali, S. & Karlin, I. V. 2002*b* Kinetic boundary conditions in the lattice Boltzmann method. *Physical Review E* **66** (2), 026311.

Ansumali, S. & Karlin, I. V. 2005 Consistent lattice Boltzmann method. *Physical review letters* **95** (26), 260605.

Ansumali, S., Karlin, I. V. & Öttinger, H. C. 2003 Minimal entropic kinetic models for hydrodynamics. *EPL (Europhysics Letters)* **63** (6), 798.

Ansumali, S., Karlin, I. V. & Öttinger, H. C. 2005 Thermodynamic theory of incompressible hydrodynamics. *Physical review letters* **94** (8), 080602.

Arcidiacono, S., Karlin, I., Mantzaras, J. & Frouzakis, C. 2007 Lattice boltzmann model for the simulation of multicomponent mixtures. *Physical Review E* **76** (4), 046703.

Asinari, P. & Karlin, I. V. 2010 Quasiequilibrium lattice boltzmann models with tunable bulk viscosity for enhancing stability. *Physical Review E* **81** (1), 016702.

Atif, M., Kolluru, P. K., Thantanapally, C. & Ansumali, S. 2017 Essentially entropic lattice boltzmann model. *Physical review letters* **119** (24), 240602.

Bakic, V. 2002 Experimental investigation of turbulent flows around a sphere. PhD thesis, Ph. D. Thesis, TUHH Hamburg, Germany.

Batchelor, G. K. 2000 *An introduction to fluid dynamics*. Cambridge university press.

Benzi, R., Bernaschi, M., Sbragaglia, M. & Succi, S. 2013 Rheological properties of soft-glassy flows from hydro-kinetic simulations. *EPL (Europhysics Letters)* **104** (4), 48006.

Benzi, R., Succi, S. & Vergassola, M. 1992 The lattice boltzmann equation: theory and applications. *Physics Reports* **222** (3), 145–197.

Bhatnagar, P. L., Gross, E. P. & Krook, M. 1954 A model for collision processes in gases. i. small amplitude processes in charged and neutral one-component systems. *Physical review* **94** (3), 511.

Bodenschatz, E., Pesch, W. & Ahlers, G. 2000 Recent developments in rayleigh-bénard convection. *Annual review of fluid mechanics* **32** (1), 709–778.

Boghosian, B. M., Love, P. J., Coveney, P. V., Karlin, I. V., Succi, S. & Yepez, J. 2003 Galilean-invariant lattice-boltzmann models with h theorem. *Physical Review E* **68** (2), 025103.

Boghosian, B. M., Yepez, J., Coveney, P. V. & Wager, A. 2001 Entropic lattice boltzmann methods. In *Proceedings of the Royal Society of London A: Mathematical, Physical and Engineering Sciences*, , vol. 457, pp. 717–766. The Royal Society.

Bowick, M. J., Kinderlehrer, D., Menon, G. & Radin, C. 2017 *Mathematics and Materials*, , vol. 23. American Mathematical Soc.

Brownlee, R. A., Gorban, A. N. & Levesley, J. 2007 Stability and stabilization of the lattice boltzmann method. *Phys. Rev. E* **75** (3), 036711.

Cercignani, C. 1975 *Theory and application of the Boltzmann equation*. Scottish Academic Press.

Chapman, S. & Cowling, T. G. 1970 *The mathematical theory of non-uniform gases: an account of the kinetic theory of viscosity, thermal conduction and diffusion in gases*. Cambridge university press.

Chen, F., Xu, A., Zhang, G., Li, Y. & Succi, S. 2010 Multiple-relaxation-time lattice boltzmann approach to compressible flows with flexible specific-heat ratio and prandtl number. *EPL (Europhysics Letters)* **90** (5), 54003.

Chen, H., Chen, S. & Matthaeus, W. H. 1992 Recovery of the navier-stokes equations using a lattice-gas boltzmann method. *Physical Review A* **45** (8), R5339.

Chen, H., Goldhirsch, I. & Orszag, S. A. 2008 Discrete rotational symmetry, moment isotropy, and higher order lattice boltzmann models. *Journal of Scientific Computing* **34** (1), 87–112.

Chen, H., Kandasamy, S., Orszag, S., Shock, R., Succi, S. & Yakhot, V. 2003 Extended boltzmann kinetic equation for turbulent flows. *Science* **301** (5633), 633–636.

Chen, H., Orszag, S. A., Staroselsky, I. & Succi, S. 2004 Expanded analogy between boltzmann kinetic theory of fluids and turbulence. *Journal of Fluid Mechanics* **519**, 301–314.

Chen, H. & Teixeira, C. 2000 H-theorem and origins of instability in thermal lattice boltzmann models. *Computer Physics Communications* **129** (1-3), 21–31.

Chen, S. & Doolen, G. D. 1998*a* Lattice boltzmann method for fluid flows. *Annual Rev. Fluid Mech.* **30** (1), 329–364.

Chen, S. & Doolen, G. D. 1998*b* Lattice boltzmann method for fluid flows. *Annual review of fluid mechanics* **30** (1), 329–364.

Chikatamarla, S., Ansumali, S. & Karlin, I. 2006*a* Entropic lattice boltzmann models for hydrodynamics in three dimensions. *Physical review letters* **97** (1), 010201.

Chikatamarla, S., Ansumali, S. & Karlin, I. 2006*b* Grad's approximation for missing data in lattice boltzmann simulations. *EPL (Europhysics Letters)* **74** (2), 215.

Chikatamarla, S., Frouzakis, C., Karlin, I., Tomboulides, A. & Boulouchos, K. 2010 Lattice boltzmann method for direct numerical simulation of turbulent flows. *J. Fluid Mech.* **656**, 298–308.

Chikatamarla, S. & Karlin, I. 2013 Entropic lattice boltzmann method for turbulent flow simulations: Boundary conditions. *Physica A: Statistical Mechanics and its Applications* **392** (9), 1925–1930.

Chikatamarla, S., Karlin, I. *et al.* 2015 Entropic lattice boltzmann method for multiphase flows. *Physical review letters* **114** (17), 174502.

Chikatamarla, S. S. & Karlin, I. V. 2006 Entropy and galilean invariance of lattice boltzmann theories. *Physical review letters* **97** (19), 190601.

Chikatamarla, S. S. & Karlin, I. V. 2009 Lattices for the lattice boltzmann method. *Physical Review E* **79** (4), 046701.

Chorin, A. J., Marsden, J. E. & Marsden, J. E. 1990 *A mathematical introduction to fluid mechanics*, , vol. 3. Springer.

Clever, R. M. & Busse, F. H. 1974 Transition to time-dependent convection. *Journal of Fluid Mechanics* **65** (4), 625645.

Conway, J. H. & Sloane, N. J. A. 2013 *Sphere packings, lattices and groups*, , vol. 290. Springer Science & Business Media.

d'Humières, D. 2002 Multiple–relaxation–time lattice boltzmann models in three dimensions. *Philosophical Transactions of the Royal Society of London A: Mathematical, Physical and Engineering Sciences* **360** (1792), 437–451.

d'Humieres, D., Lallemand, P. & Frisch, U. 1986 Lattice gas models for 3d hydrodynamics. *EPL (Europhysics Letters)* **2** (4), 291.

Einfeldt, B., Munz, C.-D., Roe, P. L. & Sjögreen, B. 1991 On godunov-type methods near low densities. *Journal of computational physics* **92** (2), 273–295.

Entezari, A., Dyer, R. & Möller, T. 2009 From sphere packing to the theory of optimal lattice sampling. In *Mathematical Foundations of Scientific Visualization, Computer Graphics, and Massive Data Exploration*, pp. 227–255. Springer.

Filippova, O. & Hänel, D. 1998 Grid refinement for lattice-bgk models. *Journal of Computational Physics* **147** (1), 219–228.

Frapolli, N., Chikatamarla, S. S. & Karlin, I. V. 2015 Entropic lattice boltzmann model for compressible flows. *Physical Review E* **92** (6), 061301.

Frapolli, N., Chikatamarla, S. S. & Karlin, I. V. 2016 Entropic lattice boltzmann model for gas dynamics: Theory, boundary conditions, and implementation. *Physical Review E* **93** (6), 063302.

Frisch, U. 1995 *Turbulence: the legacy of AN Kolmogorov*. Cambridge university press.

Frisch, U., Hasslacher, B. & Pomeau, Y. 1986 Lattice-gas automata for the navier-stokes equation. *Physical review letters* **56** (14), 1505.

Ginzburg, I., dHumières, D. & Kuzmin, A. 2010 Optimal stability of advection-diffusion lattice boltzmann models with two relaxation times for positive/negative equilibrium. *Journal of Statistical Physics* **139** (6), 1090–1143.

Girimaji, S. S. 2007 Boltzmann kinetic equation for filtered fluid turbulence. *Phys. Rev. Lett.* **99** (3), 034501.

Gorban, A. N. & Karlin, I. V. 1994 General approach to constructing models of the boltzmann equation. *Physica A: Statistical Mechanics and its Applications* **206** (3-4), 401–420.

Gorban, A. N. & Packwood, D. 2012 Allowed and forbidden regimes of entropy balance in lattice boltzmann collisions. *Phys. Rev. E* **86** (2), 025701.

Grad, H. 1949 On the kinetic theory of rarefied gases. *Communications on pure and applied mathematics* **2** (4), 331–407.

Grad, H. 1958 Principles of the kinetic theory of gases. In *Thermodynamik der Gase/Thermodynamics of Gases*, pp. 205–294. Springer.

Harting, J., Kunert, C. & Herrmann, H. J. 2006 Lattice boltzmann simulations of apparent slip in hydrophobic microchannels. *EPL (Europhysics Letters)* **75** (2), 328.

He, X. & Luo, L.-S. 1997*a* A priori derivation of the lattice Boltzmann equation. *Physical Review E* **55** (6), R6333.

He, X. & Luo, L.-S. 1997*b* Theory of the lattice Boltzmann method: From the Boltzmann equation to the lattice Boltzmann equation. *Physical Review E* **56** (6), 6811.

He, X., Shan, X. & Doolen, G. D. 1998 Discrete boltzmann equation model for nonideal gases. *Physical Review E* **57** (1), R13.

Higuera, F., Succi, S. & Benzi, R. 1989 Lattice gas dynamics with enhanced collisions. *EPL (Europhysics Letters)* **9** (4), 345.

Holmes, P., Lumley, J. L. & Berkooz, G. 1998 *Turbulence, coherent structures, dynamical systems and symmetry*. Cambridge university press.

Hussaini, M. Y. & Zang, T. A. 1987 Spectral methods in fluid dynamics. *Annual review of fluid mechanics* **19** (1), 339–367.

Johnson, T. & Patel, V. 1999 Flow past a sphere up to a reynolds number of 300. *Journal of Fluid Mechanics* **378**, 19–70.

Kang, J., Prasianakis, N. I. & Mantzaras, J. 2013 Lattice boltzmann model for thermal binary-mixture gas flows. *Physical Review E* **87** (5), 053304.

Karlin, I., Bösch, F. & Chikatamarla, S. 2014 Gibbs' principle for the lattice-kinetic theory of fluid dynamics. *Physical Review E* **90** (3), 031302.

Karlin, I., Ferrante, A. & Öttinger, H. 1999 Perfect entropy functions of the lattice boltzmann method. *EPL (Europhysics Letters)* **47** (2), 182.

Karlin, I., Sichau, D. & Chikatamarla, S. 2013 Consistent two-population lattice boltzmann model for thermal flows. *Physical Review E* **88** (6), 063310.

Karlin, I. V., Gorban, A. N., Succi, S. & Boffi, V. 1998 Maximum entropy principle for lattice kinetic equations. *Physical Review Letters* **81** (1), 6.

Kim, S. H., Pitsch, H. & Boyd, I. D. 2008*a* Accuracy of higher-order lattice boltzmann methods for microscale flows with finite knudsen numbers. *J. comput.phys* **227** (19), 8655–8671.

Kim, S. H., Pitsch, H. & Boyd, I. D. 2008*b* Accuracy of higher-order lattice boltzmann methods for microscale flows with finite knudsen numbers. *Journal of computational physics* **227** (19), 8655–8671.

Kittel, C. 2005 *Introduction to solid state physics*. Wiley.

Klick, M. & Bernt, M. 2006 Microscopic approach to an equation for the heat flow between wafer and e-chuck. *Journal of Vacuum Science & Technology B: Microelectronics and Nanometer Structures Processing, Measurement, and Phenomena* **24** (6), 2509–2517.

Koplik, J. & Banavar, J. R. 1995 Continuum deductions from molecular hydrodynamics. *Annual Review of Fluid Mechanics* **27** (1), 257–292.

Krithivasan, S., Wahal, S. & Ansumali, S. 2014 Diffused bounce-back condition and refill algorithm for the lattice boltzmann method. *Phys. Rev. E* **89** (3), 033313.

Ladd, A. J. 1993 Short-time motion of colloidal particles: Numerical simulation via a fluctuating lattice-boltzmann equation. *Physical Review Letters* **70** (9), 1339.

Ladd, A. J. 1994 Numerical simulations of particulate suspensions via a discretized boltzmann equation. part 1. theoretical foundation. *Journal of fluid mechanics* **271** (1), 285–309.

Lallemand, P. & Luo, L.-S. 2000 Theory of the lattice boltzmann method: Dispersion, dissipation, isotropy, galilean invariance, and stability. *Physical Review E* **61** (6), 6546.

Landau, L. D., Lifshitz, E. & Pitaevskij, L. 1981 *Course of theoretical physics. vol. 10: Physical kinetics*. Oxford.

Landau, L. D. & Lifshitz, E. M. 1959 Fluid mechanics, volume 6 of. *Course of Theoretical Physics* pp. 279–281.

Laney, C. B. 1998 *Computational gasdynamics*. Cambridge University Press.

Larsson, J. & Wang, Q. 2014 The prospect of using large eddy and detached eddy simulations in engineering design, and the research required to get there. *Philosophical Transactions of the Royal Society of London A: Mathematical, Physical and Engineering Sciences* **372** (2022), 20130329.

Lebowitz, J., Frisch, H. & Helfand, E. 1960 Nonequilibrium distribution functions in a fluid. *Physics of Fluids (1958-1988)* **3** (3), 325–338.

Levermore, C. D. 1996 Moment closure hierarchies for kinetic theories. *Journal of statistical Physics* **83** (5-6), 1021–1065.

Liboff, R. L. 2003 *Kinetic theory: classical, quantum, and relativistic descriptions*. Springer Science & Business Media.

Luo, L.-S. & Girimaji, S. S. 2002 Lattice boltzmann model for binary mixtures. *Physical Review E* **66** (3), 035301.

Luo, L.-S. & Girimaji, S. S. 2003 Theory of the lattice boltzmann method: two-fluid model for binary mixtures. *Physical Review E* **67** (3), 036302.

McCracken, M. E. & Abraham, J. 2005 Multiple-relaxation-time lattice-boltzmann model for multiphase flow. *Physical Review E* **71** (3), 036701.

McNamara, G. R., Garcia, A. L. & Alder, B. J. 1995 Stabilization of thermal lattice boltzmann models. *Journal of Statistical Physics* **81** (1), 395–408.

Mendoza, M., Boghosian, B., Herrmann, H. & Succi, S. 2010*a* *Phys. Rev. Lett.* **105**, 014502.

Mendoza, M., Boghosian, B., Herrmann, H. & Succi, S. 2010*b* Fast lattice boltzmann solver for relativistic hydrodynamics. *Physical review letters* **105** (1), 014502.

Namburi, M., Krithivasan, S. & Ansumali, S. 2016 Crystallographic lattice boltzmann method. *Scientific reports* **6**.

Niemela, J., Skrbek, L., Sreenivasan, K. & Donnelly, R. 2000 Turbulent convection at very high rayleigh numbers. *Nature* **404** (6780), 837.

Nourgaliev, R. R., Dinh, T.-N., Theofanous, T. G. & Joseph, D. 2003 The lattice boltzmann equation method: theoretical interpretation, numerics and implications. *International Journal of Multiphase Flow* **29** (1), 117–169.

Pareschi, G., Frapolli, N., Chikatamarla, S. S. & Karlin, I. V. 2016 Conjugate heat transfer with the entropic lattice boltzmann method. *Physical Review E* **94** (1), 013305.

Petersen, D. P. & Middleton, D. 1962 Sampling and reconstruction of wave-number-limited functions in n-dimensional euclidean spaces. *Information and control* **5** (4), 279–323.

Pope, S. B. 2000 *Turbulent flows*. Cambridge univ. press.

Prasianakis, N. I. & Karlin, I. V. 2007 Lattice boltzmann method for thermal flow simulation on standard lattices. *Physical Review E* **76** (1), 016702.

Premnath, K. N., Pattison, M. J. & Banerjee, S. 2009 Dynamic subgrid scale modeling of turbulent flows using lattice-boltzmann method. *Physica A* **388** (13), 2640–2658.

Qian, Y., d'Humières, D. & Lallemand, P. 1992 Lattice bgk models for navier-stokes equation. *EPL (Europhysics Letters)* **17** (6), 479.

Qian, Y., Wang, L., He, W. & Hu, H. 2007 Lattice boltzman simulations for 2d turbulence with passive and active particles. *Bulletin of the American Physical Society* **52**.

Qian, Y.-H. & Zhou, Y. 1998 Complete galilean-invariant lattice bgk models for the navier-stokes equation. *EPL (Europhysics Letters)* **42** (4), 359.

Shan, X. 1997 Simulation of rayleigh-bénard convection using a lattice boltzmann method. *Physical Review E* **55** (3), 2780.

Shan, X. & He, X. 1998 Discretization of the velocity space in the solution of the Boltzmann equation. *Physical Review Letters* **80** (1), 65–68.

Shannon, C. E. 1949 Communication in the presence of noise. *Proceedings of the IRE* **37** (1), 10–21.

Shet, A. G., Sorathiya, S. H., Krithivasan, S., Deshpande, A. M., Kaul, B., Sherlekar, S. D. & Ansumali, S. 2013 Data structure and movement for lattice-based simulations. *Physical Review E* **88** (1), 013314.

Shi, Y., Yap, Y. W. & Sader, J. E. 2015 Linearized lattice boltzmann method for micro-and nanoscale flow and heat transfer. *Physical Review E* **92** (1), 013307.

Singh, S., Krithivasan, S., Karlin, I. V., Succi, S. & Ansumali, S. 2013*a* Energy conserving lattice boltzmann models for incompressible flow simulations. *Communications in Computational Physics* **13** (03), 603–613.

Singh, S., Subramanian, G. & Ansumali, S. 2013*b* Lattice fokker planck for dilute polymer dynamics. *Phys. Rev. E* **88** (1), 013301.

Slotnick, J., Khodadoust, A., Alonso, J., Darmofal, D., Gropp, W., Lurie, E. & Mavriplis, D. 2014 *CFD vision 2030 study: a path to revolutionary computational aerosciences*.

Sod, G. A. 1978 A survey of several finite difference methods for systems of nonlinear hyperbolic conservation laws. *Journal of computational physics* **27** (1), 1–31.

Soe, M., Vahala, G., Pavlo, P., Vahala, L. & Chen, H. 1998 Thermal lattice boltzmann simulations of variable prandtl number turbulent flows. *Physical Review E* **57** (4), 4227.

Spalart, P. R. 2009 Detached-eddy simulation. *Annu. Rev. Fluid Mech.* **41**, 181–202.

Struchtrup, H. 2005 *Macroscopic transport equations for rarefied gas flows*. Springer.

Struchtrup, H. & Torrilhon, M. 2003 Regularization of grads 13 moment equations: derivation and linear analysis. *Physics of Fluids* **15** (9), 2668–2680.

Succi, S. 2001*a* *The lattice Boltzmann equation: for fluid dynamics and beyond*. Oxford university press.

Succi, S. 2001*b* *The Lattice Boltzmann method for Fluid Dynamics and Beyond*. Oxford University Press, USA.

Succi, S., Benzi, R. & Vergassola, M. 1992 The lattice Boltzmann-equation -theory and applications. *phys. Rep.* **222**, 145–197.

Succi, S., Filippova, O., Chen, H. & Orszag, S. 2002*a* Towards a renormalized lattice boltzmann equation for fluid turbulence. *Journal of Statistical physics* **107** (1-2), 261–278.

Succi, S., Karlin, I. V. & Chen, H. 2002*b* Colloquium: Role of the h theorem in lattice boltzmann hydrodynamic simulations. *Reviews of Modern Physics* **74** (4), 1203.

Teixeira, C. M. 1998 Incorporating turbulence models into the lattice-boltzmann method. *Int. J. Modern Phys. C* **9** (08), 1159–1175.

Thampi, S. P., Golestanian, R. & Yeomans, J. M. 2013 Velocity correlations in an active nematic. *Physical review letters* **111** (11), 118101.

Thantanapally, C., Patil, D. V., Succi, S. & Ansumali, S. 2013*a* Universal mechanism for saturation of vorticity growth in fully developed fluid turbulence. *J. Fluid Mech.* **728**, R4.

Thantanapally, C., Singh, S., Patil, D. V., Succi, S. & Ansumali, S. 2013*b* Quasiequilibrium lattice boltzmann models with tunable prandtl number for incompressible hydrodynamics. *International Journal of Modern Physics C* **24** (12), 1340004.

Tölke, J. 2002 Lattice boltzmann simulations of binary fluid flow through porous media. *Philosophical Transactions of the Royal Society of London A: Mathematical, Physical and Engineering Sciences* **360** (1792), 535–545.

Tomboulides, A. G. & Orszag, S. A. 2000 Numerical investigation of transitional and weak turbulent flow past a sphere. *J. Fluid Mech.* **416**, 45–73.

Tosi, F., Ubertini, S., Succi, S. & Karlin, I. V. 2006 Optimization strategies for the entropic lattice boltzmann method. *J. Sci. Comput.* **30** (3), 369.

Wagner, A. J. 1998 An h-theorem for the lattice boltzmann approach to hydrodynamics. *EPL (Europhysics Letters)* **44** (2), 144.

Willis, D. R. 1962 Comparison of kinetic theory analyses of linearized couette flow. *Phys Fluids (1958-1988)* **5** (2), 127–135.

Yu, D. & Girimaji, S. 2005 Dns of homogenous shear turbulence revisited with the lattice boltzmann method. *Journal of Turbulence* (6), N6.

Yudistiawan, W. P., Ansumali, S. & Karlin, I. V. 2008 Hydrodynamics beyond navier-stokes: The slip flow model. *Physical Review E* **78** (1), 016705.

Yudistiawan, W. P., S.K., K., D.V., P. & S., A. 2010 Higher-order galilean-invariant lattice boltzmann model for microflows: Single-component gas. *Phys Rev E* **82** (4), 046701.